OPEN QUANTUM SYSTEMS :
CONTROLLING SYSTEM-BATH INTERACTIONS
AND STUDYING THEIR INFLUENCE

A Dissertation

Presented to the Faculty of the Graduate School

of Cornell University

in Partial Fulfillment of the Requirements for the Degree of

Doctor of Philosophy

by

Yogesh Sharad Patil

May 2018

OPEN QUANTUM SYSTEMS :

CONTROLLING SYSTEM-BATH INTERACTIONS

AND STUDYING THEIR INFLUENCE

Yogesh Sharad Patil, Ph.D.

Cornell University 2018

All quantum systems are open to some extent, i.e. they interact with their environment. In this thesis, we develop novel techniques to control these system-bath interactions and then demonstrate through experiments their significant influence on system properties and dynamics.

We develop a novel imaging technique in the context of ultracold lattice gases. This imaging technique allows us to tune the rate at which the atoms are measured (which can be thought of as an interaction with the electromagnetic radiation environment) over several orders of magnitude, without concomitant heating or loss of the atoms. Using this technical ability, we show that in the weak measurement limit, the atoms undergo unabated quantum evolution, i.e. they freely tunnel around the lattice, whereas as the measurement strength is increased, the tunnelling gets suppressed, the coherence is lost, and the atoms approach a classical limit of slower diffusion; demonstrating the influence of the degree of system-bath interactions on the system's dynamics.

Moreover, the dissipation of open systems also allows for the realization of driven-dissipative phase transitions. We demonstrate and characterize such a phase transition in a system of ultrahigh-Q optomechanical Silicon Nitride membrane resonators, and then employ it to study the influence of system-bath interactions on criticality and phase transitions. In particular, we develop an

active feedback protocol that allows us to change not only the strength of the resonators' interactions with the bath but also the very nature of their interactions (non-Markovian *vs* Markovian). We experimentally demonstrate that these can markedly influence the criticality of the driven-dissipative phase transition through measurements of critical and scaling exponents, which significantly change with changing system-bath interactions. Furthermore, we also demonstrate that the very phases that the system supports can be influenced by the interactions – a class of non-Markovian interactions is shown to effect a phase, a nonequilibrium steady state, that has no analog in the Markovian case.

Lastly, we consider a couple of applications of these resonator systems to enhance force-sensing capabilities. We also discuss the future prospects of such control techniques and other extensions of the works presented in this thesis for gaining further insights into the influence of system-bath interactions on system properties and behavior.

BIOGRAPHICAL SKETCH

Yogesh was schooled for ten years in Bombay, Maharashtra, India, under the vigil and care of brilliant teachers at Parle Tilak Vidyalaya, headed by Principal Sharada Limaye. Then for two brief years, he was under the tutelage of professors Manoj Karmarkar, Vinayak Antarkar and Smita Chhatre. He thereafter received his Bachelors in Engineering Physics at the Indian Institute of Technology (IIT), Bombay, taught by professors par excellence, many from the Tata Institute of Fundamental Research (TIFR), Mumbai. His honors thesis project was guided and supervised by Prof. Raghava Varma. Since 2012, he has been with the Ultracold Atoms group at Cornell University, serving apprenticeship with Prof. Mukund Vengalattore.

To माझी फुलवेडी Ma...

ACKNOWLEDGEMENTS

No man is an island, entire of itself;

Every man is a piece of the continent, a part of the main...

– John Donne

Many thanks also to all those working behind the scenes to support our research group over the years, particularly since 2014. Their efforts and the sacrifices of their time are greatly appreciated.

There is also a number of teachers and friends, from my time before Cornell, whose support, encouragement and guidance I am very grateful for. A lot is because of the doors they opened and the burden they bore.

Thanks are also due to all the butterflies that flapped their wings, near and far...

TABLE OF CONTENTS

LIST OF ABBREVIATIONS

Abbreviation	Meaning
AMO	Atomic, Molecular and Optical
AOM	Acousto Optic Modulator
ASIC	Application-Specific Integrated Circuit
BAE	Back Action Evasion
ECDL	External Cavity Diode Laser
FPGA	Field Programmable Gate Array
KZ	Kibble-Zurek
LPCVD	Low Pressure Chemical Vapor Deposition
LSD	Linear Spectral Density
OP	Order Parameter
OPA	Optical Parametric Amplifier
OPO	Optical Parametric Oscillator
PA	Parametric Amplifier
PO	Parametric Oscillator
PID	Proportional-Integral-Derivative controller
PSD	Power Spectral Density
Q	Quality factor
QED	Quantum Electro Dynamics
QMFS	Quantum Mechanics Free Subspace
QND	Quantum Non Demolition
QZE	Quantum Zeno Effect
RAM	Residual Amplitude Modulation
RG	Renormalization Group
RMS	Root Mean Squared
RSC	Raman Sideband Cooling
SiN	Silicon Nitride
SNR	Signal to Noise Ration
SQL	Standard Quantum Limit
TLS	Two Level System

LIST OF PUBLICATIONS

§ Y. S. Patil, S. Chakram, L. M. Aycock, and M. Vengalattore, *Nondestructive imaging of an ultracold lattice gas*, Physical Review A **90**, 033422 (2014)

§ Y. S. Patil, S. Chakram, and M. Vengalattore, *Measurement-induced localization of an ultracold lattice gas*, Physical Review Letters **115**, 140402 (2015)

§ Y. S. Patil, S. Chakram, L. Chang, and M. Vengalattore, *Thermomechanical Two-Mode Squeezing in an Ultrahigh-Q Membrane Resonator*, Physical Review Letters **115**, 017202 (2015)

§ Y. S. Patil, H. F. H. Cheung, T. Villazon, A. G. Date, A. Polkovnikov, A. Chandran, and M. Vengalattore, *Critical behavior of a driven dissipative system : Universality beyond the Markovian regime*, to be submitted

§ Y. S. Patil, H. F. H. Cheung, and M. Vengalattore, *Emergent dynamical order and time translation symmetry breaking due to non-Markovian system-bath interactions*, to be submitted

§ Y. S. Patil, S. Chakram, and M. Vengalattore, *Back-action evading measurements of two quadratures using a parametric coupling*, to be submitted

§ S. Chakram, Y. S. Patil, and M. Vengalattore, *Multimode phononic correlations in a nondegenerate parametric amplifier*, New Journal of Physics **17**, 063018 (2015)

§ H. F. H. Cheung, Y. S. Patil, and M. Vengalattore, *Emergent phases and novel critical behavior in a non-Markovian open quantum system*, to be published in Physical Review A (2018)

§ H. F. H. Cheung, Y. S. Patil, L. Chang, S. Chakram, and M. Vengalattore, *Demonstration of enhanced force sensitivity using a transient squeezing protocol*, to be submitted

§ S. Chakram, Y. S. Patil, L. Chang, and M. Vengalattore, *Dissipation in ultrahigh quality factor SiN membrane resonators*, Physical Review Letters **112**, 127201 (2014)

CHAPTER 1

BRIEF INTRODUCTION

This thesis details the novel experimental approaches of our labs to achieve control over the system-bath interactions of open quantum systems. It then goes on to describe three studies of how such interactions with the environment can significantly influence system properties and dynamics.

Firstly, 'open' here simply refers to the interaction of a system with its environment. In contrast, a 'closed' or 'isolated' quantum system would only interact with itself, much like the universe in its entirety is today thought of as being 'isolated' and not interacting with anything 'outside' itself.

Secondly, our systems of choice are either ultracold atoms, or optomechanical resonators, or a hybrid of the two. (a) Ultracold atoms (and ions) are quantum systems that offer unparalleled and unprecedented control over system properties as also their dynamic manipulation, and therefore make for a natural choice to controllably 'open' up. (b) Optomechanics is a burgeoning research field over the last couple of decades that realizes, in the quantum regime, one of the ubiquitous building blocks of quantum mechanics – the quantum harmonic oscillator. The simplicity of this building block alone is enough to warrant selection for studying the effects of system-bath interactions, but additionally, having borrowed techniques and quantum protocols heavily from the well developed fields of AMO physics and quantum optics, optomechanics offers a promise of exquisite quantum control. (c) The combination of these disparate systems (not used in this thesis, but a huge push within our labs) is inspired and motivated by considerations well expounded in [1].

Each of the following Chapters begins with an overview. It is aimed at giving context to the work presented in the Chapter, and to put the work in perspective of open systems. Chapters 2 and 3 employ cold atoms, whereas Chapters 4, 5, 6 and 7 employ a widely used optomechanical resonator – a Silicon Nitride membrane resonator. It should be noted at the outset that the optomechanical experiments in this thesis are all implemented at the high temperature classical limit [1], though the description is retained to be quantum, given that the results and experiments can be extended into the quantum regime.

---

[1]Optomechanical experiments in the quantum regime, experiments with the hybrid systems, and other ultracold atomic experiments would have been possible and completed by now, had it not been for the extremely difficult and annoying circumstances unnecessarily forced upon our group since 2014 – the fact that majority of the optomechanical works described in this thesis, and all of our ongoing work, is possible only because of a yet-active restraining order our advisor obtained since 2016, allowing our labs to carry on with our research, speaks volumes by itself. See also [2].

CHAPTER 2

NONDESTRUCTIVE IMAGING OF AN ULTRACOLD LATTICE GAS

2.1   Overview

Imaging of ultracold atoms in the atomic, molecular and optical physics community has been conventionally associated with a concomitant "destruction" of the atomic cloud [3]. This is because the most commonly employed techniques of imaging these clouds, absorption or fluorescence imaging, employ laser light near one of the atom's electronic resonances, which causes the atoms to be electronically excited. In absorption imaging, this absorption of the near-resonant light casts a shadow in the laser beam, the laser and shadow both being recorded on a camera that is in-line with the shined laser beam. The shadow constitutes an 'image' of the atoms and thus a measurement of the atomic cloud's position, density, and other relevant quantities. In fluorescence imaging, the spontaneous emission of photons, which accompanies the relaxation of the electrons to their ground or lower-energy state, is imaged on a camera that is off the laser beam axis – the image so formed by these photons realizing the measurement.

In either scheme, the spontaneous emission of the photons is accompanied by an inevitable recoil energy being imparted to the atoms by the photons - in very much the way as the recoil of a gun imparts energy to a shooter. Each photon emission and thus recoil 'kick' increases an atom's kinetic energy. A good signal to noise ratio for the images so captured on a typical commercial inexpensive CCD camera require on the order of a hundred photons to be scattered by each atom. Coupled with the a-directionality of spontaneous emission, this implies an increase in the temperature of the atoms. This increase is significant

compared to the nanoKelvin to microKelvin temperatures of the cold atoms, rendering inaccessible the target physics, if not simply resulting in the atoms heating out of the traps being used to suspend them in ultrahigh vacuum. In experiments that employ small Bose-Einstein condensates (BEC), the imaging destroys the condensate, meaning that in-situ measurements of the condensate evolution are impossible. A new one has to be created, and the experiment repeated, to realize a stroboscopic imaging, each strobe separated by long duty cycles of the conventional evaporation-based BEC creation techniques (> 30 s). So also in lattice gas experiments, where atoms are trapped by the potential formed by standing waves of light [4]. Here, the depth of the trap needs to be sufficiently small for the atoms to tunnel across lattice sites at rates requisite for accessing interesting physics, like that of the Fermi and Bose Hubbard models [5]. Yet again, this precludes any tolerance to the heating induced by the imaging process, preventing in-situ measurements.

This chapter details our novel scheme that combines fluorescence imaging with two-photon Raman sideband cooling in a lattice gas [6]. The latter allows us to not just retain the atoms in the trap, but to do so at the low temperatures they start out at, i.e. at the lowest vibrational level of the lattice trap (as also the same internal spin state), despite the imaging. Ongoing experiments in our labs aim to extend this technique so that an adiabatic release of the atoms from the lattice results in a condensate, consequently allowing for rapid, sub-second, duty cycles for the creation and recreation of large BECs [7]. Apart from this atom-recycling, our scheme also enables the use of measurement through imaging as a controllable knob on the strength of system-bath interactions of a quantum system (the ultracold lattice gas) – the measurement process and interaction of atoms with light may be viewed as an interaction with an environment

[8, 9]. This view and concept has already been illustrated in a subsequent experiment which will be the topic of Chapter 3. Moreover, following our efforts and work, today, the combination of fluorescence imaging and two-photon Raman sideband or related cooling techniques has already been deployed by several labs worldwide, e.g. in single-lattice-site resolution 'quantum gas microscopes', enabling a range of other hitherto inaccessible experiments [10, 11, 12, 13, 14, 15].

This chapter has been previously published as *Nondestructive imaging of an ultracold lattice gas, by Y. S. Patil, S. Chakram, L. M. Aycock, and M. Vengalattore, Physical Review A **90**, 033422 (2014).* Reproduced here with permission (see Appendix A), with cosmetic changes. In this work, M.V. conceptualized the imaging scheme; M.V., S.C., and L.M.A. contributed to the development of the apparatus; Y.S.P. and M.V. performed the experiments, the data analysis and the simulations; M. V. wrote the paper with help from Y.S.P. and S.C.

2.2 Abstract

We demonstrate the nondestructive imaging of a lattice gas of ultracold bosons. Atomic fluorescence is induced in the simultaneous presence of degenerate Raman sideband cooling. The combined influence of these processes controllably cycles an atom between a dark state and a fluorescing state while eliminating heating and loss. Through spatially resolved sideband spectroscopy following the imaging sequence, we demonstrate the efficacy of this imaging technique in various regimes of lattice depth and fluorescence acquisition rate. Our work provides an important extension of quantum gas imaging to the nondestructive

detection, control, and manipulation of atoms in optical lattices. In addition, our technique can also be extended to atomic species that are less amenable to molasses-based lattice imaging.

2.3 Introduction

The creation, control, and manipulation of ultracold atomic gases in tailored optical potentials has spurred enormous interest in harnessing these mesoscopic quantum systems for the realization of ultracold analogs of correlated electronic materials [16, 5], studies of nonequilibrium dynamics in isolated quantum many-body systems [17] and quantum metrology [18]. The dilute nature of these gases and the weak interactions impose stringent restrictions on the energy, entropy, and means of manipulating and probing these systems. This has led to the development of techniques to cool and image these gases at ever increasing levels of precision and resolution. In this context, the in situ imaging of lattice gases at high spatial resolution has emerged as a powerful tool for the study of Hubbard models [19, 20, 21, 22] and quantum information processing [23].

In this article, we demonstrate a two-photon imaging technique for ultracold lattice gases. The scheme relies on extracting fluorescence from the atoms while simultaneously cooling them to the lowest band of the lattice via Raman sideband cooling (RSC) [6, 24, 25]. Through a combination of sideband spectroscopy and time-of-flight measurements, we demonstrate broad regimes of fluorescence acquisition rates and lattice depths for which the imaging scheme preserves the spatial location and also retains the atoms in the ground vibra-

tional state. As a result, this imaging scheme enables the imaging of atoms in shallow lattices with high fidelity. In addition, the two-photon scheme is less sensitive to details of atomic structure thereby permitting its extension to atomic species less amenable to molasses-based imaging.

2.4 Implementation of the imaging technique

The principle of the imaging sequence is depicted in Fig. 2.1. Raman sideband cooling is employed to cool individual atoms within an optical lattice to the lowest vibrational band while simultaneously pumping the atoms to the high field seeking state. In the case of ^{87}Rb atoms used in our study, this state is denoted by $|g\rangle = |F = 1, m_F = 1; \nu = 0\rangle$, where ν is the vibrational state of the atom within a lattice site. Importantly, this state is a dark state with respect to the optical fields used for Raman cooling. As such, the atoms do not emit any fluorescence while in this ground state. Fluorescence is induced in these atoms by shining a circularly polarized (σ_-) beam resonant with the $F = 1 \rightarrow F' = 0$ (D2) transition. Simultaneous use of RSC mitigates the increase in temperature caused by this fluorescence beam by cycling the atoms back to $|g\rangle$. Due to this cycling, fluorescence can be repeatedly extracted from the atomic distribution while leaving the atom in its original state.

For the studies described below, we use three-dimensional (3D) optical lattices that are typically detuned $2\pi \times 160$ GHz from the $F = 1 \rightarrow F'$ (D2) transition of ^{87}Rb. The lattice provides both the confining potential as well as the coherent two-photon coupling required for sideband cooling [26]. In the absence of RSC, we measure a heating rate of 11 nK/ms due to the photon scattering from
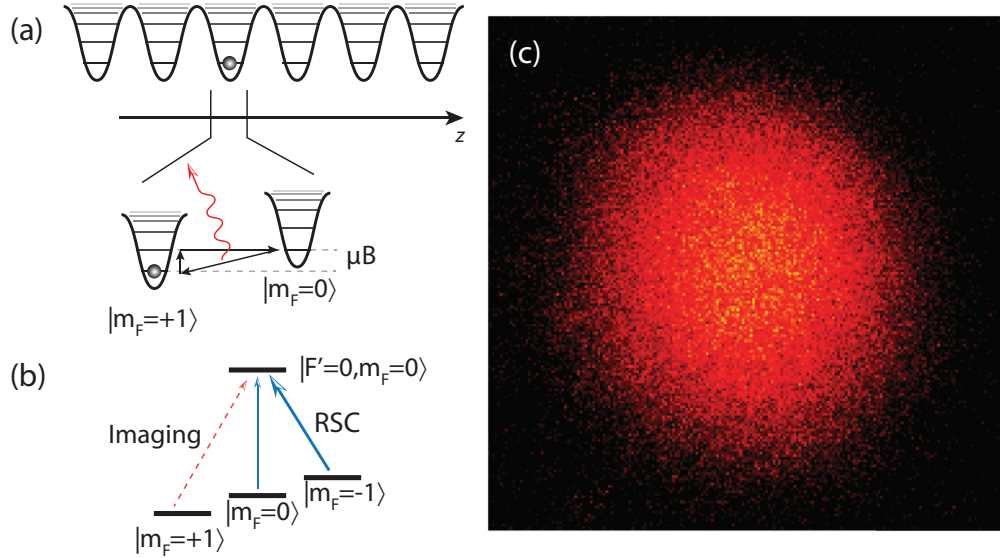
Figure 2.1: (a) Lattice imaging scheme : An atom within a lattice site is cooled to the ground state $|g\rangle \equiv |F = 1, m_F = +1; \nu = 0\rangle$ via RSC. An auxiliary imaging beam promotes the atom out of this state to a fluorescing state, which is subsequently cooled back to $|g\rangle$. Repeated cycles of this process extract fluorescence from the atom while continually restoring the atom to $|g\rangle$; (b) The near-resonance optical fields used in the imaging sequence. A cooling beam (RSC) with σ_+ and π components cools and optically pumps the atom into the dark state $|g\rangle$. A σ_- beam induces fluorescence by bringing the atom out of the dark state. (c) Raman fluorescence image of a gas of 1.5×10^6 atoms obtained within 15 ms. The field of view is $250\mu m \times 250\mu m$.

the near-resonant lattice. While this does not pose a limitation for the studies described in this work, this heating can be significantly reduced by employing separate optical fields to provide the lattice confinement and the Raman coupling.

Atoms are loaded into this lattice and initialized in the ground state $|g\rangle$ by a 10 ms period of RSC. Based on measurements of the atomic density within the lattice, we estimate filling fractions on the order of $f = 0.20 - 0.25$. The average vibrational occupation number is measured using sideband spectroscopy to be

$\langle n \rangle \le 0.01$ for the entire range of lattice depths studied here. Fluorescence images are acquired by switching on the fluorescence beam at a variable intensity. The images are acquired within exposure times of up to 30 ms following which the number of atoms and temperature of the atomic distribution are measured using a combination of time-of-flight absorption imaging and sideband spectroscopy.

We perform sideband spectroscopy to accurately quantify local changes in temperature due to fluorescence imaging. For this, we employ a pair of counterpropagating beams detuned $2\pi \times 7.5$ GHz from the $F = 1 \rightarrow F'$ (D2) transition of ^{87}Rb. The beams are focused to an approximate waist of 8 μm. The measured sideband asymmetry [27] allows a local extraction of the vibrational occupation number (Fig. 2.2). An oblique orientation of these beams with respect to the lattice coordinates ensures sensitivity of the sideband spectra to atomic motion in all three dimensions. The two-photon pulses are typically 500 μs in duration with typical pump (probe) powers of 10 μW (20 nW). We have verified that the vibrational occupation number extracted from the sideband spectra is consistent with temperatures measured by time-of-flight imaging following a rapid ($< 1\,\mu$s) extinction of the lattice [1]. Also, the observed width of the sidebands is consistent with our estimate of the coherent Raman coupling induced by the near-resonant lattice.

---

[1]For very large atom numbers ($\sim 10^8$) where the atomic cloud size is commensurate with that of the lattice waist, the time-of-flight measurements indicate slightly elevated temperatures in comparison to that extracted from the local sideband spectra. This is presumably due to the inhomogeneous variation of lattice frequencies across the atomic distribution and a reduced efficacy of RSC for atoms on the periphery. In such cases, we rely on the sideband spectra for a more reliable estimate of the temperature
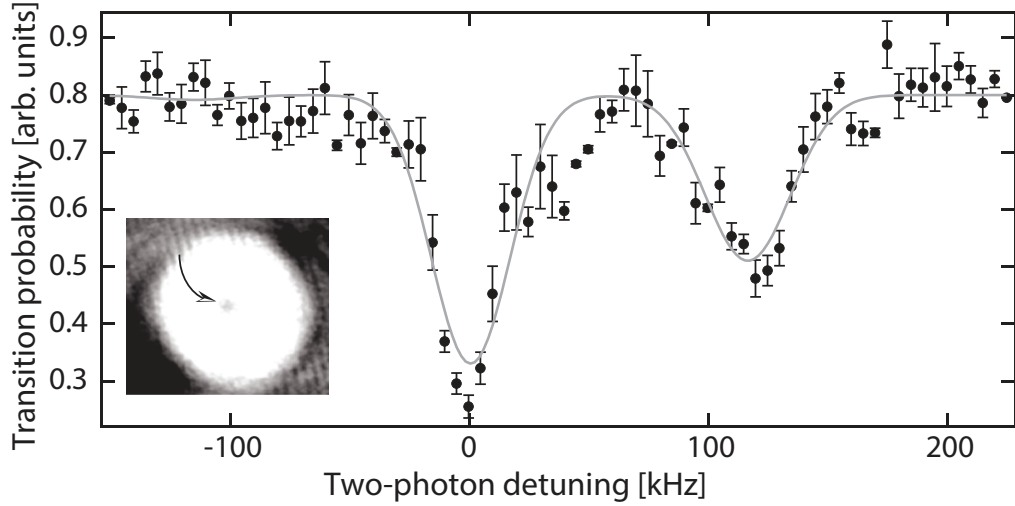
Figure 2.2: Spatially resolved sideband spectroscopy of the lattice gas following the imaging sequence yielding $\langle n \rangle = 0.01^{+0.03}_{-0.01}$. Inset: A time-of-flight absorption image of the ultracold gas following an intense interrogation pulse at the two-photon resonance. The divot near the center of the atomic distribution shows the location and relative size of the beams used for sideband spectroscopy. The field of view is $600\,\mu\text{m} \times 600\,\mu\text{m}$.

2.5 Discussion

Our imaging scheme, as constructed, relies on the competition between two processes: atomic fluorescence at a rate Γ_f that yields spatial information about the atomic distribution, and RSC at a cooling rate Γ_{RSC} that serves to cool the atoms back to the ground state within each lattice site. While the former depends solely on the intensity of the fluorescence beam, the latter is given by $\Gamma_{RSC} \sim \Gamma_{opt} \times \Omega_R^2/(\Gamma_{opt}^2 + 2\Omega_R^2)$ where Ω_R is the coherent Raman coupling between the states $|m_F, v\rangle$ and $|m_F - 1, v - 1\rangle$, and Γ_{opt} is the rate of optical pumping to the $|m_F = +1\rangle$ state [28]. As the fluorescence rate is increased significantly beyond the cooling rate, atoms can be promoted to higher bands within the lattice and can tunnel to neighboring sites. In addition to modifying the atomic dis-

10

tribution, such tunneling can also lead to multiply occupied lattice sites and subsequent loss due to light-induced collisions.

To identify the regimes of imaging where the scheme is nondestructive, we use light-induced collisional loss as a diagnostic tool to monitor atomic tunneling across lattice sites. Further, in order to clearly demarcate atomic dynamics due to the fluorescence pulse from that due to RSC, we employ a pulsed imaging sequence wherein the fluorescence pulse and RSC are employed in rapid succession with a variable duty cycle. As expected, the average vibrational occupation number measured at the end of the fluorescence pulse grows with increasing fluorescence rate [Fig. 2.3(a)]. However, RSC is very efficient at cooling the atoms back to the ground state at the end of each cycle. At the end of each RSC cycle, we measure average vibrational occupation numbers ($\sim$ 0.01) that are, within our measurement uncertainty, indistinguishable from those measured in the absence of the fluorescence pulse (Fig. 2.2). The typical measured RSC cooling rates of 13 μK/ms are also consistent with that estimated based on the intensities of the lattice and optical pumping beams.

While simultaneous cooling during fluorescence acquisition leaves the final vibrational occupation unaltered, the transient increase in temperature during the fluorescence pulse can cause tunneling of atoms to neighboring lattice sites. This tunneling rate depends sensitively on both the average vibrational occupation number as well as the lattice depth U_0, typically parametrized in units of the recoil energy $E_r = \hbar^2 k^2 / 2m$. At low rates of fluorescence acquisition [2], we observe that the total number of atoms is left unchanged subsequent to the

---

[2]The fluorescence rate is calibrated by the measured rate of Raman fluorescence acquired by the camera, and a geometrical estimate of the numerical aperture of our imaging system. This calibration is very close to the rate estimated from the measured intensity and detuning of the fluorescence beam.
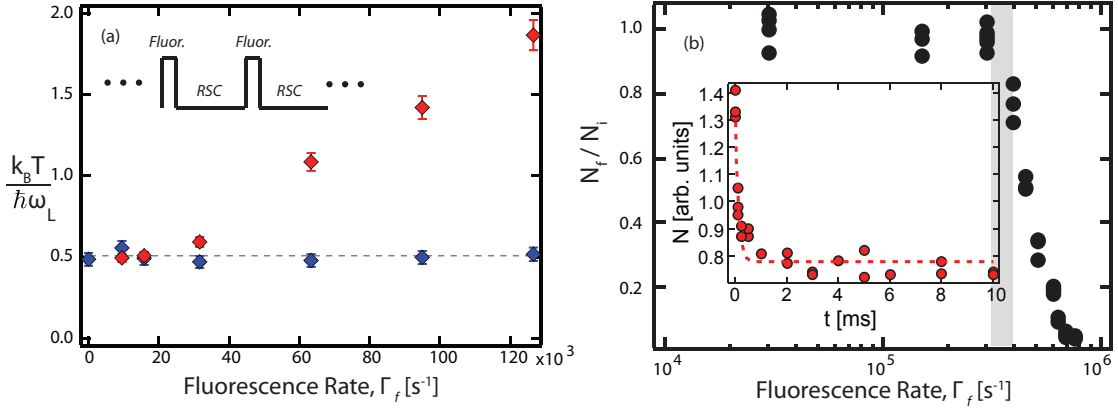
Figure 2.3: Regimes of fluorescence acquisition rates for non-destructive imaging. (a) Measured temperature of the lattice gas in a pulsed imaging sequence, in units of the vibrational frequency ω_L. The temperature during the fluorescence pulse grows (red) with increasing fluorescence rates while RSC rapidly cools the atoms back to the ground state (blue). (b) Measured atom number following the imaging sequence. At low fluorescence rates, the atom number is conserved indicating negligible levels of tunneling across sites. As the fluorescence rate is increased, the increasing temperature during the fluorescence pulse causes tunneling followed by light-induced loss. The shaded area represents the critical fluorescence rate for the onset of tunneling as identified by our measurements of light-induced loss. Inset: Evolution of atom number immediately following an intense fluorescence pulse ($\Gamma_f = 6 \times 10^5$ s^{-1}) shows that RSC quickly (within 100 μs) binds the atoms to the ground state of a lattice site thereby drastically suppressing tunneling.

imaging sequence indicating a negligible level of tunneling across sites. Beyond a certain fluorescence rate $\Gamma_{f,max}$, we observe two-body loss indicating the onset of tunneling of atoms [Fig. 2.3(b)]. As indicated by the rapid decrease of atoms for fluorescence rates past this maximal value, two-body loss is a very sensitive measure of the tunneling rates induced by the imaging sequence (see also Refs. [29, 30]). The temporal evolution of the atom number following a brief, intense fluorescence pulse indicates that RSC cools and binds the atoms to the ground state of a lattice site within 100 μs [see inset of Fig. 2.3(b)], again consistent with

12

measurements of the cooling rate.

We have performed Monte Carlo simulations of the imaging process that accurately capture the sensitivity of two-body loss to tunneling events and the threshold behavior arising from the competition of imaging, RSC, and tunneling. For the filling fractions used in this work (0.20 – 0.25), the measured critical fluorescence rate, $\Gamma_{f,max}$, as identified by the onset of light-induced loss, is within 20% of the critical fluorescence rate for the onset of tunneling. We further find that the filling fraction needs to be reduced by more than an order of magnitude before there is a significant probability of tunneling events that do not lead to measurable loss. These findings justify the correspondence between the onset of tunneling in the lattice gas and our measured onset of two-body loss.
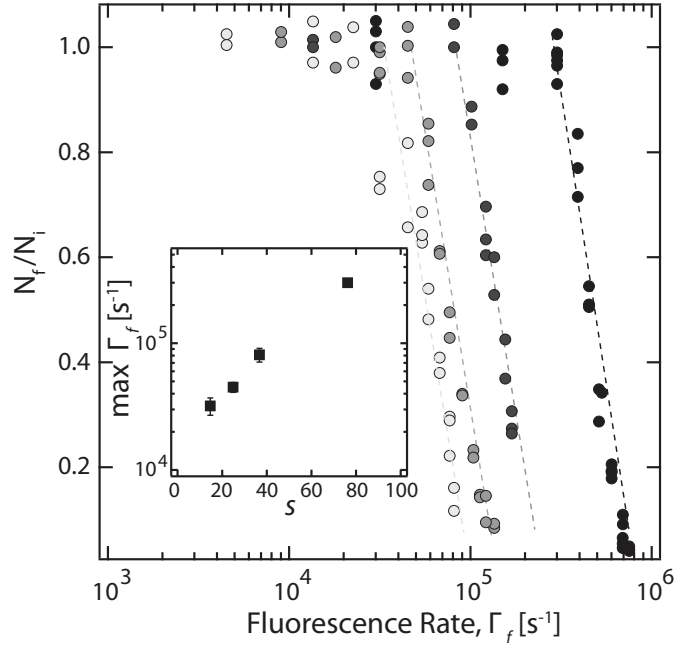
Figure 2.4: The fraction of atoms remaining after the imaging sequence (N_f/N_i) *vs* fluorescence rates for lattice depths of U_0/E_r = 14.6, 24.9, 36.7 and 76.2 (left to right). Inset: An estimate of the maximum fluorescence acquisition rate $\Gamma_{f,max}$ per atom *vs* $s = U_0/E_r$.

13

Similar considerations apply to the imaging of atoms in shallow optical lattices (Fig. 2.4). In this case, the rates of tunneling grow exponentially with decreasing lattice depth [31, 32]. This leads to a reduction of the maximal fluorescence rates that can be used while constraining atomic motion. As expected, an estimate of this maximum allowable fluorescence rate shows an exponential decrease with lower lattice depths (see inset of Fig. 2.4). Importantly, we see that fluorescence acquisition rates greater than 10^4 photons/s per atom are possible even for lattice depths around 15 recoil energies. This makes possible the use of this imaging technique to study lattice gases in regimes where coherent tunneling of atoms within the lowest band occurs on experimentally relevant time scales. In addition, it augurs the intriguing possibility of using this imaging scheme to influence or exert spatial control over such coherent tunneling processes. Nondestructive imaging of atoms in even lower lattice depths could be made possible by increasing the Raman cooling rates and operating at lower fluorescence acquisition rates.

At the lowest lattice depths, possible limitations to our imaging scheme include the reduced fidelity of RSC due to a lower Lamb-Dicke parameter and off-resonant Raman coupling to higher vibrational bands, an increased susceptibility to photon reabsorption heating [25], and faster rates of tunneling to neighboring lattice sites. As we show in Fig. 2.4, these limitations can be overcome by a suitable choice of fluorescence acquisition rate and Raman cooling rates. Already, the lowest lattice depth ($s \sim 15$) for which we demonstrate nondestructive imaging is more than two orders of magnitude below that required for molasses-based lattice imaging.

2.6 Conclusions

In summary, we demonstrate a nondestructive imaging technique for ultracold atoms confined in an optical lattice. The imaging technique is based on extracting fluorescence while simultaneously cooling the atoms to the ground state of the lattice via Raman sideband cooling. Using a combination of sideband spectroscopy and time-of-flight imaging, we demonstrate a large operational regime of fluorescence acquisition rates and lattice depths for which the imaging scheme preserves the spatial location of the atoms while leaving them in the ground vibrational state. At the largest rates of fluorescence acquisition ($\sim 10^6$ photons/s/atom) and the lowest lattice depths, the main loss mechanism occurs due to tunneling of atoms to occupied lattice sites followed by rapid light-induced loss. By using the light-induced loss as a diagnostic measure of tunneling, we show that this limitation can be alleviated by a suitable choice of fluorescence and Raman cooling rates. That said, we note that the imaging scheme demonstrated here does lead to light-induced loss in lattice sites occupied by multiple atoms. In this regard, it is similar to molasses-based imaging in its sensitivity to the parity of lattice occupancy.

Our imaging technique represents a powerful extension of lattice imaging to the nondestructive control and measurement of lattice gases. As such, it is an enabling technique to extend concepts of single-particle quantum control to the context of strongly correlated many-body systems. This scheme also permits the continuous monitoring of the out-of-equilibrium dynamics of ultracold lattice gases. We also note that while used primarily as a diagnostic tool here, spatially resolved coherent two-photon processes such as the setup used for sideband spectroscopy in our work, can also be used for subdiffraction limited quantum

control of the lattice gas [33, 34]. Lastly, our imaging scheme is also extendable to atomic species that are less amenable to molasses-based lattice imaging as well as to lattice geometries [35] where molasses-based imaging can be stymied by local polarization gradients.

CHAPTER 3

MEASUREMENT-INDUCED LOCALIZATION OF AN ULTRACOLD LATTICE GAS

3.1 Overview

Quantum mechanics is one of the two discoveries of the twentieth century that have revolutionized physics (and civilization). Yet, more than a century later, it remains poorly understood why and how the 'bizzare', or rather unintuitive, predictions of quantum mechanics do not readily manifest in everyday life; e.g. why we hardly find any furniture in a superposition of 'here' and 'there', in common parlance. A prevalent theoretical understanding is that the quantum state of a system decoheres due to its couplings or interactions with its environment [36, 37, 38]. And ideas that such decoherence-inducing interactions can fundamentally not be avoided have been theoretically explored, e.g. the inevitability of gravitational interactions for massive systems [39, 40, 41, 42]. The understanding that the quantum entanglement between the system and its bath is the very underlying cause of the emergent classicality of the system has been empirically under-studied and unexplored. Moreover, it has also been suggested that the inefficiencies of quantum measurements may play a role in the observed classicality [43, 44]. Further progress toward a deeper appreciation and understanding of how the quantum description of a system transforms or evolves into a classical or thermodynamic description as the system is allowed to increasingly interact with its bath (the so-called quantum to classical transition) would necessarily be guided empirically. And one of the aims of studying "open" quantum systems is indeed to smoothly connect quantum mechanics

and thermodynamics [45].

So far, experiments and theory are in excellent agreement in the two extremes of isolated quantum systems (no system-bath interactions), and classical thermodynamics (the system and bath interact enough to reach equilibrium at some 'temperature' T). The experimental study of intermediate regimes through an at-will control of the quantum system's interactions with its bath has, however, been elusive. The work described in this Chapter illustrates the use of our novel imaging scheme to realize precisely such a control. The already sophisticated toolbox developed over decades by the atomic physics community offers an exquisite tunability of the isolated quantum system's parameters, like densities, interaction strengths, internal degrees of freedom, etc [16, 5]. Our position-measurement/imaging scheme now adds to that toolbox a knob to tune the atomic system's interactions with its environment (the electromagnetic radiation), controllably variable over several orders of magnitude in strength. Our data demonstrates how a quantum coherent evolution (tunnelling) of atoms in a lattice is suppressed by the system's increasing interactions with the environment, morphing the atomic motion toward a classical limit.

It should be noted that recently, there has been other encouraging experimental progress on a similar front through a study of the thermalization of quantum systems, incidentally, using a quantum-gas-microscope referenced in Chapter 2 [46]. See also [47, 48, 49, 50, 51, 52, 53]. It was experimentally confirmed that while the super-system comprising of a system and its bath can be described as a pure quantum state, the state of the system (a subsystem of the super-system) can be described as a thermodynamic mixed state. Methods and

techniques like the ones described in this Chapter enable the controlled study of such quantum to classical transitions. It is but a concrete illustration of the possibilities enabled by the realization of a control over a system's interactions with its environment, here, simply the total strength of the system-bath interactions. More sophisticated protocols which also allow the control of the very *nature* of these interactions (e.g. non-Markovian vs Markovian, nonlinear vs bilinear) open vast and relatively unexplored vistas, including nonequilibrium physics. This theme of nonequilibrium open systems and the nature of system-bath interactions will recur in the following chapters, where we experimentally explore their influence on system properties and dynamics.

This chapter has been previously published as *Measurement-induced localization of an ultracold lattice gas, by Y. S. Patil, S. Chakram, and M. Vengalattore, Physical Review Letters **115**, 140402 (2015).* Reproduced here with permission (see Appendix A), with cosmetic changes. In this work, M.Vengalattore and S. Chakram contributed to the development of the apparatus. M. Vengalattore did the experiments and data analysis. Y. S. Patil performed the simulations. All authors contributed to the preparation of the manuscript.

3.2 Abstract

The process of measurement can modify the state of a quantum system and its subsequent evolution. Here, we demonstrate the control of quantum tunneling in an ultracold lattice gas by the measurement backaction imposed by the act of imaging the atoms, i.e., light scattering. By varying the rate of light scattering

from the atomic ensemble, we show the crossover from the weak measurement regime, where position measurements have little influence on tunneling dynamics, to the strong measurement regime, where measurement-induced localization causes a large suppression of tunnelinga manifestation of the quantum Zeno effect. Our study realizes an experimental demonstration of the paradigmatic Heisenberg microscope and sheds light on the implications of measurement on the coherent evolution of a quantum system.

3.3 Introduction

A fundamental distinction between a classical and a quantum system is its response to a measurement. While a classical system can be measured to arbitrary precision with negligible concomitant backaction, the act of measurement has profound consequences on the subsequent evolution of a quantum system [54]. In the extreme limit, a sequence of rapid, projective measurements can freeze the decay of an unstable quantum system [55, 29, 30, 56], suppress its coherent evolution [57, 58], or confine such coherences to Hilbert subspaces demarcated by measurement-induced boundaries [59, 60, 61]. These phenomena are different manifestations of the quantum Zeno effect (QZE) [62, 63]. In addition to its foundational implications on the nature of quantum mechanics and the measurement process, the QZE has also garnered attention as a means of stabilizing fragile quantum states, studying emergent classicality in a quantum system due to measurement [64, 65, 66], and for controlling the thermodynamic properties of an isolated quantum system [67].

In a broader context, a measurement can be regarded as an interaction be-

tween a quantum system and a bath whose intrinsic, spatial, and dynamical properties can be precisely engineered. As such, measurements can be used to coax a quantum system into novel collective phases and nonequilibrium states that might otherwise be inaccessible through more conventional means of cooling or state preparation. This is of particular relevance for ultracold atomic and molecular gases in optical lattices which have emerged as pristine realizations of correlated quantum many-body systems [5]. The inherent control and tunability of various properties of these gases have allowed for a diverse range of studies focused on the realization of ultracold analogues of correlated electronic materials [16], studies of nonequilibrium dynamics of isolated quantum many-body systems [17], and the creation of novel many-particle states of matter.

In this Letter, we use a two-photon in situ lattice imaging technique to demonstrate the measurement-induced control of quantum tunneling in an ultracold lattice gas. In contrast to molasses-based lattice imaging schemes, our imaging technique extracts fluorescence from the lattice gas while retaining the atoms in the ground vibrational band of the lattice [68]. By extending this technique down to shallow lattice depths with correspondingly large tunneling rates, we show that the process of imaging has the concomitant effect of dramatically changing the tunneling dynamics. By taking advantage of the large dynamic range of photon scattering rates that are made available by our technique, we observe the continuous crossover of tunneling dynamics from the weak measurement regime, where the act of measurement exerts negligible backaction on the lattice gas, to the strong measurement or quantum Zeno regime, where the act of measurement localizes an atom to a lattice site and leads to a strong suppression of tunneling.

3.4   Our two-photon imaging scheme

The principle of the imaging scheme is depicted in Fig. 3.1. Raman sideband cooling (RSC) [6, 24, 25, 26] is used to cool atoms within an optical lattice to the lowest vibrational band while simultaneously pumping them to the high field seeking spin state $|D\rangle \equiv |F = 1, m_F = 1; v = 0\rangle$. This state is decoupled from the light field and, as such, does not emit fluorescence. As shown in Ref. [68], fluorescence can be induced by shining an auxiliary imaging beam that controllably promotes the atoms to a bright state $|B\rangle$ and subsequently recooling them back to $|D\rangle$ [see Fig. 3.1(a)].

The fluorescence emitted by the atoms can, in principle, be captured by a detector and thus constitutes a position measurement of the emitting atom. While such position measurements nominally impart energy to the atom as a measurement backaction, the simultaneous use of RSC mitigates this increase in energy by cycling the atoms back to the lowest vibrational band. Because of this cycling, fluorescence can be repeatedly extracted from an atom while restoring it to its original state. We introduce a position measurement rate Γ_m which we define to be the scattering rate of photons from the imaging beam, and note that this underestimates the actual scattering rate since it neglects the spontaneous emissions during the subsequent recooling of atoms to $|D\rangle$.
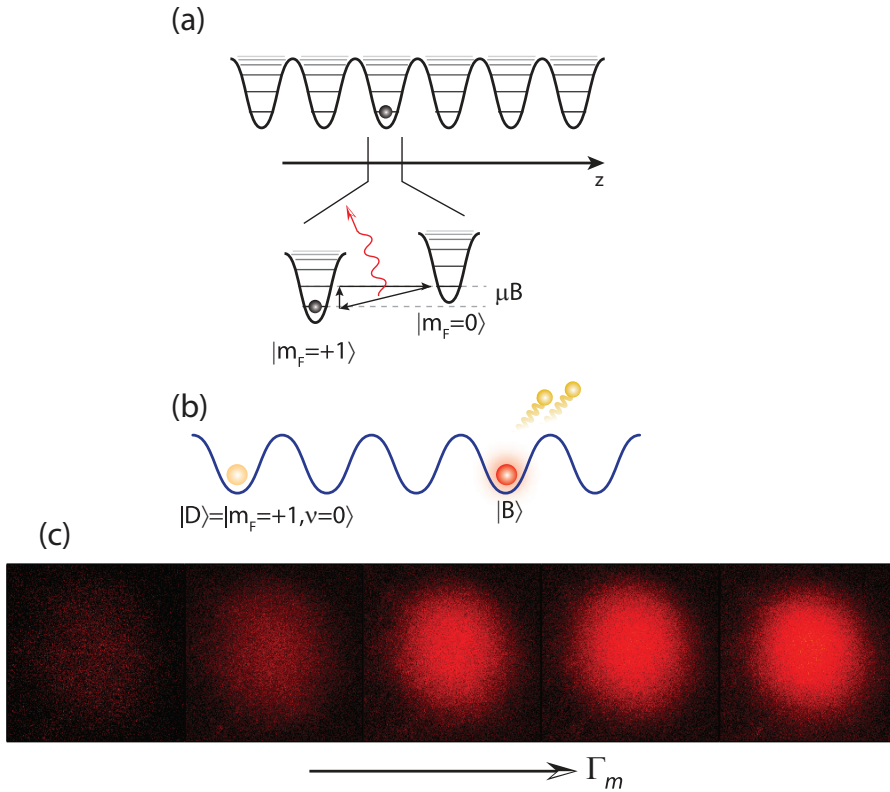
Figure 3.1: (a) Lattice imaging scheme : An atom within a lattice site is cooled to the ground state $|D\rangle \equiv |F = 1, m_F = +1; \nu = 0\rangle$ via RSC. This state is nominally a "dark state", i.e., it does not emit fluorescence. An auxiliary "imaging" beam promotes the atom out of this state to a fluorescing state $|B\rangle$ which is subsequently cooled back to $|D\rangle$. Repeated cycles of this process extract fluorescence from the atom while continually restoring the atom to $|D\rangle$. (b) The imaging scheme thus allows us to distinguish between two possible states of the atom - a bright state $|B\rangle$ that can be imaged and a dark state $|D\rangle$ that cannot be imaged. (c) Fluorescence images of a lattice gas obtained at increasing levels of the measurement rate Γ_m. The field of view of each frame is 250 μm $\times$ 250 μm.

3.5 Photoassociative loss as a measure of the quantum tunneling

In shallow lattices, the atoms can coherently tunnel across sites at a rate J that is exponentially dependent on the lattice parameter $s = U_0/E_r$, where U_0 is the

depth of the lattice and E_r is the recoil energy [31]. For the filling fractions in this Letter ($f \sim 0.25$), such tunneling events frequently lead to multiply-occupied lattice sites at a rate $\Gamma_2 = 4qJf$, where $q = 6$ is the number of nearest neighbors in the 3D lattice [69]. In the presence of the near-resonant light used for fluorescence imaging, such multiply-occupied sites are susceptible to photoassociation and subsequent atom loss at a rate $\kappa_{PA} = \beta \int |\omega_0(r)|^4 d^3r \approx (0.1 - 0.3)\Gamma_m$ (see Supplemental Material, Section 3.9.3). Here, β is the photoassociation rate coefficient and $\omega_0(r)$ is the ground band Wannier function. Thus, the effective two-body loss rate is $\kappa = \Gamma_2 \kappa_{PA}/(\Gamma_2 + \kappa_{PA})$. For our studies described here, we typically operate in the regime $\Gamma_2 \ll \kappa_{PA} < \Gamma_m$. In other words, the formation of multiply-occupied sites, at the rate Γ_2, is the rate-limiting step for photoassociative loss, i.e., $\kappa \approx \Gamma_2$. Based on these rates, we identify photoassociation loss as a sensitive probe of multiply-occupied sites and, hence, the tunneling rate of atoms within the lattice.

3.6 The quantum zeno effect in our system

Coherent tunneling of atoms within the lattice can be strongly influenced by continuous projective measurements of atomic position. Depending on the relative magnitudes of the tunneling rate J and the measurement rate Γ_m, we can identify two distinct regimes. In the weak measurement limit $\Gamma_m \ll J$, the sporadic position measurements have negligible influence on tunneling, and the photoassociation rate κ is independent of the measurement rate [Fig. 3.2(a)].

In the strong measurement limit $\Gamma_m \gg J$, repeated fluorescence emission events continually project the atom into the same lattice site. In our experiments,
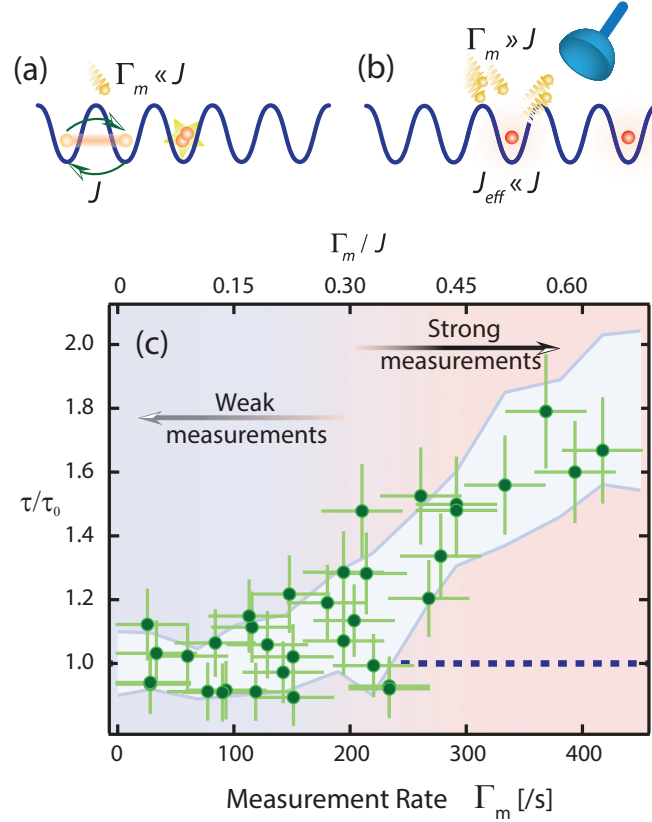
Figure 3.2: Photoassociation measurements demonstrating the crossover from the weak measurement regime ($\Gamma_m \ll J$) to the strong measurement regime ($\Gamma_m \gg J$). In the former regime, (a), position measurements have little influence on tunneling, and the two-body lifetime $\tau = \kappa^{-1}$ is independent of the imaging rate. In the latter regime (b), measurement-induced localization suppresses tunneling rates leading to an increase of the two-body lifetime. (c) Measurements of two-body lifetime vs measurement rate. These data were obtained at a lattice parameter $s = 8.5(2.0)$ with $\tau_0 = 31(3)$ ms.

the wavelength of the emitted photon is commensurate with the lattice spacing. As such, atoms are localized to within a lattice site subsequent to the emission of a photon. This frequent and stochastic localization [70] leads to an incoherent diffusion of atoms within the lattice at an effective tunneling rate given by $\tilde{J}_{eff} \sim J^2/\Gamma_m$ [71, 72]. In other words, the effective tunneling rate $\tilde{J}_{eff}$, the rate of multiply-occupied sites Γ_2, and hence the two-body loss rate κ, monotonically

decreases with increasing measurement rate. In essence, the act of observation "freezes" the lattice gas [Fig. 3.2(b)]. This quantum phenomenon, which does not have a classical equivalent, is a manifestation of the QZE.

In our experiments, we prepare ultracold gases in the ground vibrational band of a 3D lattice (see Supplemental Material). In the absence of the imaging sequence, the lattice gas has a characteristic two-body lifetime τ_0 that is dependent on the lattice depth (and corresponding bare tunneling rate) and residual light scattering due to Raman sideband cooling. In the simultaneous presence of sideband cooling, the lattice gas is subjected to either continuous or pulsed position measurements by the lattice imaging sequence at various photon scattering rates. The scattering rate is calibrated based on the measured power, beam profile and polarization of the imaging beam, and its orientation relative to the ambient magnetic field. At the lowest rates, allowing for various losses and stray light scattering, we estimate that this calibration is accurate to within a factor of 2. This rate can be tuned over a large dynamic range $[O(10^4)]$ by varying the intensity of the imaging beam that induces fluorescence, allowing us to probe both the weak and strong measurement limits as well as the crossover regime.

At low rates of imaging, we observe that the two-body lifetime is unchanged by measurement, reflecting the negligible influence of photon scattering on coherent tunneling. However, as the imaging rates increase, the two-body lifetime of the lattice gas grows [Fig. 3.2(c)]. This reflects the crossover from the weak measurement regime to the strong measurement regime, where now the measurement-induced localization of the atoms is the dominant influence on tunneling dynamics. This crossover regime offers a novel platform for quanti-

tative studies of measurement-induced emergent classicality in a quantum system.

As the rate Γ_m is made much larger than the coherent tunneling rate J, we observe the expected behavior of the effective tunneling rate $J_{eff} \sim J^2/\Gamma_m$. The measured lattice lifetime grows in linear proportion to the measurement rate [Fig. 3.3(a)]. This is a characteristic signature of the quantum Zeno effect; i.e., increasing the rate of fluorescence decreases the photoassociation rate. This suppression of tunneling can also be regarded as arising from the spectral broadening of atomic eigenstates within a lattice site when the measurement-induced width of the eigenstate becomes larger than the bare tunneling rate J. Also, by confining the lattice gas at varying depths while imaging the atoms at constant measurement rate, we show the quadratic dependence of the photoassociation rate with the bare tunneling rates [Fig. 3.3(b)]. The latter are estimated within the tight-binding model based on our calibration of the imposed lattice depth.
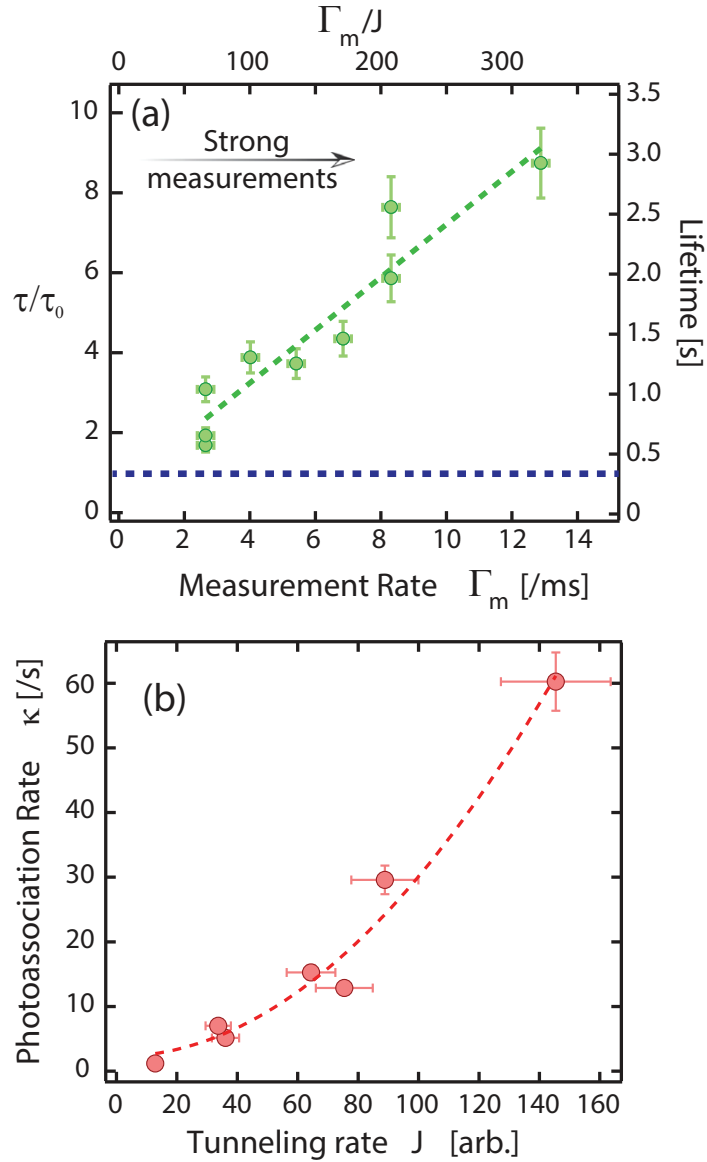
Figure 3.3: In the strong measurement regime, the effective tunneling rate is given by $\tilde{J}_{eff} \sim J^2/\Gamma_m$. This leads to a two-body lifetime $\tau = \kappa^{-1}$ that linearly increases [as seen in (a)] with the measurement rate – a clear signature of the QZE. These data were obtained for $s = 23(2)$. (b) The quadratic scaling of the effective tunneling rate (and hence, the photoassociation rate κ) with the bare lattice tunneling rate is demonstrated by measurements of κ for lattice gases confined in different lattice depths. These data were obtained by imaging the lattice gases at fixed measurement rate Γ_m. The dashed line shows a quadratic fit to the data.
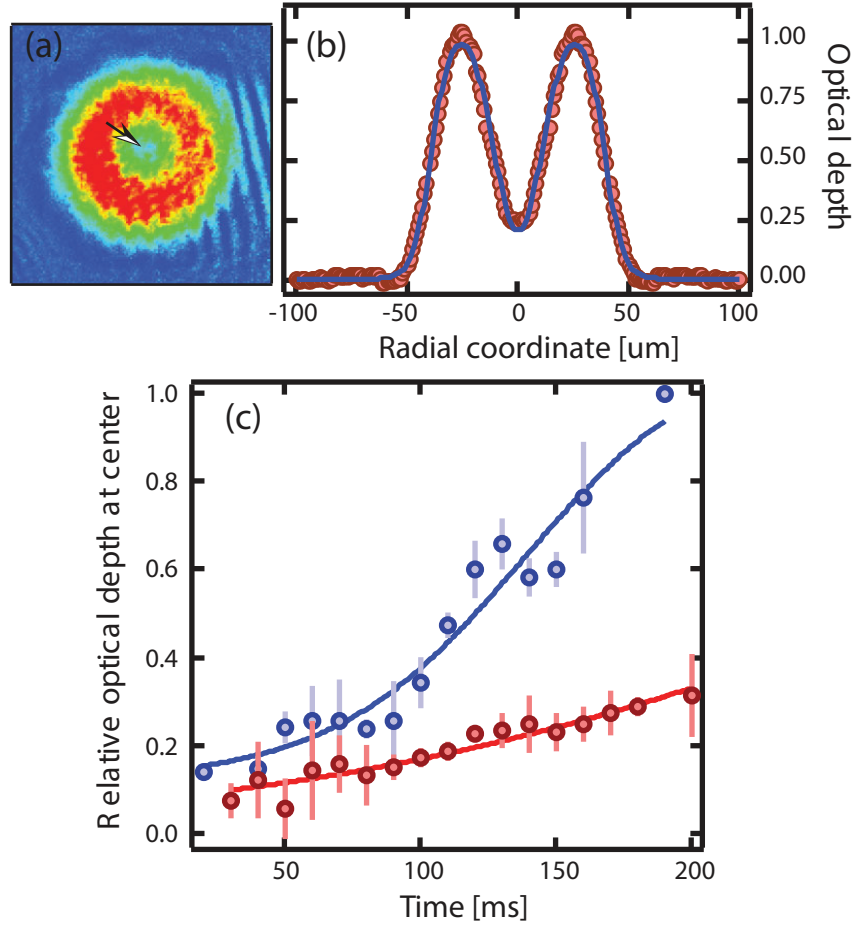
Figure 3.4: Suppression of atomic diffusion due to position measurements. A brief on-resonant optical pulse depletes the central region of the lattice gas [indicated by the arrow in (a)]. (b) Cross section of the atomic ensemble following this pulse. (c) Atoms rapidly diffuse into this central region in the absence of imaging (blue, $s = 8.5$, $\Gamma_m = 0$). In contrast, diffusion is suppressed when the atoms are continuously imaged (red, $s = 8.5$, $\Gamma_m = 1000$ s^{-1}).

We note that two-body loss can also be suppressed because of an effective repulsion arising from dissipative two-body interactions such as photoassociation (also see, for example, Refs. [29, 30, 56]). This can be regarded as a continuous Zeno effect and is distinct from the imaging-induced localization observed in this Letter. To further clarify this distinction, we measure the diffusion rate of atoms within the lattice under the influence of the imaging light. A short, fo-

cused burst of on-resonant light is used to deplete the central region of the gas [Figs. 3.4(a) and 3.4(b)]. Following this, the lattice depth is lowered to $s = 8.5$ to allow the atoms to repopulate the central region by tunneling. The population in this central region is quantified by absorption images of the gas at varying evolution times. In the absence of imaging, the central region is repopulated over time scales of $200 - 500$ ms. In contrast, atomic diffusion is suppressed by imaging [Fig. 3.4(c)], clearly demonstrating localization of the atoms due to light scattering.

3.7 Heating at high measurement rates Γ_m

At first glance, it would appear that an atom can be localized to a lattice site for arbitrary lengths of time for sufficiently large photon scattering rates. However, in general, the act of position measurement causes the atoms energy to increase linearly with time [73]. In our scheme, this increase in energy is mitigated by the simultaneous use of sideband cooling at a rate Γ_{RSC}. For measurement rates that are comparable to this cooling rate, there is a significant contribution from higher vibrational bands with correspondingly larger rates of tunneling [74]. This causes a deviation from the linear growth of the two-body lifetime with measurement rate (Fig. 3.5). Monte Carlo simulations of a noninteracting model of this competition between measurement-induced heating and Raman cooling are in good qualitative agreement with our observations. In the regime $\Gamma_m \gg \Gamma_{RSC}$, the measurement-induced heating dominates any cooling mechanism, and the atom is completely delocalized because of rapid higher-band tunneling, leading to high rates of photoassociation [Fig. 3.5 (inset)]. Based on these considerations, it is clear that the Zeno effect is most readily seen for the
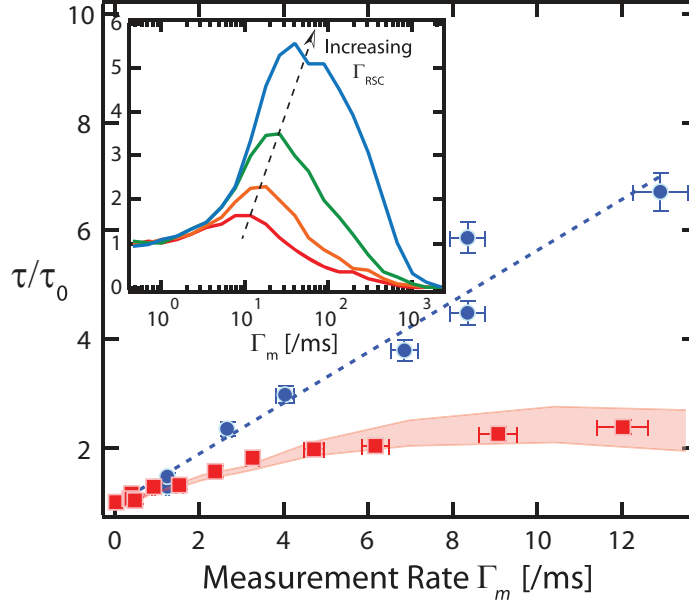
Figure 3.5: For measurement rates Γ_m that exceed the Raman cooling rate Γ_{RSC}, atoms are promoted to higher vibrational bands because of the measurement. The increased tunneling rates in these higher bands cause a deviation from the linear scaling of the lifetime τ with Γ_m. Because of the proportionate relation between the Raman cooling rate and the lattice depth, this deviation occurs more readily for atoms in shallow lattices. The data shown represent two-body lifetimes in the Zeno regime for lattice parameters s = 9.5(1.5), (filled square), s = 21(2), (filled circle). The shaded region represents a Monte Carlo simulation of a kinetic model of the measurement process. Inset: Simulated two-body lifetimes vs measurement rate : the onset of higher-band tunneling occurs at larger Γ_m for increasing Raman cooling rates (bottom to top).

regime $J \ll \Gamma_m \ll \Gamma_{RSC}$.

3.8 Conclusions

In summary, we use an *in situ* lattice imaging technique to demonstrate the measurement-induced localization of an ultracold lattice gas. By varying the

31

rate of imaging, i.e., position measurements, in relation to the tunneling rate within the lattice, we show the smooth crossover from the weak measurement regime where the act of observation causes negligible backaction on the lattice gas, to the strong measurement or Zeno regime where measurement-induced localization causes a strong suppression of coherent tunneling. The large dynamic range and quantum-limited tunability inherent to this imaging scheme should enable new forms of measurement-induced control of a lattice gas by spatially and dynamically varying measurement landscapes.

In addition to shedding light on the nature of measurements and their influence on coherent quantum evolution, we also note the relevance of this study in the context of state preparation in ultracold many-body systems. While the isolation of such systems from the environment has notably allowed for the observation of various forms of long-lived mesoscopic quantum behavior, this decoupling also stymies the creation of low entropy states within experimentally viable time scales. The phenomena observed here could lead to new techniques of backaction-induced cooling, state preparation, and spatially resolved entropy segregation in a lattice gas.

3.9   Supplementary Information

3.9.1   Experimental sequence

In our experiments, ^{87}Rb atoms are confined in a 3D optical lattice that is typically detuned $2\pi\times160$ GHz from the $F = 1 \rightarrow F'$ (D2) transition of ^{87}Rb. The optical lattice provides both the confinement and the coherent two-photon coupling

required for sideband cooling. In the absence of RSC, the measured heating rates are on the order of 5 nK/ms, about three orders of magnitude below the measured Raman cooling rates. By varying the loading conditions, the number of atoms confined in the lattice can be controlled from $10^4 - 10^8$. For the studies described here, atoms are first cooled to the ground vibrational band (average vibrational occupancy $\langle n \rangle < 0.01$) in a deep lattice ($s \sim 50 \pm 1.5$) before the lattice is slowly ramped down to a final depth in the range $s = 6 - 20$. Depending on the final lattice depth, the ambient magnetic field and the optical pumping rates are adjusted continuously during the ramp so as to ensure high fidelities of ground state cooling. Typical filling fractions at the end of this sequence is around $f = 0.25(4)$, as estimated from measurements of atom number and cloud size.

The atomic ensemble is then subjected to either pulsed or continuous position measurements, i.e. imaging, as described in [68], for variable periods of time. At the end of this imaging sequence, the atom number and temperature of the ensemble are measured using time-of-flight imaging and sideband spectroscopy.

3.9.2 Temperature and lattice depth calibration

The average vibrational occupancy is probed through both time-of-flight measurements as well as sideband spectroscopy. For lattice depths $s > 10$, both these measurements coincide at the few percent level. For the lowest lattice depths ($s < 10$), thermometry through measurements of sideband asymmetry was found to be less accurate as the spectral width of the sidebands was com-

parable to the lattice frequency. For such shallow lattices, we relied primarily on temperature measurements obtained by time-of-flight absorption imaging.

The lattice depths were calibrated via sideband spectroscopy. These measurements were performed most accurately for the deeper lattices to obtain a calibration between the measured lattice frequencies and the optical power of the imposed lattice beams. This calibration was then extrapolated to the lowest optical powers to overcome the finite resolution of the sideband spectra for lattice depths $s < 10$.

3.9.3 Relation between the photoassociation rate κ and the imaging rate Γ_m

In the presence of near-resonant light used for position measurements, pairs of atoms within the same lattice can undergo photoassociative loss. This two-body process occurs at a rate

$$\kappa_{PA} = \beta \int |\omega_0(r)|^4 d^3r \tag{3.1}$$

where β is the photoassociative rate coefficient and $\omega_0(r)$ is the ground band Wannier function. The rate coefficient β depends both on the excitation rate, i.e. Γ_m, and on details of the excited state potential characteristic of ^{87}Rb. We can rewrite the above relation to express the photoassociation rate in terms of the imaging rate Γ_m and the lattice parameter s as

$$\kappa_{PA} = \frac{\beta_{ref}}{\Gamma_{ref}} \Gamma_m \times \frac{s^{3/4}}{\pi^{3/2} a_r^3} \tag{3.2}$$

where a_r is the oscillator length corresponding to the recoil energy, and β_{ref} is the rate coefficient measured at an excitation rate Γ_{ref}. Based on the measurements

described in D. Hoffman et al, J. Opt. Soc. Am. B 11, 712 (1994), we estimate $\beta_{ref} = 0.2 \times 10^{-11}$ cm^3/s for an excitation rate $\Gamma_{ref} = 4000$ s^{-1}. This yields

$$\kappa_{PA} = (0.1 - 0.3) \times \Gamma_m \tag{3.3}$$

for the lattice depths used in our work. This relation also implies that measurement-induced localization through imaging, i.e. light scattering, dominates over the effective interatomic repulsion arising from dissipative photoassociative collisions.

Based on the rates presented above, it is clear that our studies of measurement-induced localization are performed in the regime $\Gamma_2 \ll \kappa_{PA} < \Gamma_m$. In other words, the formation of multiply-occupied lattice sites (at a rate Γ_2) is the rate-limiting process for two-body loss. Thus, the two-body loss rate is an accurate probe of the tunneling rate of atoms within the lattice.

3.9.4 Measurement of two-body lifetime

In general, the loss rate of atoms in the lattice is given by the equation $\dot{N}(t) = -\gamma N(t) - \beta n(t) N(t)$ where $n(t)$ is the density and γ is the 1-body loss rate due to background collisions, heating of atoms out of the lattice etc. In our system, the 1-body loss rate ranges from around $(30 \text{ ms})^{-1}$ for the most shallow lattices ($s \sim 6$) to around $(20 \text{ s})^{-1}$ for the deepest lattices ($s \sim 50$). The number of atoms $N(t)$ and the density $n(t)$ are measured by analysis of *in situ* images. After long evolution times, the lattice gas becomes sufficiently sparse that 1-body processes dominate. In this regime, the loss of atoms is exponential (see Fig. 3.6) and is used to constrain the 1-body loss rate γ. The loss rate of atoms at short times is dominated by two-body loss processes as seen in Fig. 3.6. By fitting these data

to the above equation with γ extracted from the long-time data, we extract the two-body lifetime τ.
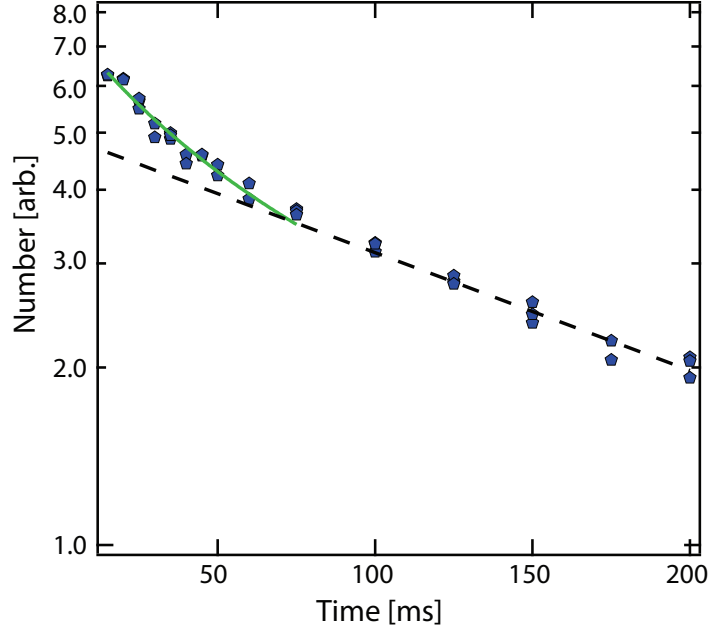
Figure 3.6: Rate of atom loss in the presence of imaging light. At long evolution times, the loss rate of the lattice gas is well described by a one-body process (dashed black line). At short evolution times, the loss rate is more rapid and is well described by a two-body process (green line) that is used to extract the two-body lifetime τ.

3.9.5 Details of Monte Carlo Simulations

To assess the competition between Raman sideband cooling and measurement-induced heating, we performed Monte Carlo simulations of atomic diffusion within the lattice under the simultaneous influence of these competing effects. The simulations were performed in the regime $J \ll \Gamma_m \sim \Gamma_{RSC}$. In this regime, atomic motion can be accurately modeled as a classical diffusive process governed by an effective hopping rate $J_{eff} = J^2/\Gamma_m$. The tunneling rate J is a strong

function of the average vibrational occupancy $\langle n \rangle$ due to the exponential dependence of tunneling rate with increasing band index. As described in our previous work [68], the average vibrational occupancy depends on the competition between sideband cooling and heating due to the imaging process. In our simulations, we used measurements of average vibrational occupancy for various parameter ranges of Γ_{RSC} and Γ_m, as described in [68].

CHAPTER 4

THERMOMECHANICAL TWO-MODE SQUEEZING IN AN
ULTRAHIGH-Q MEMBRANE RESONATOR

4.1 Overview

The efforts outlined in the previous two chapters to realize controllable open quantum systems focused on taking an isolated quantum system (the ultracold atoms) and gradually and controllably making them interact with the environment. A complementary approach is to take systems, like solid state devices, that conventionally come coupled to the environment, and to isolate them. Such an approach is natural, given the ubiquitous use of solid state devices in today's technology in sensing, computing and communications, and the motivation to somehow harvest the ultimate quantum nature of these devices may have to offer in potentially improving their sensitivities and efficiencies [75, 76, 77]. Moreover, apart from technological applications, the realization of massive macroscopic systems in the quantum regime offer unprecedented opportunities for fundamental physics.

Rapid progress in micro and nanofabrication technologies over the last two decades has resulted in our ability to realize, using solid state mechanical devices, one of the ubiquitous building blocks of quantum mechanics – the quantum harmonic oscillator. This progress has been complemented by advances in materials science, our ability to identify and mitigate coupling channels of these resonators to the environment, and the ability to cool these oscillators to the quantum ground state, with or without the use of cryogens. See [78].

Yet, as quantum as the ground state of such mechanical oscillators may be, it is a coherent state, whose observables' expectation values closely follow classical physics. Nonlinear interactions and properties, on the other hand, can bring forth the non-classical attributes of a quantum system. This Chapter deals with a simple system that realizes such a nonlinearity – a coupling of the oscillator to its surroundings, in fact, to a single other oscillator, through a parametric bilinear coupling $H_{ab} \propto (a + a^\dagger)(b + b^\dagger)$, where a and b denote the annihilation operators of the quantum oscillators. This Chapter describes how a parametric modulation of this coupling H_{ab} at the sum of the oscillator frequencies results in correlations between the oscillators' quadratures, which in the quantum regime correspond to entanglement.

Our system of choice is a square $5\text{mm} \times 5\text{mm} \times 100\text{nm}$ Silicon Nitride membrane resonator [79] supporting several vibrational modes which can be taken to the quantum regime through optomechanical cooling [78]. We experimentally realize the mechanical analogue of optical downconversion, i.e. the parametric amplifier - parametric oscillator (PA–PO) system, which in the optical domain forms the basis of heralded single photon sources, squeezed vacuum and other quantum resources with wide ranging applications in quantum information, cryptography, key distribution, Bell tests, etc [80]. An untapped potential so far is to enable analogous capabilities in such mechanical systems.

A major distinction between the optical and mechanical realizations described above is in the timescales of either system – they are separated by orders of magnitude. Optical oscillators occur at 100's of teraHertz (10^{12} Hz), coupling to the environment through the use of state-of-the-art high finesse Fabry-Perot cavities at several kiloHertz. Mechanical oscillators range from a few Hz to sev-

eral GHz in frequency, with state-of-the-art environmental dissipation rates on the order of μHz, for MHz oscillators, i.e. with mechanical Q's of $\sim 50 \times 10^9$ and coherence time of hours, at readily accessible cryo-temperatures [81]. In fact, Silicon Nitride string resonators that can undergo hundreds of quantum coherent oscillations even at room temperature were recently demonstrated [82].

Given existing applications in the communications industry, control electronics are advanced and well developed in the microwave regime, with routinely achievable delay resolutions on the order of 10's of picoseconds (10^{-12} s) for any experimental control sequences. Coupled with MHz–GHz processing using computers, ASICs and FPGAs, this allows for precise and real-time quantum control of such devices, including through feedback and feedforward algorithms. This enables hitherto inaccessible experiments, an illustration of which is Chapter 5, where we demonstrate feedback protocols to realize non-Markovian system-bath interactions of our choosing, enabling novel physics. (In regard to such control, the slower timescales of optomechanical oscillators pose a technical advantage over optical resonators, which require more rapid control.) Looking forward, as such nonlinear optomechanical and other solid-state building blocks are developed and refined in the quantum regime over the coming decades, their combinatorial fusions will rapidly expand our capabilities, both in technology and in the pursuit of fundamental physics.

This chapter has been previously published as *Thermomechanical Two-Mode Squeezing in an Ultrahigh-Q Membrane Resonator, Y. S. Patil, S. Chakram, L. Chang, and M. Vengalattore, Physical Review Letters* **115**, *017202 (2015)*. Reproduced here with permission (see Appendix A), with cosmetic changes. In this work, Y. S. Patil, S. Chakram and L. Chang performed the experimental work and data ac-

quisition. Y. S. Patil and S. Chakram carried out the data analysis and modeling. M. Vengalattore supervised all stages of the work. All authors contributed to the preparation of the manuscript.

The theoretical treatment of the general mechanical PA–PO system realized in this Chapter was considered as a part of a separate piece of work with S. Chakram [83], and is included in Appendix B.

4.2   Abstract

We realize a quantum-compatible multimode interaction in an ultrahigh Q mechanical resonator via a reservoir-mediated parametric coupling. We use this interaction to demonstrate nondegenerate parametric amplification and thermomechanical noise squeezing, finding excellent agreement with a theoretical model of this interaction over a large dynamic range. This realization of strong multimode nonlinearities in a mechanical platform compatible with quantum-limited optical detection and cooling makes this a powerful system for nonlinear approaches to quantum metrology, transduction between optical and phononic fields and the quantum manipulation of phononic degrees of freedom.

4.3 Introduction

The control, measurement and manipulation of mesoscopic mechanical resonators by coherent optical fields has garnered widespread attention in recent years for potential applications to quantum metrology as well as to foundational studies of the quantum-to-classical transition and the quantum mechanics of macroscopic objects [84, 85, 86, 78]. Notable accomplishments in recent years include the optical cooling of mechanical modes to the quantum regime [87, 88] and the detection of mechanical motion with an imprecision below the standard quantum limit [89, 90].

Building upon these developments, attention has now been directed towards the creation of nonclassical mechanical states and the manipulation of phononic fields in a manner akin to quantum optics in nonlinear media. In contrast to the cooling and detection of mechanical motion, the creation of nonclassical states requires strong nonlinear interactions involving the mechanical degree of freedom. Accordingly, several studies have been devoted to the realization of such interactions through parametric processes [91, 92, 93, 94, 95], optically mediated nonlinearities [96], dispersive coupling to an auxiliary quantum system [97, 98], backaction-evading measurements [99, 100] and active feedback [101, 102, 103, 104]. Notwithstanding the diversity of such schemes, it has remained a significant challenge to juxtapose strong, tunable and quantum-compatible nonlinear interactions with the stringent constraints for ground state cooling and quantum control of a mechanical resonator.

Here, we demonstrate that strong mechanical nonlinearities can co-exist with low dissipation by exploiting the concept of reservoir engineering [105,

106, 107, 108] - the control of interactions within a system by appropriate design of its environment. While most proposals along these lines have centered on mechanical control by tuning the properties of an optical reservoir, we show that reservoir engineering can be effected through purely mechanical means. This opens the concomitant prospect of realizing a wide range of novel interactions in micro- and nanomechanical systems through appropriate geometric and material design. In this Letter, a strong nonlinear interaction between distinct modes of a membrane resonator is realized by the parametric mediation of a substrate excitation. We use this nonlinearity to demonstrate nondegenerate parametric amplification and thermomechanical noise squeezing, finding excellent agreement with a theoretical model of this nonlinear interaction over a large dynamic range. The combination of strong multimode mechanical nonlinearities, optical addressability of individual mechanical modes, large $f \times Q$ products [79], compatibility with optomechanical cooling to the quantum regime [109, 110] and quantum-limited optical measurement makes this a powerful system for quantum-enhanced metrology and the quantum manipulation of phononic fields.

4.4   Our experimental system

The mechanical resonators in our study are LPCVD silicon nitride (SiN) membrane resonators manufactured by NORCADA Inc. The membranes are deposited on single crystal silicon wafers and have typical lateral dimensions of 5 mm. In previous work [79], we have identified the role of the substrate in inducing the hybridization of proximal eigenmodes and in modifying the dissipation of the resultant hybridized modes. This leads to the robust formation

43

of a large number of mechanical modes with quality factors $Q \sim 50 \times 10^6$ and $f \times Q \sim 1 \times 10^{14}$ Hz.

In addition to modifying the modal geometry and dissipative properties, the substrate can also mediate and enhance nonlinear interactions between distinct eigenmodes of the resonator. This is especially significant for parametric processes that involve the interaction of two membrane modes mediated by a discrete excitation of the substrate, since the coupling strength is now enhanced by the quality factor of the relevant substrate mode. In our work, this nonlinear interaction between mechanical modes at frequencies ω_i, ω_j is induced by parametrically actuating the substrate at frequencies near $\omega_i + \omega_j$, either by a piezo-electric voltage or a photothermal modulation.

A schematic of the experimental system is shown in Fig. 4.1. The mechanical motion of the membrane is optically detected in a Michelson interferometer with a displacement sensitivity of 0.03 pm/Hz$^{1/2}$ for typical powers of 200 μW incident on the membrane. Distinct eigenmodes are resolved through phase sensitive lock-in detection. The membrane modes exhibiting the two-mode nonlinearities studied in this work are characterized by eigenfrequencies $\omega_i/2\pi \approx 1.5$ MHz, quality factors $Q > 10 \times 10^6$, typical mechanical linewidths $\gamma_i/2\pi < 100$ mHz and $|\omega_i - \omega_j| > 10^6 \gamma_{i,j}$. While the large quality factors are crucial to realizing long coherence times, the narrow linewidths also pose stringent requirements of thermal stability in order to resolve thermomechanical motion and the presence of non-thermal correlations. To achieve the requisite frequency stability, the membrane modes are actively stabilized by photothermal feedback (see Supplementary Information, Section 4.10.1, see also [111]).
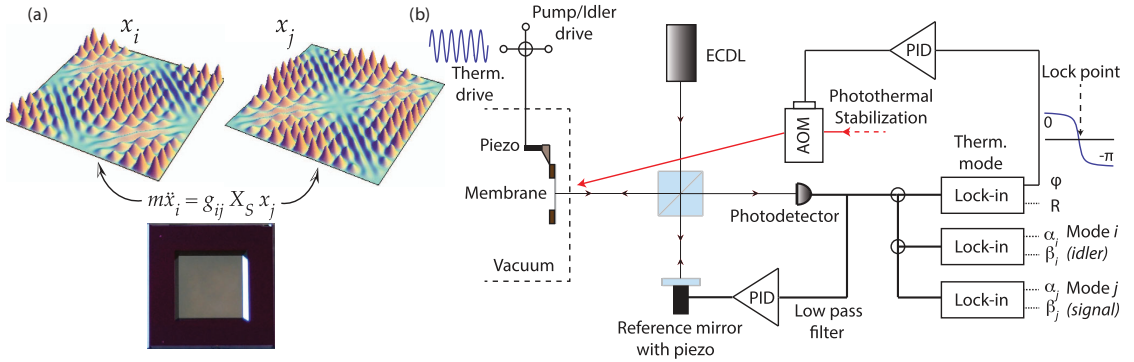
Figure 4.1: (a) The resonator consists of a high-stress silicon nitride membrane deposited on a silicon substrate. Distinct eigenmodes of the membrane resonator (representative eigenfunctions shown) with frequencies $\omega_{i,j}$ are coupled via a substrate-mediated interaction. This two-mode interaction can be controlled by actuating the substrate to an amplitude X_S at frequencies close to $\omega_i + \omega_j$. (b) Experimental schematic: Mechanical motion of the membrane is optically detected in a Michelson interferometer, with the two membrane modes (i, j) distinguished by phase-sensitive lock-in detection. The eigenfrequency of a third, high-Q mechanical mode is continuously monitored and acts as a mechanical 'thermometer'. The resonator modes are actively frequency stabilized to this thermometer mode by photothermal feedback. In the presence of this feedback, the frequency stability of each resonator mode is better than 1 ppb over 1000 seconds. ECDL – External cavity diode laser; AOM – Acousto-optic modulator; PID – Proportional-Integral-Derivative controller.

4.5   Effective two-mode parametric coupling model

The substrate-mediated coupling between a pair of membrane modes can be modeled by an interaction $\mathcal{H}_{ij} = -g_{ij}X_S x_i x_j$ where g_{ij} parametrizes the strength of the two-mode coupling, X_S is the displacement of the substrate (or 'pump') mode and $x_{i,j}$ denotes the displacement of the two membrane modes. This interaction can be attributed to a parametric excitation of a discrete mode of the substrate at a frequency $\omega_S = \omega_i + \omega_j$, that couples the membrane modes. Actu-

ation of the substrate at this frequency thus leads to nondegenerate parametric amplification of the individual membrane modes.

As is well known in such parametric amplifiers, a sufficiently strong interaction (or a large actuation of the pump field) leads to an instability and self-oscillation of the individual membrane modes. In the case of resonant actuation, our two-mode model predicts a threshold amplitude for self-oscillation given by (see Supplementary Information, Section 4.10.5),

$$X_{S,th}(g) = 2 \sqrt{\frac{1}{g^2} \times \frac{1}{\chi_i \chi_j}} \propto \sqrt{\frac{1}{g^2} \frac{1}{Q_i Q_j}} \tag{4.1}$$

where $\chi = (m\omega\gamma)^{-1}$ are the on-resonant mechanical susceptibilities of the two membrane modes and g is the strength of the two-mode coupling. The inverse dependence of the threshold pump amplitude on the quality factors of the high-Q membrane modes leads to strong nonlinear behavior even for pump displacements on the order of 10 fm. Past the instability threshold, we observe amplification of the membrane modes by more than 30 dB (see Fig. 4.2(a)).

4.6 Parametric modification of dissipation rates

While the parametric amplification of the membrane modes can be regarded as a down-conversion of substrate excitations, a related process is the up-conversion of excitations from the membrane into the substrate. In the absence of substrate motion, actuation of the membrane modes can lead to coherent transfer of energy from the membrane into the substrate. From the perspective of either membrane mode, this parametric transfer of energy into the far lossier substrate results in a dissipation rate that is dependent on the amplitude of the other membrane mode.
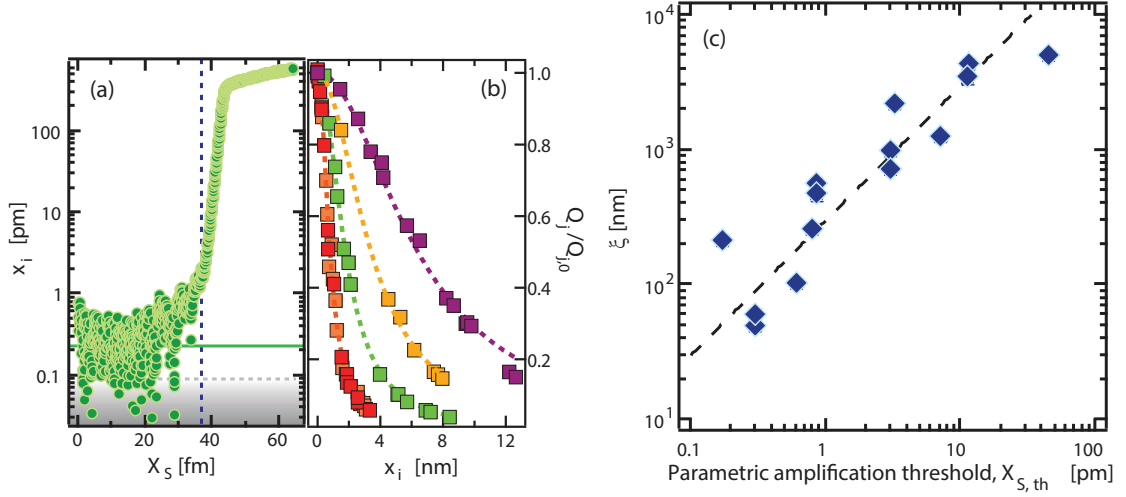
Figure 4.2: (a) Parametric amplification of a membrane mode due to actuation of the substrate. The vertical line indicates the threshold for parametric instability. The solid green line indicates the thermomechanical amplitude of the membrane mode. The dashed grey line shows the detection noise floor. (b) In the absence of the parametric drive, large amplitude oscillations of either membrane mode (x_i) results in increased dissipation (and a lower quality factor Q_j) of the other mode due to upconversion of excitations into the substrate. The variation of the normalized dissipation ($Q_j/Q_{j,0}$), shown above for various pairs of coupled modes, is well described by a characteristic length scale ξ (see text). (c) The linear dependence of the length scale ξ (extracted from data such as shown in (b)) *vs* the threshold amplitude for parametric instability, as predicted by the two-mode model. See Supplementary Information, Section 4.10.8, for details of the various modes depicted above.

To study this process, the mechanical ring-down time τ of a membrane mode j was measured in the presence of a large amplitude actuation of its partner mode i. Care was taken in these measurements to maintain the amplitude of mode j in the linear response regime. The two-mode upconversion process results in an effective quality factor $Q_j(x_i) = \omega_j \tau(x_i)/2$ and an effective mechanical linewidth $\gamma_j(x_i) = 2/\tau(x_i)$ that is in excellent agreement with the prediction of

the two-mode model (see Supplementary Information, Section 4.10.6),

$$\gamma_j(x_i) \approx \frac{\gamma_S}{2}\left[1 + \frac{2\gamma_j}{\gamma_S} - \sqrt{1 - \left(\frac{x_i}{\xi}\right)^2}\right] \tag{4.2}$$

where $\gamma_j \ll \gamma_S$ are the intrinsic mechanical linewidths of membrane mode j and the substrate mode (see Fig. 4.2(b)). The length scale ξ denotes the characteristic amplitude of mode i when the dissipation rate of the membrane mode j matches that of the substrate, i.e. the maximal rate of up-conversion of energy from the membrane into the substrate. Because of the large mismatch between the intrinsic dissipation rates and masses of the substrate and the membrane, this up-conversion process requires displacements of the membrane modes that are more than five orders of magnitude larger than typical thermomechanical motion (see Fig. 4.2), and much larger than the typical amplitudes of motion considered in this Letter.

While seemingly distinct processes observed at vastly differing scales of displacement (fm vs nm), nondegenerate parametric amplification and nonlinear dissipation due to up-conversion of excitations into the substrate both owe their origins to the two-mode nonlinearity. Indeed, the model predicts that the length scale ξ that parametrizes two-mode control of mechanical dissipation, can be related to the threshold amplitude $X_{S,th}$ according to the relation $\xi(g) = \frac{1}{2}(\gamma_S/\gamma_i)^{1/2}(\chi_j/\chi_S)^{1/2} \times X_{S,th}(g)$. Given that the quantity $(\gamma_S/\gamma_i)^{1/2}(\chi_j/\chi_S)^{1/2}$ does not vary significantly for the mode pairs studied (see Supplementary Information, Section 4.10.8), we expect a linear relation between $\xi(g)$ and $X_{S,th}(g)$. Through independent measurements of parametric amplification thresholds and nonlinear two-mode dissipation for a wide range of membrane mode pairs, we have verified this linear dependence (see Fig. 4.2(c)). As can be seen, the various mode pairs that were studied exhibit interaction strengths that vary over

three orders of magnitude. The close agreement between our measurements and the predictions of the model over a large dynamic range of parameters further affirms the robustness and fidelity of this nonlinear interaction in our system.

4.7 Realization of a phase-sensitive amplifier

Having established the accuracy of our two-mode model, we now discuss the dynamics of this nondegenerate parametric amplifier for a pump field driven below the threshold $X_{S,th}$. In this regime, weak actuation of a membrane mode i (idler mode) results in the phase coherent production of down-converted phonons in the other membrane mode j (signal mode). This down-converted field, which has a well determined phase relationship with the pump and idler fields, can coherently interfere with any pre-existing signal field. Thus, the amplification of the signal field acquires a strong dependence on the pump phase ϕ according to the relation (see Supplementary Information, Section 4.10.5)

$$G_j(\phi) = \frac{1}{1 - \mu^2} \sqrt{1 + \mu^2 \eta^2 - 2\mu\eta \cos \phi} \tag{4.3}$$

where $\mu = X_S/X_{S,th}$ is the pump amplitude normalized to the threshold amplitude for parametric instability, and $\eta = (\chi_j/\chi_i)^{1/2} \times (\bar{x}_i/\bar{x}_j)$ where $\bar{x}_{i,j}$ are the amplitudes of the membrane modes in the absence of the pump. As can be seen, the parameter $G_j(\phi)$ depends on both the amplitude and phase of the input signal field. In this sense, Eq. (4.3) can be regarded as the mechanical equivalent of phase-sensitive amplification observed in nondegenerate optical parametric amplifiers (see, for example, [112]).

We demonstrate phase-sensitive amplification by simultaneously monitor-
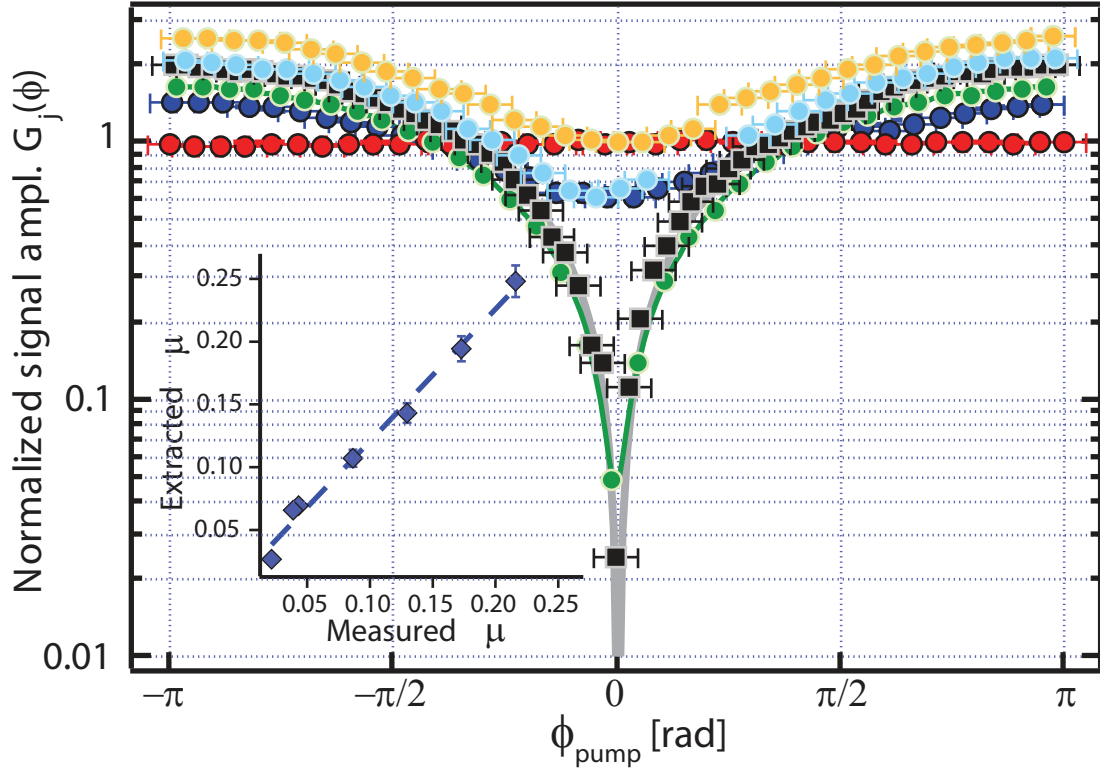
Figure 4.3: Phase-sensitive amplification, $G_j(\phi)$, versus the phase of the pump excitation. Data shown correspond to normalized pump amplitudes $\mu = X_S/X_{S,th} = 0, 0.021, 0.038, 0.042, 0.086, 0.13$ (red, blue, green, black, cyan, orange). For these data, the threshold for parametric self-oscillation corresponds to $X_S = 40$ fm, the signal and idler modes are driven to $35(k_BT/m\omega_j^2)^{1/2}$ and $400(k_BT/m\omega_i^2)^{1/2}$, respectively, corresponding to $\eta = 14.4$. Inset: Estimate of the pump amplitude from fits to these data agree with the actual pump amplitude to within 5%.

ing the amplitudes of the signal and idler fields in the presence of the pump field. For these measurements, the signal and idler modes were weakly actuated while keeping their phases fixed. The pump (substrate) was actuated to different amplitudes below threshold while its phase, relative to the signal and idler, was slowly changed. The phase dependent amplification of the signal mode for different values of the normalized pump amplitude μ and pump phase ϕ is shown in Fig. 4.3. For these data, the signal mode was actuated

to an amplitude of $35 \times (k_B T/m\omega_j^2)^{1/2}$ while the idler mode was actuated to an amplitude of $400 \times (k_B T/m\omega_i^2)^{1/2}$. The data show excellent agreement with the above expression, with observed parametric deamplification exceeding 20 dB. The pump amplitudes extracted from fits to these data are in agreement with the independently measured amplitudes to within 5% (Fig. 4.3 (inset)).

4.8 Demonstration of two-mode thermomechanical squeezing

We make use of this nondegenerate parametric amplifier to demonstrate thermomechanical two-mode noise squeezing. In the absence of any actuation, the signal and idler membrane modes are subject only to thermomechanical noise. In this situation, if the pump field is driven below threshold, the membrane modes become highly correlated, with the correlations being manifest as a squeezing of a composite quadrature formed from linear combinations of quadratures of the individual membrane modes. This is the thermomechanical analog of two-mode squeezing seen in optical parametric amplifiers [113].

To quantify the degree of two-mode squeezing, we construct cross-quadratures from the displacements of the membrane modes, according to the relations $x_{a,b} = (\alpha_i \pm \alpha_j)/\sqrt{2}, y_{a,b} = (\beta_i \pm \beta_j)/\sqrt{2}$ where $\{\alpha_i, \beta_i\}$ are the respective quadratures of the individual membrane modes normalized to thermomechanical amplitudes. Phase-space distributions of these quadratures, accumulated over typical durations of 300 s, are shown in Fig. 4.4. The phase space distributions, which are symmetric in the absence of down-conversion, acquire a large ellipticity for increasing amplitudes of the pump field. The data are in excellent agreement with our two-mode thermomechanical noise squeezing model

51
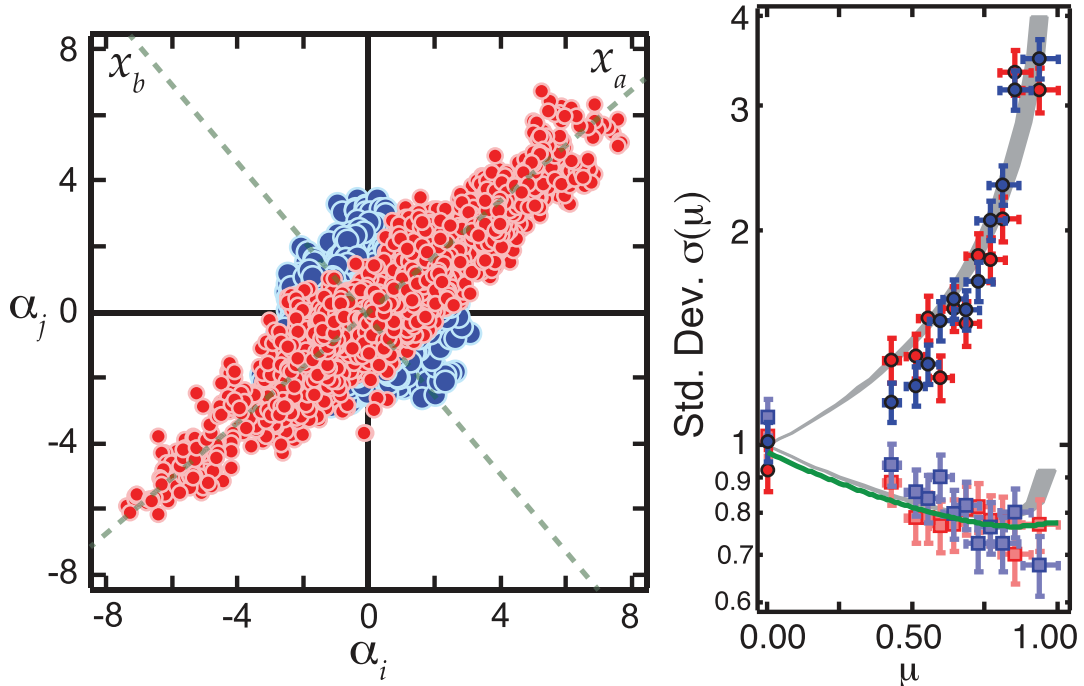
Figure 4.4: Steady-state thermomechanical two-mode squeezing. Left: Phase space distributions of the quadratures α_i, α_j in the absence (blue) and presence (red) of the pump field, showing the emergence of correlations, i.e. noise squeezing, due to nondegenerate parametric amplification. Right: The standard deviations of the cross-quadratures x_a, y_b (red, blue), (amplified) and x_b, y_a (red, blue) (squeezed) *vs* pump amplitude. The shaded curves indicate the no-free-parameter prediction of our noise squeezing model based on independently measured parameters of our system. The green trace represents the expected degree of squeezing taking into account a finite measurement duration (see Supplementary Information, Section 4.10.7).

(see Fig. 4.4 and Supplementary Information, Section 4.10.7). While an arbitrarily large degree of coherent deamplification may be obtained for specific phase relationships between the signal, idler and pump fields, our noise squeezing model predicts that the maximal degree of steady-state thermomechanical noise squeezing is limited by thermal averaging across all possible phases between the fields. Nonetheless, by harnessing weak measurements and feedback, we

estimate that mechanical squeezing of more than 40 dB may be obtained with our demonstrated parameters [101].

4.9   Conclusion

In summary, we realize strong, quantum-compatible multimode interactions in a macroscopic mechanical resonator through reservoir engineering, and use this nonlinear coupling to demonstrate nondegenerate parametric amplification and two-mode squeezing. This combination of strong nonlinear interactions, large $f \times Q$ products ($\gg k_B T/h$), low dissipation ($\gamma < (10 \text{ s})^{-1}$) and compatibility with cavity optomechanical cooling and quantum-limited detection, provides a powerful tool for nonlinear approaches to quantum sensing and QND measurements of mechanical degrees of freedom. In addition, our work also paves the way towards the quantum manipulation of phononic fields for studies of macroscopic entanglement.

4.10   Supplementary Information

4.10.1   Photothermal frequency stabilization

The mechanical modes of the membrane are susceptible to large drifts in frequency due to temperature fluctuations and the differential expansion between the silicon substrate and the Silicon nitride membrane. We measure drifts on the order of 500 Hz ($10^3 - 10^4 \gamma$) per Kelvin for the modes studied in this work.

Thus, resolving thermomechanical motion and non-thermal two-mode correlations requires active sub-linewidth stabilization of the mechanical eigenfrequencies.

The frequencies of the mechanical modes are stabilized by photothermal control of the silicon substrate. Based on our observation that temperature fluctuations cause frequency drifts that are highly correlated across the various modes of the membrane, we implement active stabilization by continuously monitoring the frequency of a high-Q membrane mode at 2.736 MHz – far from the modes that exhibit the two-mode nonlinearity studied in this work. This 'thermometer mode' has a quality factor in excess of 8×10^6 ($\gamma/2\pi < 340$ mHz). Phase sensitive detection of this mode results in an error signal with an on-resonant phase slope of 5.91 radians/Hz. Active photothermal stabilization of the substrate is accomplished with typical optical powers of 600 μW, leading to rms frequency fluctuations of this thermometer mode below 2 mHz (equivalent to temperature fluctuations of the substrate of less than 2 μK). For the mechanical modes relevant to this work, this stabilization translates to frequency fluctuations less than $0.002 \times \gamma$.

4.10.2 Calibration of mechanical motion

Each membrane mode was calibrated with respect to its thermal motion. For this, the optical beam incident on the membrane was positioned to align with an antinode of membrane motion. The measured interferometric signal, when converted to a rms membrane displacement, agreed with the expected thermomechanical amplitude to within 10%, limited mainly by the uncertainty of the spot

size at the plane of the membrane. This ruled out any spurious noise sources that could potentially mask thermomechanical motion. Having established this calibration, the membrane motion measured for modes probed away from the antinode were rescaled to the theoretically expected thermal amplitude, thereby calibrating out the dependence on probe alignment (see for example, [114]). The thermal motion of all the membrane modes was detected with a lock-in amplifier with a bandwidth exceeding 100γ and a sampling rate around 500γ, over a duration of $200/\gamma$ where γ is the damping rate of the relevant mode.

The substrate motion was calibrated by actuating the substrate at frequencies far from any membrane resonance, and assuming that the entire system, i.e. membrane and substrate, move as a rigid body such that the measured membrane displacement is equal to the substrate displacement perpendicular to the substrate plane. This calibration is then extrapolated to the low actuation voltages required for the measurements described in this work. The extracted motion X_S is the overall motion of the substrate and is proportional to the force acting on the substrate mode.

While we do not directly detect the substrate resonance, there are several pieces of evidence that point to a substrate mode involving in-plane motion, e.g. shear mode, whose displacement would lead to a parametric modulation of the membrane tension. Firstly, the threshold actuation force for parametric instability can be changed over at least an order of magnitude by thermally tuning the signal and idler modes such that their sum frequency varies across this resonance. Further, finite element simulations accurately predict shear modes of the substrate at frequencies coincident with the sum frequencies of several pairs of membrane modes studied in this work (See Fig. 4.5 and Table II). While para-

metric modulation of the membrane modes could possibly occur even away from a substrate resonance, the requisite actuation force needed to reach the parametric instability would be higher by a factor proportional to the quality factor of the substrate mode. Indeed, we do observe that membrane mode pairs whose sum frequency is located far from predicted substrate modes, do exhibit a very high instability threshold.

$\nu_S = 2.699\text{MHz}$ $\nu_S = 2.711\text{MHz}$

$\nu_S = 2.712\text{MHz}$ $\nu_S = 2.739\text{MHz}$
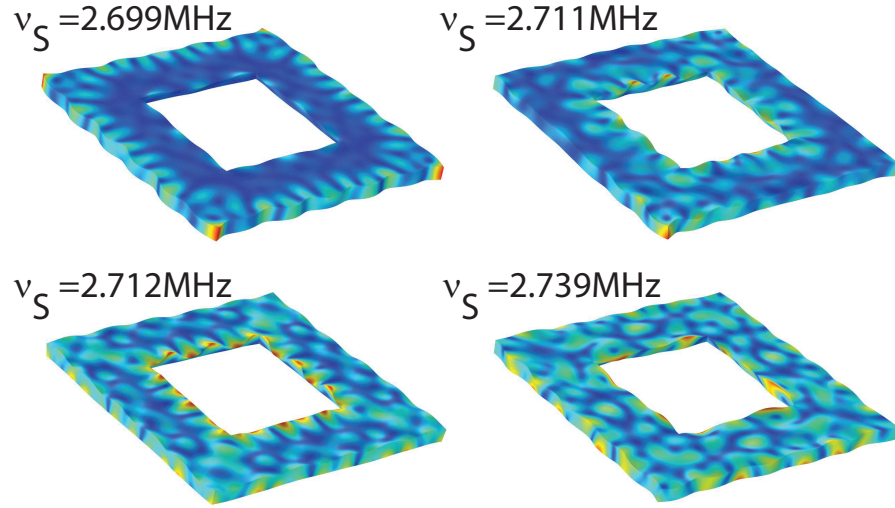
Figure 4.5: Simulated eigenmodes of the substrate near 2.7 MHz.

4.10.3 Measurement of X_S

The measurement of the threshold displacement amplitude $X_{S,th}$ is obtained by a suitable scaling of the measured threshold piezo-actuation voltage V_{th} as described below. These two quantities are linearly related as $X_{S,th} = \alpha V_{th}$ where the constant $\alpha = 20$ fm/mV is obtained by measuring the substrate motion along the interferometer axis at very large piezo voltages (~ 10 volts) and extrapolating to the threshold piezo voltages required for parametric instability (≤ 10 mV). Thus, $X_{S,th}$ is the gross center-of-mass motion of the substrate at threshold

and is effectively, a measure of the actuation force at threshold. This is given by

$$F_{th} = \frac{2}{g\chi_S \sqrt{\chi_i \chi_j}} \propto V_{th} = \alpha^{-1} X_{S,th} \tag{4.4}$$

The two-mode model predicts a linear relation between the length scale $\xi(g)$ and the threshold force F_{th}, and hence between $\xi(g)$ and $X_{S,th}$ as well.

$$\xi = \frac{1}{2} \sqrt{\frac{\chi_j}{m_S \omega_S \gamma_i}} F_{th} \propto \frac{1}{2} \sqrt{\frac{\chi_j}{m_S \omega_S \gamma_i}} X_{S,th} \tag{4.5}$$

As mentioned previously, this relation is only linear within any possible variation of the prefactor. For the modes studied in this work, the prefactor varies by around 25%.

Importantly, we note that there is no dependence of this prefactor on the damping rate of the substrate mode γ_S. Also, the effective mass of the substrate mode is related to its physical mass through a geometric factor which we expect to be of similar magnitude for the substrate modes mediating the parametric interaction.

The reported substrate displacement X_S and the normalized pump amplitude $\mu = X_S/X_{S,th}$ is obtained by measuring the applied piezo voltage and normalizing it to the applied voltage at the instability threshold, i.e. $X_S = (V/V_{th})X_{S,th}$ and $\mu = X_S/X_{S,th} = V/V_{th}$.

4.10.4 Linear relation between $\xi(g)$ and $X_{S,th}(g)$

Our two-mode model predicts a linear relation between $\xi(g)$ and $X_{S,th}(g)$ given by $\xi(g) = F X_{S,th}(g)$ where

$$F = \frac{1}{2} \left(\frac{\gamma_S}{\gamma_i} \right)^{1/2} \left(\frac{\chi_j}{\chi_S} \right)^{1/2} \tag{4.6}$$

$$= \frac{1}{(\gamma_i \gamma_j)^{1/2}} \left(\frac{\omega_S}{\omega_j} \right)^{1/2} \left(\frac{m_S}{m_j} \right)^{1/2} \frac{\gamma_S}{2} \tag{4.7}$$

This factor F, if it varies significantly, will alter the expected linear relation between $\xi(g)$ and $X_{S,th}(g)$. For the data shown in Fig. 4.2, F varies by around 25% (See Table II). Here, we have assumed that the substrate modes have similar effective masses and damping ($Q \sim 5000$). The former assumption is justified based on COMSOL simulations of the mode shapes. The latter assumption is supported by our measurement of several flexural substrate modes to be around $10^3 - 10^4$ within the relevant frequency range.

Moreover, the linear relation between ξ and $X_{S,th}$ continues to hold even if the parametric resonance at the sum frequency, $\omega_i + \omega_j$ is detuned from the substrate mode resonance, ω_S by Δ. This is because for the detuned case, with $\gamma_{i,j} \ll \gamma_S$, both the upconversion and downconversion processes are suppressed by a factor of $\sqrt{1 + 4\Delta^2/\gamma_S^2}$ compared to the on-resonant case, resulting in an increase in both ξ and $X_{S,th}$ by the same factor.

4.10.5 Nondegenerate parametric amplifier below threshold : Phase-sensitive amplification

We model the nonlinear interaction between membrane modes by a Hamiltonian given by $\mathcal{H}_{ij} = -gX_S x_i x_j$ where g is the interaction strength, X_S is the displacement of the substrate and $x_{i,j}$ represent the displacement of the membrane modes. Within the rotating wave approximation, this results in equations of motion of the form

$$\ddot{z}_i + \gamma_i \dot{z}_i + \omega_i^2 z_i = \frac{1}{m_i}(F_i(t) + \frac{g}{2} Z_S z_j^*) \tag{4.8}$$

and similar equations for the other membrane mode and the substrate. Here, $x_i = Re(z_i)$ and z_i is the (complex) displacement of the mode, F_i represents both the classical actuation as well as thermomechanical noise forces and ω, γ are the eigenfrequencies and mechanical linewidths. The coupled equations of motion can be solved using the methods of two time scale perturbation theory [115]. This gives rise to coupled equations of the form

$$2\dot{A}_i = \gamma_i \left[-A_i + i\chi_i \left(\frac{g}{2} A_j^* A_S + \tilde{F}_i \right) \right] \tag{4.9}$$

$$2\dot{A}_j = \gamma_j \left[-A_j + i\chi_j \left(\frac{g}{2} A_i^* A_S + \tilde{F}_j \right) \right] \tag{4.10}$$

where $z_i = A_i e^{-i\omega_i t}$ and A_i is the complex amplitude of the mode in a frame rotating at its eigenfrequency. We have ignored terms such as $\ddot{A}_i, \gamma_i \dot{A}_i$ in the slow time approximation and $\tilde{F}_{i,j}$ are the slowly varying (complex) amplitudes of the external forces on the individual membrane modes. Even in the absence of external forces $\tilde{F}_{i,j}$, these coupled equations allow for non-zero steady state amplitudes, i.e. parametric self-oscillation, above a threshold substrate amplitude given by

$$X_{S,th} = 2 \sqrt{\frac{1}{g^2} \frac{1}{\chi_i \chi_j}} \tag{4.11}$$

While we focus on the below-threshold behavior of this nondegenerate parametric amplifier in this work, these coupled equations also accurately describe various nonlinear aspects of the amplifier above threshold.

In the presence of external actuation of the individual membrane modes and the substrate ('pump') mode, i.e. $\tilde{F}_{i,j} \neq 0, A_S \neq 0$, the amplitude of each mode is a coherent superposition of its individual response to the external force and the down-converted phonons arising from the two-mode nonlinearity. Thus, the complex amplitudes in steady state are given by

$$A_i = \frac{e^{i(\phi_i - \pi/2)}}{1 - \mu^2} \left(\chi_i |\tilde{F}_i| + \mu \sqrt{\chi_i \chi_j} |\tilde{F}_j| e^{i\delta\phi} \right) \tag{4.12}$$

$$A_j = \frac{e^{i(\phi_j - \pi/2)}}{1 - \mu^2} \left(\chi_j |\tilde{F}_j| + \mu \sqrt{\chi_i \chi_j} |\tilde{F}_i| e^{i\delta\phi} \right) \tag{4.13}$$

where $\mu = X_S/X_{S,th}$ is the pump amplitude normalized to the threshold for parametric instability and $\delta\phi = \phi_S - \phi_i - \phi_j$ with $\phi_{i,j,S}$ being the various phases associated with the external forces.

The above equation can be recast in terms of a phase-dependent amplification $G_{i,j}(\delta\phi) = |A_{i,j}|/|A^0_{i,j}|$ where $A^0_{i,j}$ are the steady state amplitudes of the respective modes in the absence of down-conversion, and $|A^0_{i,j}| = \bar{x}_{i,j}$. This phase-dependent amplification is then given by

$$
\begin{aligned}
G_j(\delta\phi) &= \frac{1}{1 - \mu^2} \\
\Psi \quad &\times \quad \sqrt{1 + \mu^2 \frac{\chi_i}{\chi_j} \left(\frac{|\tilde{F}_i|}{|\tilde{F}_j|} \right)^2 - 2\mu \left(\frac{\chi_i}{\chi_j} \right)^{1/2} \frac{|\tilde{F}_i|}{|\tilde{F}_j|} \cos(\delta\phi)} \\
\Psi &= \frac{1}{1 - \mu^2} \sqrt{1 + \mu^2 \eta^2 - 2\mu\eta \cos(\delta\phi)} \tag{4.14}
\end{aligned}
$$

where $\eta = (\chi_j/\chi_i)^{1/2} \times (\bar{x}_i/\bar{x}_j)$ and $\bar{x}_{i,j}$ are the amplitudes of the membrane modes in the absence of the pump. A no-free-parameter fit of this expression is in agreement with our data to within 5% (Fig. 4.3).

As can be seen from the above expression, the phase-dependent amplifica-
tion $G_j(\delta\phi)$ is dependent on both the input signal phase and amplitude. For
equal amplitudes of signal and idler (i.e. $\eta = 1$), this expression equates to
$G_j = \frac{1}{2}$ for $\phi = 0$, similar to a degenerate parametric amplifier. However, for
large η, this expression can be made arbitrarily small and equates to $G_j = 0$ for
$\phi = 0, \mu = 1/\eta$ (see Fig. 4.6).
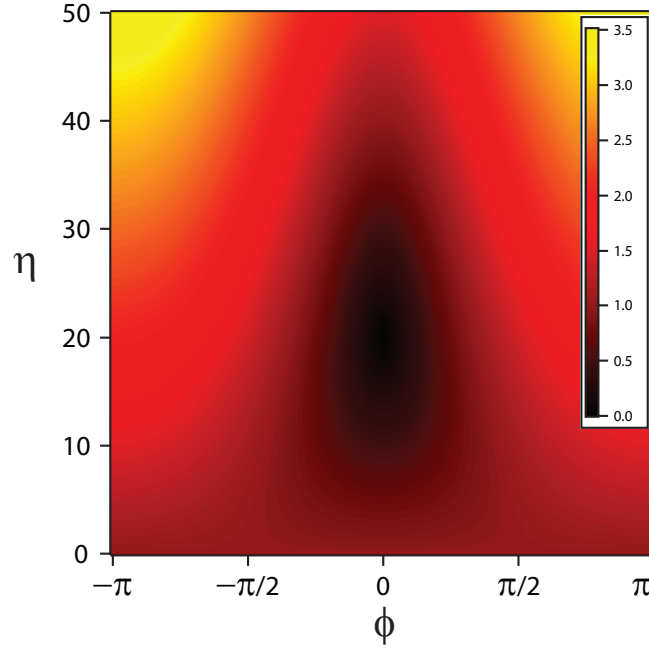
Figure 4.6: Phase-dependent amplification $G_j(\delta\phi)$ *vs* the phase difference
$\delta\phi$ and the ratio of idler and signal amplitudes $\eta = (\chi_j/\chi_i)^{1/2} \times$
$(\bar{x}_i/\bar{x}_j)$, for $\mu = 0.05$.

4.10.6   Two-mode control of mechanical dissipation

For sufficiently large amplitudes of membrane motion, the two-mode nonlin-
earity can result in the coherent upconversion of excitations into the substrate.
In our system, we typically measure quality factors of $Q_S \sim 10^3 - 10^4$ for the sub-
strate modes (e.g. flexural modes), about three orders of magnitude lower than

those of the membrane. Due to the relatively large dissipation rate of substrate modes ($\gamma_S/\gamma_{i,j} > 10^3$), this upconversion process can be regarded as nonlinear two-mode dissipation where the dissipation rate of a mode i is influenced by the motion of its partner mode j.

The modified dissipation rate $\gamma_i(x_j)$ of a mode i can be most easily seen by writing the coupled equations of motion for the slowly varying amplitudes $A_{i,j,S}$. Here, we assume that mode j is actuated externally to a large amplitude in the absence of substrate (pump) actuation. The coupled equations become

$$2\dot{A}_i + \gamma_i A_i = \gamma_i \chi_i \frac{g}{2}|A_j|A_S \tag{4.15}$$

$$2\dot{A}_S + \gamma_S A_S = -\gamma_S \chi_S \frac{g}{2}|A_j|A_i \tag{4.16}$$

where we assume that A_j is purely imaginary. Diagonalizing these equations leads to a modified damping rate of mode i given by

$$\gamma_i(\bar{x}_j) = \frac{1}{2}\left[\gamma_S + \gamma_i - \sqrt{(\gamma_S - \gamma_i)^2 - \gamma_S^2 \frac{\bar{x}_j^2}{\xi^2}}\right] \tag{4.17}$$

where $\xi = \frac{1}{2}(\gamma_S/\gamma_i)^{1/2}(\chi_j/\chi_S)^{1/2} \times X_{S,th}$. This can be recast in terms of a normalized quality factor $Q_i(\bar{x}_j)/Q_{i,0} = (\gamma_i(\bar{x}_j)/\gamma_i)^{-1}$ where $Q_{i,0}$ is the quality factor of membrane mode i in the absence of the two-mode nonlinearity.

Our data are in excellent agreement with this expression for a wide range of mode pairs that were seen to exhibit this two-mode nonlinearity (see, for example, Fig. 4.7).

As can be seen in Fig. 4.7, a significant modification to the dissipation rate of a membrane mode i requires large amplitude actuation of its partner mode j, typically over 4-5 orders of magnitude larger than thermomechanical amplitudes and much larger than the typical scale of motion for the studies presented
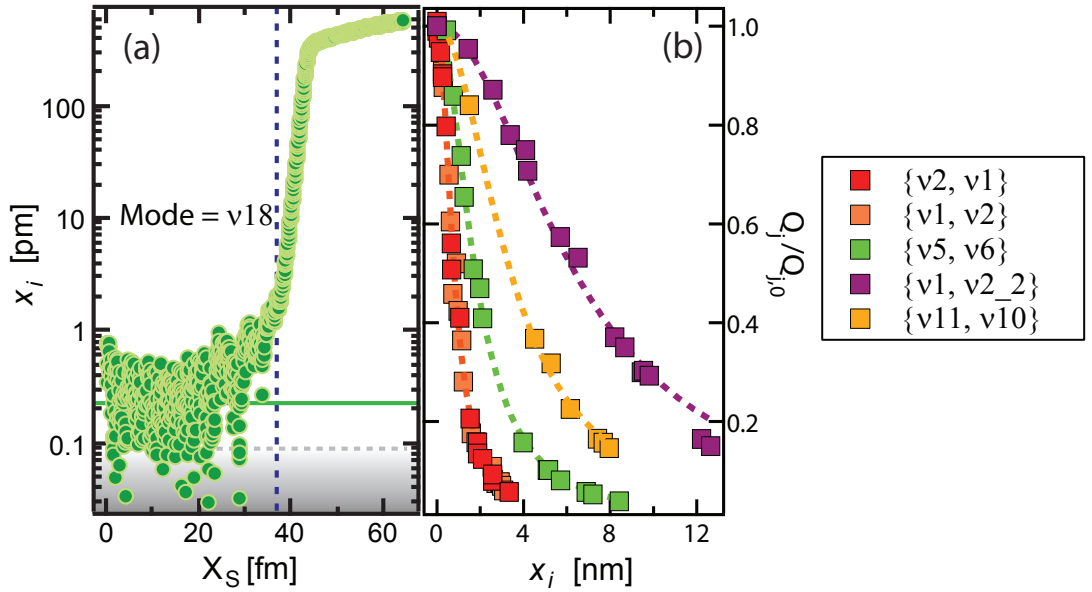
Figure 4.7: Modes used in Fig. 4.2(a,b) of the paper. See Table I for details
of these modes.

in this work. Thus, while these measurements constitute an important vali-
dation of our two-mode model, the two-mode contribution to the individual
dissipation rates are negligible for our studies on parametric amplification and
thermomechanical squeezing.

4.10.7 Thermomechanical two-mode squeezing

The nondegenerate parametric amplifier, when driven below threshold, devel-
ops correlations between the non-degenerate modes. These correlations are
manifest as a squeezing of a composite quadrature formed from linear combina-
tions of the individual membrane modes. We analyze the coupled equations for
the membrane mode under the influence of a classical actuation of the substrate
mode below threshold. Furthermore, we assume that the membrane modes are

subject to thermomechanical noise forces. The influence of such noise forces on the substrate mode can be neglected due to the large classical drive imposed on this mode. Finally, for each membrane mode, we distinguish between its mean amplitude and its fluctuations by writing $z_{i,j} = (\bar{A}_{i,j} + \delta A_{i,j})e^{-i\omega_{i,j}t}$ where $\langle \delta A_{i,j} \rangle = 0$. The coupled equations for the fluctuations can be written as

$$
2\begin{pmatrix} \Psi\delta\dot{A}_i \\ \delta\dot{A}_j \\ \delta\dot{A}_S \end{pmatrix} = \begin{pmatrix} -\gamma_i & 0 & i\gamma_i\chi_i\frac{g}{2}\bar{A}_j^* \\ \Psi 0 & -\gamma_j & i\gamma_j\chi_j\frac{g}{2}\bar{A}_i^* \\ i\gamma_S\chi_S\frac{g}{2}\bar{A}_j & i\gamma_S\chi_S\frac{g}{2}\bar{A}_i & -\gamma_S \end{pmatrix}\begin{pmatrix} \Psi\delta A_i \\ \delta A_j \\ \delta A_S \end{pmatrix}
$$

$$
+ \begin{pmatrix} 0 & i\gamma_i\chi_i\frac{g}{2}\bar{A}_S & 0 \\ \Psi i\gamma_j\chi_j\frac{g}{2}\bar{A}_S & 0 & 0 \\ 0 & 0 & 0 \end{pmatrix}\begin{pmatrix} \Psi\delta A_i^* \\ \delta A_j^* \\ \delta A_S^* \end{pmatrix} + i\begin{pmatrix} \Psi\gamma_i\chi_i F_i \\ \gamma_j\chi_j F_j \\ \gamma_S\chi_S F_S \end{pmatrix}
$$

where the thermomechanical noise forces obey

$$
\langle F_i(t) \rangle = \langle F_i(t)F_j(t') \rangle = 0, \tag{4.18}
$$

$$
\langle F_i(t)F_j^*(t+\tau) \rangle = 8\gamma_i m_i k_B T \delta_{ij}\delta(\tau) \tag{4.19}
$$

Using the decomposition

$$
\delta\mathbf{A} = \delta\vec{\alpha} + i\delta\vec{\beta} \tag{4.20}
$$

$$
\mathbf{v} = \mathbf{v}_\alpha + i\mathbf{v}_\beta \tag{4.21}
$$

where $\delta\mathbf{A} = (\delta A_i, \delta A_j, \delta A_S)^T$,

$\mathbf{v} = \frac{i}{2}(\gamma_i\chi_i F_i, \gamma_j\chi_j F_j, \gamma_S\chi_S F_S)^T$, etc. leads to the following equations of motion

$$
\dot{\delta\vec{\alpha}} = \mathbf{M}_\alpha\delta\vec{\alpha} + \mathbf{v}_\alpha \tag{4.22}
$$

$$
\dot{\delta\vec{\beta}} = \mathbf{M}_\beta\delta\vec{\beta} + \mathbf{v}_\beta \tag{4.23}
$$

where

$$
\mathbf{M}_{\alpha,\beta} = \frac{1}{2}\begin{pmatrix} -\gamma_i & \pm\gamma_i\chi_i\frac{g}{2}|\bar{A}_S| & \gamma_i\chi_i\frac{g}{2}|\bar{A}_j| \\ \pm\gamma_j\chi_j\frac{g}{2}|\bar{A}_S| & -\gamma_j & -\gamma_j\chi_j\frac{g}{2}|\bar{A}_i| \\ -\gamma_S\chi_S\frac{g}{2}|\bar{A}_j| & \gamma_S\chi_S\frac{g}{2}|\bar{A}_i| & -\gamma_S \end{pmatrix} \tag{4.24}
$$

and the elements of $\mathbf{v}_{\alpha,\beta}$ satisfy $\langle v_i \rangle = 0$, $\langle v_k(t)v_l(t+\tau) \rangle = \frac{\gamma_l k_B T}{m_l \omega_l^2} \delta_{kl}\delta(\tau)$. The spectrum in steady state is thus given by the matrix equation

$$\mathbf{S}_{\alpha,\beta}(\omega) = \frac{1}{2\pi}(\mathbf{M}_{\alpha,\beta} + i\omega\mathbf{I})^{-1}\mathbf{D}(\mathbf{M}_{\alpha,\beta}^T - i\omega\mathbf{I})^{-1} \tag{4.25}$$

where $\mathbf{I}$ is the identity and

$$\mathbf{D} = k_B T \begin{pmatrix} \frac{\gamma_i}{m_i\omega_i^2} & 0 & 0 \\ 0 & \frac{\gamma_j}{m_j\omega_j^2} & 0 \\ 0 & 0 & \frac{\gamma_S}{M\omega_S^2} \end{pmatrix} \tag{4.26}$$

is the diffusion matrix.

The zero-time correlations in steady state can be obtained from the spectrum using the Wiener-Khintchine theorem, and are given by

$$\langle \delta\alpha_i\delta\alpha_i \rangle = \frac{k_B T}{m_i\omega_i^2} \frac{1}{1-\mu^2}\left[1 - \delta\mu^2 + \mu^2\frac{\gamma_j}{2\bar{\gamma}}\left(\frac{\omega_i}{\omega_j} - 1\right)\right]$$

$$\langle \delta\alpha_j\delta\alpha_j \rangle = \frac{k_B T}{m_j\omega_j^2} \frac{1}{1-\mu^2}\left[1 + \delta\mu^2 + \mu^2\frac{\gamma_i}{2\bar{\gamma}}\left(\frac{\omega_j}{\omega_i} - 1\right)\right]$$

$$\langle \delta\alpha_i\delta\alpha_j \rangle = \frac{k_B T}{\sqrt{m_i\omega_i^2}\sqrt{m_j\omega_j^2}}\left[\frac{\mu(1-\delta^2)^{1/2}}{2(1-\mu^2)}\left(\sqrt{\frac{\omega_i}{\omega_j}} + \sqrt{\frac{\omega_j}{\omega_i}}\right)\right]$$

where $\delta = (\gamma_i - \gamma_j)/(\gamma_i + \gamma_j)$ is the 'loss asymmetry' and $\bar{\gamma} = (\gamma_i + \gamma_j)/2$.

In our measurements, we quantify the degree of two-mode squeezing by defining cross-quadratures constructed from $\{\alpha_{i,j}, \beta_{i,j}\}$ normalized to their respective thermomechanical amplitudes, according to the relations $x_{a,b} = (\alpha_i \pm \alpha_j)/\sqrt{2}$, $y_{a,b} = (\beta_i \pm \beta_j)/\sqrt{2}$. The standard deviations of these cross-quadratures can be calculated from the above expressions. These are shown in Fig. 4.4 for the independently measured parameters of our nondegenerate parametric amplifier. These data are obtained with a measurement filter bandwidth of $\Delta\nu = 10$ Hz, i.e. $\Delta\nu > 10^2 \gamma_{i,j}/2\pi$. Thus, the correlations calculated above by integrating

over all frequencies (i.e. infinite bandwidth), are a good approximation to our measurements. As can be expected, the degree of squeezing increases monotonically with decreasing filter bandwidth, reaching the 6 dB limit for $\Delta \nu < \gamma_{i,j}/2\pi$.

Due to the diverging mechanical susceptibility and response time near the parametric instability, the squeezing spectra measured over a finite duration can deviate significantly from those calculated in steady state. In particular, the existence of a non-zero loss asymmetry results in a degradation of squeezing near the instability threshold (as shown by the upturn in the gray theory band in Fig. 4.4). This was calculated for an infinite measurement duration. The actual measured degree of squeezing for a finite measurement duration τ_m are extracted by truncating the integral of the spectral densities by the measurement duration [83]. This is represented by the green curve in Fig. 4.4 and is seen to agree with our measurements very accurately.

4.10.8 Table of modes

We include below details of the various mechanical modes used in this study. The mode indices are identified through a combination of spectroscopy (based on the known membrane dimensions) and interferometric imaging as shown in [79]. In cases where the measured eigenfrequency was between two very closely spaced modes, the identification of the mode index was ambiguous and we have indicated both candidate modes.

The mode pairs used for the measurements shown in Fig. 4.2 are indicated in Fig. 4.7. In addition, the data shown in Fig. 4.3, 4.4 of the paper were obtained with the mode pair $\{\nu 18, \nu 19\}$.

Mode label	Frequency (Hz)	Quality Factor	Linewidth (Hz)	Mode index
$\nu 1$	1202554	2.27×10^7	0.0530	(14,15) + (15,14)
$\nu 2$	1494736	2.32×10^7	0.0644	(17,19) - (19,17)
$\nu 3$	1243589.3	2.42×10^7	0.0514	(15,15)
$\nu 4$	911997	2.17×10^7	0.0420	(11,11) or (4,15)
$\nu 5$	1254745.23	1.43×10^7	0.0877	(13,17)
$\nu 7$	1254672.68	2.00×10^7	0.0627	(17,13)
$\nu 6$	1442154.99	4.94×10^6	0.292	(11,22)
$\nu 2\_2$	1494833.76	1.42×10^7	0.105	(11,23)
$\nu 2\_3$	1494669.99	2.60×10^6	0.575	(23,11)
$\nu 2\_4$	1494880	4.80×10^5	3.11	(5,25) or (17,19)
$\nu 8$	1301806.27	2.18×10^7	0.0597	(13,18)
$\nu 9$	1408452.95	1.54×10^7	0.0914	(1,24)
$\nu 10$	1232664.95	1.35×10^7	0.0913	(9,19)
$\nu 11$	1479774.69	2.26×10^7	0.0655	(14,21)
$\nu 12$	1280371.09	1.82×10^7	0.0704	(21,6)
$\nu 13$	1409424.06	1.66×10^7	0.0849	(23,7)
$\nu 14$	1077794.35	2.01×10^7	0.0536	(13,13)
$\nu 15$	1617797.75	8.48×10^6	0.191	(19,20) - (20,19)
$\nu 16$	1265534.72	1.02×10^5	12.4	(21,5)
$\nu 17$	1448118.81	1.23×10^7	0.118	(9,23)
$\nu 18$	1232863.825	1.77×10^7	0.0696	(9,19) or (1,21)
$\nu 19$	1466057.27	1.10×10^7	0.133	(15,20) or (7,24)

Table 4.1: Mode labels, frequencies, quality factors, linewidths and mode indices of the mechanical modes.

Mode Pair (i, j)	V_{th} (mV)	$X_{S,th}$ (pm)	$\xi_{i,j}$ (nm)	Nearest Substrate Mode (Hz)	Detuning (Hz)	$\sqrt{\frac{\gamma_s \chi_j}{\gamma_i \chi_s}}$ ($\times 10^6$)
$\nu12, \nu13$	40	0.8	263.4	2698891	-9096	2.34
$\nu14, \nu15$	163	3.26	2188.8	2698891	-3299	1.67
$\nu5, \nu6$	30	0.6	102.2	2698891	-1991	1.12
$\nu2, \nu1$	15	0.3	49.8	2698891	-1601	3.37
$\nu1, \nu2$	15	0.3	60.6	2698891	-1601	3.03
$\nu2\_2, \nu1$	43	0.86	572.7	2698891	-1503	2.63
$\nu1, \nu2\_2$	43	0.86	483.7	2698891	-1503	2.36
$\nu9, \nu8$	350	7	1264.7	2698891	30	2.58
$\nu11, \nu10$	8.5	0.17	214.3	2710927	-668	2.54
$\nu17, \nu16$	558	11.16	3540.2	2711884	555	0.16
$\nu3, \nu2$	151	3.02	982.8	2711884	1769	3.14
$\nu2, \nu3$	151	3.02	728.1	2738167	158	3.44
$\nu2, \nu7$	580	11.6	4338.4	2738167	158	3.12
$\nu2, \nu5$	2233	44.66	5099.9	2747202	2206	2.64

Table 4.2: Coupled mode pairs, piezo-actuation threshold voltages (V_{th}), threshold substrate displacements ($X_{S,th}$), $\xi_{i,j}$'s, nearest substrate modes to the parametric resonance, detuning of the nearest substrate mode from the parametric resonance and the factor $(\gamma_S/\gamma_i)^{1/2}(\chi_j/\chi_S)^{1/2}$, for the mode pairs studied in this work.

CHAPTER 5

CRITICAL BEHAVIOR OF A DRIVEN DISSIPATIVE SYSTEM :
UNIVERSALITY BEYOND THE MARKOVIAN REGIME

5.1   Overview

One aspect of open quantum systems that has not yet been explicitly mentioned
has been brought about and used in Chapter 4 – open systems can be continu-
ously driven. For many closed systems, a drive can lead to an increase in its
energy, which eventually 'destroys' it; e.g., ultracold atoms in shaken optical
lattices heat up and leave the trap; mechanical harmonic oscillators without
damping, when driven, get increasingly displaced so that nonlinearities can-
not be ignored, making them anharmonic. We note that this is not always
the case, e.g. in saturable systems like a two-level atom driven by a coherent
drive at the level spacing. Nonetheless, in open quantum systems, the work
done on the system by the drive can be lost to the environment, while coax-
ing the system into a dynamic equilibrium. This implies a competition between
the drive strength (rate at which energy is pumped into the system) and the
dissipation to the environment (rate at which energy is lost to the surround-
ings). These competing rates can effect a 'transition', the suggestively called
driven-dissipative phase transition, which is the subject of study of this Chap-
ter [116, 117, 118, 119, 120, 121, 122, 123, 124, 125].

Phase transitions can be influenced by fluctuations, whether the fluctuations
be thermal or quantum, though possibly, quantum phase transitions can dif-
fer from their classical counterparts due to the differing origin of fluctuations
[126, 127, 128]. On the other hand, perhaps the difference between a $T = 0$

'true' quantum phase transition, and the $T \neq 0$ classical case is not as pressing a concern. After all, considerable theoretical and experimental efforts are geared toward understanding and identifying the signatures and properties of a true quantum phase transition *through* finite temperature transitions and observables [126, 127]. Our focus has thus instead been on the role of the *nature* of system-bath interactions on driven-dissipative phase transitions, and the associated system properties and dynamics.

To that end, in this Chapter, we use Kibble-Zurek physics and dynamical hysteresis to probe our system's critical behavior [129, 130, 131]. We first empirically confirm the Kibble-Zurek paradigm/mechanism, both quantitatively and qualitatively, for the case of Markovian system-bath interactions, albeit in the driven-dissipative PA-PO system of Chapter 4. We thereafter employ the Kibble-Zurek paradigm to infer the change in critical behavior, to wit, the critical exponents, as the system-bath interactions are made non-Markovian; effected here by taking advantage of the long system-bath timescales of the Silicon Nitride membrane resonators, using feedback. We find that the nature of system-bath interactions can markedly influence criticality and the associated scaling laws. Further, we model the evolution under non-Markovian system-bath coupling, which is tractable for the minimal two-oscillator PA-PO system, and find an excellent agreement with the experiments. The future implementation of such non-Markovian interactions, possibly involving arrays or circuits of solid state quantum oscillators, would allow for exploring the role of spatial dimensionality on criticality, the role of energy flow to and from the bath on the system dynamics, and the role of system-bath entanglement in quantum thermodynamics, among numerous other potential experiments. Moreover, it would also provide further impetus to the longstanding search for a theoretical

language for describing the physics of nonequilibrium open quantum systems [132, 133, 134].

This chapter will be submitted for peer-review with requisite modifications as *Critical behavior of a driven dissipative system : Universality beyond the Markovian regime, by Y. S. Patil, H. F. H. Cheung, T. Villazon, A. G. Date, A. Polkovnikov, A. Chandran and M. Vengalattore*. In this work, Y. S. Patil, H. F. H. Cheung and A.G. Date performed the experimental work, data acquisition and data analysis. Y. S. Patil, H. F. H. Cheung, T. Villazon carried out the theoretical modeling and simulations. A. Polkovnikov and A. Chandran supervised the theoretical modeling. M. Vengalattore supervised all stages of the work. All authors contributed to the preparation of the manuscript.

5.2 Abstract

Through steady state measurements of divergent susceptibilities and critical exponents, we experimentally establish a continuous phase transition in a paradigmatic two-mode driven-dissipative system of a pair of nondegenerate, parametrically coupled, optomechanical oscillators. We demonstrate that universality near the transition manifests in the out-of-equilibrium dynamics of slow ramps across the transition, and is captured qualitatively and quantitatively by Kibble-Zurek scaling laws with two scaling parameters. We further investigate the influence of the system-bath interactions on the critical behavior by engineering power-law non-Markovian system-bath interactions through an active feedback protocol. While this non-Markovian system-bath interactions

changes critical exponents, both the Kibble-Zurek paradigm and universality of the dynamics remain valid. We thus show that non-equilibrium ramps can be used to extract universal exponents in driven dissipative systems, opening new avenues to study the theoretically challenging cases of system-bath interactions and their influence on critical phenomena.

5.3 Introduction

Phase transitions and criticality in open systems are active areas of research [135, 136]. Open systems need not fall under conventional universality classes [137, 138, 139], and it is unclear if conventional paradigms like the Landau-Ginzburg formalism even apply [140]. The nonequilibrium critical dynamics of such phase transitions and their universality is even less understood. Moreover, open systems inherently come in huge variety, depending on the nature of their interactions with the environment. The influence of these system-bath couplings on the system's properties and its critical behavior has been studied only fairly recently [141, 142, 143], and corresponding experiments are scarce.

In this work, we experimentally explore a paradigmatic yet simple realization of such an open system, consisting of a pair of signal and idler modes with annihilation operators $a_{s,i}$ at frequencies $\omega_{s,i}$, parametrically coupled to each other through a third, coherently driven, pump mode a_P at frequency $\omega_P = \omega_s + \omega_i$. Each mode is also dissipatively coupled to its bath at a finite temperature, at rates $\gamma_s, \gamma_i, \gamma_P$, respectively, with $\gamma_{s,i} \ll \gamma_P$. Such an open system has a myriad of physical realizations in optics, optomechanics, nanomechanics, cold atoms and cavity QED [144, 91, 145, 146, 147, 148, 149, 150]. In this work,

we implement it in a pair of mechanical modes of a single LPCVD silicon nitride membrane resonator on a silicon substrate [150, 79] (also, see Supplementary Information, Section 5.9.12).

In the rotating wave approximation, the coherent evolution of such a system in a rotating frame is described by the Hamiltonian,

$$\mathcal{H} = -\hbar g(a_s^\dagger a_i^\dagger a_P + a_P^\dagger a_i a_s) - \hbar(F_P a_P^\dagger + F_P^* a_P)$$

where g parametrizes the strength of the inter modal coupling, F_P represents the classical pump drive, and the dissipation is captured through Heisenberg-Langevin equations (see SI, [151]). Below a critical drive strength of $\mu \equiv \frac{F_P}{|F_{cr}|} = 1$, the signal and idler modes dissipate to the environment at a rate faster than the pump parametrically actuates them, so that each mode remains unoccupied with $\langle a_{s,i} \rangle = 0$, where $\langle \cdot \rangle$ denotes a thermal ensemble average. As the drive strength is increased beyond criticality, the rate of down conversion into the signal and idler modes grows larger than the rate of dissipation out to the environment, and the system exhibits the onset of a non-zero order, i.e. amplitude $a_{s,i} = |a_{s,i}|e^{i\phi_{s,i}}$, with $\phi_{s,i}$ being the modes' oscillation phases. This phase transition can be described through an effective potential which reduces to a Mexican hat, $\mathcal{H}_{\text{eff}} \approx \gamma_0(1 - \mu)|a_s|^2 + \frac{2g^2}{\gamma_P}|a_s|^4$, for the experimentally realized case of equal signal and idler damping rates, $\gamma_{s,i} = \gamma_0 = 0.50(1)$ s^{-1} (see Supplementary Information, Section 5.9.2).
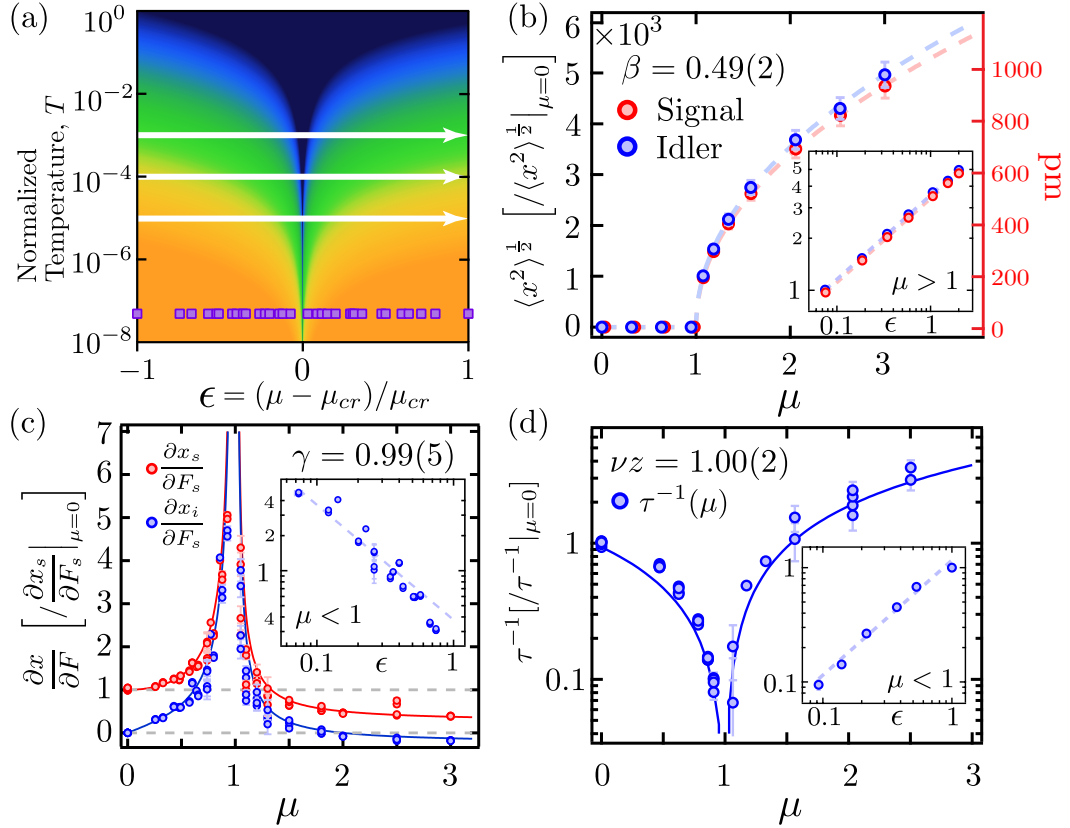
Figure 5.1: **(a) Schematic of the phase diagram for the driven-dissipative transition**, in temperature T and drive strength μ. Temperature has been normalized to T_{nl}, the temperature at which the system is nonlinear even without any drive ($\mu = 0$). A sharp phase transition exists only for $T = 0$, morphing into a crossover for finite T. Darker shading denotes a growing influence of finite temperature, with fluctuations dominating inside the dark blue region (see Supplementary Information, Section 5.9.5). Squares mark the steady-state experiments realized in this work. The white arrows depict the finite-time, finite-T quenches across the phase transition. **(b-d) Establishing the phase transition:** (b) Steady-state order, measured as $|a_{s,i}|$, with parametric drive strength μ, (c) Divergent susceptibility of order to external forces, and (d) Critical slowing down of the system. Dashed lines show a power-law fit with $\epsilon = (\mu - \mu_{cr})/\mu_{cr}$, the reduced distance from criticality. Solid lines show no-free-parameter estimates of the model described in the text. (Insets) The measured exponents $\beta = 0.49(2)$, $\gamma = 0.99(5)$ and $\nu z = 1.00(2)$, with $\langle x^2 \rangle \propto \epsilon^\beta$, $\partial x_i/\partial F_s \propto |\epsilon|^{-\gamma}$ and $\tau^{-1} \propto |\epsilon|^{\nu z}$ are all captured well by the predictions of the model, $\beta_{mf} = 1/2$, $\gamma_{mf} = 1$ and $\nu z_{mf} = 1$. All dashed lines denote fits.

5.4 Finite temperature phase diagram and steady-state characterization

A schematic of the phase diagram is shown in Fig. 5.1(a), where $\epsilon = \frac{\mu - \mu_{cr}}{\mu_{cr}}$ is the reduced distance from criticality, and the temperature at which the modes are thermalized has been normalized to T_{nl}, the temperature at which the system is nonlinear even without any drive ($\mu = 0$). The system undergoes a true continuous phase transition only in the limit of zero temperature, while the phase boundary is blurred into a crossover at finite temperature. Within the dark blue region, universal physics of the critical point is obscured by the dominant effects of a finite temperature. Well outside this region, observables scale in accordance with a Gaussian theory of fluctuations. See Supplementary Information Section 5.9.5 for details.

We first establish the phase transition through several steady state measurements, wherein the system observables are measured as the pump is continuously driven at a constant strength. The experimental steady-state measurements in this work avoid the crossover regime, as marked by the squares in Fig. 5.1(a), thereby essentially accessing the $T = 0$ physics. The measured amplitude $\langle x^2 \rangle^{1/2} \propto |a_{s,i}| \propto \epsilon^{\beta}$ yields an exponent of $\beta = 0.49(2)$ [Fig. 5.1(b)], where $x_{s,i} \propto (a_{s,i} + a^{\dagger}_{s,i})$. Secondly, as is usual in continuous phase transitions, the susceptibility of the order to external forces is observed to diverge near criticality. This susceptibility is measured by applying a force F_s at the signal frequency ω_s and measuring the steady state response of either of the signal or idler modes. The extracted exponent of $|\partial x_i / \partial F_s| \propto |\epsilon|^{-\gamma}$ is $\gamma = 0.99(5)$ [Fig. 5.1(c)]. Finally, we observe that the system exhibits critical slowing down, with the re-

laxation rate vanishing at criticality. To measure these vanishing rates, the system is first allowed to reach its steady state at a particular ϵ, following which a force F_s is applied. The decay of the perturbed $x_{s,i}$ values back to their steady state is then fit to an exponential. Empirically, the relaxation time diverges as $\tau \propto |\epsilon|^{-\nu z}$, $\nu z = 1.00(2)$ [Fig. 5.1(d)] [1]. Each of the experimentally measured exponents is well captured by the predictions of the model ($\beta = 1/2, \gamma = 1, \nu z = 1$), whose dynamics is described by 'Model A' of Hohenberg-Halperin in the rotating frame [152] (see Supplementary Information, Section 5.9.2).

5.5 Kibble-Zurek physics

Having established that there is a continuous phase transition in our driven dissipative system, we turn to critical dynamics and test the Kibble-Zurek (KZ) paradigm. Our experimental system is ideally suited for the study of finite-time dynamic protocols, such as KZ, given that its intrinsic timescales are on the order of seconds. Moreover, our system's observables (displacements) can be probed *in situ*, enabling measurement of system dynamics for each individual dynamical trajectory, as opposed to just an ensemble measure.

In brief, the KZ paradigm pertains to a system's evolution as it is slowly quenched across a continuous phase transition. The system undergoes adiabatic evolution when sufficiently far away from the critical point, due to its finite and small relaxation time, small compared to the quench rate inverse. However, as the quench brings the system close to criticality, it undergoes critical slowing

---

[1] In this effectively 0−dimensional work, an independent explicit correlation length exponent ν is ill-defined. However, following convention, we retain the notation of νz as the relaxation time exponent.

down, i.e. the relaxation timescale diverges, and the system deviates from its equilibrium or steady state. The premise of the KZ paradigm is that beyond this point, the system "freezes out", in that the system observables do not change appreciably with the changing control parameter, and that the system "thaws" or restarts responding to the changing control parameter only when it is sufficiently far on the other side of criticality, where it again has a small enough response time. These essential dynamical features of a quench across criticality are captured in the representative data of our system, shown in Fig. 5.2.

For slow ramps, the dynamics of such KZ quenches becomes universal, and can be isolated in a scaling limit [153]. In this work, we study linear quenches of the system across criticality, with $\epsilon(t) = \dot{\epsilon}t$. Typical quenches are denoted by the white arrows in Fig. 5.1(a), showing that the experiments are restricted to finite temperature, so that the quenches do not pass through the true critical point at $T = 0$. Like in quantum phase transitions, this system exhibits a finite temperature scaling. As such, a *two* parameter scaling is required to extract the system's universal behavior. This universal scaling is exhibited by the ensemble-averaged signal and idler modes' amplitude-squares in the slow ramp limit of $\dot{\epsilon} \to 0$. For a Markovian dissipative coupling of the modes to their environments, this translates to

$$\langle x^2(t) \rangle_{\dot{\epsilon}} \sim C_{\dot{\epsilon}} \times \mathcal{G}\left(\frac{t}{t_{KZ,\dot{\epsilon}}}, T\, t_{KZ,\dot{\epsilon}}^2\right) \tag{5.1}$$

where both the temperature T and time t scale according to a characteristic freeze-out or Kibble-Zurek time, $t_{KZ,\dot{\epsilon}}$, and $\mathcal{G}$ is a universal scaling function. Moreover, the KZ paradigm predicts a scaling of $t_{KZ,\dot{\epsilon}} \propto \dot{\epsilon}^{-\frac{\nu z}{1+\nu z}} = \dot{\epsilon}^{-1/2}$, and $C_{\dot{\epsilon}} \propto \dot{\epsilon}^{\frac{2\beta}{1+\nu z}} = \dot{\epsilon}^{1/2}$ (see Supplementary Information, Section 5.9.6).

Fig. 5.3(a) demonstrates this universality over two orders of magnitude of
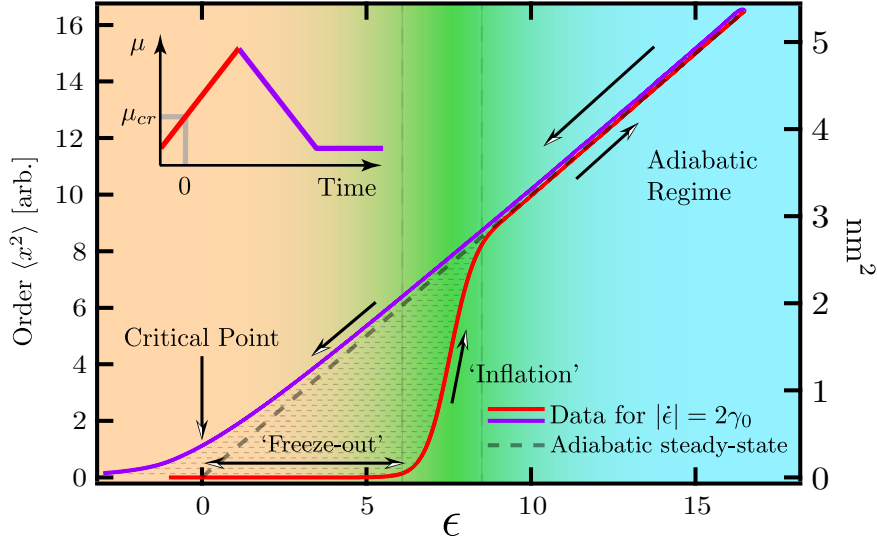
Figure 5.2: **Experimental protocol (inset):** The system is initialized in the disordered phase and linearly quenched well into the ordered phase by ramping the strength of the pump drive, μ. For hysteresis analyses (see text), the quench is reversed till the system is again disordered. **Kibble-Zurek physics and the measured growth of order:** Despite entering the ordered phase for $\mu > \mu_{cr}$ (red curve), we observe that macroscopic order is not established over a finite "freeze-out" period. The system lags behind the steady-state response (dashed line) near criticality. Once sufficiently far away, however, the system enters an adiabatic regime where the dynamic response follows the steady-state response. On the reverse quench toward disorder (violet curve), the system again deviates from adiabaticity near criticality. The KZ paradigm holds even for such driven-dissipative continuous phase transitions. Data here is shown for $|\dot{\epsilon}| = 2\gamma_0$, where γ_0 is the mechanical dissipation rate.

the quench rate $\dot{\epsilon}$. In order to isolate the temporal part of the scaling function $\mathcal{G}$, the temperature for each quench rate ensemble is varied to hold $T t_{KZ,\dot{\epsilon}}^2 \sim T/\dot{\epsilon}$ fixed. The inset shows the measured growth of $\langle x^2(t) \rangle$ for various quench rates, each ensemble consisting of data from $40 - 100$ quenches. Slow quenches reach adiabaticity nearer to criticality ($\epsilon = 0$) than faster quenches, as expected. In accordance with Eqn.(5.1), the measured growth curves collapse onto each other over four orders of magnitude of $\langle x^2 \rangle$ when the time and amplitude are

rescaled. The scaling exponents extracted from this collapse yield $t_{KZ,\dot{\epsilon}} \propto \dot{\epsilon}^{-0.500(4)}$ and $C_{\dot{\epsilon}} \propto \dot{\epsilon}^{0.500(6)}$, in good agreement with the KZ predictions. The KZ paradigm is thus shown to extend to this paradigmatic driven dissipative phase transition.
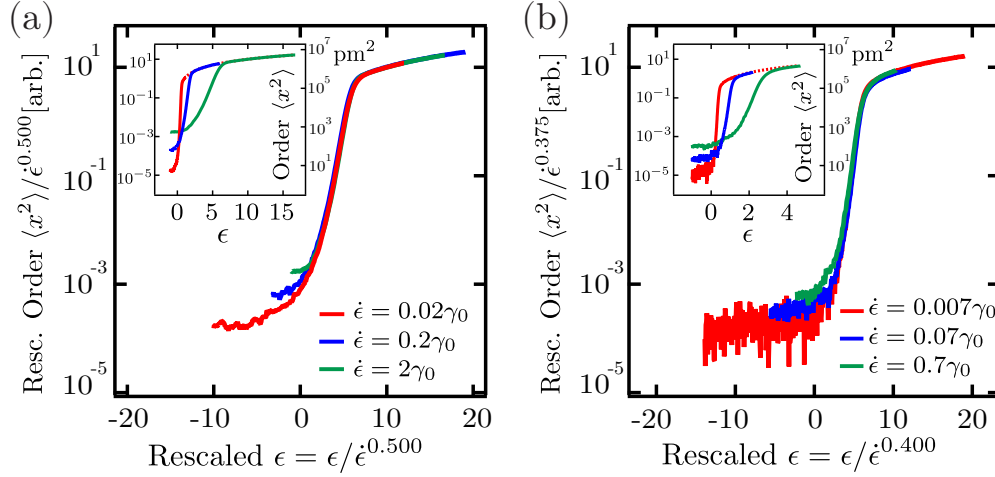
Figure 5.3: **Universality in a driven dissipative phase transition:** (a) Measured growth of order for quenches varying over two orders of magnitude in quench rate $\dot{\epsilon}$. Each curve represents the ensemble average $\langle x^2 \rangle$ over $40 - 100$ iterations. The unscaled growth curves (inset) collapse onto a universal function when time and order $\langle x^2 \rangle$ are scaled appropriately. Note that because temperature is a relevant parameter for this universal scaling, it is varied across different quench rates (see text). (b) The quench dynamics for power-law non-Markovian system-bath interactions is also universal, albeit with modified scaling exponents (see text).

5.6   Effects of non-Markovian system-bath interactions

non-Markovian system-bath interactions have been theorized to lead to new universality classes of phase transitions, to dramatically alter phase diagrams, and to induce novel dynamics [154, 155, 156, 157, 143]. Anomalous critical exponents measured in the open Dicke model, which is closely related to the system described in this work, have previously been attributed to potential non-

Markovian system-bath interactions [141, 142]. In this work, we employ active feedback techniques to implement *any* non-Markovian system-bath interactions of our choosing to study their influence on critical phenomena (see Supplementary Information, Section 5.9.15). Not only can we test KZ universality in the presence of complex system-bath interactions, but given the precision of our measurements, also determine any concomitant changes to critical exponents.

An ubiquitous class of non-Markovian system-bath interactions is one with colored noise, where the environmental noise buffeting the system is characterized by a scale-invariant power-law spectrum $\propto |\omega|^s$ for small frequencies $|\omega|$, and $0 < s < 1$. Following the fluctuation-dissipation relation, the dissipation is correspondingly modified, with a long-time asymptote given by a power-law damping kernel $\gamma(t) \propto |t|^{-(1+s)}$ [151]. For such non-Markovian system-bath interactions, the universal dual-scaling of our system is modified as

$$\langle x^2(t)\rangle_{\dot{\epsilon}} \sim C_{\dot{\epsilon}} \times \mathcal{G}\left(\frac{t}{t_{KZ,\dot{\epsilon}}}, T\, t_{KZ,\dot{\epsilon}}^{3s-1}\right) \tag{5.2}$$

where now $t_{KZ,\dot{\epsilon}} \propto \dot{\epsilon}^{-\frac{1}{1+s}}$ and $C_{\dot{\epsilon}} \propto \dot{\epsilon}^{\frac{s}{1+s}}$ (see Supplementary Information, Section 5.9.6).

We experimentally implement such non-Markovian system-bath interactions with $s = 0.70(2)$ for each of the two harmonic oscillators of our system, where the $|\omega|$ of the power law spectrum is now referenced to the rotating frame. We find that the critical pump drive of $\mu_{cr} = 1$ is unchanged as the integrated damping strength is unchanged (see Supplementary Information, Section 5.9.3). Furthermore, for linear KZ quenches with $T t_{KZ,\dot{\epsilon}}^{3s-1}$ held fixed, the collapse of the measured growth of order over two orders of magnitude of the quench rate, shown in Fig. 5.3(b), demonstrates that the dynamics remains universal for the realized non-Markovian system-bath coupling, albeit with modified exponents.

The exponents extracted from the collapse, $t_{KZ} \propto \dot{\epsilon}^{-0.600(14)}$ and $C_{\dot{\epsilon}} \propto \dot{\epsilon}^{0.375(15)}$, are modified significantly from their Markovian values, and compare well with the theoretical expectation of $-1/(1 + s) \approx -0.588$ and $s/(1 + s) \approx 0.412$ respectively.

We can also make explicit measurements of the Kibble-Zurek times, i.e. when the system begins to develop a macroscopic order, illustrated in Fig. 5.2 as the "freeze-out" time. Without apriori knowledge or guess of the universal scaling with temperature, we perform quenches at a fixed temperature and measure those times when the amplitude-rescaled order grows larger than a particular "macroscopic" value, an ad hoc 10^{-3} in this work (see Supplementary Information, Section 5.9.10). As shown in Fig. 5.4(a), these explicit $t_{KZ,\dot{\epsilon}}$ measurements yield a scaling of $t_{KZ,\dot{\epsilon}} \propto \dot{\epsilon}^{-0.501(3)}$ and $t_{KZ,\dot{\epsilon}} \propto \dot{\epsilon}^{-0.590(3)}$ for the Markovian and non-Markovian cases respectively.

The KZ prediction of the scaling exponent of $t_{KZ,\dot{\epsilon}}$ is the same for both the varying-T and constant-T quench protocols described above, i.e. $t_{KZ,\dot{\epsilon}} \propto \dot{\epsilon}^{-\frac{vz}{1+vz}}$ (see Supplementary Information, Sections 5.9.6 & 5.9.10), thereby relating the critical exponent vz to our measurements. Based on the explicit $t_{KZ,\dot{\epsilon}}$ measurements, vz is thus measured to significantly change from 1.00(1) in the Markovian case, to 1.44(2) for the realized non-Markovian case. This change is corroborated by the vz exponent extracted from the dual scaling measurements of the varying-T quenches, i.e. $vz = 1.00(2)$ and $vz = 1.50(9)$, respectively. Both these measurements can be compared to the theoretical expectation of 1 and $1/0.70 \approx 1.43$, respectively (see Supplementary Information, Sections 5.9.2 & 5.9.3). These measurements provide clear evidence of the significant influence of non-Markovian system-bath interactions on dynamical critical exponents and universality.
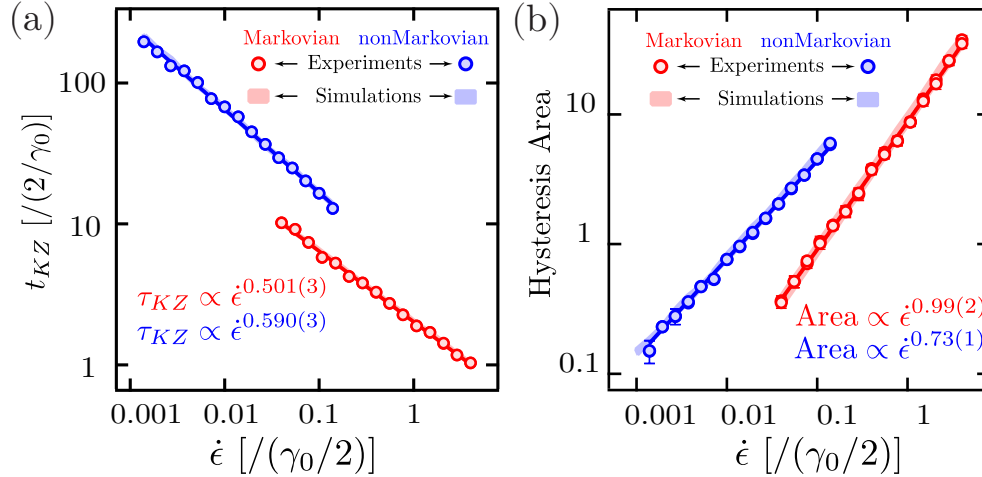
Figure 5.4: **Scaling of the Kibble-Zurek time and hysteretic area in a driven-dissipative phase transition:** (a) Experimentally measured Kibble-Zurek times $t_{KZ,\dot{\epsilon}}$ and their scaling with quench rate $\dot{\epsilon}$. Critical exponents extracted from this scaling yield $\nu z = 1.00(1)$ (Markovian, red) and $\nu z = 1.44(2)$ (power-law non-Markovian, blue), in close agreement with theory (see text, Supplementary Information, Sections 5.9.2 & 5.9.3). (b) Work is done by the parametric drive μ over each cycle of quench into the ordered phase and then back into the disordered phase. This work, proportional to the hysteretic area illustrated in Fig. 5.2, scales as a power-law with the quench rate. The scaling is influenced by the system-bath interactions, as demonstrated here for the Markovian (red) and non-Markovian (blue) cases, and relates to the system's critical exponents (see text, Supplementary Information, Section 5.9.11). Shaded regions denote expected hysteretic areas, based on no-free-parameter simulations.

5.7 Universal scaling of the hysteresis-area

In equilibrium phase transitions, the density of defects formed following a linear finite-time quench into an ordered phase usually follows a scaling law [129]. The energy of this excited state of the system due to its nonadiabatic evolution during such a quench is approximately proportional to the defect density, and thus also follows a scaling law. Analogously, in our driven dissipative sys-

tem, work is done by the parametric drive μ during the system's nonadiabatic evolution. This dissipated energy is proportional to the area E enclosed by the hysteretic response of $\langle x^2 \rangle$ with ϵ between the forward and backward quenches across criticality, as depicted by the patterned region in Fig. 5.2 (see Supplementary Information, Section 5.9.11). Note that while hysteresis is typically associated with discontinuous phase transitions, hysteresis phenomena also occur in continuous phase transitions if they are crossed at a finite rate [148, 130].

We observe that E indeed scales as a universal power-law with the quench rate [Fig. 5.4(b)], with $E \propto \dot{\epsilon}^{0.99(2)}$ and $E \propto \dot{\epsilon}^{0.73(1)}$ in the Markovian and power-law non-Markovian case, respectively (see also [148, 130]). Both, an integral of the universal scaling forms established earlier and a KZ heuristic capture power-law behavior of E – predicting $\dot{\epsilon}^{1}$ and $\dot{\epsilon}^{0.82}$ in the respective cases (see Supplementary Information, Section 5.9.11). Apart from being another measure which demonstrates changing critical exponents with changing system-bath interactions, the reduced exponent of E for the non-Markovian case hints at possible advantages of engineering system-bath interactions to mitigate the effects of heating in state preparation protocols involving phase transitions.

5.8   Conclusions and outlook

We experimentally realize and establish a driven-dissipative continuous phase transition, measure its critical exponents through steady state measurements, demonstrate its universal dynamics, and ascertain the validity of the Kibble-Zurek paradigm. Furthermore, through active feedback protocols, we experimentally implement an instance of a generic power-law non-Markovian

system-bath coupling, and reveal the significant influence of the non-Markovian system-bath interactions on the system's dynamical critical exponents. We also explain the experimental observations through a model including Gaussian fluctuations (see Supplementary Information). We conclude that in principle, such non-equilibrium ramps can be used to extract both equilibrium and non-equilibrium universal exponents in driven dissipative systems. Including the possibility to extract the nature of system-bath interactions and to determine if a Markovian approximation is appropriate.

While valid in this work, there is no apriori reason to expect that the KZ paradigm remains applicable for *all* non-Markovian system-bath interactions, and identifying deviations from KZ predictions is a subject of ongoing experimental studies. Further exploration of the influence of non-Markovian system-bath interactions on critical phenomena, including tests of the KZ paradigm in its original context of topological defects, can be pursued by considering coupled, spatially extended versions of the two-mode systems described in this work. More generally, this work can serve as an effective touchstone in the development of a field theoretic understanding of criticality, universality and dynamics of open driven-dissipative systems with non-Markovian system-bath interactions [158, 159]. We also envisage that engineering novel system-bath interactions, either passively or actively, should allow for the robust preparation and preservation of conventionally fragile states, e.g. squeezed states, potentially useful for enhanced metrology.

5.9 Supplemental Information

5.9.1 System Hamiltonian

In the lab frame, the signal-idler-pump system is described by the Hamiltonian

$$\mathcal{H} = \sum_{k \in \{s,i,P\}} \hbar\omega_k a_k^\dagger a_k - \frac{\hbar g}{x_{0,s} x_{0,i} x_{0,P}} x_s x_i x_P$$

$$- \hbar(F_P e^{-i\omega_P t} a_P^\dagger + F_P^* e^{i\omega_P t} a_P)$$

where g characterizes the bi-linear coupling between the signal and idler modes through the driven pump mode, $x_{0,s}, x_{0,i}, x_{0,P}$ represent the zero point motion, $x_k = x_{0,k}(a_k + a_k^\dagger)$, and F_p parametrizes the strength of the pump drive. In a rotating frame of the signal, idler and pump modes, transformed through $U = \prod_k U_k = \prod_k e^{-i\omega_k a_k^\dagger a_k t}$, the Hamiltonian changes as $\mathcal{H} \rightarrow \mathcal{H}_{rot} = U^\dagger \mathcal{H} U - \sum_k \hbar\omega_k a_k^\dagger a_k$. Using $U_k^\dagger a_k U_k = a_k e^{-i\omega_k t}$, and making the rotating wave approximation, we get the Hamiltonian in the main text,

$$\mathcal{H}_{rot} = -\hbar g(a_s^\dagger a_i^\dagger a_P + a_P^\dagger a_i a_s) - \hbar(F_P a_P^\dagger + F_P^* a_P)$$

Note that the first term signifies the downconversion from the pump mode into the signal and idler modes ($a_s^\dagger a_i^\dagger a_P$) and the conjugate ($a_P^\dagger a_i a_s$) signifies the upconversion from the signal and idler modes into the pump mode. The second term denotes the coherent drive of the pump mode ($F_P a_P^\dagger + F_P^* a_P$).

For future reference, note that $x_{s,i} = x_{0,s,i}(a_{s,i} + a_{s,i}^\dagger)$ and $y_{s,i} = -ix_{0,s,i}(a_{s,i} - a_{s,i}^\dagger)$ are independent quadratures of motion. The experimentally measured complex amplitudes of motion, $z_{s,i} = x_{s,i} + iy_{s,i}$, are nothing but $z_{s,i} = 2x_{0,s,i}a_{s,i}$.

5.9.2 Markovian case

In this section, we solve for the steady-state solutions to the system's equations of motion in the noise-free limit (no fluctuations), for the Markovian case, and locate the critical point. We also derive the steady-state and dynamical critical exponents associated with this driven dissipative continuous phase transition.

Equations of motion

The equations of motion for the signal, idler and pump modes are given by the Heisenberg-Langevin master equation [151]. These include (a) the Hermitian evolution of the modes, (b) the non-Hermitian dissipation of the modes to their environment, captured by the terms involving $\gamma_{s,i,P}$, (c) the terms $i f_{s,i,P}$, which account for the stochastic forces acting on the modes because of their coupling to a finite temperature bath, and (d) the terms $i F_{s,i}$, which account for coherent forces applied on the signal and idler modes –

$$
\dot{a}_{s,i} = i g a_{i,s}^\dagger a_P - \frac{\gamma_{s,i}}{2} a_{s,i} + i F_{s,i} + i f_{s,i}
$$
$$
\dot{a}_P = i g a_i a_s - \frac{\gamma_P}{2} a_P + i F_P + i f_P
$$

(5.3)

The stochastic terms are related to the dissipation terms via the fluctuation dissipation relation, and satisfy

$$
\langle f_k(t) f_l^\dagger(t') \rangle = \gamma_k (\bar{n}_{th,k} + 1) \delta(t - t') \delta_{kl}
$$

where $k, l \in \{s, i, P\}$ and

$$
\bar{n}_{th,s,i,P} = \left[\exp\left(\frac{\hbar \omega_{s,i,P}}{k_B T} \right) - 1 \right]^{-1}
$$

In the remainder of this work, unless noted otherwise, we will consider the experimentally valid high temperature (classical) regime of $k_B T \gg \hbar \omega_{s,i}$, so that $\bar{n}_{th,s,i} \approx k_B T / (\hbar \omega_{s,i}) \gg 1$ and $\bar{n}_{th,s,i} \propto T$. Unless otherwise noted, we also set the

pump noise to zero ($f_P \to 0$), given the relatively large coherent drive F_P.

Effective potential and the Mexican hat

Given that $\gamma_P \gg \gamma_{s,i}$ in the experiments, we adiabatically eliminate a_P from Eqn.(5.3) by setting $a_P = \frac{2}{\gamma_P}(iga_ia_s + iF_P)$. In the absence of external forces or fluctuations, i.e. $F_{s,i}, f_{s,i} \to 0$, the semi-classical equations of motion ($a_{s,i}^\dagger \to a_{s,i}^*$) reduce to

$$\dot{a}_{s,i} = -\left(\frac{\gamma_{s,i}}{2} + \frac{2g^2}{\gamma_P}|a_{i,s}|^2\right)a_{s,i} - \frac{2gF_P}{\gamma_P}a_{i,s}^* \tag{5.4}$$

These equations of motion are equivalently given by $\dot{a}_{s,i} = -\partial \mathcal{H}_{\text{eff}}/\partial a_{s,i}^*$, where $\mathcal{H}_{\text{eff}}$ is the effective potential of the system,

$$\mathcal{H}_{\text{eff}} = \frac{\gamma_s}{2}|a_s|^2 + \frac{\gamma_i}{2}|a_i|^2 + \frac{2g^2}{\gamma_P}|a_s|^2|a_i|^2$$
$$+ \frac{\sqrt{\gamma_s\gamma_i}}{2}\mu(a_s^*a_i^* + a_sa_i) \tag{5.5}$$

Here, μ is the normalized parametric drive

$$\mu = \left|\frac{F_P}{F_{cr}}\right|, \text{where } |F_{cr}| = \frac{\gamma_P\sqrt{\gamma_s\gamma_i}}{4g} \tag{5.6}$$

sets the critical pump strength beyond which $\mathcal{H}_{\text{eff}}$ is minimized for $|a_{s,i}| > 0$, i.e. for finite order. For $\mu < 1$, $\mathcal{H}_{\text{eff}}$ is minimized for $|a_{s,i}| = 0$, i.e. disorder. F_{cr} is equivalently obtained by setting $f_{s,i} \to 0$, $F_{s,i} \to 0$ and solving Eqn.(5.3) for the onset of nontrivial ($|a_{s,i}| \neq 0$) steady state ($\dot{a}_k = 0$) solutions.

The Mexican hat potential is easily evident in the experimentally relevant case of symmetric damping of the two modes, $\gamma_{s,i} = \gamma_0$. In this case, $a_{s,i} \approx -a_{i,s}^*$, and the equations of motion excluding the fluctuations are given by

$$\dot{a}_s = -\frac{\partial \mathcal{H}_{\text{eff}}}{\partial a_s^*} \approx -\frac{\gamma_0}{2}(1 - \mu)a_s - \frac{2g^2}{\gamma_P}|a_s|^2a_s \tag{5.7}$$

And the corresponding effective potential is

$$\mathcal{H}_{\text{eff}} \approx \gamma_0(1-\mu)|a_s|^2 + \frac{2g^2}{\gamma_P}|a_s|^4 \tag{5.8}$$

which is a Mexican hat for $\mu > 1$.

In the experiments, $\gamma_0 = 0.50(1)$ s^{-1}. Unless otherwise noted, we consider equal signal and idler damping for the remainder of this work.

Predictions of critical exponents

The stable steady state solutions of Eqn.(5.3) are

$$|a_{s,i}| = \begin{cases} 0 & \mu \le 1 \\ \sqrt{\gamma_P\gamma_0}/2g \times \sqrt{\mu-1} & \mu > 1 \end{cases}$$
$$|a_P| = \begin{cases} \mu\gamma_0/2g & \mu \le 1 \\ \gamma_0/2g & \mu > 1 \end{cases} \tag{5.9}$$

directly yielding $\beta = 1/2$ for $\mu > 1$, where $|a_{s,i}| \propto \epsilon^\beta$, $\epsilon = (\mu - \mu_{cr})/\mu_{cr} = \mu - 1$.

We note that in the absence of fluctuations ($f_{s,i} \to 0$), Eqn.(5.3) constrains the phase sum $\phi_s + \phi_i$ to be equal to the pump phase, but the phase difference $\phi_s - \phi_i$ is unconstrained, reflecting a spontaneous symmetry breaking. This is also reflected in the effective potential $\mathcal{H}_{\text{eff}}$ of Eqn.(5.5), which depends only on Arg$[a_s a_i] = \phi_s + \phi_i$. However, at finite temperature, the fluctuations cause the phase difference to diffuse over time [143], so that there is no "true" spontaneous symmetry breaking.

To get the critical exponent γ, the susceptibility to a force $\propto F_s \in \mathbb{R}$ can be derived as follows. Eqn.(5.4) is diagonalized by linearizing about the steady state solution Eqn.(5.9) assuming $x_{0,s,i} = x_0$. Below criticality, the evolution of

the cross-quadratures $x_\pm = (x_s \pm x_i)/\sqrt{2}$ is then given by

$$\frac{\dot{x}_\pm}{x_0} = -\frac{\gamma_0}{2}(1 \pm \mu)\frac{x_\pm}{x_0} + 2iF_\pm + if_\pm \tag{5.10}$$

$$\Rightarrow x_\pm = \frac{4ix_0 F_\pm}{\gamma_0(1 \pm \mu)} \Rightarrow x_i \xrightarrow{\mu \to 1} \frac{1}{|\epsilon|}\frac{2ix_0 F_s}{\gamma_0}$$

This gives $|\partial x_i/\partial F_s| \propto |\epsilon|^{-\gamma}$ with the exponent $\gamma = 1$. Here, $\sqrt{2}F_\pm = F_s \pm F_i^0$ and $\sqrt{2}f_\pm = (f_s - f_s^\dagger) \pm (f_i - f_i^\dagger)$.

In the absence of external forces and noise, i.e. $F_\pm, f_\pm \to 0$, Eqn.(5.10) also gives the scaling of the relaxation time with ϵ as

$$x_\pm(t) = x_\pm(0)e^{-\frac{\gamma_0}{2}(1 \pm \mu)t}$$

$$\Rightarrow x_{s,i}(t) = \frac{x_+(0)}{2}e^{-\frac{\gamma_0}{2}(1+\mu)t} \pm \frac{x_-(0)}{2}e^{-\frac{\gamma_0}{2}(1-\mu)t}$$

The longest time scale being given by

$$\tau_{s,i} = \frac{2}{\gamma_0(1 - \mu)} \xrightarrow{\mu \to 1} \frac{2}{\gamma_0}\frac{1}{|\epsilon|}$$

This gives $\tau \propto |\epsilon|^{-\nu z}$, $\nu z = 1$, as measured and described in the main text.

5.9.3   Non-Markovian case

In this section, we detail how the system's equations of motion change in the non-Markovian case *vis-à-vis* the Markovian case of the previous section. We also show how the non-Markovian system-bath interactions change the phase transition's dynamical critical exponent.

Equations of motion

For generic non-Markovian system-bath interactions, the equations of motion in the rotating frame, given by Eqn.(5.3), are modified as

$$\dot{a}_{s,i} = iga_{i,s}^{\dagger}a_P - \frac{1}{2}\int_{-\infty}^{t} dt' \gamma_{s,i}(t-t')a_{s,i}(t') + if_{s,i} \tag{5.11}$$

$$\dot{a}_P = iga_i a_s - \frac{\gamma_P}{2}a_P + iF_P + if_P$$

where $\gamma_{s,i}(t)$ is the dissipation kernel [151], and we have assumed that both the signal and idler are described by the same kernel, as realized in the experiments. Note that the stochastic force terms satisfy the fluctuation dissipation relation

$$\langle f_k(t)f_l^{\dagger}(t')\rangle = \frac{1}{2}(\bar{n}_{th,k} + 1)\gamma_k(|t-t'|)\delta_{kl} \tag{5.12}$$

where $k \in \{s, i\}$ The Markovian case is retrieved by setting the dissipation kernel as $\gamma_{s,i}(t) = \gamma_{s,i}\delta(t)$. Note that when evaluating Eqn.(5.12) in the Markovian case, an appropriate limit of $\gamma_k(t)$ needs to be taken such that it reduces to the delta function $\delta(t)$, also ensuring the usual requirement that $\gamma_k(t)$ is causal, i.e. $\gamma_k(t) = 0, \forall t < 0$.

Predictions of critical exponents (Power law non-Markovian case)

The steady state and noise-free ($\dot{a}_k, f_k \rightarrow 0$) evaluation of the critical drive strength, above-threshold solutions, and the exponents β and γ, proceed as before. The steady state solutions considered in the previous section for the Markovian case are still valid solutions, for which only the total strength of the damping matters, given by the integral $\int dt\gamma_{s,i}(t) = \gamma_{s,i}$. For the non-Markovian system-bath interactions considered in this work, these are the only stable steady state solutions. Eqn.(5.11) thus yields the same results as Eqn.(5.3). In particular, the critical drive strength F_{cr}, and the values of $\beta = 1/2$, $\gamma = 1$ remain

unchanged. Dynamics, on the other hand, *is* affected by a power law kernel, as described below. In the remainder of this work, we consider the experimentally relevant case of symmetric non-Markovian damping for the signal and idler modes, i.e. $\gamma_{s,i} = \gamma(t)$, unless otherwise noted.

Below threshold, we linearize Eqn.(5.11) around the $\mu < 1$ solution of Eqn.(5.9), and then diagonalize to get

$$\dot{x}_\pm = \mp \frac{\gamma_0 \mu}{2} x_\pm - \frac{1}{2} \int_{-\infty}^{t} dt' \gamma(t - t') x_\pm(t') + i f_\pm$$

In Fourier space, this simplifies to

$$\tilde{x}_\pm(\omega) = \frac{1}{\frac{\tilde{\gamma}(\omega)}{2} \pm \frac{\gamma_0 \mu}{2} - i\omega} \, i\tilde{f}_\pm = \chi_\pm(\omega) \, i\tilde{f}_\pm \tag{5.13}$$

where $\chi_\pm(\omega)$ defines the susceptibility. Here, $\tilde{\gamma}(\omega)$ is the complex Fourier transform of the kernel $\gamma(t)$. The complex poles ω_n of $\chi(\omega)$ characterize the system response, with the relaxation rates scaling as $-\text{Im}[\omega_n]$. Note that in general, we may not always be able to characterize the system response by complex poles of susceptibilities, e.g. when the susceptibility is not Lorentzian [142], or does not have well defined poles.

In the Markovian case, $\tilde{\gamma}(\omega) = \gamma_0 \, \forall \omega \in \mathbb{C}$ is the complex extension of the kernel $\tilde{\gamma}(\omega) = \gamma_0 \, \forall \omega \in \mathbb{R}$. Thus $\omega_n = -i\frac{\gamma_0}{2}(1 \pm \mu)$, the least negative imaginary part of which is $-\frac{\gamma_0}{2}(1 - \mu) = -\frac{\gamma_0}{2}|\epsilon|^1$, implying that $\tau \propto |\epsilon|^{-\nu z}$, $\nu z = 1$, as otherwise derived and considered before.

In the non-Markovian experiments, we consider and realize power law non-Markovian system-bath interactions with a damping kernel $\tilde{\gamma}(\omega) = \tilde{\gamma}'(\omega) + i\,\tilde{\gamma}''(\omega)$, with

$$\tilde{\gamma}'(\omega) = \gamma_0 + \gamma_{pl}|\omega/\omega_0|^s e^{-|\omega|/\omega_c}$$

being the real part, and $\tilde{\gamma}''$ being the imaginary part. The two are related through

the Kramers-Kronig relation, giving a low frequency asymptotic form of

$$\tilde{\gamma}(\omega) = \gamma_0 + \gamma_{pl}|\omega/\omega_0|^s \left(1 - i \, \text{sgn}(\omega) \tan \pi s/2\right)$$

which decides the divergence of the relaxation time scale. Note that in this power-law kernel, the ultraviolet divergence is avoided through an exponential tail with cutoff frequency ω_c. The corresponding non-Markovian kernel $\gamma(t)$ evaluates to

$$\gamma(t) = \gamma_0 \delta(t) + \left[\frac{2}{\pi}\gamma_{pl}\omega_0^{-s}\omega_c^{1+s}\Gamma(1+s)\right] \times$$

$$\cos\left[(1+s)\arctan(\omega_c t)\right] \times (1 + \omega_c^2 t^2)^{-\frac{1+s}{2}} \times \Theta[t] \tag{5.14}$$

where $\Theta[\cdot]$ is the Heaviside function, and the kernel asysmptotes to a power-law decay, for time $t \gg \omega_c^{-1}$, i.e. $\gamma(t \gg \omega_c^{-1}) \propto -|t|^{-1-s}$. In our experiments, $s = 0.70(2)$, $\gamma_0 = 1.00(2)$ s^{-1}, $\gamma_{pl} = 2.12(4)$ s^{-1}, $\omega_0 = 1$ s^{-1} and $\omega_c = 6$ s^{-1}. Note that ω_0 is just a normalization constant, with no physical significance independent of γ_{pl}.

$\chi_\pm(\omega)$, the susceptibility for real ω, is then given by Eqn.(5.13) as

$$\left[\frac{\gamma_0}{2}(1 \pm \mu) + \gamma_{pl}|\omega/\omega_0|^s \left(1 - i \, \text{sgn}(\omega) \tan \pi s/2\right) - i\omega\right]^{-1} \tag{5.15}$$

The characteristic frequency scale of the parametrically driven system near criticality ($\epsilon \to 0$), characterized by the full width at half maximum of the susceptibility $\chi_-(\omega)$, is proportional to $|\epsilon|^{1/s}$, yielding $\tau \propto |\epsilon|^{-vz}$, $vz = 1/s$. In the experiments, $s = 0.70(2)$, predicting that $vz \approx 1.43(4)$. This analysis sufficiently explains the experimentally measured exponent 1.44(2), as described in the main text.

Note that the experimentally realized power-law non-Markovian kernel contains a Markovian component γ_0. The Markovian component contributes to a net positive total damping, $\int_0^\infty dt\gamma(t) > 0$, which is required for the very exis-

tence of a continuous phase transition at a parametric drive $\mu_{cr} > 0$ (the contribution from the power-law part integrates to zero). Moreover, real systems usually do have finite damping at low frequency, and the Markovian component γ_0 represents a broad class of dissipation kernels where the damping is frequency independent at low frequency ($\omega \to 0$).

5.9.4 Divergence of fluctuations in the linearized limit

In this section, we calculate the steady-state behavior of the observable $\langle x^2 \rangle$ for both the Markovian and non-Markovian cases, and evaluate the power-law of its divergence at criticality in a Gaussian theory of fluctuations. In later sections, we will relate this scaling to the the system's universal nonequilibrium quench behavior.

The susceptibility $\chi_-(\omega)$ (Eqn.(5.13)) allows us to evaluate the critical divergence of the amplified quadrature $\langle x_-^2 \rangle$ below criticality, i.e. in the disordered phase, as

$$\langle x_-^2 \rangle = \frac{1}{2\pi} \int_{-\infty}^{+\infty} d\omega |\chi_-(\omega)|^2 \mathrm{PSD}_{f_-}(\omega)$$

where $\mathrm{PSD}_{f_-}(\omega)$ denotes the power spectral density of the noise f_-. Following Eqn.(5.12), note that $\mathrm{PSD}_{f_-}(\omega) \propto (\bar{n}_{th} + 1) \propto T$. We evaluate this divergence for future reference, and define the exponent ζ as $\langle x_-^2 \rangle \propto |\epsilon|^{-\zeta}$.

Markovian case: Following from Eqn.(5.13) and the fact that PSD_{f_-} is frequency

independent (the noise is delta-correlated in time),

$$\text{PSD}_{x_-}(\omega) \propto \frac{T}{[\frac{\gamma_0}{2}\epsilon]^2 + \omega^2}$$

$$\Rightarrow \quad \langle x_-^2 \rangle \propto T|\epsilon|^{-1}$$

i.e. $\zeta = 1$ for the Markovian case.

Power law non-Markovian case: Like the Markovian case, the divergence of $\langle x^2 \rangle$ for the considered power-law non-Markovian case occurs at $\omega \to 0$. This is because for large $|\omega|$, $|\chi_-(\omega)|^2 \propto \frac{1}{\omega^2}$, which has a finite integral over large $|\omega|$. For small $|\omega| \to 0$, $\text{Re}[\chi_-^{-1}(\omega)] \to \frac{\gamma_0}{2}|\epsilon|$ and $\text{Im}[\chi_-^{-1}(\omega)] \to \#|\omega|^s$, for $0 < s < 1$. And the Markovian component of the dissipation, $\text{PSD}_{f_-}(\omega) \to$ constant as $\omega \to 0$. This leads to

$$\text{PSD}_{x_-}(\omega) \sim \frac{T}{[\frac{\gamma_0}{2}\epsilon]^2 + \#|\omega|^{2s}}$$

$$\Rightarrow \quad \langle x_-^2 \rangle \sim T|\epsilon|^{-(2-\frac{1}{s})}$$

for $1 > s > 1/2$. Therefore, $\zeta = 2 - 1/s$ for the considered power-law non-Markovian system-bath interactions.

We note in passing that for $0 < s < 1/2$, there is no divergence of $\langle x^2 \rangle$. Such non-Markovian system-bath interactions are hot beds for possible violations of the KZ paradigm, and will be explored elsewhere.

5.9.5 Finite temperature phase diagram (Markovian Case)

In this section, we evaluate the interplay between the inherent nonlinearity of the system and the temperature induced fluctuations near criticality. A 'true' critical divergence of $\langle x^2 \rangle$ is prevented by the intrinsic nonlinearity. The phase

transition is sharp only at $T = 0$, and morphs into a crossover for finite T.

This is most easily seen through the effective Mexican hat potential described earlier, Eqn.(5.8),

$$\mathcal{H}_{\text{eff}} = \gamma_0(1 - \mu)|a_s|^2 + \frac{2g^2}{\gamma_P}|a_s|^4 \tag{5.8}$$

At $T = 0$, in the absence of fluctuations, $|a_{s,i}|^2 = 0$ for $\mu < 1$. However, as we have seen in the previous section using the linearized equations of motion below criticality, finite noise in fact leads to divergent fluctuations near criticality – In semi-classical terms,

$$\langle |a_{s,i}|^2 \rangle \propto \frac{\langle x_-^2 \rangle}{2} \approx \frac{1}{|\epsilon|}\frac{k_B T}{\hbar\omega} = \frac{2a_{th}^2}{|\epsilon|} \tag{5.16}$$

for $1 \ll \bar{n}_{th,s} \approx \bar{n}_{th,i} \approx k_B T/\hbar\omega = 2a_{th}^2$.

The linearized description fails when the quartic term of Eqn.(5.8) (corresponding to the nonlinear term in the equations of motion) is commensurate or larger in magnitude than the quadratic term (corresponding to the linear term in the equations of motion). This occurs for $\gamma_0|1-\mu| = \gamma_0|\epsilon| \lesssim \frac{2g^2}{\gamma_P}\langle |a_s|^2 \rangle = \frac{\gamma_0}{2}\langle |a_{s,i}|^2 \rangle/a_{ss}^2$, where $a_{ss} = \sqrt{\gamma_P\gamma_0}/2g$ is the steady-state order at $\epsilon = +1$, on the ordered side (see Eqn.(5.9)). Using Eqn.(5.16), we find that the fluctuations invalidate the linear approximation for

$$\frac{a_{th}^2}{a_{ss}^2} \gtrsim |\epsilon|^2 \tag{5.17}$$

This sets a natural temperature scale of the system, T_{nl}, as that when $\tilde{a}_{th}^2 := a_{th}^2/a_{ss}^2 = 1$. Above this temperature, the system is dominated by thermal fluctuations even at $\mu = 0$, i.e. even without the divergence induced by the parametric drive. The ratio $\tilde{a}_{th}^2/|\epsilon|^2$, of the linear term to the nonlinear term, is the shading used in the finite temperature phase diagram in Fig. 5.1(a) of the main-text. Dark blue shading depicts the region where this ratio is larger than unity.

Typically, in our experiments, $a_{ss} \approx 500 \text{ pm}/(\sqrt{2}x_0) \approx 6 \times 10^6$, where $x_0 = \sqrt{\hbar/(2m\omega)} \approx 60$ am is the zero point motion of the oscillator. As such, the T_{nl} for our experiments is given by

$$\frac{k_B T_{nl}}{2\hbar\omega} = a_{ss}^2 \approx 36 \times 10^{12}$$

$$\Rightarrow \quad T_{nl} \approx 4 \times 10^9 \text{ K}$$

The room temperature steady state measurements reported in Fig. 5.1(a) of the main text are thus nearly seven orders of magnitude lower in temperature than T_{nl}.

The fluctuations derived in the previous section and used in Eqn.(5.16) are obtained by linearizing the equations of motion in the disordered phase ($\mu < 1$). In the ordered phase above criticality, the linearization is done about the steady-state order. It was previously shown that the relevant divergent fluctuation quadrature is the amplitude sum, which diverges as $\mu \times 2\tilde{a}_{th}^2/\epsilon$ [83]. The linearization here breaks down when the fluctuations equal the steady-state order, i.e. $\mu \times 2\tilde{a}_{th}^2/\epsilon \approx \mu - 1 = \epsilon$, giving the relevant ratio as $\mu \times \tilde{a}_{th}^2/\epsilon^2$, which is plotted in Fig. 5.1(a) for $\epsilon > 0$.

Note that the lowest experimental temperature realized in this work is room temperature $T \approx 285$ K, for which $a_{th,RT} \approx \sqrt{k_B T/m\omega_{s,i}^2}$, whereas $a_{ss} \gtrsim 2000 \times a_{th,RT}$. As such, quantum effects are not observable in the shown phase diagram of Fig. 5.1(a) - the temperatures would need to be orders of magnitude lower.

5.9.6 Kibble-Zurek prediction of scaling exponents

In this section, we use the Kibble-Zurek paradigm to relate the steady-state critical exponents derived in earlier sections to the scaling exponents of the nonequilibrium quenches across criticality, for both the Markovian and the non-Markovian cases. The amplitude scaling and the time scaling are successfully retrieved for either case. We further use the KZ paradigm to predict the temperature scaling required to reveal the universality.

The Kibble-Zurek time t_{KZ} is computed by equating the instantaneous relaxation time at a given point during a ramp to the time remaining for the system to reach criticality. The relaxation time diverges as $|\epsilon|^{-\nu z}$, where ν and z are the conventional critical exponents [2]. For a linear quench at rate $\dot{\epsilon}$ with $\epsilon(t) = \dot{\epsilon}t$, and where ϵ_{KZ} is defined as $\epsilon(t_{KZ})$, we have

$$t_{KZ} \quad \propto \quad |\epsilon_{KZ}|^{-\nu z} = (\dot{\epsilon}t_{KZ})^{-\nu z}$$

$$\Rightarrow t_{KZ} \quad \propto \quad \dot{\epsilon}^{-\frac{\nu z}{1+\nu z}}, \ \epsilon_{KZ} \propto \dot{\epsilon}^{\frac{1}{1+\nu z}} \tag{5.18}$$

$\nu z = 1$ and $1/s$ for the Markovian and power-law non-Markovian cases, respectively, and as such, $t_{KZ} \propto \dot{\epsilon}^{-\frac{1}{2}}$ and $t_{KZ} \propto \dot{\epsilon}^{-\frac{1}{1+s}}$, respectively, as quoted in the main text. Moreover, according to the KZ paradigm, observables "freeze out" or evolve negligibly for $|t| < t_{KZ}$. As such, for a quench of rate $\dot{\epsilon}$, the value of $\langle x^2 \rangle$ at criticality $\langle x^2(t = 0) \rangle = C_{\dot{\epsilon}}$ (Eqn.(5.1)) equates to its value at t_{KZ}. Applying this KZ heuristic in the ordered phase, where $|x| \propto |\epsilon|^{\beta}$, we get

$$C_{\dot{\epsilon}} = \langle x^2 \rangle|_{t_{KZ}} \propto |\epsilon_{KZ}|^{2\beta} \propto \dot{\epsilon}^{\frac{2\beta}{1+\nu z}}.$$

$\beta = 1$ for both the Markovian and the power-law non-Markovian cases, whereas $\nu z = 1$ and $1/s$ respectively, giving $C_{\dot{\epsilon}} \propto \dot{\epsilon}^{\frac{1}{2}}$ and $C_{\dot{\epsilon}} \propto \dot{\epsilon}^{\frac{s}{1+s}}$ respectively, as quoted

---

[2]In this effectively 0−dimensional work, an independent explicit correlation length exponent ν is ill-defined. However, following convention, we retain the notation of νz as the relaxation time exponent.

in the main text.

Temperature scaling

If the dynamics of the system is indeed universal, and if the KZ paradigm does indeed apply, then the temperature scaling in Eqn.(5.1) and Eqn.(5.2) of the main text can be derived by applying the paradigm on both sides of the criticality. Given a steady state critical divergence of $\langle x^2 \rangle \propto |\epsilon|^{-\zeta}$ in the disordered phase, the KZ paradigm predicts that

$$C_{\dot{\epsilon}} \propto T|\epsilon_{KZ}|^{-\zeta} \propto T\dot{\epsilon}^{-\frac{\zeta}{1+\nu z}} \tag{5.19}$$

wherein the proportionality to temperature T on the disordered side follows from Maxwell's equipartition $\frac{1}{2}m\omega^2\langle x^2 \rangle = \frac{1}{2}k_B T$ for a harmonic oscillator. Equating this to the scaling derived in the previous section using the KZ paradigm on the ordered side, i.e. $C_{\dot{\epsilon}} \propto \dot{\epsilon}^{\frac{2\beta}{1+\nu z}}$, we have

$$T\dot{\epsilon}^{-\frac{\zeta}{1+\nu z}} \propto \dot{\epsilon}^{\frac{2\beta}{1+\nu z}}$$

$$\Rightarrow \quad T \propto \dot{\epsilon}^{\frac{2\beta+\zeta}{1+\nu z}} \propto t_{KZ}^{-\frac{2\beta+\zeta}{\nu z}}$$

$$\Rightarrow \quad T t_{KZ}^{\frac{2\beta+\zeta}{\nu z}} = \text{constant}$$

In the Markovian case, where $\beta = 1$, $\zeta = 1$, and $\nu z = 1$, this translates to $T t_{KZ}^2 = \text{constant}$, whereas in the power-law non-Markovian case, where $\beta = 1$, $\zeta = 2 - \frac{1}{s}$ and $\nu z = \frac{1}{s}$, the condition is $T t_{KZ}^{3s-1} = \text{constant}$. In order to bring out the universality in the experiments, we enforce these constraints by varying the temperature across different quench rates.

5.9.7 Rescaling arguments for parameter scalings in the Markovian case

In this section, we give a rescaling argument to derive the universal scaling described in the main text. We note at the outset that the following derivation is for a linear quench, and does not depend on the initial conditions of the system. It implicitly assumes that the quench spans from $t = -\infty$ to $t = +\infty$ and thus from $\epsilon = -\infty$ to $\epsilon = +\infty$. While this assumption does not correspond to the experiments (the quenches start at a finite time with $\epsilon = -1$), the behavior near criticality is independent of the initial conditions for small quench rates $\dot{\epsilon} \to 0$. More broadly, this argument can be extended in the limit of $\dot{\epsilon} \to 0$ to cases where $|\epsilon|$ is bounded, e.g. $\epsilon(t) = \tanh(\dot{\epsilon}t)$.

The equation of motion (Eqn.(5.7)) including the finite temperature fluctuations is given by

$$\frac{dx(t)}{dt} = \frac{\gamma_0}{2}(\dot{\epsilon}t)x(t) - \frac{\gamma_0}{2}\frac{|x(t)|^2}{x_{ss}^2}x(t) + \sqrt{\gamma_0}x_{th}\xi(t) \tag{5.20}$$

wherein for simplicity of notation, we have replaced a_s by x, $\frac{2g^2}{\gamma_P} = \frac{\gamma_0}{2}\frac{1}{a_{ss}^2}$ by $\frac{\gamma_0}{2}\frac{1}{x_{ss}^2}$ and also included the noise term, for which $x_{th}^2 = \frac{k_BT}{\hbar\omega}$ and ξ is delta correlated, $\langle \xi(t)\xi(t')\rangle = \delta(t-t')$. We have also assumed a linear quench $\epsilon(t) = \dot{\epsilon}t$.

Eqn.(5.20) is invariant under the rescaling of time by u, and the parameters

as

$$\gamma_0' = w \, \gamma_0 \tag{5.21a}$$

$$\dot{\epsilon}' = \frac{u^2}{w} \dot{\epsilon} \tag{5.21b}$$

$$x_{ss}' = v \sqrt{\frac{w}{u}} \, x_{ss} \tag{5.21c}$$

$$x_{th}' = v \sqrt{\frac{u}{w}} \, x_{th} \tag{5.21d}$$

The experiments, wherein the dissipative coupling γ_0 and the intrinsic-nonlinearity dependent $x_{ss} = \sqrt{\gamma_P \gamma_0}/2g$ are fixed, constrain us to $w = 1$ (Eqn.(5.21a)) and $v = \sqrt{u}$ (Eqn.(5.21c)), so that $\dot{\epsilon}' = u^2 \dot{\epsilon}$ and $x_{th}' = u x_{th}$. The latter condition is equivalently stated as $T' = u^2 T$, because thermal motion RMS x_{th} and temperature T are related through equipartition as $\langle x_{th}^2 \rangle \propto T$. The universality with quench rate is exposed by choosing the rescaling which eliminates the $\dot{\epsilon}'$ dependence, i.e. $u = (K_1/\dot{\epsilon})^{1/2}$ and concomitantly $v \propto \dot{\epsilon}^{-1/4}$, where K_1 is a constant. This thus gives the universal scaling function quoted in the main text –

$$v^2 \langle x^2(t; \dot{\epsilon}; T) \rangle = \langle x^2(p; \dot{\epsilon}'; T') \rangle$$

$$\Rightarrow \langle x^2(t; \dot{\epsilon}; T) \rangle = v^{-2} \langle x^2(t/u; u^2 \dot{\epsilon}; u^2 T) \rangle$$

$$\Rightarrow \langle x^2(t; \dot{\epsilon}; T) \rangle \propto \dot{\epsilon}^{1/2} \langle x^2(t/u; K_1; u^2 T) \rangle$$

$$\text{or} \quad \langle x^2(t; \dot{\epsilon}; T) \rangle = C_{\dot{\epsilon}} \, \mathcal{G}\left(\frac{t}{t_{KZ,\dot{\epsilon}}}, T t_{KZ,\dot{\epsilon}}^2 \right)$$

where $C_{\dot{\epsilon}} \propto \dot{\epsilon}^{1/2}$, $\mathcal{G} \propto \langle x^2(t/u; K_1; u^2 T) \rangle$, and $t_{KZ,\dot{\epsilon}} \propto u \propto \dot{\epsilon}^{-1/2}$ is the Kibble-Zurek time. Here, $\mathcal{G}$ is a universal scaling function that does not depend on microscopic details or the shape of the protocol away from $\epsilon = 0$ [153].

5.9.8 Extracting exponents through collapse of dynamics

In this section, we describe the analysis of the experimental data for extracting the KZ scaling exponents through a collapse of the order-growth curves.

The dynamical growth of $\langle x^2(t) \rangle$ measured over varying quench rates $\dot{\epsilon}$ scales according to the equation

$$\langle x^2(t) \rangle_{\dot{\epsilon}} = C_{\dot{\epsilon}} \times \mathcal{G}\left(\frac{t}{t_{KZ,\dot{\epsilon}}}, K_2\right)$$

where K_2 is held constant across different $\dot{\epsilon}$ to eliminate the temperature dependence of $\mathcal{G}$ as described in the previous section. The KZ paradigm predictions for the exponents of $t_{KZ,\dot{\epsilon}}$ and $C_{\dot{\epsilon}}$ with $\dot{\epsilon}$ have been described in previous sections. To extract these exponents from the collapse of the experimental data, we scale all the measured growth curves in amplitude and time, with exponents a and b, over the entire quench, i.e. we define

$$\tilde{x}^2_{a,b}(t'; \dot{\epsilon}) := \dot{\epsilon}^{\,a} x^2\left(\frac{t}{\dot{\epsilon}^{\,b}}\right)$$

(Note that the critical point, being at $t = 0$, does not get scaled in time.) We then minimize the time-averaged variance over the exponents (a, b), i.e.

$$\mathrm{Var}_{\min} = \min_{a,b} \frac{1}{(T_1 + T_2)} \int_{-T_1}^{+T_2} dt' (\tilde{x}^2_{a,b}(t') - \langle \tilde{x}^2_{a,b} \rangle(t'))^2$$

where the $\langle \cdot \rangle(t')$ now denotes the average over the various quench rates $\dot{\epsilon}$, at the rescaled time t'. The range $[-T_1, T_2]$ is the largest common domain of rescaled time over which experimental data was acquired for all of the quench rates being collapsed. Note that a perfect collapse would make this variance measure vanish. The quoted extracted exponent is that (a_0, b_0) which minimizes the variance. The error bars quoted for the collapse-extracted exponents are determined by the extremes of the (a, b)-contour defined by $\mathrm{Var}(a, b) = 2 \times \mathrm{Var}_{\min}$. The evaluation of this variance and contour is shown in Fig. 5.5 for the Markovian case.
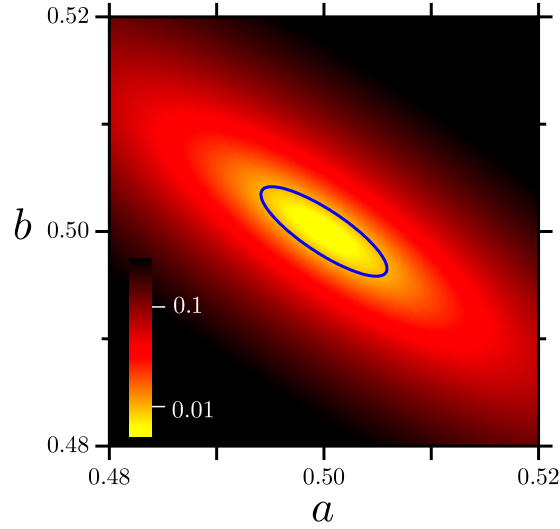
Figure 5.5: Time-averaged variance of the rescaled growth curves in the Markovian case for $\dot{\epsilon} = \{0.02\gamma_0, 0.2\gamma_0, 2\gamma_0\}$ (see Supplementary Information, Section 5.9.8). The blue curve defines the contour $\mathrm{Var}(a, b) = 2 \times \mathrm{Var}_{\min}$.

For the Markovian case, this collapse was evaluated over 3 quench rates varying over two orders of magnitude, $\dot{\epsilon} = \{0.02\gamma_0, 0.2\gamma_0, 2\gamma_0\}$, where γ_0 is the mechanical dissipation rate. For the non-Markovian case also, the collapse was evaluated over 3 quench rates varying over two orders of magnitude, with $\dot{\epsilon} = \{0.007\gamma_0, 0.07\gamma_0, 0.7\gamma_0\}$. The extracted exponents for $(C_{\dot{\epsilon}}, t_{KZ,\dot{\epsilon}})$ are, as presented in the main text, $(-0.500(4), 0.500(6))$ and $(-0.600(14), 0.375(15))$, respectively for the Markovian and non-Markovian cases.

5.9.9 Non-universal contributions

The above-mentioned exponents are in good agreement with the respective theoretical predictions of $(-1/2, 1/2)$ and $(-\frac{1}{1+s}, \frac{s}{1+s}) \approx (-0.588, 0.412)$. In this section, we discuss sources of non-universal contributions that may account for

experimentally measured discrepancies in the exponents, especially in the non-Markovian case.

The statement of universality is precise in the limit of $\dot{\epsilon} \to 0$, in that the system dynamics has a simple description in terms of universal scaling forms given by Eqns. (5.1) and (5.2). Naturally, experiments can only finitely approach the $\dot{\epsilon} \to 0$ limit. In this work, the smallest rates are around $\dot{\epsilon} = 0.007\gamma_0$, realized in the slowest ramps for the non-Markovian case. Indeed, Monte Carlo simulations of the dynamical curves, using the experimentally realized parameters over an ensemble of 100 iterations for each quench rate, show that the collapse is optimized for exponents $(-0.607(6), 0.390(10))$, consistent with the experiment.

In the Markovian case, the extracted exponents match the theoretical predictions better. This may be rationalized as follows. In the Markovian case, the only relevant intrinsic rate for the system is γ_0. No other frequency scale competes with $\dot{\epsilon}$, and the condition $\dot{\epsilon} \ll \gamma_0$ is well defined, which may be interpreted as realizing the limit $\dot{\epsilon} \to 0$. On the other hand, in the non-Markovian case, the system retains a "memory" of the initial conditions over all finite time scales. For example, the dynamical decay of the mode amplitudes following a perturbation is not exponential, as occurs the Markovian case. In fact, it has a power-law tail. This finite-time influence is only reduced as we consider ramps at slower rates (smaller $\dot{\epsilon}$'s), but may not sufficiently vanish. The consistent exponents based on both the Monte-Carlo simulations and the experiments suggest that the finite $\dot{\epsilon}$ may indeed account for the discrepancy from the analytic expectation.

Further, non-universal effects can be enhanced in the non-Markovian case due to the existence of the competing frequencies $\dot{\epsilon}$, γ_0, γ_{pl} and ω_c (see Eqn.(5.14) above). Ideally, ω_c should be much larger than all other frequencies, serving as a

high-frequency cutoff. And the power-law component of $\gamma(t)$ should dominate over its Markovian part ($\gamma_{pl} \gg \gamma_0$). And to realize the scaling limit, $\dot{\epsilon}$ should be much smaller than any of these competing frequencies. One can then expect that the finite-rate ramps across criticality will well approximate and follow the universal dynamics described above. The finite separation of these frequency scales in the experiment can thus additionally contribute to the deviations in measured exponents as compared to the analytic expectations.

5.9.10 Scaling exponents for equal temperature quenches

In this section, we use both rescaling arguments and the Kibble-Zurek paradigm to predict a universal behavior of quenches performed at *equal* temperatures, and its scaling exponents. The universal dynamics of $\langle x^2(t) \rangle$ across criticality in this case is restricted to the linear regime of the system. We also present experimental data corroborating this prediction.

Similar rescaling arguments as those described previously can be made for quenches performed at a constant temperature. In particular, for the regime of time when the order $x^2(t) \ll x_{ss}^2$, the nonlinear contribution is negligible (Eqn.(5.20)), so that

$$\frac{dx(t)}{dt} = \frac{\gamma_0}{2}(\dot{\epsilon}t)x(t) + \sqrt{\gamma_0}x_{th}\xi(t) \tag{5.22}$$

The rescalings of Eqn.(5.21a), Eqn.(5.21b) and Eqn.(5.21c) apply, and are experimentally constrained to $w = 1$ and $v = 1/\sqrt{u}$ by the fixed γ_0 and fixed temperature, respectively. The universality with quench rate is exposed by choosing the rescaling which eliminates the $\dot{\epsilon}'$ dependence, i.e. $u = (K_3/\dot{\epsilon})^{1/2}$ and concomitantly $v \propto \dot{\epsilon}^{1/4}$, where K_3 is a constant. We thus expect the universal behavior to

be given by

$$\langle x^2(t;\dot{\epsilon})\rangle = C_{\dot{\epsilon}}\,\mathcal{K}\left(\frac{t}{t_{KZ,\dot{\epsilon}}}\right)$$

with $C_{\dot{\epsilon}} \propto \dot{\epsilon}^{-1/2}$, $\mathcal{K} \propto \langle x^2(t/u; K_3)\rangle$, and $t_{KZ,\dot{\epsilon}} \propto u \propto \dot{\epsilon}^{-1/2}$, again being the Kibble-Zurek time. We extract the Kibble-Zurek times from such fixed-temperature quenches as those times when $\mathcal{K} = 10^{-3}$. For this, the experimentally measured $\langle x^2(t;\dot{\epsilon})\rangle$, normalized to x_{ss}, is scaled by $C_{\dot{\epsilon}} \propto \dot{\epsilon}^{-1/2}$ and the abscissa of ordinate 10^{-3} is quoted as the Kibble-Zurek time $t_{KZ,\dot{\epsilon}}$, as shown in Fig. 5.4(a) of the main text. We note that the choice of 10^{-3} is ad hoc, though bounded on the lower end by the experimentally realized constant temperature, and on the higher end by the neglected nonlinear term.

A collapse of the measured order growth curves for constant temperature quenches is shown in Fig. 5.6. The data collapses very well in the linear regime, but not at steady state amplitudes above criticality where the nonlinear effects are dominant.

Kibble-Zurek scaling predictions for constant-T quenches

The Kibble-Zurek paradigm described in earlier sections can also be used to predict the exponents for the constant temperature quenches. Eqn.(5.19) at constant temperature implies that

$$C_{\dot{\epsilon}} \propto \dot{\epsilon}^{-\frac{\zeta}{1+\nu z}}$$

And the Kibble-Zurek time scaling of Eqn.(5.18) is still valid. In the Markovian case, for which $\zeta = 1$, and $\nu z = 1$, this gives $C_{\dot{\epsilon}} \propto \dot{\epsilon}^{-1/2}$, $t_{KZ,\dot{\epsilon}} \propto \dot{\epsilon}^{-1/2}$, whereas in the power-law non-Markovian case, for which $\zeta = 2 - 1/s$ and $\nu z = 1/s$, we have $C_{\dot{\epsilon}} \propto \dot{\epsilon}^{-0.23(4)}$, $t_{KZ,\dot{\epsilon}} \propto \dot{\epsilon}^{-0.588(7)}$ for $s = 0.70(2)$.
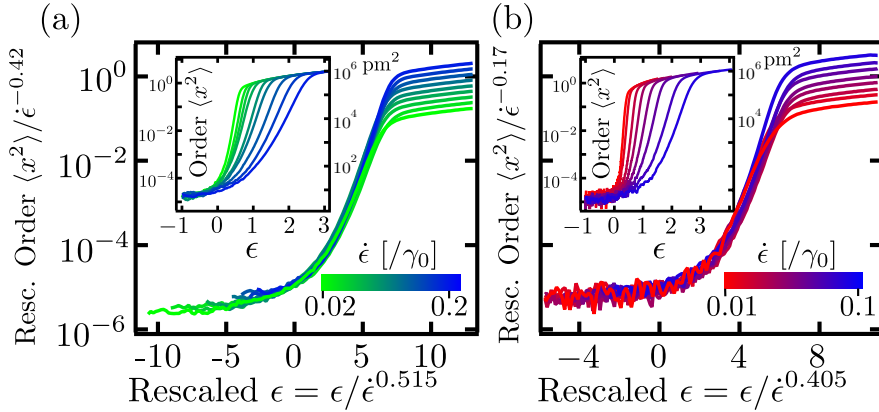
Figure 5.6: **Universality in constant-T quenches:** The dynamics of growth of order $\langle x^2(t) \rangle$ is universal in the quench rate $\dot{\epsilon}$ – the distinct growth curves at varying $\dot{\epsilon}$, shown in the inset, collapse into a single curve on rescaling time with the Kibble-Zurek time $t_{KZ,\dot{\epsilon}}$, and an appropriate scaling of the amplitude. Note that the collapse for these constant-T quenches is partial, occurring only in the linear regime of exponential growth of order (see Supplementary Information, Section 5.9.10). Shown for the (a) Markovian case and (b) power-law non-Markovian case.

5.9.11 Hysteresis area and its scaling

In this section, we discuss the hysteretic area enclosed by the signal/idler amplitude curves during the forward-backward ramps. We first establish the physical basis of the hysteresis area as a measure of the energy dissipated during the non-adiabatic ramp. We then use the universal scaling of the nonequilibrium dynamics derived earlier to demonstrate that the hysteretic area also scales as a power law in the quench rate, and further predict this power. We also present a Kibble-Zurek heuristic for the hysteretic area, predicting the same power law scaling.

Physical basis of the hysteresis area

We can define an (effective) work done on the system by the external drive μ in the rotating frame as

$$
\begin{aligned}
W &\equiv \int d\mu \frac{\partial \mathcal{H}_{\text{eff}}}{\partial \mu} \\
&\approx -\gamma_0 \int d\mu |a_s|^2 \, ,
\end{aligned}
$$

where we use the $\mathcal{H}_{\text{eff}}$ of Eqn.(5.8). This definition of work is analogous to the *inclusive work* in Jarzynski's [160, 161]. See also [132].

While this definition is valid for any ramp protocol of the drive μ, we focus here on a piece-wise linear cyclic ramp, which starts at $\mu = 0$, continues linearly beyond the phase transition, immediately turns around at some $\mu_f > \mu_{cr} = 1$ and returns linearly to $\mu = 0$. In the following, we denote this cyclic protocol by the integral $\oint$. In the experiments, we measure the average work as

$$
\langle W \rangle = -\gamma_0 \oint d\mu \langle |a_s|^2 \rangle
$$

where the average is taken over stochastic realizations of the noise due to the environment. Thus the net work done by the coupling μ on the system is proportional to the hysteretic area of $|a_s|^2$ with μ. Note that we extend this definition of work to the non-Markovian case as $\langle W \rangle \propto \oint d\mu \langle |a_s|^2 \rangle$.

Given that the protocol is cyclic, it does not change the internal energy of the system, and $\langle W \rangle$ is a measure of the energy dissipated during the non-equilibrium ramp. Throughout this work, we thus denote the hysteretic area by E.

Derivation of scaling based on universality

The scaling of the hysteretic area with quench rate $\dot\epsilon$ can be obtained using the universal scaling form that governs the system dynamics. The rescaling argument used for the Markovian case in previous sections is insensitive to the sign of $\dot\epsilon$ – The argument is equally valid for both a forward and a backward quench as long as the initial conditions do not matter, which holds true for deep, slow quenches.

The hysteresis area can be written as

$$E \propto \int_{-1}^{\epsilon_f} d\epsilon \langle x^2_{\text{backward}}(t = \epsilon/\dot\epsilon; T)\rangle - \langle x^2_{\text{forward}}(t = \epsilon/\dot\epsilon; T)\rangle$$

We take the scaling limit of $\dot\epsilon \to 0$ while holding $t/t_{KZ}, Tt_{KZ}^{3s-1}$ fixed and express $\langle x^2 \rangle$ in the universal scaling form, to get

$$E \propto \int_{-\infty}^{\infty} d\epsilon C_{\dot\epsilon}\left[\mathcal{G}_{\text{backward}}\left(\frac{\epsilon/\dot\epsilon}{t_{KZ,\dot\epsilon}}, Tt_{KZ,\dot\epsilon}^{3s-1}\right)\right.$$
$$\left.-\mathcal{G}_{\text{forward}}\left(\frac{\epsilon/\dot\epsilon}{t_{KZ,\dot\epsilon}}, Tt_{KZ,\dot\epsilon}^{3s-1}\right)\right]$$
$$\propto \int_{-\infty}^{\infty} dx\ \dot\epsilon^{\frac{1}{1+\nu z}}\dot\epsilon^{\frac{2\beta}{1+\nu z}}[\mathcal{G}_{\text{backward}}(x, C_2)$$
$$-\mathcal{G}_{\text{forward}}(x, C_2)]$$
$$\Rightarrow E \propto \dot\epsilon^{\frac{1+2\beta}{1+\nu z}}$$

where $C_2 = Tt_{KZ,\dot\epsilon}^{3s-1}$ is held constant with varying quench rates, and $x = \frac{\epsilon/\dot\epsilon}{t_{KZ,\dot\epsilon}} \propto \epsilon/\dot\epsilon^{\frac{1}{1+\nu z}}$. This gives the area scaling to be $E \propto \dot\epsilon^{\frac{1+2\beta}{1+\nu z}}$.

In Markovian case, $\beta = 1/2$, $\nu z = 1$, so that the area scaling is $E \propto \dot\epsilon^1$. For the the power law non-Markovian case, $\beta = 1/2$, $\nu z = 1/s$, so that the expected area scaling is $E \propto \dot\epsilon^{\frac{2s}{1+s}}$, which for $s = 0.70(2)$ gives $E \propto \dot\epsilon^{0.82(1)}$. See Fig. 5.7 for experimental comparison. See also Fig. 5.4 of the main text, shown for quenches performed at equal temperatures.
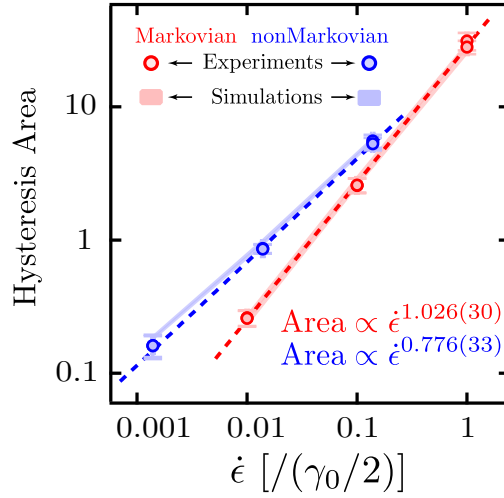
Figure 5.7: **Scaling of the hysteretic area in a driven-dissipative phase transition:** Work is done by the parametric drive μ over each cycle of quench into the ordered phase and then back into the disordered phase. This work, proportional to the hysteretic area illustrated in Fig. 5.2, scales as a power-law with the quench rate. The scaling is influenced by the system-bath interactions, as demonstrated here for the Markovian (red) and non-Markovian (blue) cases.

Derivation of scaling using a Kibble-Zurek heuristic

The hysteretic curve can be approximated as a triangle (see Fig. 5.2) with base determined by the Kibble-Zurek freeze-out, $\epsilon_{KZ} \propto \dot{\epsilon}^{\frac{1}{1+\nu z}}$, and height determined by the steady-state order, $\langle x^2 \rangle|_{\epsilon=\epsilon_{KZ}} \propto \epsilon_{KZ}^{2\beta} = \dot{\epsilon}^{\frac{2\beta}{1+\nu z}}$, giving an area scaling of $E \propto \dot{\epsilon}^{\frac{1+2\beta}{1+\nu z}}$.

5.9.12 Experimental parameters

The mechanical resonator used in this work is a 100 nm thick, $L = 5$ mm square, high tensile stress ($\sigma \sim 1$ GPa), silicon nitride membrane, that was LPCVD

grown on a silicon substrate by NORCADA, Inc. Such a resonator has eigenmodes with eigenfrequencies $\omega_{mn} = 2\pi \sqrt{\sigma/4\rho L^2} \sqrt{m^2 + n^2}$, where $\rho \sim 2.7$ g/cm^3 is the silicon nitride mass density. The eigenmodes at $\omega_s \sim 1.233$ MHz and $\omega_i \sim 1.466$ MHz were used as the signal and idler modes respectively. The natural linewidths of these modes is $\gamma_s \sim 2\pi \times 80$ mHz and $\gamma_i \sim 2\pi \times 110$ mHz, corresponding to intrinsic timescales of $\tau_s = 2/\gamma_s \sim 3.9$ s and $\tau_i = 2/\gamma_i \sim 2.9$ s, and quality factors of $Q_s \sim 15 \times 10^6$ and $Q_i \sim 13 \times 10^6$. The pump mode is an eigenmode of the silicon substrate, whose modes have typical quality factors of $Q_p \sim 10^3 - 10^4$, more than three orders of magnitude lesser than the signal or idler modes, i.e. $\gamma_{s,i}/\gamma_p < 10^{-3}$. Correspondingly, its dynamics are much faster than the signal and idler modes, allowing for its adiabatic elimination.

5.9.13   Optical detection of the signal and idler modes

The out of plane displacement of the mechanical signal and idler modes are detected using a Michelson interferometer with a position sensitivity of $\sim$ 14 fm/ $\sqrt{\text{Hz}}$ at the signal and idler frequencies, achieved through a lock-in amplifier (Zurich Instruments, HF2LI). A typical power of 630 μW is incident on the mechanical silicon nitride membrane, as also in the reference arm of the interferometer. The light source is an external cavity diode laser operating at 795 nm with linewidth < 100 kHz.

At low frequencies (< 3 Hz), the optical interferometer used for the detection of mechanical displacement is susceptible to residual amplitude modulation (RAM) which we ascribe to the gradual temperature fluctuation and temperature dependent birefringence of various optical elements. In our experi-

ment, this low frequency amplitude noise convolves with the mechanical displacement signal, leading to a 0.75% contamination of the detected membrane displacement. Consequently, the signal to noise ratio (SNR) for the mechanical thermal motion degrades to 1 as the amplitude of motion approaches 150 times the room temperature thermal amplitude. To ensure that the finite time quench experiments are conducted with thermal fluctuations that are detected with SNR > 1, we ensure that the system is driven with a large effective thermal noise, with the effective temperature being much larger than room temperature (> 100 times larger).

5.9.14 Feedback stabilization of the signal and idler modes

Due to the differential thermal expansion of the silicon nitride membrane and the supporting silicon substrate, the signal and idler frequencies change with ambient temperature. Empirically, this change is by ~ 1.4 linewidths per milliKelvin. Given that ambient temperatures vary over ~ 200 mK within a day, precise measurement of thermomechancial motion and steady state responses requires active feedback to achieve sub-linewidth stabilization of the mode frequencies. We accomplish this using the differential thermal expansion to our advantage, through photothermal control of the silicon substrate. As also described in previous work [150], we continuously monitor the mechanical frequency of a high-Q thermometer mode at 2.736 MHz - far from the signal and idler frequencies studied in this work. Phase detection of this mode generates an error signal with an on-resonant slope of 5.91 radians/Hz. Active photothermal stabilization is accomplished by feeding back to an optical control beam of 600μW average power, generated by a diode laser operating at 830 nm, and

amplitude controlled using an acousto optic modulator (AOM). The RMS frequency fluctuations of the thermometer mode thus achieved are measured to be below 2 mHz, equivalent to temperature fluctuations of less than 2 μK.

5.9.15   Feedback protocols

Implementation of arbitrary non-Markovian system-bath interactions

The role of the non-Markovian system-bath interactions is fully captured by their influence on the equations of motion of the system. Due to the minimalist nature of this work's physical realization of the described driven dissipative phase transition, we can use active feedback to enforce a particular equation of motion, and thereby simulate a non-Markovian system-bath interaction of our choosing.

In particular, the evolution of the complex amplitudes of motion $z_{s,i}$ is governed by the equations

$$\dot{z}_{s,i} = -\frac{\gamma_{s,i}}{2}\left(z_{s,i} + \chi_{s,i}V_{s,i}\right) + if_z^{\text{Mark}}$$

where $V_{s,i}$ is the feedback voltage applied to the piezo transducer that the silicon substrate, which hosts the signal and idler modes, is mounted on, and $\chi_{s,i}$ is the experimentally measured transfer function of the applied PZT voltage into signal and idler motion. Here, the first term refers to the modes' intrinsic Markovian damping, and the last term f_z^{Mark} refers to the associated Markovian thermal noise. By comparing to Eqn.(5.11) and enforcing

$$V_{s,i} = \frac{2}{\gamma_{s,i}\chi_{s,i}}\left[-\frac{\gamma_{s,i}}{2}z_{s,i} + \frac{1}{2}\int_{-\infty}^{t}dt'\gamma(t-t')z_{s,i}(t') + if_z\right]$$

we simulate a non-Markovianity of our choice. Here, $f_z = 2f_{s,i}$ denotes the

added non-Markovian noise related to our choice of the damping kernel $\gamma(t)$ through the fluctuation dissipation relation as described in previous sections. Note that while the first term of $V_{s,i}$ counters the intrinsic Markovian damping and effectively cancels it, $V_{s,i}$ does not compensate for the associated noise f_z^{Mark}. To ensure that it is the non-Markovian noise that dominates the stochastic behavior of the system, we set its effective temperature to be ~ 100 times the temperature of the intrinsic Markovian noise f_z^{Mark}, thus overwhelming it. We note that the feedback voltage $V_{s,i}$ described here is a complex representation in a rotating frame of the real-life voltage applied to the piezo transducer, $\mathcal{V}_{s,i}(t) = \text{Re}[V_{s,i}]\cos(\omega_{s,i}t) + \text{Im}[V_{s,i}](\sin\omega_{s,i}t)$.

In the experiments, we implement this realtime feedback digitally, using NI LabView. The signal and idler mode motions $z_{s,i}$ are continuously measured and recorded at 1800 Hz. This recorded history of $z_{s,i}(t')$ is numerically convolved with our choice of kernel $\gamma(t)$ as a discrete sum, with the lower limit on the integral $\int dt'$ being the time at which we start applying the feedback. A pre-computed non-Markovian noise sequence f_z with the appropriate noise spectral density $\propto \tilde{\gamma}'(\omega)$ is also added.

To give a sense of the numbers involved in the feedback implemented here – The feedback rate is ~ 15 Sa/s, which, because of the ultra-high Q resonators used in this work, is more than a 100 times the modes' natural linewidths. The least significant bit of the digital feedback voltage amplitude is ~ 76 nV, more than a 100 times smaller than the typical non-Markovian noises f_z peak-to-peak voltages of ~ $15 - 20\,\mu$V.

Implementation of matched dissipation

For the experiments in this work, we use the feedback protocol described above to also match the damping rates of the signal and idler modes. For the Markovian experiments, $\gamma_{s,i} = \gamma_0 = 0.50(1)$ s^{-1}. For the power-law non-Markovian experiments, the Markovian component for both modes is $\gamma_0 = 1.00(2)$ s^{-1}.

Implementation of varying temperatures

We vary the realized temperatures of the experiments by appropriately scaling the amplitude of the noise forces as $f_{s,i}^z \propto \sqrt{T}$. This realization of the artificial temperatures is calibrated for each ensemble by measuring the RMS motion in the presence of the feedback for a time $> 200\gamma_0^{-1}$. Each calibration affirms that our realization of the artificial thermal motion is within 7% of the target, 7% being the expected statistical uncertainty of RMS motion when monitored over $200\gamma_0^{-1}$.

5.9.16 Error in implementation of power law non-Markovian system-bath interactions

We estimate the error in the power law exponent via step response measurements. For fixed $\gamma_0 = 0.5$ s^{-1}, $\gamma_{pl} = 0.411$ s^{-1}, $\omega_0 = 1$ s^{-1}, $\omega_c = 6$ s^{-1}, we simulate step responses for non-Markovianity with different s. Shown in the graphs are the experimental data (grey), and simulations for $s = 0.68$ (red), $s = 0.70$ (blue), and $s = 0.72$ (green) (see Fig. 5.8).
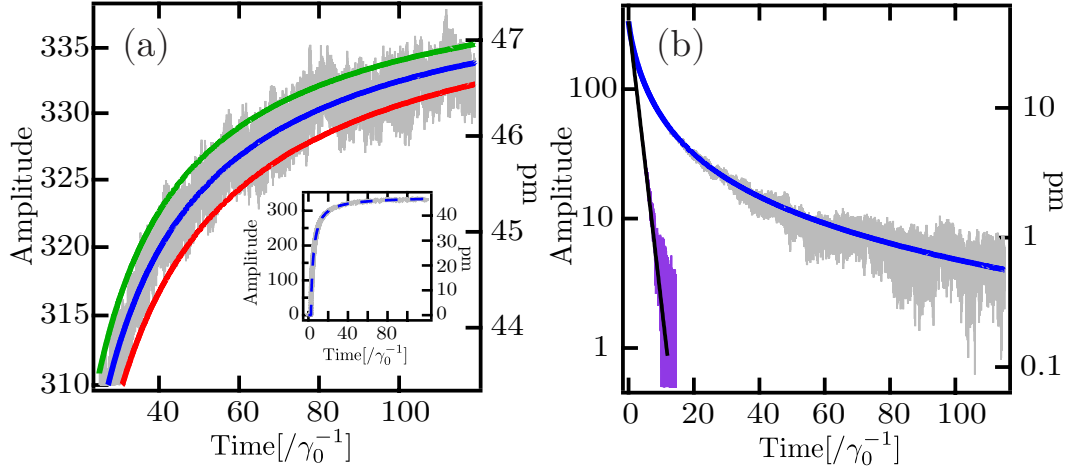
Figure 5.8: **Error estimates of power law non-Markovian system bath interactions:** Amplitude normalized to single quadrature thermal rms. (a) Zoomed in step responses of experimental data (grey), simulations for $s = 0.68$ (red), $s = 0.70$ (blue), and $s = 0.72$ (green). (Inset) Full step response from data and simulation for $s = 0.7$. (See Supplementary Information, Section 5.9.16) (b) Ringdown measurement for power law non-Markovian with $s = 0.7$ - experimental (grey), simulation (blue), and Markovian ringdown for $\gamma_0 = 0.5$ s^{-1}, experimental (purple) and simulation (black).

We estimate the error in s ($s = 0.70(2)$) based on the region of simulated step responses bounding the experimental data to within ~ 1 standard deviation of the experimental noise. In Fig. 5.8(b), we show the ringdown curves for both Markovian and power law non-Markovian curves. As shown in the figure, the power law non-Markovian system decays much slower than the Markovian system.

CHAPTER 6

EMERGENT DYNAMICAL ORDER AND TIME TRANSLATION SYMMETRY BREAKING DUE TO NON-MARKOVIAN SYSTEM-BATH INTERACTIONS

6.1   Overview

The previous Chapter focused on how the nature of system-bath interactions in open systems can markedly affect and change the critical behavior of the driven-dissipative phase transition. We saw how power-law non-Markovian system-bath interactions changed the critical exponents of the phase transition *vis-a-vis* the Markovian counterpart. Yet, in a certain sense, it is not substantial an effect - the phases on either side of the transition retained their 'character', so to speak, as the system-bath interactions were morphed. Previous works reached similar conclusions, theoretically [155], somewhat dis-satisfyingly.

The work presented in this Chapter explores the influence of the system-bath interactions on the properties of the phases themselves. In particular, we experimentally identify and demonstrate how a particular class of non-Markovian interactions ("exponential non-Markovianity") can alter the dynamical steady state of the ordered phase of the two-mode PA-PO system. Here, as will be explained in detail later, the system-bath interactions are characterized by two timescales – a coherent timescale on which energy can return back from the environment to a decaying oscillator ('coherent' is used loosely here), and an ultimate decay timescale on which energy is ultimately lost to the bath. The competition between these two timescales sets the stage for a non-Markovian interaction-induced phase transition, replete with divergences and scaling in-

variances. One of the central results of the work presented in this Chapter is thus the identification of the ability of varying system-bath interactions to effect different phases in a given, otherwise isolated, system.

The order parameter in this new "$U(1) \times \mathbb{Z}_2$" phase is the frequency offset Δ at which the signal oscillates, offset with respect to the original signal frequency. Firstly, we find that Δ breaks a $\mathbb{Z}_2$ symmetry – it can either oscillate at $+|\Delta|$ or $-|\Delta|$, a choice that is made indeterministically due to relevant fluctuations. Secondly, this oscillation, assumed for the time being to be at a fixed Δ, breaks a continuous time translation symmetry, much like the crystallization of molten sugar breaks a continuous translation symmetry of space. The corresponding continuous symmetry that is broken here is the phase of the oscillation, which has a $U(1)$ symmetry. For a single signal-idler pair, this choice of phase is constant in time only in the limit of zero temperature; any finite temperature fluctuations cause the phase to diffuse, correspondingly causing the frequency offset Δ (the time derivative of the phase) to meander. In other words, the single signal-idler pair realizes a 'true' phase transition only in the $T = 0$ limit. Ongoing theoretical and numerical work, considering a spatial multi-dimensional extension of this system with nearest-neighbor dissipatively-coupled signal-idler pairs is expected to show spontaneous or 'true' continuous time translation symmetry breaking even at finite temperatures in > 2–D. Such extensions of the system to arrays would bear on the question of whether long range interactions or localization are indeed needed for breaking time translation symmetry [162, 163]. In addition, such systems would open an optomechanical platform for the study of lattice physics and quantum synchronization with non-Markovian open systems (see also [164, 106, 165]).

Moreover, in a different context, one of the goals of 'reservoir engineering' of open systems has been to realize target ground or steady states that decouple from the environment (sometimes referred to as 'dark' states, motivated by AMO jargon), with the objective that they remain unaffected by environment-induced decoherence [166, 167, 168, 169]. In a similar vein, our system supports, for the chosen class of non-Markovian system-bath interactions, a transient two-mode squeezed state first introduced in Chapter 4 that retains its enhanced correlations or entanglement even at finite temperatures, outperforming its Markovian counterpart. These calculations and the theoretical treatment of the non-Markovian system-bath interactions employed in this Chapter were evaluated as a part of a separate piece of work with H. F. H. Cheung [143], and are included in Appendix C. Our developed capability to impose non-Markovian system-bath interactions of choice will allow for the realization of other reservoir engineered states with other requisite target properties.

This chapter will be submitted for peer-review with requisite modifications as *Emergent dynamical order and time translation symmetry breaking due to non-Markovian system-bath interactions, by Y. S. Patil, H. F. H. Cheung and M. Vengalattore*. In this work, Y. S. Patil and H. F. H. Cheung performed the experimental work, data acquisition, data analysis, modeling and simulations. M. Vengalattore supervised all stages of the work. All authors contributed to the preparation of the manuscript.

6.2 Abstract

We experimentally determine the phase diagram of an open driven dissipative system of parametrically coupled non-degenerate mechanical oscillators by tuning their interactions with the environment from being Markovian to non-Markovian. For the class of non-Markovian system-bath interactions we engineer, we observe three distinct phases separated by continuous phase transitions, confirming that system-bath interactions can significantly modify the phase diagram, as recently theorized in [143]. The emergent phase on making the non-Markovian interactions dominant is characterized by a dynamic order parameter that breaks a $U(1) \times \mathbb{Z}_2$ symmetry, where the $U(1)$ symmetry corresponds to the invariance of the system equations of motion under a continuous time translation. Our experiments set the stage for using optomechanical systems in the study of dynamical critical phenomena, and open potential avenues for the realization of time translation symmetry broken phases through reservoir engineering.

6.3 Introduction

Phase transitions occur not only in a myriad of physical systems, but also in almost every field of the sciences, including physics, cosmology, chemistry, biology, medicine and even sociology, linking them all through the common underlying principles of self-similarity and universality of critical phenomena. In the physical sciences, the renormalization group apparatus has been a crowning jewel of our understanding of critical behavior. Its applicability for intrinsically nonequilibrium systems like the ubiquitous open system is an active area of

119

research [135, 136]. Such systems can undergo phase transitions, and it is natural to ask if our conventional paradigms are sufficient to explain their critical behavior [137, 138, 139].

Recent theoretical considerations suggest that interactions with their environment can modify the critical exponents of open systems [141, 142, 155], leading to new universality classes of phase transitions and novel dynamics [154, 155, 156, 157]. Moreover, owing to the interplay between these interactions and the system's intrinsic driven dynamics, the phase diagram can be significantly modified. We have previously proposed the emergence of a phase with novel broken symmetries in a paradigmatic parametrically coupled, two mode, driven dissipative system [143]. The model may be realized in a myriad of physical systems including optics, optomechanics, nanomechanics, cold atoms and cavity QED [144, 91, 145, 146, 147, 148, 149, 150], and in this work, we realize it in an optomechanical system of two coupled oscillators, map out its phase diagram and study its properties.

6.4 The experimental mechanical nondegenerate parametric amplifier-oscillator system

Our experimental system consists of two out-of-plane vibrational eigenmodes of a 100 nm thick, 5mm square, silicon nitride membrane resonator, LPCVD grown on a silicon substrate [150, 79] (also, see Supplementary Information, Section 6.9.4). The signal and idler modes are at frequencies $\omega_s \sim 1.233$ MHz, $\omega_i \sim 1.466$ MHz, and are each coupled to a room temperature thermal reservoir through weak Markovian interactions, undergoing damping at a rate $\gamma_{s,i}/2\pi \sim$

100 mHz. Moreover, the two modes are parametrically coupled to each other through a third, pump mode at their sum frequency, $\omega_P \sim 2.699$ MHz. The pump mode is a shear eigenmode of the silicon substrate, and has a dissipation rate $\gamma_P \sim 2\pi \times 10^3$ Hz $\gg \gamma_{s,i}$ [150]. A coherent classical drive of the pump mode parametrically actuates the signal and idler, and constitutes the drive essential for realizing a phase transition in this open driven dissipative system. In the rotating wave approximation, the coherent evolution of such a system in a rotating frame is described by the Hamiltonian,

$$\mathcal{H} = -\hbar g(a_s^\dagger a_i^\dagger a_P + a_P^\dagger a_i a_s) - \hbar(F_P a_P^\dagger + F_P^* a_P)$$

where $a_{s,i}$ denote the annihilation operators of the signal and idler modes, g parametrizes the strength of their inter modal coupling, F_P represents the classical pump drive, and the dissipative coupling to the environment is captured through the Heisenberg-Langevin equations [151] (also, see Supplementary Information, Section 6.9.1).

A crucial ingredient in this work is an ability to imprint and tune non-Markovian system-bath interactions. We take advantage of the extremely long dissipation timescales, of the order of seconds, to morph the natural, Markovian interactions into non-Markovian interactions by employing active feedback. We measure both quadratures of motion of either mode using an optical Michelson interferometer, and construct the complex amplitudes of motion, $z_{s,i} = x_{s,i} + iy_{s,i} = 2a_{s,i}$. A recorded history of $z_{s,i}$ is used to compute the feedback force required to effect non-Markovian system-bath interactions, and the feedback is applied through a piezo transducer that hosts the silicon substrate and resonators. We verify that this protocol successfully imprints a non-Markovianity of our choosing through mechanical susceptibility measurements (see Supplementary Information, Section 6.9.8).

We thus realize the non-Markovian equations of motion

$$\dot{a}_{s,i} = iga_{i,s}^\dagger a_P - \frac{1}{2}\int_{-\infty}^t dt'\gamma(t-t')a_{s,i}(t') + if_{s,i}$$

$$\dot{a}_P = -\frac{\gamma_P}{2}a_P + iga_ia_s + iF_P \tag{6.1}$$

where $\gamma(t)$ is the non-Markovian dissipation kernel and $f_{s,i}$ are the fluctuation forces associated with the dissipation, related to the kernel $\gamma(t)$ through the fluctuation dissipation relation (see Supplementary Information, Section 6.9.2). In this work, we implement non-Markovian dissipation kernels of the form $\gamma(t) = \gamma_0\tau_r^{-1}e^{-t/\tau_r}$, where τ_r defines the reservoir coherence time. $\gamma_0 = \int_0^\infty dt\gamma(t)$ defines an effective total damping rate, determining the steady-state susceptibility. Under such exponential non-Markovian system-bath interactions, the equations of motion are invariant under the transformation $(a_i, a_s) \rightarrow (a_ie^{+i\phi}, a_se^{-i\phi})$ for $\phi \in [0, 2\pi)$. And for real F_P, which can be assumed real without loss of generality, the equations of motion are invariant also under the transformation $(a_i, a_s, a_P) \rightarrow (a_i^\dagger, a_s^\dagger, -a_P^\dagger)$. The equations of motion thus possess both a $U(1)$ symmetry and a $\mathbb{Z}_2$ symmetry. Moreover, note that at zero temperature (noise $f_{s,i} \rightarrow 0$), the equations have a time translational invariance – a time translated solution $a_{s,i}(t) \rightarrow a_{s,i}(t+\tau)$ remains a solution for all τ.

6.5 The phase diagram

To map out the phase diagram, γ_0 was held fixed at 1 s^{-1}. For each τ_r, the system was initialized in the disordered phase at zero pump drive strength, and then instantaneously quenched to a final non-zero pump drive strength. The system dynamics and steady state behavior was recorded for each τ_r. The phase diagram so measured is shown in Fig.6.1(a).
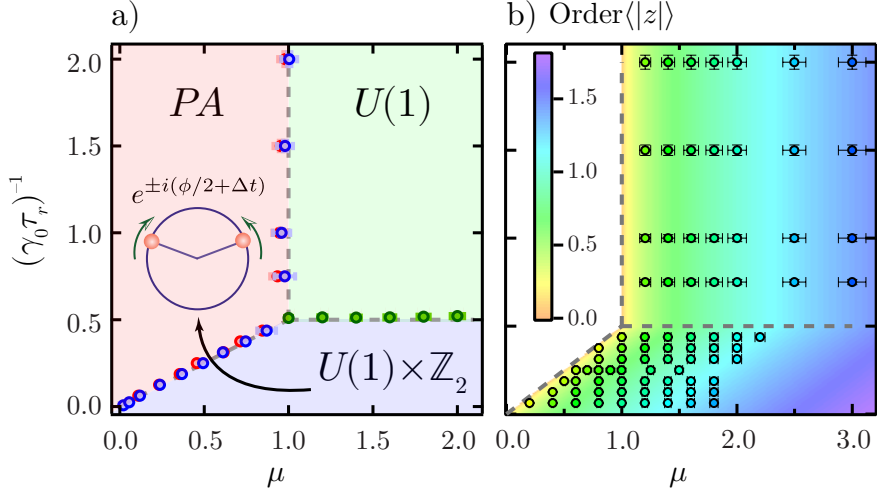
Figure 6.1: **Phase diagram:** (a) Our open driven dissipative system displays three distinct phases. For large normalized reservoir decay rates $(\gamma_0 \tau_r)^{-1}$, a disordered parametric amplifier phase (shaded red) occurs at low drive strengths $\mu \equiv \frac{|F_P|}{|F_{cr,m}|}$, whereas the system enters an ordered phase which breaks the $U(1)$ symmetry (shaded green) for drives beyond a critical threshold drive. For small reservoir decay rates, the system orders into a $U(1) \times \mathbb{Z}_2$ symmetry broken phase with a dynamic order parameter that oscillates at angular frequency Δ (inset). Data points denote the extrapolated phase boundaries. (b) Magnitude of the measured amplitude order in the three phases, at steady state. Background color shading denotes estimated amplitude order based on the model in [143]. The phase boundaries between the PA and ordered phases (red data in (a)) are extracted by extrapolating the measured amplitude order, as a function of drive μ, to zero. Dotted lines in (a–b) show the phase boundaries predicted by the model.

In the regime of small reservoir coherence time $(\gamma_0 \tau_r)^{-1} > 1/2$, below a critical drive of $\mu \equiv \frac{|F_P|}{|F_{cr,m}|} = 1$, where the critical pump drive $|F_{cr,m}| = \frac{\gamma_P \gamma_0}{4g}$, the signal and idler modes dissipate to the environment at a rate faster than the pump parametrically actuates them, and each mode remains disordered with $z_{s,i} = 0$. As the drive is increased beyond $\mu = 1$, the rate of down conversion into the signal and idler grows larger than the rate of dissipation out to the environment, marking the onset of a non-zero amplitude order $z_{s,i} = |z_{s,i}|e^{\pm i\phi/2}$ [Fig.6.1(b)]. Here,

the difference between the modes' oscillation phases ϕ has a $U(1)$ symmetry [170, 83], because of which we call it the $U(1)$ phase.

This phase boundary between the disordered parametric amplifier (PA) phase and the $U(1)$ phase, marked by the onset of order, is determined by extrapolating to zero the measured, steady state, amplitude order as a function of μ [red data points in Fig.6.1(a)] (see Supplementary Information, Section 6.9.9). Independently, we measure the growth rate of order when the system is suddenly quenched into the $U(1)$ phase, as a function of the quench depth, and identify as the critical drive that drive where the growth rate vanishes [blue data points in Fig.6.1(a)]. This growth rate is determined by the eigenvalues of the disordered phase above criticality, which in this regime of short reservoir coherence, are real at all drive strengths μ and lead to an exponential growth of order (see Supplementary Information, Section 6.9.9). Through both these measurements, we observe that in this regime, the critical pump drive is independent of the reservoir coherence time, and equals that measured in the Markovian limit to within 5%. As such, the $PA - U(1)$ phase boundary shown in Fig.6.1(b) occurs at a constant drive of $\mu = 1$.

In the regime of long reservoir coherence times $(\gamma_0 \tau_r)^{-1} < 1/2$, two changes occur prominently. Firstly, the critical drive that separates the PA phase and the ordered phase no longer occurs at $\mu = 1$. It reduces inversely with τ_r, i.e. $\mu_{cr} = 2(\gamma_0 \tau_r)^{-1}$, and in fact vanishes for very long reservoir coherence times [Fig.6.1(a)]. As before, we extract this phase boundary both through the amplitude growth as a function of drive μ, and through a vanishing growth rate. However, the functional form of the growth in this regime is different than before. Here, above criticality, the eigenvalues of the mean field solution expanded
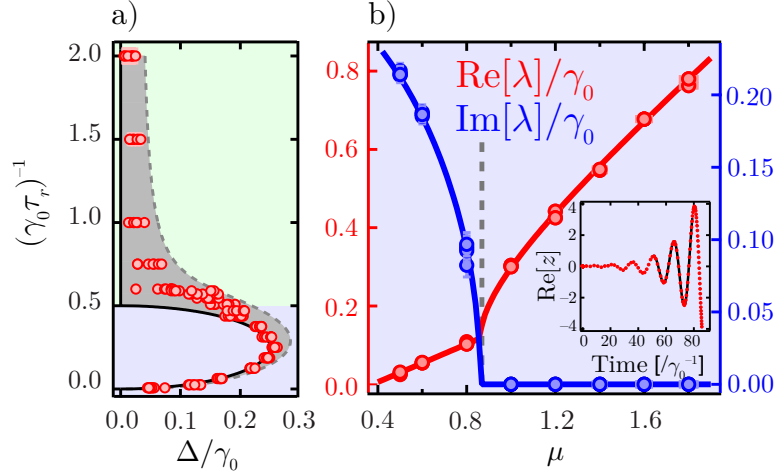
Figure 6.2: (a) Oscillation frequency Δ, of the order parameter as a function of the normalized reservoir decay rate (red data, shown for the $\mu \in (0,3)$ data in Fig. 6.1(b)). The solid line denotes estimates of the model, and the dashed line accounts for additional deviations introduced by our experimental realization (see Supplementary Information, Section 6.9.7). The $U(1)$ to $U(1) \times \mathbb{Z}_2$ phase boundary (green data in Fig. 6.1(a)) is extracted by extrapolating Δ to zero, as a function of the reservoir decay rate, for small $(\gamma_0 \tau_r)^{-1}$. (b) The growth of order for a *PA* to $U(1)$ transition is exponential, characterized by a real growth rate, whereas for the *PA* to $U(1) \times \mathbb{Z}_2$ transition, the growth of order is an underdamped exponential, characterized by a complex growth rate. The measured real and imaginary parts of this growth rate (see text) are shown as red and blue data respectively, for $(\gamma_0 \tau_r)^{-1} = 3/16$. The phase boundary between the *PA* and ordered phases is independently extracted (blue data in Fig. 6.1(a)) by extrapolating the real part of the growth rate, as a function of drive μ, to zero. Solid lines show the estimates based on the model. (Inset) Typical time trace of the underdamped development of $U(1) \times \mathbb{Z}_2$ order. Shown for $\mu = 0.5$, data in red and fit in black. All data is for $\gamma_0 = 1\ \mathrm{s}^{-1}$.

around the disordered phase can be complex, resulting in an oscillatory exponential growth of order, whose oscillation frequency is given by the imaginary part of the eigenvalue, and whose exponential envelope is determined by the real part [Fig.6.2(b)]. We find that the measured complex eigenvalues are in excellent agreement with predictions of the model.

Importantly, the order that develops in this regime is dynamic, with $z_s = |z_s|e^{\pm i(\phi/2 + \Delta t)}$ and $z_i = |z_i|e^{\mp i(\phi/2 + \Delta t)}$. The signal and idler now oscillate not at their natural frequencies $\omega_{s,i}$, but at shifted frequencies $\omega_s \rightarrow \omega_s \pm \Delta$ and $\omega_i \rightarrow \omega_i \mp \Delta$. This ordered phase thus not only breaks a $U(1)$ symmetry in ϕ, as before, but also a discrete $\mathbb{Z}_2$ symmetry in Δ, because of which we refer to this as the $U(1) \times \mathbb{Z}_2$ phase. We further find that Δ varies continuously with τ_r [Fig.6.2(a)] and defines an order parameter separating the $U(1) \times \mathbb{Z}_2$ and $U(1)$ phases. For each pump drive μ, we extract the critical τ_r that defines this phase boundary by extrapolating the measured Δ to zero, according to the equation $|\Delta| = \tau_r^{-1}\sqrt{\frac{\gamma_0 \tau_r}{2} - 1}$ [Fig.6.2(a)] [143], and as shown in Fig.6.1(a) by the green data points. Note that along this phase boundary, the point $(\gamma_0 \tau_r)^{-1} = 1/2$, $\mu = 1$ defines a multi-critical point occurring at the intersection of three phases.

In the phase space of drive strength μ and reservoir coherence time τ_r, we thus measure three distinct phases of this open driven dissipative system, including one with a dynamic order and an exotic $U(1) \times \mathbb{Z}_2$ broken symmetry. At zero temperature (noiseless case of $f_{s,i} \rightarrow 0$), the time-periodicity of this phase breaks the continuous time translation symmetry of the equations of motion Eqn.(6.1), reflected by the choice of the phase ϕ that has an associated continuous $U(1)$ symmetry. At finite temperatures, however, there is no *spontaneous* symmetry breaking because the fluctuations cause the phase to diffuse over time, thereby washing away any long-time order, i.e. $\lim_{\tau \rightarrow \infty} \langle \cos [\phi(t) - \phi(t + \tau)] \rangle \rightarrow 0$; reminiscent of the Mermin-Wagner theorem, which conventionally relates to spatial order. Spontaneous time translation symmetry breaking is expected to be retrieved at finite temperatures in a >2-D multi-dimensional extension of the system, and is the subject of ongoing work.

6.6 Universal dynamics
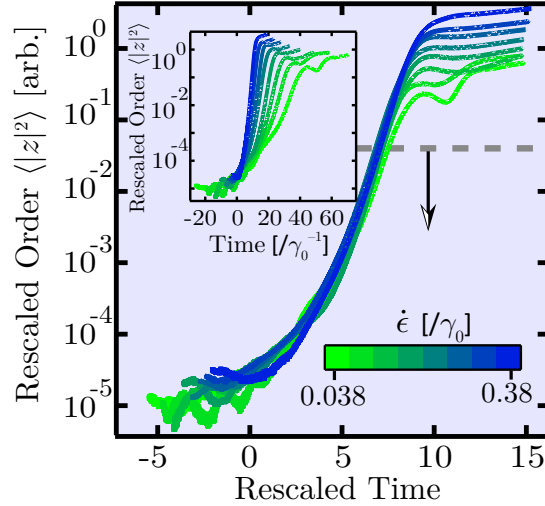
Figure 6.3: **Universal critical dynamics:** Growth of amplitude order as the system is quenched in a finite time from the disordered *PA* phase into the $U(1) \times \mathbb{Z}_2$ phase at different quench rates. Each quench starts at zero drive and continues beyond criticality ($t = 0$) well into the ordered $U(1) \times \mathbb{Z}_2$ phase at rate $\dot{\epsilon}$, where $\epsilon = \frac{\mu - \mu_{cr}}{\mu_{cr}}$ is the reduced drive parameter. Note that while faster quenches result in faster growth, a rescaling of the amplitude order with quench rate $\left(|z(t)|^2 \to \dot{\epsilon}^{\,0.36 \pm 0.03} \times |z(t)|^2\right)$ causes the curves to intersect at $\epsilon = 0$ (inset), a classic signature of criticality. (Main figure) If time is also rescaled with quench rate as $t \to \dot{\epsilon}^{\,-0.57 \pm 0.02} \times t$, all growth curves collapse onto a single universal function in rescaled time, in the limit of slow quenches $\dot{\epsilon} \to 0$. This collapse shown here is for an order of magnitude in quench rate, and occurs over three orders of magnitude in rescaled amplitude, as indicated by the arrow, beyond which the order saturates.

In light of the observation of a dynamic order parameter with a novel broken symmetry, it is natural to wonder if conventional paradigms continue to be valid for the phase transition between the PA and the $U(1) \times \mathbb{Z}_2$ phases. Motivated by the novel dynamics of this open driven dissipative phase transition, we study here its critical dynamics. Well in the regime of long reservoir coherence times, at $(\gamma_0 \tau_r)^{-1} = 1/5$, we perform a finite time linear quench the system from

a pump drive of $\mu = 0$ (*PA* phase) to deep into the $U(1) \times \mathbb{Z}_2$ phase, and measure the growth of order during the quench, shown in the inset of Fig. 6.3 for various quench rates $\dot{\epsilon}$, where ϵ is the reduced distance from criticality, $\epsilon = \frac{\mu - \mu_{cr}}{\mu_{cr}}$. The faster the finite time quench, the faster the onset and evolution of order. However, when the amplitude order and time are both scaled with the quench rate, all these curves collapse well onto a single universal curve for over more than three orders of magnitude of rescaled order, i.e.

$$\langle |z_{s,i}(t; \dot{\epsilon})|^2 \rangle \propto \dot{\epsilon}^{-a} \times \mathcal{G}\left(\dot{\epsilon}^b t\right)$$

where $\langle \cdot \rangle$ denotes an ensemble average, $\mathcal{G}$ is a normalized universal function with $\mathcal{G}(0) = 1$, a, b are universal scaling exponents, and the system crosses criticality at time $t = 0$ with $\epsilon(t) = \dot{\epsilon}t$. This collapse for an order an magnitude of quench rates is shown in Fig. 6.3, yielding the empirically extracted exponents of $a = 0.36 \pm 0.03$ and $b = 0.57 \pm 0.02$. We thus observe universal critical dynamics even for this driven dissipative phase transition.

6.7   Hysteresis area scaling

While the observed universal dynamics suggests conformity of critical behavior in this open driven dissipative system to conventional understanding of phase transitions, there are signatures that the picture is incomplete. The density of defects formed after a finite time quench across a phase transition has conventionally been used as a measure of the excess heat in the system caused by the quench. It is also a measure of nonadiabaticity of the system's evolution during a finite time quench. Such excess heat vanishes in the limit of very slow quenches, and is typically expected to scale as a single power law with quench

rate.

The hysteretic area of $\langle |z|^2 \rangle$ in our system, as it is linearly quenched forward into the ordered $U(1) \times \mathbb{Z}_2$ phase and then linearly quenched back into the disordered PA phase, can be considered to be a proxy for this excess heat [Fig.6.4(a)]. However, instead of a single power law, we observe a kink in the hysteresis area as a function of quench rate [Fig.6.4(b)], challenging our current understanding [148, 130]. We note that for quenches occurring over timescales much longer than the reservoir coherence times, the system-reservoir interactions are essentially Markovian, and we expect the hysteresis area scaling to revert to the single power law of the Markovian limit, with exponent 1.

6.8 Conclusion and outlook

In this work, we experimentally measure the phase diagram of a driven dissipative system that has non-Markovian system-bath interactions. We demonstrate that the phase diagram is significantly influenced by the characteristics of these interactions – here, it leads to a new emergent phase that has dynamical order. We further confirm quantitatively that the dynamics is captured by the model of [143]. Moreover, while the scaling of the amplitudes measured for a quench across criticality suggests conformance to conventional phase transition paradigms, which predict such scalings, the hysteresis area data also suggests that our current understanding presents only an incomplete picture of the critical behavior of such systems.
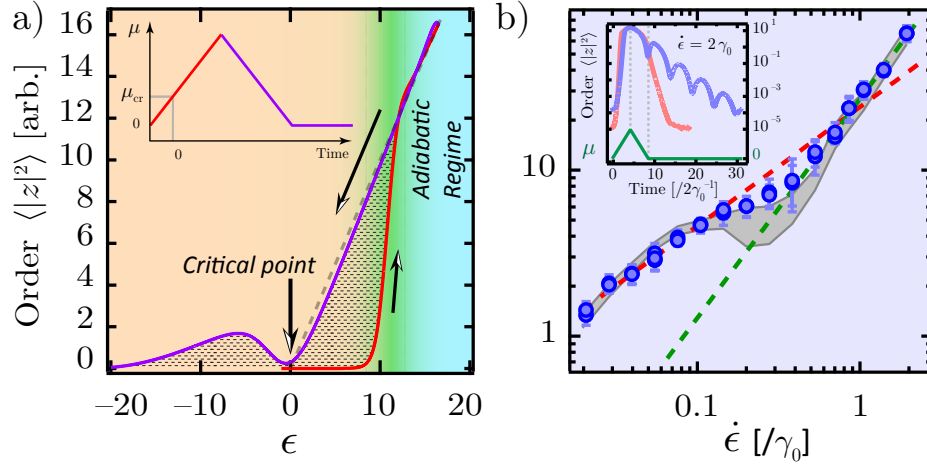
Figure 6.4: **Hysteresis area scaling:** (a) (Inset) Finite time quench proto-
col from the disordered *PA* phase into the $U(1) \times \mathbb{Z}_2$ phase (red)
and then back into the disordered phase (violet). (Main figure)
Measured growth of order during the forward quench (red)
and decay of order during the reverse quench (violet), shown
for $|\dot{\epsilon}| = 2\gamma_0$. Near criticality, the measured order deviates
from the expected adiabatic steady state order (dotted line),
whereas deep in the ordered phase, it adiabatically follows
it. The hysteresis between the forward and reverse quenches
defines a bounded area (shaded region), denoting an excess
heat due to the quench cycle. (b) The observed dependence
of this excess heat on the quench rate deviates significantly
from the expectation of a single power law scaling. The data
suggests one power law ($\dot{\epsilon}^{\,0.72\pm0.05}$) at low quench rates, and a
kinked, inflected transition to a significantly different power
law ($\dot{\epsilon}^{\,1.32\pm0.09}$) at large quench rates.

6.9   Supplemental Information

6.9.1   System Hamiltonian

In the lab frame, the signal-idler-pump system is described by the Hamiltonian

$$\mathcal{H} = \sum_{k \in \{s,i,P\}} \hbar\omega_k a_k^\dagger a_k - \frac{\hbar g}{x_{0,s} x_{0,i} x_{0,P}} x_s x_i x_P$$

$$- \hbar(F_P e^{-i\omega_P t} a_P^\dagger + F_P^* e^{i\omega_P t} a_P)$$

130

where g characterizes the bi-linear coupling between the signal and idler modes through the driven pump mode, $x_{0,s}, x_{0,i}, x_{0,P}$ represent the zero point motion, and F_p parametrizes the strength of the pump drive. In a rotating frame of the signal, idler and pump modes, transformed through $U = \prod_k U_k = \prod_k e^{-i\omega_k a_k^\dagger a_k t}$, the Hamiltonian changes as $\mathcal{H} \rightarrow \mathcal{H}_{rot} = U^\dagger \mathcal{H} U - \sum_k \hbar\omega_k a_k^\dagger a_k$. Using $x_k = x_{0,k}(a_k + a_k^\dagger)$ and $U_k^\dagger a_k U_k = a_k e^{-i\omega_k t}$, and making the rotating wave approximation, we get the Hamiltonian in the main text,

$$\mathcal{H}_{rot} = -\hbar g(a_s^\dagger a_i^\dagger a_P + a_P^\dagger a_i a_s) - \hbar(F_P a_P^\dagger + F_P^* a_P) \tag{6.2}$$

Note that the first term signifies the downconversion from the pump mode into the signal and idler modes ($a_s^\dagger a_i^\dagger a_P$) and the conjugate ($a_P^\dagger a_i a_s$) signifies the upconversion from the signal and idler modes into the pump mode. The second term denotes the coherent drive of the pump mode ($F_P a_P^\dagger + F_P^* a_P$). The critical pump strength for the onset of order can be evaluated through the Heisenberg equations of motion given by $i\hbar \dot{a}_k = [a_k, \mathcal{H}_{rot}]$, i.e.

$$\dot{a}_{s,i} = iga_{i,s}^\dagger a_P - \frac{1}{2}\int_{-\infty}^{t} dt' \gamma_{s,i}(t - t')a_{s,i}(t') + if_{s,i}$$
$$\dot{a}_P = iga_i a_s - \frac{\gamma_P}{2}a_P + iF_P + if_P \tag{6.3}$$

Here, the dissipation terms of $\gamma_{s,i,P}$ are not accounted for by the Hamiltonian, but rather derived through a master equation approach [151]. $\gamma_{s,i}(t)$ is the non-Markovian dissipation kernel, and we have made the assumption that both the signal and idler are described by the same kernel, as realized in the experiments. For completeness, we note that the Markovian case is a special instance, described by a kernel $\gamma_{s,i}(t) = \gamma_{s,i}\delta(t)$. We also include in the above equations the fluctuation forces $f_{s,i,P}$ associated with the dissipation. These forces are related to the damping kernel $\gamma(t)$ through the fluctuation dissipation relation as described below.

Note that the experimentally measured complex amplitudes of motion $z_{s,i} =$

$x_{s,i} + i y_{s,i}$, where $x_{s,i} = a_{s,i} + a^\dagger_{s,i}$ and $y_{s,i} = -i(a_{s,i} - a^\dagger_{s,i})$ are the quadratures of motion, are nothing but $z_{s,i} = 2a_{s,i}$.

6.9.2 Fluctuation dissipation relation

The noise spectrum associated with a generic system bath coupling is described in [151]. In this work, where we are concerned with only a narrow band signal near the modes' natural frequencies, the power spectral density of the noise $f_z = 2f_{s,i}$ is well approximated by

$$\tilde{\chi}(\omega) \equiv \int_{-\infty}^{\infty} \frac{\langle f_z(t)f_z(0)^\dagger + f_z(t)^\dagger f_z(0)\rangle}{2} \cos \omega t \, dt$$
$$= \frac{2\hbar(\bar{n}_{th} + 1/2)}{m\omega} \tilde{\gamma}'(\omega)$$

where $\bar{n}_{th} = (e^{\hbar\omega/k_B T} - 1)^{-1}$ is the thermal phonon occupancy, and m is the effective mass [79].

At high temperatures $k_B T \gg \hbar\omega$, $\tilde{\chi}(\omega) \approx \frac{2k_B T}{m\omega^2}\tilde{\gamma}'(\omega)$. Because the x and y quadratures are uncorrelated ($\langle f_z(t)f_z(0)\rangle = \langle f_z(t)^\dagger f_z(0)^\dagger\rangle = 0$), their RMS fluctuations equal $\langle x^2_{s,i}\rangle = \langle y^2_{s,i}\rangle = \frac{\hbar}{m\omega_{s,i}}(\bar{n}_{th} + 1/2) \approx \frac{k_B T}{m\omega^2_{s,i}}$. Recall that the displacement in lab frame is the sum of the two quadrature motions, i.e. $\text{Re}[z_{s,i}(t)] = z_{s,i,lab} = x_{s,i}(t)\cos(\omega_{s,i}t) + y_{s,i}(t)\sin(\omega_{s,i}t)$, so that we have $\langle z^2_{s,i,lab}\rangle = \frac{1}{2}(\langle x^2_{s,i}\rangle + \langle y^2_{s,i}\rangle) = \frac{\hbar}{m\omega_{s,i}}(\bar{n}_{th} + 1/2) \approx \frac{k_B T}{m\omega^2_{s,i}}$, satisfying the equipartition theorem.

6.9.3 Mean field phase diagram

To evaluate the critical drive strength, $F_{cr,m}$, we solve Eqn.(6.3) for the nontrivial steady state solutions, $|z_{s,i}| \neq 0$, and ansatz $z_{s,i}$ to be a constant. For steady state

observables, only the total strength of the damping matters, given by the integral $\int dt \gamma_{s,i}(t) = \gamma_{s,i}$. Letting $\dot{z}_k, f_z \to 0$, and adiabatically eliminating z_P, given that $\gamma_P \gg \gamma_{s,i}$, we get

$$|F_{cr,m}| = \frac{\gamma_P \sqrt{\gamma_s \gamma_i}}{4g}$$

The drive can now be parametrized in units of this critical pump strength as $\mu = \frac{|F_P|}{|F_{cr,m}|}$. Here, we use the subscript m to denote that this critical drive strength is the same as in the Markovian case of $\gamma_{s,i}(t) = \gamma_{s,i}\delta(t)$. However, as shown below, a constant $z_{s,i}$ is not the only permissible steady state solution for the non-Markovianity considered in this work. An ansatz of the form

$$z_{s,i} = \bar{z}_{s,i} e^{-i\Delta_{s,i} t}$$

$$z_P = \bar{z}_P$$

when substituted into the equation of motion Eqn.(6.3) yields

$$-i\Delta_i \bar{z}_i e^{-i\Delta_i t} = -\frac{1}{2} e^{-i\Delta_i t} \bar{z}_i \tilde{\gamma}(\Delta_i) + i\frac{\gamma_0}{2} \bar{z}_s^* \bar{z}_P e^{i\Delta_s t}$$

$$-i\Delta_s \bar{z}_s e^{-i\Delta_s t} = -\frac{1}{2} e^{-i\Delta_s t} \bar{z}_s \tilde{\gamma}(\Delta_s) + i\frac{\gamma_0}{2} \bar{z}_i^* \bar{z}_P e^{i\Delta_i t}$$

$$0 = -\frac{1}{2}\gamma_P \bar{z}_P + i\frac{\gamma_P}{2} \bar{z}_i \bar{z}_s e^{-i(\Delta_i + \Delta_s)t} + i\frac{\gamma_P}{2}\mu$$

where $\tilde{\gamma}(\omega) = \int dt \gamma(t) e^{i\omega t} = \gamma_0(1 - i\omega\tau_r)^{-1}$ is the fourier transform of kernel $\gamma(t) = \gamma_0 \tau_r^{-1} e^{-t/\tau_r}$. These equations always admit the trivial solution $\bar{z}_s = \bar{z}_i = 0, \bar{z}_P = i\mu$. For the system to have non-zero steady state signal and idler amplitudes, these equations imply that $\Delta_s + \Delta_i = 0$, so that we define $\Delta \equiv \Delta_s = -\Delta_i$. They further imply that

$$\left(\frac{\tilde{\gamma}(\Delta)}{2} - i\Delta\right)\left(\frac{\tilde{\gamma}(-\Delta)}{2} + i\Delta\right)^* \bar{z}_i = \frac{\gamma_0^2}{4}|\bar{z}_P|^2 \bar{z}_i$$

Since $\tilde{\gamma}(-\omega) = \tilde{\gamma}^*(\omega)$, this simplifies to

$$\left(\frac{\tilde{\gamma}(\Delta)}{2} - i\Delta\right)^2 = \frac{\gamma_0^2}{4}|\bar{z}_P|^2$$

indicating that $\frac{\tilde{\gamma}_0}{2} \equiv \frac{\tilde{\gamma}(\Delta)}{2} - i\Delta$ is real and positive. Now solving for the signal and idler amplitudes, we get

$$\left(\frac{\tilde{\gamma}_0}{\gamma_0}\right)^2 \left[1 + \left|\frac{\gamma_0}{\tilde{\gamma}_0}\right| |\bar{z}_{s,i}|^2\right]^2 = \mu^2$$

$$\Rightarrow |\bar{z}_{s,i}| = \sqrt{\mu - \frac{\tilde{\gamma}_0}{\gamma_0}}$$

Accordingly, we define the critical pump as $\mu_{cr} = \tilde{\gamma}_0/\gamma_0$, indicating the onset of self oscillations. To solve for the oscillation frequency Δ, we note that $\tilde{\gamma}_0$ is real and positive.

$$\frac{1}{2}\tilde{\gamma}(\Delta) - i\Delta = \frac{1}{2}\frac{\gamma_0}{1 + \tau_r^2\Delta^2} + i\Delta\left(\frac{1}{2}\frac{\gamma_0\tau_r}{1 + \tau_r^2\Delta^2} - 1\right) \in \mathbb{R}$$

This has solutions $\Delta = 0, \pm\tau_r^{-1}\sqrt{\frac{\gamma_0\tau_r}{2} - 1}$. Note that the latter solution is only meaningful for $(\gamma_0\tau_r)^{-1} \leq 1/2$. Based on these relations, we can characterize the phases as follows, also shown in Fig.6.5.
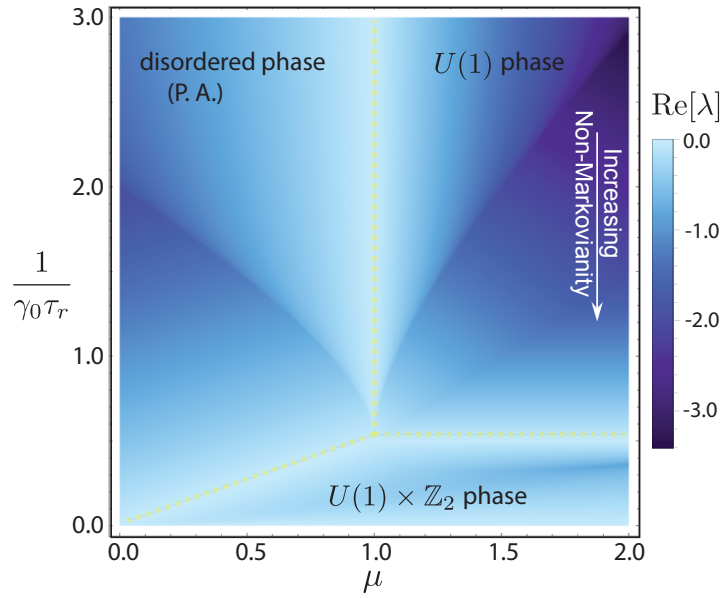
Figure 6.5: Phase diagram as a function of normalized pump drive μ and normalized reservoir decay rate $(\gamma_0\tau_r)^{-1}$. Color scale corresponds to least negative real part of eigenvalues, where the phase boundaries (dashed lines) correspond to points where the real part vanishes. See text for explanation of the *PA*, *U*(1), and *U*(1) × $\mathbb{Z}_2$ phases. Adapted from [143].

134

For $(\gamma_0\tau_r)^{-1} > 1/2$, the coherence time of the reservoir is small compared to the signal and idler damping times. Here, $\Delta = 0$ and $\tilde{\gamma}_0 = \gamma_0$. The critical drive is $\mu_{cr} = 1$. For $\mu < 1$, the system is in the *PA* phase, where $\bar{z}_{s,i} = 0$, $\bar{z}_P = i\mu$. As the drive strength is increased beyond $\mu_{cr} = 1$, the *PA* phase becomes unstable, and the stable steady state solution is the parametric oscillator characterized by $\bar{z}_{s,i} = ie^{\pm i\phi/2}\sqrt{\mu - 1}, \bar{z}_P = i$. The signal-idler phase difference ϕ is unconstrained, corresponds to a spontaneous breaking of the $U(1)$ symmetry associated with the choice of this phase, because of which we denote this phase as the $U(1)$ phase.

For $(\gamma_0\tau_r)^{-1} < 1/2$, the coherence time of the reservoir is long compared to the signal and idler damping times. In this regime there are two kinds steady state solutions, one with $\Delta = 0$ and the other with $\Delta \neq 0$. For $\mu < \mu_{cr} = 2(\gamma_0\tau_r)^{-1}$, the only solution is the disordered *PA* solution with $\bar{z}_{s,i} = 0$, $\bar{z}_P = i\mu$. For drive strength, $\mu_{cr} < \mu < 1$, the disordered phase is unstable, and the only self oscillatory solution is with non-zero $\Delta = \tau_r^{-1}\sqrt{\frac{\gamma_0\tau_r}{2} - 1}$, where $\bar{z}_{s,i} = ie^{\pm i(\phi/2 + \Delta t)}\sqrt{\mu - \mu_{cr}}$, $\bar{z}_P = i\mu_{cr}$. This solution is stable, and in this phase, the signal and idler modes oscillate at frequencies shifted from their natural resonance frequencies by an amount Δ. In addition to the breaking of the $U(1)$ symmetry associated with the signal-idler phase difference, there is another breaking of a $\mathbb{Z}_2$ symmetry associated with the choice of the sign of Δ. As such, we denote this phase as the $U(1) \times \mathbb{Z}_2$ phase. For $\mu > 1$, all the above three solutions exist, but only the $U(1) \times \mathbb{Z}_2$ solution is stable.

6.9.4 Optical detection of the signal and idler modes

The out of plane displacement of the mechanical signal and idler modes are detected using a Michelson interferometer with a position sensitivity of $\sim$ 14 fm/$\sqrt{\text{Hz}}$ at the signal and idler frequencies. A typical power of 630 μW is incident on the mechanical silicon nitride membrane, as also in the reference arm of the interferometer. The light source is an external cavity diode laser operating at 795 nm with linewidth < 100 kHz.

At low frequencies (< 3 Hz), the optical interferometer used for the detection of mechanical displacement is susceptible to residual amplitude modulation (RAM) which we ascribe to the gradual temperature fluctuation and temperature dependent birefringence of various optical elements. In our experiment, this low frequency amplitude noise convolves with the mechanical displacement signal, leading to a 0.75% contamination of the detected membrane displacement. Consequently, the signal to noise ratio (SNR) for the mechanical thermal motion degrades to 1 as the amplitude of motion approaches 150 times the room temperature thermal amplitude. To ensure that the finite time quench experiments are conducted with thermal fluctuations that are detected with SNR > 1, we ensure that the system is driven with a large effective thermal noise, with the effective temperature being much larger than room temperature.

6.9.5 Feedback stabilization of the signal and idler modes

Due to the differential thermal expansion of the silicon nitride membrane and the supporting silicon substrate, the signal and idler frequencies change with ambient temperature. Empirically, this change is by $\sim$ 1.4 linewidths per

milliKelvin. Given that ambient temperatures vary over ~ 200 mK within a day, precise measurement of thermomechancial motion and steady state responses requires active feedback to achieve sub-linewidth stabilization of the mode frequencies. We accomplish this using the differential thermal expansion to our advantage, through photothermal control of the silicon substrate. As also described in previous work [150], we continuously monitor the mechanical frequency of a high-Q thermometer mode at 2.736 MHz - far from the signal and idler frequencies studied in this work. Phase detection of this mode generates an error signal with an on-resonant slope of 5.91 radians/Hz. Active photothermal stabilization is accomplished by feeding back to an optical control beam of 600μW average power, generated by a diode laser operating at 830 nm, and amplitude controlled using an acousto optic modulator (AOM). The RMS frequency fluctuations of the thermometer mode thus achieved are measured to be below 2 mHz, equivalent to temperature fluctuations of the substrate of less than 2 μK.

6.9.6 Residual frequency drift stabilization

In order to quantitatively map out the phase boundaries, the signal and idler frequencies need to be stabilized to well within their natural linewidths. While the photothermal feedback described above is effective in tracking and compensating short term frequency changes, there remains a long term (over $40-400$ s, i.e. $20-200$ γ_0^{-1}) residual frequency drift on the order of $0.2\gamma_0$, that can measurably alter the phase diagram. To attain better frequency stability, we identify a monitor mode that is highly correlated to the signal and idler frequencies. This monitor mode was offset by ~ 500 linewidths from the signal mode. By tracking

the signal and idler frequencies using the monitor mode phase response, we further suppress even the long term frequency drifts. The pump drive frequency is also changed such that it is always equals the sum of the tracked signal and idler frequencies.

6.9.7 Feedback implementation of non-Markovian system-bath interactions

The role of the non-Markovian system-bath interactions is fully captured by their influence on the equations of motion of the system. Due to the minimalist nature of this work's physical realization of the described driven dissipative phase transition, we can use active feedback to enforce a particular equation of motion, and thereby simulate a non-Markovian system-bath interaction of our choosing.

In particular, the evolution of the complex amplitudes of motion $z_{s,i}$, detected using the Michelson interferometer and a lock-in amplifier (Zurich Instruments, HF2LI), is governed by the equations

$$\dot{z}_{s,i} = -\frac{\gamma_{s,i}}{2}\left(z_{s,i} + \chi_{s,i}V_{s,i}\right) + if_z^{\text{Mark}}$$

where $V_{s,i}$ is the feedback voltage applied to the piezo transducer that the silicon substrate, which hosts the signal and idler modes, is mounted on, and $\chi_{s,i}$ is the experimentally measured transfer function of the applied PZT voltage into signal and idler motion. Here, the first term refers to the modes' intrinsic Markovian damping, and the last term f_z^{Mark} refers to the associated Markovian

thermal noise. By comparing to Eqn.(6.3) and enforcing

$$V_{s,i} = \frac{2}{\gamma_{s,i}\chi_{s,i}} \left[-\frac{\gamma_{s,i}}{2} z_{s,i} + \frac{1}{2} \int_{-\infty}^{t} dt' \gamma(t - t') z_{s,i}(t') + if_z \right]$$

we simulate a non-Markovianity of our choice. Here, $f_z = 2f_{s,i}$ denotes the added non-Markovian noise related to our choice of the damping kernel $\gamma(t)$ through the fluctuation dissipation relation as described above. Note that while the first term of $V_{s,i}$ counters the intrinsic Markovian damping and effectively cancels it, $V_{s,i}$ does not compensate for the associated noise f_z^{Mark}. To ensure that it is the non-Markovian noise that dominates the stochastic behavior of the system, we set its effective temperature to be ~ 100 times the temperature of the intrinsic Markovian noise f_z^{Mark}, thus overwhelming it. We note that the feedback voltage $V_{s,i}$ described here is a complex representation in a rotating frame of the real-life voltage applied to the piezo transducer, $\mathcal{V}_{s,i}(t) = \text{Re}[V_{s,i}] \cos(\omega_{s,i}t) + \text{Im}[V_{s,i}](\sin \omega_{s,i}t)$.

In the experiments, we implement this realtime feedback digitally, using NI LabView. The signal and idler mode motions $z_{s,i}$ are continuously measured and recorded at 1800 Hz. This recorded history of $z_{s,i}(t')$ is numerically convolved with our choice of kernel $\gamma(t)$ as a discrete sum, with the lower limit on the integral $\int dt'$ being the time at which we start applying the feedback. A precomputed non-Markovian noise sequence f_z with the appropriate noise spectral density $\propto \tilde{\gamma}'(\omega)$ is also added.

To give a sense of the numbers involved in the feedback implemented here – The feedback rate is ~ 15 Sa/s, which, because of the ultra-high Q resonators used in this work, is more than a 100 times the modes' natural linewidths. The least significant bit of the digital feedback voltage amplitude is ~ 76 nV, more than a 100 times smaller than the typical non-Markovian noises f_z peak-to-peak

voltages of $\sim 15 - 20\,\mu$V.

Effects of the discretization of feedback

The discrete nature of the feedback described above leads to a systematic deviation of the achieved non-Markovian damping kernel from the target kernel. There are three aspects to this feedback imperfection – a finite time delay, the approximation of an integral by a discrete trapezoidal sum, and the piece-wise constant nature of the implemented feedback over each sampling period. We explain below the contributions of each of the above mentioned effects. Firstly, if a feedback update based on a measurement at time $t = 0$ is delayed by time t_{delay} and is implemented at $t = t_{\text{delay}}$, it effects a frequency response of $e^{i\omega t_{\text{delay}}}$. In our experiments, the feedback for each of the signal and idler modes is delayed by a mean time of $\Delta t/2$ with a standard deviation of $\Delta t/20$. Here, Δt is the sampling period separating two successive samples, and approximately equals 1/15 s. Secondly, the integral is approximated by a discrete sum, and the output at step n, $F[n]$, is given by

$$F[n] = (\frac{1}{2}z[n]\gamma[0] + \sum_{k=1}^{N_0-2} z[n-k]\gamma[k]$$
$$+ \frac{1}{2}z[n+1-N_0]\gamma[N_0-1])\Delta t$$

where $\gamma[k] = \gamma(t = k\Delta t) = \gamma_0\tau_r^{-1}\exp(-k\Delta t/\tau_r)$ is the discretized kernel, $z[n] = z(t = n\Delta t)$ is the nth complex amplitude sample, and N_0 is the length of the kernel. We ensure that $N_0\Delta t \gg \tau_r$, and in fact that $N_0\Delta t$ is longer than the experimental duration. To evaluate the effective kernel then, we can consider the upper bound of the above sum to be ∞. The frequency response is thus given by

$$\gamma_0\tau_r^{-1}\Delta t \left(\frac{1}{2} + \frac{\exp((i\omega - \tau_r^{-1})\Delta t)}{1 - \exp((i\omega - \tau_r^{-1})\Delta t)} \right)$$

140

Lastly, the feedback force is piece-wise constant over the sampling period of Δt. A step output has a frequency response of

$$\int_0^{\Delta t} 1 \times e^{i\omega t} dt = \frac{e^{i\omega \Delta t} - 1}{i\omega \Delta t}$$

The frequency response of the effected feedback kernel is the product of the three expressions above. The role of this discretization is accounted for when verifying the feedback induced non-Markovianity as described in the section below.

Additionally, the sampling period Δt jitters by $\sim 15\%$, leading to a random error in the feedback kernel. We expect that this jitter has no first order effect on the effected kernel, and note that its effects are not apparent in the parameter regime explored in this work.

Effects of detection frequency offset

A major source of error in the feedback comes from the drifting frequencies of the signal and idler modes. Such drifts cause an offset between the natural resonance of the modes and the local oscillator detection frequencies set on the lock-in amplifier, leading to unwanted changes in the feedback kernel. Recall that the equation of motion of a single mode is given by

$$\dot{z} = -\frac{\gamma}{2}z - \frac{1}{2} \int_{-\infty}^{t} dt' \gamma_{\text{fb}}(t - t')z(t')$$

where $\gamma_{\text{fb}}(t)$ includes also the part that cancels the Markovian damping as described above, with the subscript fb denoting feedback. Because the natural resonance frequency of the mode need not coincide with the local oscillator detection frequency, either due to an error in initial calibration, or due to frequency drifts over the experimental timescales, the equation of motion of the detected

amplitude $z(t)$ is modified to

$$\dot{z} = -\frac{\gamma}{2}z - i\Delta\omega z - \frac{1}{2}\int_{-\infty}^{t} dt'\, \gamma(t-t')z(t')$$

where $\Delta\omega$ is the difference between natural resonance and the local oscillator detection frequency. The non-zero $\Delta\omega$ causes a phase shift in the feedback, and thus leads to a change in the above-threshold oscillation frequency Δ, given by the phase matching condition of

$$\left(\frac{\tilde{\gamma}_s(\Delta)}{2} - i\Delta\right)\left(\frac{\tilde{\gamma}_i(-\Delta)}{2} + i\Delta\right)^*$$

being real and positive as discussed above. The $\tilde{\gamma}_{s,i}$ here denote the modified dissipation kernels due to the frequency offset and feedback imperfection, and Δ denotes the modified oscillation frequency.
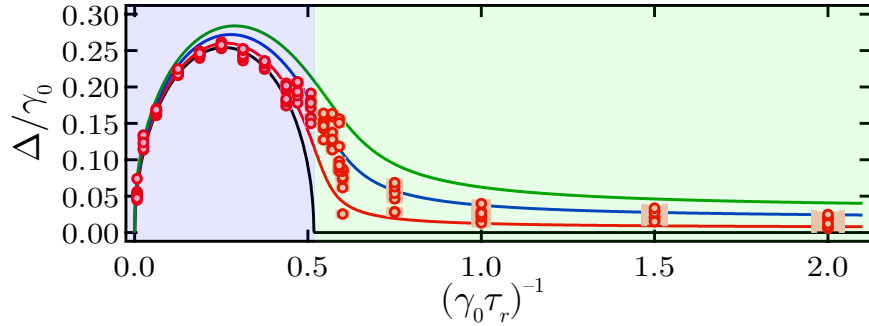
Figure 6.6: Predicted oscillation frequency Δ vs $(\gamma_0\tau_r)^{-1}$. The black curve represents on-resonant detection. The colored curves are predictions for both the signal and idler modes having a local oscillator detection frequency offset ($\Delta\omega$, see text) of $0.01\gamma_0$ (red), $0.03\gamma_0$ (blue) and $0.05\gamma_0$ (green). The experimental data (red points) lie within the band defined by a frequency offset of $0.01 - 0.05\gamma_0$, the range of estimated frequency offsets for the experiments.

The change in the above threshold oscillation frequency is pronounced near the phase boundary $(\gamma_0\tau_r)^{-1} = 1/2$, as shown in Fig. 6.6 and Fig. 6.2(a) of the main text. This is further corroborated by the fact the susceptibility to frequency shifts diverges near the phase boundary $(\gamma_0\tau_r)^{-1} = 1/2$ [143]. For the finite time

linear quench experiments in this work, we operate deep in the $U(1) \times \mathbb{Z}_2$ phase at $(\gamma_0 \tau_r)^{-1} = 1/5$, where the oscillation frequency Δ is much less susceptible to the local oscillator detection frequency offset.

6.9.8 Verification of the feedback induced non-Markovianity
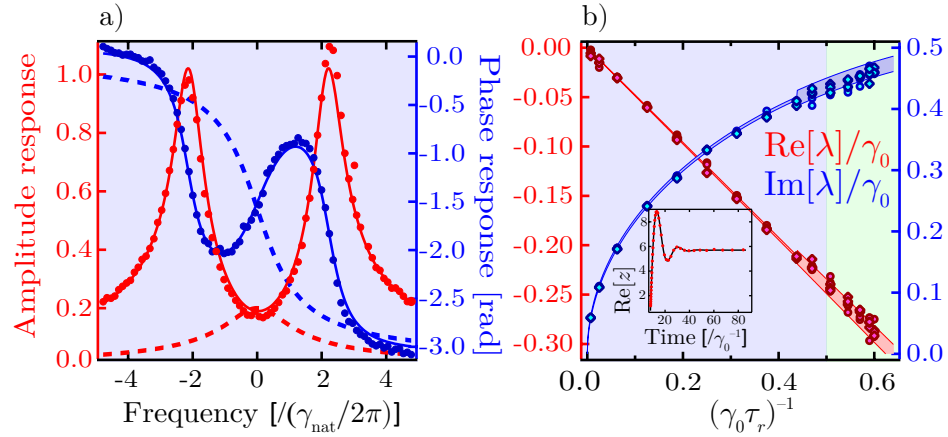
Figure 6.7: Verifying the feedback fidelity: (a) Steady state susceptibility measurements with the implemented feedback-induced non-Markovianity. The measured amplitude response (red) and phase response (blue) are shown as filled circles, with calculated estimates shown as solid lines. The expected pure Markovian response is shown as dashed lines for comparison. Data shown here for $\gamma_0 = 10\gamma_{nat}$ and $\tau_r = 1/\gamma_{nat}$, where $\gamma_{nat} \approx 2\pi \times 100$ mHz is the natural Markovian decay rate. (b) Real and imaginary parts of the single mode decay rates for the feedback induced non-Markovian system, for both the signal (circles) and idler (diamonds) modes. Solid lines and colored bands show the expected decay rates as a function of $(\gamma_0 \tau_r)^{-1}$, including the effects of the local oscillator detection frequency offset and discretization of feedback (see text). The estimated frequency offset for this data is $0.01\gamma_0$ ($0.05\gamma_0$) for data with $(\gamma_0 \tau_r)^{-1} < 7/16$ ($> 7/16$). (Inset) Typical single mode step response, shown here for $(\gamma_0 \tau_r)^{-1} = 5/16$, with data (red points) and predicted response (solid black curve).

To verify the non-Markovian kernel implemented through feedback as de-

scribed in the previous section, we measure the single mode steady state susceptibility at zero pump drive ($\mu = 0$), and find excellent agreement with the target kernel [see Fig.6.7(a)]. For this measurement, we drive the mode at a constant drive at near-resonant frequencies and measure its steady state amplitude and phase response. The non-Markovian amplitude response has two susceptibility peaks, a precursor to the $\mathbb{Z}_2$ symmetry breaking in the $U(1) \times \mathbb{Z}_2$ phase. The measured data (filled circles) and calculated estimates (solid lines) show very good agreement. In contrast, a pure Markovian amplitude response would have been lorentzian, as shown by the estimates plotted for reference (dashed lines). The feedback parameters are $\gamma_0 = 10\gamma_{nat}, \tau_r = 1/\gamma_{nat}$, where γ_{nat} is the natural or intrinsic Markovian damping rate.

In addition, we also measure the single mode decay rate by measuring the single mode step response [see Fig. 6.7(b)]. Note that in general, the decay rate is complex, implying a decay accompanied by an oscillatory response. For each $(\gamma_0 \tau_r)^{-1}$ value, we measure the step response of the signal and idler modes and fit them for a complex decay rate. As shown, we find very good agreement between the measured and predicted single mode decay rates. In the shown predictions, we have include the effects of the technical imperfections discussed in the previous section.

6.9.9 Extracting phase boundaries

All phase boundaries are extracted by extrapolating to zero the measured data – the steady state amplitude order, or the growth rate, or the oscillation frequency Δ. The steady state amplitude order has a functional form $A_0 \sqrt{\mu - \mu_{cr}}$, which is

fit for the measured above-threshold steady state amplitudes to extract μ_{cr}. For the quenches into the $U(1)$ phase, the growth rate is real [Fig.6.8(a)]. For the quenches into the $U(1) \times \mathbb{Z}_2$ phase, the growth rate is complex for small pump drives μ, and becomes real for large pump drives [Fig.6.8(b)]. The growth rate is given by the eigenvalues with the largest real part [143], i.e.

$$\lambda = \frac{1}{2\tau_r}\left[\left(\frac{\mu}{\mu_{cr}} - 1\right) + \sqrt{\left(\frac{\mu}{\mu_{cr}} + 1\right)^2 - 2\gamma_0\tau_r}\right] \qquad (\gamma_0\tau_r)^{-1} \leq 1/2$$

$$\lambda = \frac{\gamma_0}{4}\left[\left(\frac{\mu}{\mu_{cr}} - \frac{2}{\gamma_0\tau_r}\right) + \sqrt{\left(\frac{\mu}{\mu_{cr}} + \frac{2}{\gamma_0\tau_r}\right)^2 - \frac{8}{\gamma_0\tau_r}}\right] \qquad (\gamma_0\tau_r)^{-1} > 1/2$$

We thus fit for μ_{cr}, allowing γ_0 and τ_r to vary within their error bounds. The $U(1) - U(1) \times \mathbb{Z}_2$ phase boundary is extracted for each pump drive μ by fitting the oscillation frequency Δ to the functional form $\tau_r^{-1}\sqrt{\frac{\tau_r}{\tau_{r,cr}} - 1}$, where we denote by $\tau_{r,cr}$ the reservoir coherence time at the phase boundary [Fig.6.8(c)]. We exclude the data for $(\gamma_0\tau_r)^{-1} \geq 7/16$ in the fits, as we observe the measured Δ to have a large scatter due to its increased susceptibility to the local oscillator detection frequency offset, being near the phase boundary, as discusses in the previous sections. The phase boundary extracted at various pump drives μ show that it is indeed independent of the pump drive strength, and occurs at $(\gamma_0\tau_r)^{-1} =$ 0.515 $\pm$ 0.005, which compares very well with the expectation of 1/2 [Fig.6.1(a) of main text].

6.9.10 Relation of noise bandwidth and simulation time step

For the purposes of the simulations shown in this work, we consider strictly non-Markovian system-bath interactions, in that the Markovian dissipation and forces ($\gamma_{s,i}$ and f_z^{Mark}) are set to zero. For simulations in reference to experiments, however, the residual Markovian noise can be accounted for, as in the equations above. Note that the Markovian forces f_z^{Mark} are zero mean, gaussian and white.
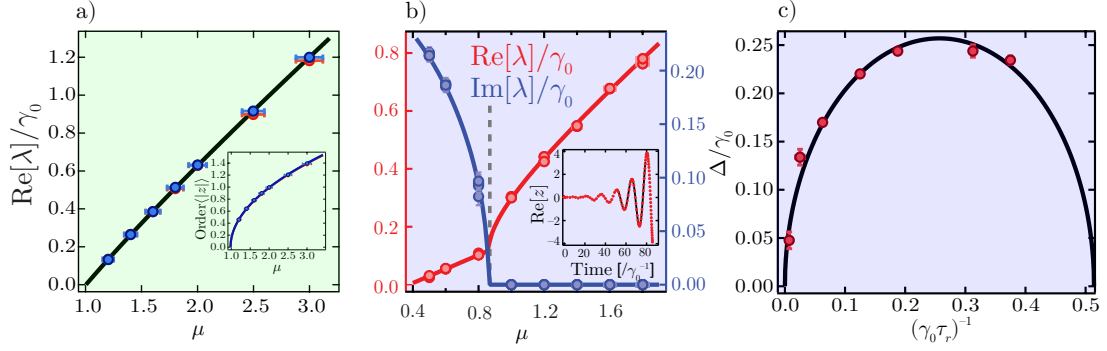
Figure 6.8: Extraction of phase boundaries: (a) Growth rate of order for a sudden quench into the $U(1)$ phase as a function of pump drive μ, for the signal (red) and idler (blue) modes. The growth rate is real in the regime of short reservoir coherence times, $(\gamma_0 \tau_r)^{-1} > 1/2$. Data shown here is for $(\gamma_0 \tau_r)^{-1} = 2$. (Inset) Steady state amplitude as a function of pump drive μ. (b) Measured growth rates of order for a sudden quench into the $U(1) \times \mathbb{Z}_2$ phase, with both the real (red) and imaginary (blue) parts. In this regime of long reservoir coherence times, $(\gamma_0 \tau_r)^{-1} < 1/2$, the growth rate is complex for small pump drives and exhibits an exceptional point (dashed line) where the complex rates become real. (Inset) Typical time trace showing the growth of order, here shown for $\mu = 0.5$ and $(\gamma_0 \tau_r)^{-1} = 3/16$ – measured (red) and fit (solid black curve). For (a-b), the critical pump drive is extracted by fitting either the measured amplitude order or the measured growth rates as a function of pump drive μ. The solid curves denote fits made as described in the text. c) Measured, above-threshold oscillation frequency Δ vs the normalized reservoir coherence rate $(\gamma_0 \tau_r)^{-1}$ for a pump drive of $\mu = 1.2$ (red data). A vanishing Δ at finite reservoir coherence time τ_r defines the $U(1) - U(1) \times \mathbb{Z}_2$ phase boundary, and is extracted through fits like the one shown (solid black line).

As such, their bandwidth extends beyond the simulations' Nyquist frequency, $f_{\text{Ny}} = \frac{\Delta t^{-1}}{2}$. The variance of the displacement induced for a f_z^{Mark} of specified variance (i.e. temperature) is proportional to the simulation time step Δt. As such, the influence of the Markovian thermal forces is effected as a $f_z^{\text{Mark}} \sqrt{\Delta t}$ in the propagation [171]. In contrast, for the choice of exponential dissipation kernel considered here, most of the thermal power of the non-Markovian noise f_z

is contained within a finite bandwidth. Therefore, so long as the simulations'
Nyquist frequency is large enough, the non-Markovian noise forces f_z need not
scale with the simulation time step. In the simulations for this work, τ_r = 5 s
and Δt = 0.05 s, so that the simulations' Nyquist frequency is 10 Hz, as com-
pared to a frequency window of $[-1, 1]$ Hz which contains about 98% of the
non-Markovian thermal power. We further assume that the pump mode is co-
herently driven to large amplitudes, and has a temperature much smaller than
the signal and idler temperatures, so that we set $f_{z,P} \rightarrow 0$.

6.9.11   Spectral properties of noise

The thermal noise forces f_z are set to satisfy the fluctuation dissipation relations
as discussed in previous sections. While a generic algorithm can be prescribed
to generate thermal forces related to an arbitrary memory kernel starting from
white gaussian noise, we describe here the same for the exponential kernel $\gamma(t) = \gamma_0 \tau_r^{-1} \exp(-t/\tau_r)$. Given an independent zero mean gaussian noise $g[n]$ of unit
variance, we recursively define noise $r[n]$ at step n as

$$r[0] \;\; = \;\; g[0]$$

$$r[n+1] \;\; = \;\; e^{-\Delta t/\tau_r} r[n] + \sqrt{1 - e^{-2\Delta t/\tau_r}} \, g[n+1]$$

$r[n]$ then are zero mean, unit variance gaussian variables with correlation
$\langle r[n]r[m] \rangle = e^{-|n-m|\Delta t/\tau_r}$ [172].

CHAPTER 7

BACK-ACTION EVADING MEASUREMENTS OF TWO QUADRATURES USING A PARAMETRIC COUPLING

7.1 Overview

In the preceding Chapters, we have referred to potential applications of reservoir-engineered environments to effect enhanced sensing capabilities. This Chapter gives a concrete theoretical illustration of how the driven PA–PO coupling between two harmonic oscillators can lead to improvements in sensing.

The so-called measurement problem of quantum mechanics illustrates how a measurement of a system can dramatically perturb it [36]. Such disturbances of system properties due to measurement back-action lead to a compromise – the strength of measurement cannot be arbitrarily increased to yield higher precision – an example of which is the standard quantum limit [173, 174, 54]. Sensing technologies may thus seem to be ultimately limited by the inevitable quantum nature of any system. However, back-action can be reduced or avoided [175, 176, 173, 99] or compensated [177, 178, 179, 180], by creative design of the measurement process, or by a clever choice of the measurement itself [181, 173, 174, 54, 182], allowing conventional quantum limits like the standard quantum limit to be beaten. (These three refer to back-action evading measurements, quantum noise cancellation measurements or quantum non-demolition measurements, respectively.)

In this work, we employ a well-developed and recently demonstrated two-tone back-action evasion scheme in optomechanics [173, 183, 99], in conjunction

with the PA-PO coupling introduced in Chapter 4. We use the coupling to dynamically link a quadrature of one oscillator with a quadrature of another, and show that these two quadratures form a quantum mechanical free subspace, i.e. the subspace of these two quadratures (out of a total of four quadratures) evades measurement back-action and follows classical dynamics [182]. In the context of sensing, we show that by coupling the different quadratures of a force to the two quadratures of this subspace, we can realize a BAE measurement for both force quadratures, as opposed to just the one achievable without the nonlinear coupling. Yet another scheme for harnessing the PA–PO nonlinearity for enhanced sensing capabilities was developed and implemented along with H. F. H. Cheung, and is detailed in Appendix D, where we experimentally demonstrate a > 12dB improvement in displacement sensitivity. Open quantum systems and the ability to coherently couple them through an active drive thus affords unique possibilities that can be harnessed for higher sensing precision and bandwidth.

This chapter will be submitted for peer-review with requisite modifications as *Back-action evading measurements of two quadratures using a parametric coupling, by Y. S. Patil, S. Chakram and M. Vengalattore*. In this work, Y. S. Patil and S. Chakram performed the calculations and the modeling. M. Vengalattore supervised all stages of the work. All authors contributed to the preparation of the manuscript.

7.2 Abstract

Single-mode optomechanics probed with backaction evading (BAE) measurements allows for detection sensitivities of one mechanical quadrature that are beyond the limits set by quantum mechanics, at the expense of amplifying an unmeasured orthogonal quadrature. By using a parametric coupling between resonators, in conjunction with a two-tone BAE measurement scheme, we show that a quantum nondemolition measurement of two (or more) quadratures can be achieved simultaneously. We explicitly consider such a scheme for two parametrically coupled modes of a resonator probed by a Fabry-Perot cavity, and consider the practicalities of the BAE measurement. Finally, we show that the scheme is robust to experimental parameters, and does not require any fine-tuning to achieve backaction evasion.

7.3 Introduction

There has been a tremendous push over the last decade to observe quantum effects in micro and nano mechanical systems. The technical abilities and measurement precision required for that are being increasingly achieved in a variety of physical systems [78]. That the compromise between the measurement strength required for such precision and its concomitant backaction leads to the standard quantum limit (SQL), is now well accepted [174, 173]. In fact, radiation backaction has been experimentally demonstrated [184], albeit not at the quantum limit. Recently, considerable effort has also been invested in developing schemes that surpass the fundamental limits of precision with which such systems can be measured and controlled, limits set by quantum mechan-

150

ics. These schemes are necessarily based on reducing or avoiding backaction [175, 99, 176], or on backaction cancellation [177, 179, 178, 180]. The detection sensitivities thusly achievable, coupled with recent advances in optomechanical cooling [87, 88], reservoir engineering [108, 185, 150], and realizing hybrid quantum systems have opened the floodgates to precision studies of macroscopic entanglement [186, 187, 188, 189, 190], nonequilibrium dynamics [191, 192], quantum-to-classical transitions [193, 194, 195] and quantum-enhanced metrology [76, 100, 83].

Most of the above schemes, however, are restricted to the measurement of one quadrature of the system under consideration. Here, we propose to couple orthogonal quadratures of a perturbation to two distinctly addressable modes of the same resonator. We show that by introducing an active parametric coupling between two quadratures of these modes, the backaction evading (BAE) measurement of one allows for a quantum nondemolition (QND) measurement of *both* quadratures. This enables both their detection sensitivities to go below the quantum zero-point limits [178].

The details that follow demonstrate the robust realization of a BAE measurement of two quadratures by parametrically coupling them. The paper is organized as follows. In Section 7.4, we describe the scheme. In Section 7.5, we consider the practical limits to the two-tone backaction evasion in the presence of a parametric coupling. Sections 7.6 - 7.7 describe the requisite parameter space for beyond-SQL sensing, concluding with possible extensions of the scheme. Detailed calculations have been relegated to the Supplementary Information.

7.4 Scheme

We consider an experimental setup of a mechanical resonator with two modes of interest. These modes are coupled to each other through an active parametric coupling. The parametric coupling strength between the modes depends on the amplitude of the parametric drive. The motion of both mechanical modes is coupled to light in a single-mode Fabry-Perot cavity, through the standard dispersive optomechanical coupling. This light is used to probe the modes' motion through homodyne detection. Such a system is described by the Hamiltonian

$$\hat{H} = \hat{H}_{cav} + \hat{H}_{mech} + \hat{H}_{om} \tag{7.1}$$

Here, the mechanics is captured by

$$\hat{H}_{mech} = \hbar\omega_i \hat{b}_i^\dagger \hat{b}_i + \hbar\omega_j \hat{b}_j^\dagger \hat{b}_j + \hat{H}_{\gamma_i} + \hat{H}_{\gamma_j} - \hbar g x_S \hat{x}_i \hat{x}_j \tag{7.2}$$

where $\omega_{i,j}$ is the mechanical frequency of modes (i, j), $\hat{x}_{i,j} = x_{i,j,zpt}(\hat{b}_{i,j} + \hat{b}_{i,j}^\dagger)$ describe the motion of modes, $x_{i,j,zpt} = \sqrt{\frac{\hbar}{2m_{i,j}\omega_{i,j}}}$ denote their respective zero-point motion, and $\hat{H}_{\gamma_i,\gamma_j}$ capture their mechanical damping. Importantly, the last term captures the active parametric coupling of the two mechanical modes through a classical excitation

$$x_S(t) = \bar{x}_S \sin[(\omega_i + \omega_j)t + \phi_p] \tag{7.3}$$

as demonstrated in [150]. Without loss of generality, we set $\phi_p = 0$. The single-mode optical cavity is captured by

$$\hat{H}_{cav} = \hbar\omega_c[\hat{a}^\dagger \hat{a} - \langle \hat{a}^\dagger \hat{a} \rangle] + \hat{H}_{drive} + \hat{H}_\kappa \tag{7.4}$$

where ω_c is the cavity resonance frequency, $\hat{a}$ describes the intracavity field, and $\hat{H}_{drive}$ and $\hat{H}_\kappa$ capture the external cavity drive and cavity losses respectively, with κ denoting the cavity linewidth. Note that we have set the energy-zero of

the cavity to be at $\hbar\omega_c\langle\hat{a}^\dagger\hat{a}\rangle$. The optomechanical interaction is captured by

$$\hat{H}_{om} = -\hbar G_i\hat{x}_i[\hat{a}^\dagger\hat{a} - \langle\hat{a}^\dagger\hat{a}\rangle] - \hbar G_j\hat{x}_j[\hat{a}^\dagger\hat{a} - \langle\hat{a}^\dagger\hat{a}\rangle] \tag{7.5}$$

This optomechanical coupling is dispersive for both modes (i, j), and we retain different coupling strengths for them, $G_{i,j}$. We subtract the static shift in the resonator position to get the above equation.

Our objective is to use this system to make a BAE measurement of two quadratures of an applied perturbation. If such a perturbation couples to both modes of the resonator considered above, we can probe both these modes to deduce the applied perturbation. Two mechanical modes are characterized by *four* independent quadratures. To implement a backaction evading measurement of two of them, the measurement should couple to at most two of these four quadratures. This allows for the resultant measurement backaction to be only on the unmeasured conjugate quadratures. The system considered above realizes a BAE measurement of two quadratures under the simultaneous influence of a cavity drive at the mechanical sidebands of mode i at $\omega_c \pm \omega_i$ and a nonzero parametric coupling between the two mechanical modes. This is readily seen through the Heisenberg-Langevin equations of motion (see Supplementary Information, Section 7.9.1),

$$\dot{\hat{\mathbf{Z}}} = \mathbf{M}\hat{\mathbf{Z}} + \hat{\mathbf{v}} + \hat{\mathbf{F}}_{BA}, \tag{7.6}$$

$$\begin{pmatrix} \dot{\hat{X}}_i \\ \dot{\hat{X}}_j \\ \dot{\hat{Y}}_i \\ \dot{\hat{Y}}_j \end{pmatrix} = \begin{pmatrix} -\gamma_i/2 & -G_{par} & 0 & 0 \\ -G_{par} & -\gamma_j/2 & 0 & 0 \\ 0 & 0 & -\gamma_i/2 & G_{par} \\ 0 & 0 & G_{par} & -\gamma_j/2 \end{pmatrix} \begin{pmatrix} \hat{X}_i \\ \hat{X}_j \\ \hat{Y}_i \\ \hat{Y}_j \end{pmatrix} + \begin{pmatrix} \hat{v}_{X,i} \\ \hat{v}_{X,j} \\ \hat{v}_{Y,i} \\ \hat{v}_{Y,j} \end{pmatrix} + \hat{\mathbf{F}}_{BA} \tag{7.7}$$

where $\hat{\mathbf{Z}} = (\hat{X}_i, \hat{X}_j, \hat{Y}_i, \hat{Y}_j)^T$ is the quadrature vector, $\hat{\mathbf{v}} = (\hat{v}_{X,i}, \hat{v}_{X,j}, \hat{v}_{Y,i}, \hat{v}_{Y,j})^T$ describes the mechanical modes' Langevin noise baths, $\mathbf{M}$ is the evolution matrix, $G_{par} = g\frac{\bar{x}_S}{2}x_{i,zpt}x_{j,zpt}$ parametrizes the parametric coupling between the modes,

and $\hat{\mathbf{F}}_{BA}$ captures the measurement backaction.

Measurement of the $\hat{X}_i$ quadrature is achieved through the described two-tone drive [174, 54, 196]. Because $\hat{X}_i$ and $\hat{X}_j$ are dynamically linked, this measurement constitutes a measurement of the $\hat{X}_j$ quadrature as well. Neither of these quadratures dynamically couple to their conjugates $\hat{Y}_i$ or $\hat{Y}_j$, which reside in an exclusive subspace. Due to this, and because equally importantly the cavity field couples only to $\hat{X}_i$, and not any other mechanical quadrature, the backaction on the mechanical modes due to the cavity light is restricted to $\hat{Y}_i$, the quadrature conjugate to $\hat{X}_i$, The backaction is given by (see Supplementary Information, Section 7.9.3)

$$\hat{\mathbf{F}}_{BA} = (0, 0, 2G_{i,BA}\hat{X}_c, 0)^T \tag{7.8}$$

where $G_{i,BA}$ parametrizes the backaction coupling between $\hat{X}_i$ and $\hat{Y}_i$, and $\hat{X}_c$ is the X-quadrature of the cavity light. Because of the dynamic coupling between $\hat{Y}_i$ and $\hat{Y}_j$, the measurement of $\hat{X}_i$ has an indirect backaction on $\hat{Y}_j$. However, these backactions do not couple back to the measured observables $\hat{X}_{i,j}$ Eqn. (7.7). This allows for the BAE and QND measurement of *two* quadratures of the mechanical modes – $\hat{X}_i$ and $\hat{X}_j$. Note that the system thus realizes a quantum-mechanics-free-subspace as formulated by Tsang and Caves [182].

Distinct schemes describing the BAE or weak measurement of two cross-quadratures of two mechanical modes have been previously considered [197, 198]. However, such schemes pose challenges as described therein – the requisite matched frequency-, dissipation- and optomechanical-coupling- asymmetries are nontrivial to achieve experimentally. In contrast, the above scheme is BAE for any nonzero parametric coupling between any two mechanical modes and is robust to both dissipation asymmetries ($\gamma_i \neq \gamma_j$) and optomechanical cou-

pling asymmetries ($G_i \neq G_j$).

7.5 Residual backaction

In this section, we thoroughly consider the degradation of BAE due to a finite cavity linewidth and due to the parametric coupling. In the ideal limit of a good cavity ($\kappa/\omega_{i,j} \to 0, \kappa/|\omega_j - \omega_i| \to 0$) there is no backaction on either $\hat{X}_i$ or $\hat{X}_j$. This dependence on κ is most readily understood through the optomechanical coupling term in the Hamiltonian Eqn. (7.32). Averaged over several oscillation periods, the cavity field $\hat{X}_c$ does not measure $\hat{Y}_i$. If there exist any field-fluctuations at the frequency $2\omega_i$, the cavity field *does* couple to $\hat{Y}_i$, thereby inducing backaction on the conjugate observable $\hat{X}_i$, degrading the backaction evasion. Secondly, because of the dynamic coupling between $\hat{X}_i$ and $\hat{X}_j$ Eqn. (7.7), fluctuations of the latter introduce noise in the former. Both these noise terms which degrade the BAE can be read off the noise spectral densities given by (see Supplementary Information Section 7.9.2)

$$S_{X_i}(\omega) = \frac{1}{2} \int_{-\infty}^{\infty} dt e^{i\omega t} \langle \{\hat{X}_i(t), \hat{X}_i(0)\} \rangle = \langle \hat{X}_i^\dagger(\omega) \hat{X}_i(\omega) \rangle$$

$$= \frac{\frac{\gamma_i/2}{\omega^2 + (\gamma_i/2)^2}[(1 + 2n_{eq,i} + 2n_{bad,i}) + \frac{(\gamma_j/2)^2}{\omega^2 + (\gamma_j/2)^2}\mu^2(1 + 2n_{eq,j} + 2n_{bad,j})]}{\left| 1 - \frac{1}{1 - i\frac{2\omega}{\gamma_i}} \frac{1}{1 + i\frac{2\omega}{\gamma_j}} \mu^2 \right|^2} \tag{7.9}$$

$$S_{Y_i}(\omega) = \frac{1}{2} \int_{-\infty}^{\infty} dt e^{i\omega t} \langle \{\hat{Y}_i(t), \hat{Y}_i(0)\} \rangle = \langle \hat{Y}_i^\dagger(\omega) \hat{Y}_i(\omega) \rangle$$

$$= \frac{\frac{\gamma_i/2}{\omega^2 + (\gamma_i/2)^2}[(1 + 2n_{eq,i} + 2n_{BA,i} + 2n_{bad,i}) + \frac{(\gamma_j/2)^2}{\omega^2 + (\gamma_j/2)^2}\mu^2(1 + 2n_{eq,j} + 2n_{bad,j})]}{\left| 1 - \frac{1}{1 + i\frac{2\omega}{\gamma_i}} \frac{1}{1 - i\frac{2\omega}{\gamma_j}} \mu^2 \right|^2}$$

$$\tag{7.10}$$

where $\hat{X}_i(\omega)$, $\hat{Y}_i(\omega)$ are the Fourier components of the quadrature operators. μ is the parametric drive x_S normalized to the parametric instability threshold [83],

$$\mu = \frac{x_S}{x_{S,th}}, \quad x_{S,th} = \frac{2}{g\hbar} \sqrt{m_i \omega_i \gamma_i} \sqrt{m_j \omega_j \gamma_j} \tag{7.11}$$

In the limit $\mu = 0$, these noise spectra reduce to those of [183], as expected. It is for $\mu \neq 0$ that we realize the BAE scheme for two quadratures.

$$n_{eq,i,j} = \left(\exp\left[\frac{\hbar \omega_{i,j}}{k_B T} \right] - 1 \right)^{-1} \tag{7.12}$$

is the equilibrium phonon occupancy of the mechanical modes (i, j) at the surrounding bath temperature T, and

$$n_{BA,i} = 2 \frac{G_i^2 x_{i,zpt}^2}{\kappa \gamma_i} \bar{a}_{max}^2 := \frac{8 \, G_{i,BA}^2}{\kappa \gamma_i} \tag{7.13}$$

both captures the $\hat{X}_i-$measurement backaction on $\hat{Y}_i$ and parametrizes the measurement strength based on the light intensity used.

$$n_{bad,i} = \frac{n_{BA,i}}{8} \left(\frac{\kappa}{2\omega_i} \right)^2 \frac{1}{1 + \frac{\kappa^2}{4(2\omega_i)^2}} \tag{7.14}$$

parametrizes, in phonon number, the residual backaction on $\hat{X}_i$ because of the cavity being 'bad', i.e. $\kappa/\omega_i \neq 0$.

Corresponding terms for the backaction on $\hat{Y}_j$ and $\hat{X}_j$ are given by

$$n_{BA,j} = 2 \frac{G_j^2 x_{j,zpt}^2}{\kappa \gamma_j} \bar{a}_{max}^2 := \frac{8 G_{j,BA}^2}{\kappa \gamma_j} \tag{7.15}$$

$$n_{bad,j} = \frac{n_{BA,j}}{8} \left[\left(\frac{\kappa}{\omega_i + \omega_j} \right)^2 \frac{1}{1 + \frac{\kappa^2}{4(\omega_i+\omega_j)^2}} + \left(\frac{\kappa}{\omega_j - \omega_i} \right)^2 \frac{1}{1 + \frac{\kappa^2}{4(\omega_j-\omega_i)^2}} \right] \tag{7.16}$$

Eqn.s (7.14,7.16) show that the residual backaction is minimized for $\kappa/\omega_i \ll 1$ and $\kappa/|\omega_j - \omega_i| \ll 1$. Both these conditions are accessible by current experiments – the former is a prerequisite for optomechanical cooling to the quantum regime that is increasingly being achieved for a variety of optomechanical systems, and the latter is also experimentally accessible, as demonstrated in [150]. Intuitively, the latter condition disallows the formation of cavity sidebands at $\omega_c \pm \omega_j$, which would otherwise measure both $\hat{X}_j$ and $\hat{Y}_j$, thereby preventing

backaction evasion. As the cavity field does not directly couple to $\hat{X}_j$, there is no direct backaction on $\hat{Y}_j$. A residual backaction due to the nonideal cavity however persists, even for mode j.

Another approach to alleviate the residual backaction on mode j is to make its optomechanical coupling

$$G_j \to 0 \tag{7.17}$$

In this case, both $n_{BA,j} \to 0$ and $n_{bad,j} \to 0$, cf. Eqn.s (7.15,7.16). Such a zero coupling to mode j can be achieved by having the cavity spatial mode overlap with a node of mode j, while still retaining a substantial coupling to mode i. The hybridization of proximal and nominally degenerate modes of a SiN square membrane resonator into orthogonal modes shown in [79] ensures that a maximal coupling to one mode implies a minimal coupling to the other, because of the modes' orthogonality. In this sense, $\kappa/|\omega_j - \omega_i| \ll 1$ is not a necessary requirement to achieve the BAE nature of the proposed scheme.

7.6 Beyond SQL

To compare the sensitivity of measurement realized in such a scheme with the SQL, we consider the measured mechanical noise spectrum, $S_{X_i,m}(\omega)$. $S_{X_i,m}(\omega)$ is measured through the cavity output spectrum at ω_c within a bandwidth κ. Assuming a single sided cavity with a shot noise limited drive, the homodyne detected spectrum equates to [183]

$$S_{X_i,m}(\omega) = S_{X_i}(\omega) + \frac{\kappa}{32\,G_{i,BA}^2} \tag{7.18}$$

The noise added in the measurement of $\hat{X}_i$ due to residual backaction and coupling to mode j is evaluated in comparison to the added noise at the SQL (L_{SQL})

as

$$\frac{L_i(\omega,\mu,n_{BA,i})}{L_{i,SQL}(\omega)} = \frac{(1 + 2n_{bad,i}) + \frac{(\gamma_j/2)^2}{\omega^2+(\gamma_j/2)^2}\mu^2(1 + 2n_{bad,j})}{\left|1 - \frac{1}{1-i\frac{2\omega}{\gamma_i}}\frac{1}{1+i\frac{2\omega}{\gamma_j}}\mu^2\right|^2} - 1 + \frac{1}{8n_{BA,i}}\frac{\omega^2 + (\gamma_i/2)^2}{(\gamma_i/2)^2} \quad (7.19)$$

where we have set $n_{eq,i,j} = 0$ to get to the SQL, and

$$L_{i,j,SQL}(\omega) = \frac{\gamma_{i,j}/2}{\omega^2 + (\gamma_{i,j}/2)^2} \quad (7.20)$$

is the measurement noise at the SQL. For an ideal cavity, the backaction noise goes to zero, i.e. $n_{bad,i,j} \to 0$. The imprecision noise ($\propto 1/n_{BA,i}$) can also be made to go to zero by using higher intensity of light. The measurement noise is then only limited by the quantum motion of the two modes. A larger coupling to mode j, and in particular to its quantum fluctuations, leads to a larger noise in $\hat{X}_i$. These quantum motions are also amplified by the parametric drive, limiting the permissible coupling strength between the modes for realizing sub-SQL sensing.

Fig. 7.1 illustrates the typical parameter space over which the SQL is beaten. As seen in Fig. 7.1(b), the quantum motion of mode j leads to an increased noise in $S_{X_i,m}$ at $\omega = 0$, concentrated within a bandwidth γ_j. For a fixed parametric coupling G_{par}, this noise can be spread out over a larger bandwidth by using larger γ_j, thereby effecting an improved sensitivity at $\omega = 0$ – see Fig. 7.2. As such, even in the presence of a parametric coupling, sub-SQL sensitivity can be achieved beyond a measurement strength of $n_{BA,i} \approx \frac{1}{8}$. The backaction evasion and sub-SQL measurement sensitivity remain robust over a large range of parametric coupling strengths and measurement bandwidths.
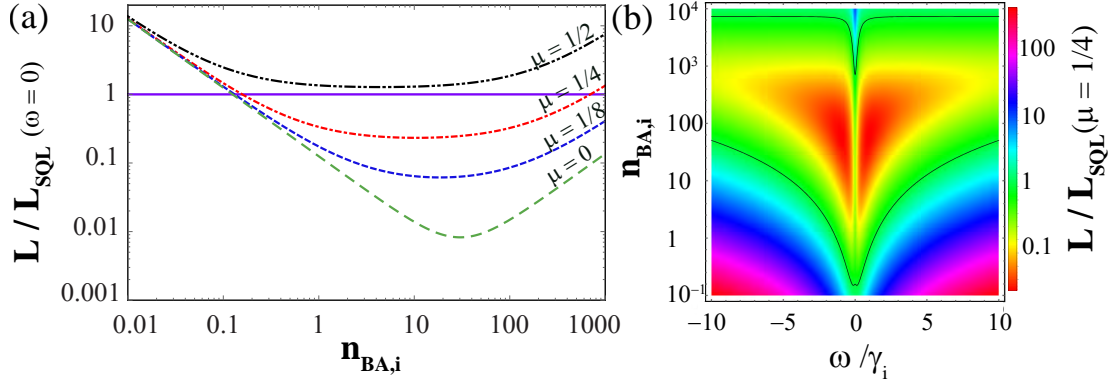
Figure 7.1: Comparison with the SQL, of noise added to the measurement of $\hat{X}_i$ due to residual backaction and coupling to noise of mode j at $T = 0$, cf. Eqn. (7.19). (a) Increased coupling (μ) of mode i to mode j is at the expense of increased measurement noise, caused by quantum fluctuations in the latter, shown here for $\omega = 0$, i.e. on resonance. The horizontal line at 1 denotes the SQL. (b) Larger measurement strengths allow for larger sub-SQL detection bandwidths, shown here for $\mu = 1/4$. The black line denotes the SQL contour. The peak feature at $\omega = 0$ denotes the increased noise, though still sub-SQL, due to the quantum noise of mode j. This noise is concentrated in a bandwidth of γ_j, shown here for $\gamma_j/\gamma_i = 1/4$. Guided by the experimental values of [150], these graphs are evaluated for $\kappa/\omega_{i,j} \approx 0.05$ and $\kappa/(\omega_i - \omega_j) \approx 0.25$.

7.7 Force sensing

Having demonstrated sub-SQL detection sensitivity for $\hat{X}_i$, we now consider if such a system can be used for beyond-SQL sensing of both quadratures of a force. In general, a force couples to motion as an additional term in the Hamiltonian, given by

$$\hat{H}_f = -F(t)\hat{x}_i - F(t)\hat{x}_j$$

$$\Rightarrow \hat{H}_{f,int} = -F(t)x_{i,zpt}(\hat{b}_i e^{-i\omega_i t} + h.c.) - F(t)x_{j,zpt}(\hat{b}_j e^{-i\omega_j t} + h.c.) \qquad (7.21)$$

159
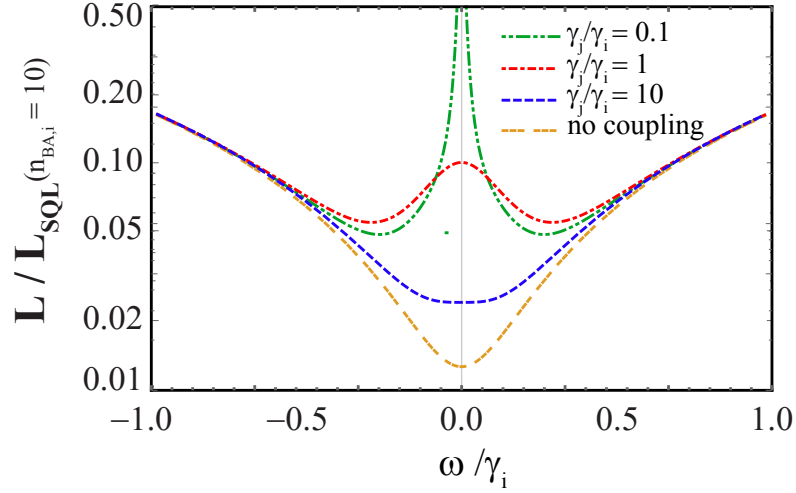
Figure 7.2: Effect of mode j linewidth on the noise added to the measurement of $\hat{X}_i$. The $\gamma_j/\gamma_i = 1$ curve (red) forms the reference. As mode j becomes broader (see $\gamma_j/\gamma_i = 10$, blue), for a constant parametric coupling strength G_{par}, lesser noise is parametrically mixed back to mode i within a given bandwidth around $\omega = 0$. As such, the noise grows lower near $\omega = 0$. Conversely, as mode j becomes narrower (see $\gamma_j/\gamma_i = 0.1$, green), most of the noise gets coupled at $\omega = 0$, driving up the noise there, but correspondingly reducing it at farther frequencies. The no-coupling curve is shown for comparison.

The coupling of this force to our BAE observables $\hat{x}_i$ and $\hat{x}_j$ is $\propto \text{Im}[F(t)e^{-i\omega_i t}]$ and $\text{Im}[F(t)e^{-i\omega_j t}]$ respectively, which can be easily seen as the F−dependent terms in the equation of motion given by $\frac{i}{\hbar}[\hat{H}_{f,int}, \hat{x}_{i,j}]$.

The change in mechanical susceptibility induced by the parametric coupling needs to be accounted for when comparing the sensitivity of this scheme to the SQL. For the proposed scheme, the modified susceptibility is equal or larger than its bare value, and therefore implies a sub-SQL force sensitivity at ω_i. To see this, consider the susceptibilities in the presence of the parametric coupling, which can be read off the spectral density (see Supplementary Information, Sec-

tion 7.9.4)

$$\hat{X}_i(\omega) = \frac{\chi_i(\omega)}{1-\chi_i(\omega)\chi_j(-\omega)G^2_{par}}[\text{Im } F_i](\omega) - \frac{\chi_i(\omega)\chi_j(-\omega)G_{par}}{1-\chi_i(\omega)\chi_j(-\omega)G^2_{par}}[\text{Im } F_j](-\omega) \quad (7.22)$$

where $\chi_{i,j}(\omega)$ are the bare susceptibilities of the modes and $F_{i,j} :=$ $-\frac{\sqrt{2}x_{i,j,zpt}}{\hbar}F(t)e^{i\omega_{i,j}t}$. Clearly, the parametric-coupling modified susceptibility of mode i,

$$\chi_{ii,par}(\omega) = \frac{\chi_i(\omega)}{1-\chi_i(\omega)\chi_j(-\omega)G^2_{par}} \quad (7.23)$$

is larger than its bare susceptibility $\chi_i(\omega)$, enabling sub-SQL detection at ω_i. For a sub-SQL force sensing at ω_j, we correspondingly need

$$\frac{\frac{1}{|\chi_{ij,par}(\omega)|^2}S_{X_i,m}(\omega,\mu,n_{BA,i})}{2\frac{1}{|\chi_j(\omega)|^2}L_{j,SQL}(\omega)} = \left(\frac{\frac{1}{|\chi_{ij,par}(\omega)|^2}}{\frac{1}{|\chi_j(\omega)|^2}}\right)\left[\frac{S_{X_i,m}(\omega,\mu,n_{BA,i})}{2L_{j,SQL}(\omega)}\right] < 1 \quad (7.24)$$

where $\chi_{ij,par}$ is the susceptibility of $\hat{X}_i$ to an actuation at mode j in the presence of the parametric coupling. Even though $\chi_{ij,par}$ diverges as G_{par} approaches the parametric instability, so does the detected noise $S_{X_i,m}(\omega,\mu,n_{BA,i})$, due to parametric amplification of quantum noise. In the ideal cavity and strong measurement limit, Eqn. (7.24) reduces to $\mu^2 > 1 + \frac{4\omega^2}{\gamma_j^2}$. The best sensitivity achievable at ω_j is thus the SQL, achieved as $\mu \to 1$ – there is a compromise between an increased susceptibility and increased noise for force sensing at ω_j. The sensitivity at ω_j being clamped at the SQL is distinct from the usual SQL – Here, the limit arises because of the quantum fluctuations of the modes, and *not* due to a measurement backaction. The backaction is still being evaded.

Such a scheme can be employed to detect both quadratures of a force. In the above, both $\hat{x}_i$ and $\hat{x}_j$ couple to the same quadrature of the applied force. However, by changing the phase of the parametric coupling drive Eqn. (7.3), any quadrature of mode j can be made to replace $\hat{X}_j$, and its corresponding orthogonal quadrature to replace $\hat{Y}_j$. In particular, a change of phase by $\pi/2$ would couple $\hat{Y}_j$ to $\hat{X}_i$, and because $\hat{Y}_j$ couples to Re F, the system is now coupled

to both quadratures of the force. This enables the BAE measurement of *both* quadratures of the force.

The above analysis does not account for the projection or conditional squeezing caused by the measurement. With an increasing measurement strength on $\hat{X}_i$, this projection would indeed cause the detection noise to go below the quantum zero-point limit [183, 199]. This would enable the beyond-SQL detection of both quadratures of the applied force for a well realized BAE measurement.

7.8   Conclusions

We propose a scheme to avoid measurement backaction on two of four quadratures of two modes of a mechanical resonator. This is achieved through a two-tone driven-cavity measurement of one of the modes, and a parametric coupling of the two mechanical modes. We demonstrate the robustness and experimental amenability of BAE using this scheme, with parameters accessible by current experiments. We explicitly calculate the requisite measurement strength and coupling parameters for beating the SQL, and thoroughly consider the effects of quantum noise of the mechanical modes on sub-SQL sensing. When coupled to two quadratures of an applied perturbation, this readily realizes a scheme for beyond-SQL sensing through the BAE of two quadratures.

The nonlinear coupling between resonators used in this work has been previously shown to be ubiquitous and robust. Parametric couplings between distinct modes of the same resonator [150], a nanomechanical resonator and a transmission line resonator, or two distinct electrical resonators [200], can all be achieved in the quantum regime. By introducing additional parametric cou-

plings between the resonators, the backaction evasion can be extended to include more than two observables, so long as the BAE nature of the measurement is preserved with additional constraints like Eqn.s (7.16, 7.17). This allows for the generalization of the scheme to larger quantum-mechanics-free-subspaces and larger sets of observables.

7.9 Supplementary Information

7.9.1 Equations of motion

We drive the cavity with a symmetric two-tone classical drive at the mechanical sidebands of mode i at $\omega_c \pm \omega_i$, which leads to an amplitude modulated drive. Working in the Heisenberg picture, $\hat{H}_{drive} = \hat{d}_{in}(t)$, with

$$\langle \hat{d}_{in}(t) \rangle := \bar{d}_{in}(t) = \frac{\bar{d}}{2} \sin(\omega_i t) e^{-i\omega_c t} \tag{7.25}$$

We drive the cavity sufficiently hard that we can linearize the optomechanical coupling, as is the case experimentally. As such, we split the cavity field as a steady state classical occupation and quantum fluctuations –

$$\hat{a}(t) = \bar{a}(t) + \hat{\delta a}(t) \tag{7.26}$$

where $\bar{a}(t)$ is determined completely by the cavity response to $\hat{H}_{drive}$ as

$$\bar{a}(t) = \bar{a}_{max} \cos(\omega_i t + \delta) e^{-i\omega_c t} \tag{7.27}$$

where

$$\bar{a}_{max} = \bar{d} \sqrt{\frac{\kappa}{4\omega_i^2 + \kappa^2}} \gg 1 \tag{7.28}$$

$$\delta = \arctan(\kappa/\omega_i) \tag{7.29}$$

with ω_i entering the picture simply because we are driving the cavity at that detuning. δ sets the zero of the reference phase and as such, without loss of generality, we set it to 0. Retaining terms to first order in $\bar{a}_{max}$

$$[\hat{a}^\dagger \hat{a} - \langle \hat{a}^\dagger \hat{a} \rangle] = \bar{a}^*(t)\hat{\delta a}(t) + \bar{a}(t)\hat{\delta a}^\dagger(t) = \bar{a}_{max}\cos(\omega_i t)[e^{i\omega_c t}\hat{\delta a}(t) + e^{-i\omega_c t}\hat{\delta a}^\dagger(t)] \quad (7.30)$$

The linearized interaction Hamiltonian with respect to $\hat{H}_0 = \hbar\omega_c \hat{a}^\dagger \hat{a} + \hbar\omega_i \hat{b}_i^\dagger \hat{b}_i + \hbar\omega_j \hat{b}_j^\dagger \hat{b}_j$ thus takes the form

$$\begin{aligned}
\hat{H}_{int} = & - \hbar G_i x_{i,zpt}(\hat{b}_i e^{-i\omega_i t} + \hat{b}_i^\dagger e^{i\omega_i t}) \times \bar{a}_{max}\cos(\omega_i t)[\hat{\delta a}(t) + \hat{\delta a}^\dagger(t)] \\
& - \hbar G_j x_{j,zpt}(\hat{b}_j e^{-i\omega_j t} + \hat{b}_j^\dagger e^{i\omega_j t}) \times \bar{a}_{max}\cos(\omega_i t)[\hat{\delta a}(t) + \hat{\delta a}^\dagger(t)] \\
& + \hat{H}_{\gamma i,int} + \hat{H}_{\gamma j,int} + \hat{H}_{\kappa,int} \\
& - \hbar g \bar{x}_S x_{i,zpt} x_{j,zpt}(\hat{b}_i e^{-i\omega_i t} + \hat{b}_i^\dagger e^{i\omega_i t}) \times (\hat{b}_j e^{-i\omega_j t} + \hat{b}_j^\dagger e^{i\omega_j t})\sin[(\omega_i + \omega_j)t] \quad (7.31)
\end{aligned}$$

which reduces to

$$\begin{aligned}
\hat{H}_{int} = & - \hbar G_{i,BA} \times [\hat{X}_i(1 + \cos[2\omega_i t]) + \hat{Y}_i \sin[2\omega_i t]][\hat{\delta a}(t) + \hat{\delta a}^\dagger(t)] \\
& - \hbar G_{j,BA} \times [\hat{X}_j(\cos[(\omega_i + \omega_j)t] + \cos[(\omega_j - \omega_i)t]) \\
& + \hat{Y}_j(\sin[(\omega_i + \omega_j)t] + \sin[(\omega_j - \omega_i)t])][\hat{\delta a}(t) + \hat{\delta a}^\dagger(t)] \\
& + \hat{H}_{\gamma i,int} + \hat{H}_{\gamma j,int} + \hat{H}_{\kappa,int} \\
& + \hbar G_{par}[i\hat{b}_i\hat{b}_j(1 - e^{-2i(\omega_i+\omega_j)t}) + h.c. + i\hat{b}_i\hat{b}_j^\dagger(e^{2i\omega_j t} - e^{-2i\omega_i t}) + h.c.] \quad (7.32)
\end{aligned}$$

where

$$\hat{X}_{i,j} = \frac{\hat{b}_{i,j} + \hat{b}_{i,j}^\dagger}{\sqrt{2}}, \ \hat{Y}_{i,j} = -i\frac{\hat{b}_{i,j} - \hat{b}_{i,j}^\dagger}{\sqrt{2}} \quad (7.33)$$

are the $x-$ and $y-$ quadratures of motion of the two mechanical modes, i.e.

$$\hat{x}_{i,j}(t) = \sqrt{2}x_{i,j,zpt}\left(\hat{X}_{i,j}(t)\cos\omega_{i,j}t + \hat{Y}_{i,j}(t)\sin\omega_{i,j}t\right) \quad (7.34)$$

and the parametric coupling between the mechanical modes is parametrized by

$$G_{par} = g\frac{\bar{x}_S}{2}x_{i,zpt}x_{j,zpt} = \frac{\mu}{2}\sqrt{\gamma_i \gamma_j} \quad (7.35)$$

with μ as defined in Eqn. (7.11). The Heisenberg equations of motion are thus

$$\dot{\hat{\delta a}} = -\frac{\kappa}{2}\hat{\delta a} - \sqrt{\kappa}\hat{\xi}(t)e^{-i\omega_c t} + iG_{i,BA}[\hat{b}_i(1 + e^{-2i\omega_i t}) + h.c.]$$

$$+ iG_{j,BA}[\hat{b}_j(e^{-i(\omega_i+\omega_j)t} + e^{i(\omega_i-\omega_j)t}) + h.c.] \tag{7.36}$$

$$\dot{\hat{b}}_i = -\frac{\gamma_i}{2}\hat{b}_i - \sqrt{\gamma_i}\hat{\eta}_i(t)e^{-i\omega_i t} + iG_{i,BA}(1 + e^{i2\omega_i t})[\hat{\delta a}(t) + \hat{\delta a}^\dagger(t)]$$

$$- G_{par}[\hat{b}_j^\dagger(1 - e^{i2(\omega_i+\omega_j)t}) + \hat{b}_j(e^{-i2\omega_j t} - e^{i2\omega_i t})] \tag{7.37}$$

$$\dot{\hat{b}}_j = -\frac{\gamma_j}{2}\hat{b}_j - \sqrt{\gamma_j}\hat{\eta}_j(t)e^{-i\omega_j t} + iG_{j,BA}(e^{i(\omega_i+\omega_j)t} + e^{-i(\omega_i-\omega_j)t})[\hat{\delta a}(t) + \hat{\delta a}^\dagger(t)]$$

$$- G_{par}[\hat{b}_i^\dagger(1 - e^{i2(\omega_i+\omega_j)t}) + \hat{b}_i(e^{i2\omega_j t} - e^{-i2\omega_i t})] \tag{7.38}$$

where $\hat{\xi}$ is the noise operator of the cavity drive $\hat{d}_{in}$ Eqn. (7.25). Assuming that the cavity drive is shot noise limited, we have

$$\langle\hat{\xi}(t)\hat{\xi}^\dagger(t')\rangle = \delta(t - t'); \; \langle\hat{\xi}^\dagger(t)\hat{\xi}(t')\rangle = 0 \tag{7.39}$$

Similarly, $\hat{\eta}_{i,j}$ are the noise operators of the thermal baths of modes (i, j) which obey

$$\langle\hat{\eta}(t)\hat{\eta}^\dagger(t')\rangle = (n_{eq,i,j} + 1)\delta(t - t'); \; \langle\hat{\eta}^\dagger(t)\hat{\eta}(t')\rangle = n_{eq,i,j}\delta(t - t') \tag{7.40}$$

in the Markovian limit, where $n_{eq,i,j}$ is the occupancy of the resonator modes $\{i, j\}$ at the bath temperature T, given by Eqn. (7.12).

In Eqn.s (7.36-7.38), we retain the off-resonant rotating terms in order to quantify their role in the degradation of back-action evasion. However, if we only retain the resonant terms, an intuitive picture is more easily got by writing

the equations of motion as

$$\dot{\hat{X}}_c = -\frac{\kappa}{2}\hat{X}_c - \sqrt{\kappa}\hat{X}_c^{in} \tag{7.41}$$

$$\dot{\hat{Y}}_c = -\frac{\kappa}{2}\hat{Y}_c - \sqrt{\kappa}\hat{Y}_c^{in} + 2G_{i,BA}\hat{X}_i \tag{7.42}$$

$$\dot{\hat{X}}_i = -\frac{\gamma_i}{2}\hat{X}_i - \sqrt{\gamma_i}\hat{X}_i^{th} - G_{par}\hat{X}_j \tag{7.43}$$

$$\dot{\hat{Y}}_i = -\frac{\gamma_i}{2}\hat{Y}_i - \sqrt{\gamma_i}\hat{Y}_i^{th} - G_{par}\hat{Y}_j + 2G_{i,BA}\hat{X}_c \tag{7.44}$$

$$\dot{\hat{X}}_j = -\frac{\gamma_j}{2}\hat{X}_j - \sqrt{\gamma_j}\hat{X}_j^{th} - G_{par}\hat{X}_i \tag{7.45}$$

$$\dot{\hat{Y}}_j = -\frac{\gamma_j}{2}\hat{Y}_j - \sqrt{\gamma_j}\hat{Y}_j^{th} - G_{par}\hat{Y}_i \tag{7.46}$$

where $\hat{X}_c^{in}, \hat{Y}_c^{in}$ characterize the input noise to the cavity, and similarly, $\hat{X}_i^{th}, \hat{Y}_i^{th}, \hat{X}_j^{th}, \hat{Y}_j^{th}$ characterize the thermal bath of the resonator modes. The latter four equations are Eqn.s (7.6) – (7.8) of the main text.

7.9.2   Mechanical noise spectrum

Eqn.s (7.36) – (7.38) are readily solved in the Fourier space. Defining the mechanical and cavity susceptibilities

$$\chi_{i,j}(\omega) = \frac{1}{-i\omega + \gamma_{i,j}/2}$$

$$\chi_c(\omega) = \frac{1}{-i\omega + \kappa/2}, \tag{7.47}$$

$$\hat{X}_c(\omega) = \left(\frac{\hat{\delta a} + \hat{\delta a}^\dagger}{\sqrt{2}}\right)(\omega) = -\chi_c(\omega)\sqrt{\frac{\kappa}{2}}\left[\hat{\xi}^\dagger(\omega + \omega_c) + \hat{\xi}(\omega - \omega_c)\right] \tag{7.48}$$

$$\hat{X}_i(\omega) = -\chi_i(\omega)\sqrt{\frac{\gamma_i}{2}}\left(\hat{\eta}_i(\omega+\omega_i) + \hat{\eta}_i^\dagger(\omega-\omega_i)\right)$$

$$+ i\chi_i(\omega)G_{i,BA}\left(\hat{X}_c(\omega-2\omega_i) - \hat{X}_c(\omega+2\omega_i)\right)$$

$$- \chi_i(\omega)G_{par}\left\{\hat{X}_j(-\omega) - \hat{b}_j^\dagger(\omega+2(\omega_i+\omega_j))/\sqrt{2} - \hat{b}_j(\omega-2(\omega_i+\omega_j))/\sqrt{2}\right\}$$

$$- \chi_i(\omega)G_{par}\frac{1}{\sqrt{2}}\left\{-\hat{b}_j(\omega-2\omega_i) + \hat{b}_j(\omega+2\omega_j) - \hat{b}_j^\dagger(\omega+2\omega_i) + \hat{b}_j^\dagger(\omega-2\omega_j)\right\}$$

$$(7.49)$$

$$\hat{Y}_i(\omega) = i\chi_i(\omega)\sqrt{\frac{\gamma_i}{2}}\left(\hat{\eta}_i(\omega+\omega_i) - \hat{\eta}_i^\dagger(\omega-\omega_i)\right)$$

$$+ \chi_i(\omega)G_{i,BA}\left(2\hat{X}_c(\omega) + \hat{X}_c(\omega-2\omega_i) + \hat{X}_c(\omega+2\omega_i)\right)$$

$$+ i\chi_i(\omega)G_{par}\left\{i\hat{Y}_j(-\omega) - \hat{b}_j^\dagger(\omega+2(\omega_i+\omega_j))/\sqrt{2} + \hat{b}_j(\omega-2(\omega_i+\omega_j))/\sqrt{2}\right\}$$

$$+ i\chi_i(\omega)G_{par}\frac{1}{\sqrt{2}}\left\{-\hat{b}_j(\omega-2\omega_i) + \hat{b}_j(\omega+2\omega_j) + \hat{b}_j^\dagger(\omega+2\omega_i) - \hat{b}_j^\dagger(\omega-2\omega_j)\right\}$$

$$(7.50)$$

and similarly the equations for $\hat{X}_j(\omega)$ and $\hat{Y}_j(\omega)$. We simultaneously solve these equations to evaluate the noise spectra $S_{X_{i,j}}(\omega)$ and $S_{Y_{i,j}}(\omega)$ of Eqn.s (7.9, 7.10) using the noise properties given by Eqn.s (7.39, 7.40). In doing so, we approximate contributions from terms of the form $|\chi_i(\omega)|^2 G_{par}^2\langle\hat{b}_j^\dagger(\omega-\Omega)\hat{b}_j(\omega-\Omega)\rangle \approx 0$. These terms signify contributions of the counter-rotating terms to the parametric coupling, which can be made insignificant in the limit $\gamma_i/\omega_i \to 0$ and $|\Omega| > 2\omega_{i,j}$. Given that experimentally, $\gamma_i/\omega_i < 10^{-6}$, this approximation is greatly valid. Note that the fluctuations of x_S, and thus correspondingly of G_{par}, at frequencies $2\omega_i$, $2\omega_j$ and $2(\omega_i + \omega_j)$ couple these terms to the measured observables $\hat{X}_{i,j}(\omega)$. Experimentally, x_S is very well described by a large classical narrowband drive, i.e. $\sigma_{x_S} \ll \bar{x}_S$, and the above approximation rigorously holds.

7.9.3 Backaction

Eqn.s (7.37, 7.38) clearly show that averaged over several oscillator periods, the cavity field $\hat{X}_c$ has a nonzero contribution only to $\dot{\hat{Y}}_i$. I.e. there is no $\hat{X}_c$ dependence of $\dot{\hat{X}}_i$, $\dot{\hat{X}}_j$ or $\dot{\hat{Y}}_j$. This is the Mathematical statement that the cavity measurement has a backaction only on $\hat{Y}_i$, as mentioned in Eqn. (7.8). The backaction coupling coefficient equates to

$$G_{i,BA} = \frac{\bar{a}_{max}}{2} G_i x_{i,zpt} \tag{7.51}$$

We define a corresponding $G_{j,BA}$ for mode j.

$$G_{j,BA} = \frac{\bar{a}_{max}}{2} G_j x_{j,zpt} \tag{7.52}$$

7.9.4 Susceptibility to forces

Here, we calculate the spectrum of $\hat{X}_i$ in the presence of an external force and parametric coupling between the i and j modes. With a force as in Eqn. (7.21), the equations of motion for the modes change from Eqn.s (7.37, 7.38) to

$$\dot{\hat{b}}_i = -\frac{\gamma_i}{2}\hat{b}_i + \frac{i}{\hbar}x_{i,zpt}F(t)e^{i\omega_i t} - G_{par}\hat{b}_j^\dagger$$
$$\dot{\hat{b}}_j = -\frac{\gamma_j}{2}\hat{b}_i + \frac{i}{\hbar}x_{j,zpt}F(t)e^{i\omega_j t} - G_{par}\hat{b}_i^\dagger \tag{7.53}$$

where we have omitted the noise, cavity and off-resonant terms to easily get to the susceptibility. In the Fourier space, these reduce to

$$\hat{X}_{i,j}(\omega) = \chi_{i,j}(\omega) \times -\frac{\sqrt{2}x_{i,j,zpt}}{\hbar}[\text{Im } F(t)e^{i\omega_{i,j}t}](\omega) - \chi_{i,j}(\omega)G_{par}\hat{X}_{j,i}(-\omega) \tag{7.54}$$

Solving these equations simultaneously gives Eqn. (7.22).

APPENDICES

Reproduced below are other works that I contributed substantially to, along with S. Chakram and H. F. H. Cheung. These works further and complement the studies reported in the Chapters above.

APPENDIX A

REPRINT PERMISSIONS

Permissions to reproduce Chapters 2, 3 and 4 in this thesis are attached in the following pages.

Appendix B is licensed under the Creative Commons Attribution 3.0 Unported License. To view a copy of this license, visit creativecommons.org/ licenses/by/3.0/ or send a letter to Creative Commons, PO Box 1866, Mountain View, CA 94042, USA.

26-Mar-2018

This license agreement between the American Physical Society ("APS") and Yogesh Patil ("You") consists of your license details and the terms and conditions provided by the American Physical Society and SciPris.

Request Details

Does your reuse require significant modifications: No

Specify intended distribution locations:	Worldwide
Reuse Category:	Reuse in a thesis/dissertation
Requestor Type:	Author of requested content
Items for Reuse:	Whole Article
Format for Reuse:	Electronic

Information about New Publication:

University/Publisher:	Cornell University
Title of dissertation/thesis:	To be decided
Author(s):	Yogesh Patil
Expected completion date:	May. 2018

License Requestor Information

Name:	Yogesh Patil
Affiliation:	Individual
Email Id:	y@ysspatil.com
Country:	United States

American Physical Society
Reuse and Permissions License
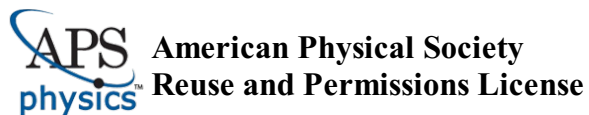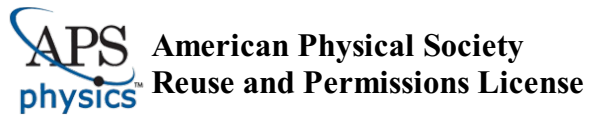
19-Mar-2018

This license agreement between the American Physical Society ("APS") and Yogesh Patil ("You") consists of your license details and the terms and conditions provided by the American Physical Society and SciPris.

<u>**Licensed Content Information**</u>

License Number:	**RNP/18/MAR/002353**
License date:	19-Mar-2018
DOI:	10.1103/PhysRevLett.115.017202
Title:	Thermomechanical Two-Mode Squeezing in an Ultrahigh-Q Membrane Resonator
Author:	Y. S. Patil et al.
Publication:	Physical Review Letters
Publisher:	American Physical Society
Cost:	USD $ 0.00

<u>**Request Details**</u>

Does your reuse require significant modifications: No

Specify intended distribution locations:	Worldwide
Reuse Category:	Reuse in a thesis/dissertation
Requestor Type:	Author of requested content
Items for Reuse:	Figures/Tables
Number of Figure/Tables:	4
Figure/Tables Details:	Figures to be used in dissertation
Format for Reuse:	Electronic

<u>**Information about New Publication:**</u>

University/Publisher:	Cornell University
Title of dissertation/thesis:	To be decided
Author(s):	Yogesh Patil
Expected completion date:	May. 2018

<u>**License Requestor Information**</u>

Name:	Yogesh Patil
Affiliation:	Individual
Email Id:	y@ysspatil.com
Country:	United States

MULTIMODE PHONONIC CORRELATIONS IN A NONDEGENERATE PARAMETRIC AMPLIFIER

This chapter has been previously published as *Multimode phononic correlations in a nondegenerate parametric amplifier, S. Chakram, Y. S. Patil and M. Vengalattore, New Journal of Physics **17**, 063018 (2015).* Reproduced here with permission (see Appendix A), with cosmetic changes. In this work, S. Chakram and Y. S. Patil performed the modeling and the calculations. M. Vengalattore supervised all stages of the work. All authors contributed to the preparation of the manuscript.

B.1 Abstract

We describe the realization of multimode phononic correlations that arise from nonlinear interactions in a mechanical nondegenerate parametric amplifier. The nature of these correlations differs qualitatively depending on the strength of the driving field in relation to the threshold for parametric instability. Below this threshold, the correlations are manifest in a combined quadrature of the coupled mechanical modes. In this regime, the system is amenable to back-action evading measurement schemes for the detection of weak forces. Above threshold, the correlations are manifest in the amplitude difference between the two mechanical modes, akin to intensity difference squeezing observed in optical parametric oscillators. We discuss the crossover of correlations between these two regimes and applications of this quantum-compatible mechanical system

to nonlinear metrology and out-of-equilibrium dynamics.

B.2 Introduction

The quantum control, detection and manipulation of macroscopic mechanical systems has made enormous strides from its origins in the context of gravitational wave detection [174, 173, 201] to current efforts on cavity optomechanics [202, 203, 204, 78, 86] and quantum non-demolition measurements [99, 205, 176, 174, 173]. With increasing sophistication of experimental techniques and material platforms amenable to such studies, a broader range of questions have come into focus including the use of such mesoscopic mechanical systems for studies of macroscopic entanglement [206, 207, 187, 188], out-of-equilibrium thermodynamics [208, 192] and the quantum-to-classical transition [42, 193, 194].

A key enabling ingredient for these studies is the realization of mechanical systems with low dissipation and strong, quantum-compatible nonlinear interactions. While mesoscopic mechanical systems exhibit a wide range of mechanical nonlinearities [115], it is typically the case that such nonlinear effects are weak and only arise at large amplitudes of motion or are present in highly dissipative systems. In either scenario, these preclude quantum-limited operation. Alternately, such nonlinear couplings can also be realized through optical mediation [96, 209]. However, the experimental constraints posed by such optically mediated interactions remain challenging to satisfy.

An alternate avenue to combining low intrinsic dissipation and strong nonlinear interactions exploits the notion of reservoir engineering [105, 106, 107,

108] - the control of the properties and effective interactions of the system through appropriate design of its environment. Most proposals to date have focused on tuning the properties of an optical reservoir that is coupled to the mechanical system via radiation pressure, a coupling that is typically weak in current optomechanical systems. However, reservoir engineering can also be effected through purely mechanical means, i.e. the interactions between distinct modes of a resonator can be mediated and enhanced by discrete excitations of a massive supporting substrate. This has recently been realized experimentally in an ultrahigh Q membrane resonator in [150], where mechanical parametric non-linearities, down-conversion and two-mode thermomechanical noise squeezing is demonstrated in a system compatible with established techniques of radiation pressure cooling to the quantum regime [87, 88] and quantum-limited optical detection [89, 90]. Such non-linear phenomena have also been engineered through a geometric coupling between distinct electromechanical beam resonators [95, 210].

The engineering of strong two-mode parametric nonlinearities in quantum-compatible mechanical resonators [150] has set the stage for the creation of non-classical mechanical states and the manipulation of phononic fields in a manner akin to that in optical parametric amplifiers and oscillators (OPA/OPOs) in quantum optics. In OPA/OPOs, nonclassical correlations between distinct optical fields can be realized at the single photon level as a result of the coherent down-conversion of a high frequency photon into two lower frequency photons. OPA/OPOs have also been used to generate squeezed light [144], demonstrate continuous variable EPR entanglement [211, 212] and have several applications in quantum information [213], communication [214, 215] and metrology [216]. Similarly, the realization of quantum-compatible nonlinear phononic processes

176

in mechanical systems offers rich prospects for studies of nonlinear metrology, the robust generation of entangled mechanical states and the quantum dynamics of mesoscopic mechanical systems.

Apart from realizing mechanical analogs of the phenomena in OPA/OPOs, parametric nonlinear process in quantum-compatible mechanical systems also offer unique opportunities in their own right. Unlike in OPA/OPOs where the intracavity fields can only be indirectly detected, mechanical systems allow for the direct nondestructive detection of their displacement - the phononic analog of the intracavity light field. This allows for novel implementations of interferometric schemes in mechanical systems that surpass the standard quantum limit [217]. Furthermore, the extremely low rates of thermalization realized in these mechanical systems [79] open novel avenues for studies of non-equilibrium physics of open quantum systems. For instance, the parametric two-mode nonlinearity described in this work can be harnessed for studies of critical dynamics and entanglement, and the robust generation of non-gaussian states by appropriate reservoir engineering [218, 219].

Given this range of opportunities, we present a comprehensive description of this two-mode nonlinearity describing various regimes of operation. We emphasize the nature and fidelity of the multimode phononic correlations arising from the nonlinear coupling. While we have focused on nonlinearities that have been engineered through coupling to a reservoir of substrate modes [150], our analysis and the calculated squeezing spectra are also valid for nonlinear interactions engineered through other means [95].

The paper is organized as follows – In section B.3 we describe the two-mode nonlinearity arising from the parametric interaction between the resonator and

its supporting substrate. This interaction realizes a phononic version of a nondegenerate parametric amplifier involving a substrate excitation (pump) and two resonator modes (signal, idler). Such amplifiers are characterized by a threshold pump amplitude beyond which the system is susceptible to self-oscillation. In section B.4 we describe the behavior of this system below threshold. We discuss the onset of two-mode squeezing and calculate the limits of such squeezing in the presence of dissipation, frequency asymmetries and finite pump detuning from parametric resonance. In section B.5, we describe the behavior of this system above threshold where the parametric oscillator exhibits amplitude difference squeezing. Finally, in section B.6 we describe the crossover regime around the instability threshold and applications of this system to nonlinear metrology and mesoscopic quantum dynamics.

B.3 Nondegenerate parametric amplifier: Model and Phenomenology

We begin by describing the phenomenology of the two-mode parametric nonlinearity. To motivate the discussion, we consider the physical system described in previous work [150]. The mechanical resonator consists of a silicon nitride (SiN) membrane under high tensile stress that is deposited on a single-crystal silicon substrate. These membranes are a promising optomechanical platform due to their low optical absorption and ultralow dissipation [220, 221]. Their excellent mechanical properties are due to a combination of high intrinsic stress and substrate-induced suppression of anchor loss. This leads to the robust formation of a large number of mechanical modes with low dissipation and high

degree of isolation from the environment [79]. Furthermore, the supporting substrate can parametrically mediate multimode interactions within the membrane. As shown in [150], such nonlinear interactions are especially significant when the parametric resonance coincides with a discrete excitation of the substrate, as the coupling strength is now enhanced by the quality factor of the mediating excitation (see Fig. B.1).

We describe the parametric two-mode nonlinearity by an interaction of the form $\mathcal{H} = -gX_S x_i x_j$ where g parametrizes the strength of the interaction, X_S is the amplitude of the substrate excitation and $x_{i,j}$ are the amplitudes of the individual membrane resonator modes.

Within the rotating wave approximation, this results in equations of motion of the form,

$$\ddot{x}_i \;+\; \gamma_i \dot{x}_i + \omega_i^2 x_i = \frac{1}{m_i}(F_i(t) + \frac{g}{2}X_S x_j^*)$$

$$\ddot{X}_S \;+\; \gamma_S \dot{X}_S + \omega_S^2 X_S = \frac{1}{M_S}(F_S(t) + \frac{g}{2}x_i x_j)$$

with the corresponding equation for mode j obtained by substituting $i \leftrightarrow j$ in equation (B.1). Here, we have taken $x_{i,j}, X_S$ to denote the (complex) displacements of the individual modes. The external actuating force and thermomechanical noise forces acting on the various modes are together represented by $F_{i,j,S}$, and $\omega_{i,j,S}$, $\gamma_{i,j,S}$ and $m_{i,j,S}$ are the eigenfrequencies, mechanical linewidths and the masses of the modes. For now, we assume that $\omega_S = \omega_i + \omega_j$, i.e. the pump actuation is at the parametric resonance. Lastly, in keeping with the experimental scenario, we assume that the dissipation rate of the substrate excitation is significantly larger than that of the membrane modes ($Q_S = \omega_S/\gamma_S \sim 10^3 - 10^4$, $Q_{i,j} = \omega_{i,j}/\gamma_{i,j} \sim 10^7$).
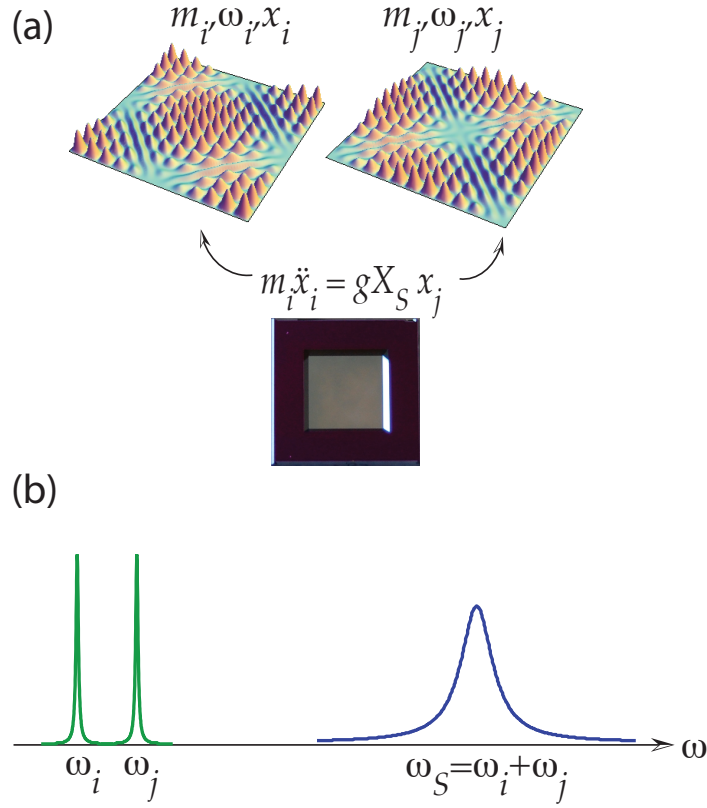
Figure B.1: (a) Distinct eigenmodes of the membrane resonator are coupled through parametric excitation of the supporting substrate. (b) The strength of the two-mode interaction is enhanced when the parametric interaction between membrane eigenmodes at $\omega_{i,j}$ is mediated by a substrate excitation at $\omega_S = \omega_i + \omega_j$.

The coupled equations of motion can be solved using the methods of two timescale perturbation theory [115]. This gives first order coupled equations of the form,

$$2\dot{A}_i = \gamma_i\left[-A_i + i\frac{g}{2}\chi_i A_j^* A_S + i\chi_i \tilde{F}_i(t)\right]$$

$$2\dot{A}_j = \gamma_j\left[-A_j + i\frac{g}{2}\chi_j A_i^* A_S + i\chi_j \tilde{F}_j(t)\right]$$

$$2\dot{A}_S = \gamma_S\left[-A_S + i\frac{g}{2}\chi_S A_i A_j + i\chi_S \tilde{F}_S(t)\right]$$

where $x_k = A_k e^{-i\omega_k t}$, $k \in [i, j, S]$. Also, $\tilde{F}_k$, $k \in [i, j, S]$ are the slowly varying

(complex) amplitudes of the external forces on the individual modes, and $\chi_k = (m_k \omega_k \gamma_k)^{-1}$ are the magnitudes of the on-resonant susceptibility of the various modes. We have ignored terms such as $\ddot{A}_k, \gamma_i \dot{A}_k$ in the slow time approximation.

As the actuating force on the substrate is increased from zero, the substrate (pump) displacement increases in linear proportion until it reaches a threshold amplitude

$$|A_{S,cr}| = \chi_S \tilde{F}_{S,cr} \quad = \quad \frac{2}{g \sqrt{\chi_i \chi_j}} \propto \sqrt{\frac{1}{Q_i Q_j}}$$

Below this critical amplitude, the steady-state amplitudes of the membrane modes (signal, idler), denoted by $\bar{A}_{i,j}$, remain at zero and the system realizes a nondegenerate parametric amplifier. Once the parametric drive exceeds the critical value, the membrane modes exhibit an instability to self-oscillation with $\bar{A}_{i,j} \neq 0$, and the system realizes a phononic version of an optical parametric oscillator. At the threshold, the system is characterized by a divergent mechanical susceptibility and response time. The behavior of the parametric system in the vicinity of this threshold can be described in terms of a nonequilibrium continuous phase transition.

As can be seen from the above expression, the two-mode coupling is enhanced by the quality factors of the individual resonator modes, resulting in strong multimode interaction strengths even in the presence of low dissipation.

As the pump actuation is further increased, the substrate amplitude remains at the threshold value while the signal and idler amplitudes grow as

$$|\bar{A}_{i,j}| = \frac{2}{g \sqrt{\chi_{j,i} \chi_S}} \sqrt{\mu - 1} \tag{B.1}$$

This behavior of the pump, signal and idler mode amplitudes as a function of the normalized drive, $\mu = \frac{|F_S|}{|F_{S,cr}|}$ is shown in Fig. B.2.
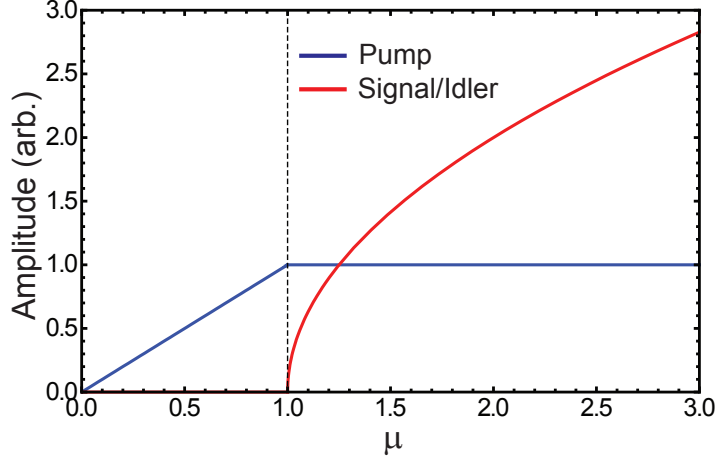
Figure B.2: Pump (blue) and Signal/Idler (red) amplitudes as a function of the normalized parametric drive, $\mu = \frac{|F_S|}{|F_{S,cr}|}$.

This parametric process can be viewed as the down-conversion of one phonon from the pump mode to a pair of phonons, one in each of the signal and idler modes. At the quantum limit, this results in the entanglement of motion of these modes. In the classical regime, this down-conversion is manifest as correlations in the mechanical motion of the two modes. Below threshold, the nonlinear interaction realizes a parametric amplifier with a gain that is dependent on the relation between the phases of the resonator modes and that of the pump. This phase-dependent gain results in thermomechanical squeezing of composite quadratures formed from linear combinations of the quadratures of the individual mechanical modes [150, 95].

Above threshold, the rate of phonon down-conversion exceeds the intrinsic loss from either resonator mode, leading to self-oscillation. In this regime, the correlated production of down-converted phonons manifests as a reduction in the variance (squeezing) of the difference in the amplitude fluctuations of the signal and idler modes. This is the thermomechanical analog of intensity differ-

ence squeezing in optical parametric oscillators.

B.4   Below threshold dynamics : Two-mode squeezing

In this section, we evaluate the dynamics of the nondegenerate parametric amplifier that arise for pump actuation below the instability threshold. In this regime, the system exhibits correlations between the displacements of the signal and idler modes. These correlations are manifest as two-mode squeezing of a combined quadrature composed from the individual modes.

In general, the correlations can be obtained using the coupled equations for the membrane modes in the simultaneous presence of a classical pump actuation and thermomechanical Langevin forces. The detailed derivation of the noise spectra is given in B.8.1 and we only briefly outline the procedure here. The analysis of the thermal fluctuation spectra is analogous to that for quantum fluctuations of optical parametric amplifiers [113, 222, 223]. This similarity is due to both quantum and thermal fluctuations being approximated as gaussian. In addition, both the thermal Langevin forces in mechanical systems and the quantum noise in OPA/OPOs are typically assumed to be Markovian. This approximation has been shown to breakdown in the thermal baths of mechanical resonators [218]. The consequences of this breakdown and the nature of the squeezing spectra in the presence of non-Markovian corrections to thermal fluctuations will be described elsewhere.

We separate the mean displacement and fluctuations about the mean, by writing $x_{i,j} = (\bar{A}_{i,j} + \delta A_{i,j})e^{-i\omega_{i,j}t}$ with $\langle \delta A_{i,j} \rangle = 0$. Further, the fluctuations are decomposed into their quadrature components as $\delta A_{i,j} = \delta\alpha_{i,j} + i\delta\beta_{i,j}$. Below

threshold, the fluctuations of the individual quadratures are given by equations (B.14, B.15) of B.8.1 with $\bar{A}_{i,j} = 0$.

We then define cross-quadratures constructed from $\{\alpha_{i,j}, \beta_{i,j}\}$, here normalized to their respective thermomechanical amplitudes, according to the relations,

$$
\begin{aligned}
x_{\pm} &= (\alpha_i \pm \alpha_j)/\sqrt{2} \\
y_{\pm} &= (\beta_i \pm \beta_j)/\sqrt{2}
\end{aligned}
$$

The two-mode correlations are manifest as amplification and squeezing of the above quadratures. We represent the fluctuations in these cross-quadratures, along with the fluctuation of the substrate mode in the form of the column vectors $\mathbf{X} = (\delta x_+, \delta x_-, \delta x_S)^T$, $\mathbf{Y} = (\delta y_+, \delta y_-, \delta y_S)^T$. These are related to the original quadrature fluctuations $\delta \vec{\alpha}$, $\delta \vec{\beta}$ via,

$$
\mathbf{X} = \mathbf{R}\delta\tilde{\alpha}; \quad \mathbf{Y} = \mathbf{R}\delta\tilde{\beta}; \quad \mathbf{R} = \frac{1}{\sqrt{2}} \begin{pmatrix} 1 & 1 & 0 \\ 1 & -1 & 0 \\ 0 & 0 & 1 \end{pmatrix}
$$

Finally, the correlations of the cross quadratures are obtained through a corresponding transformation of the spectral densities $\mathbf{S}_{\alpha/\beta}(\omega)$, for example,

$$
\mathbf{S}_X(\omega) = \left\langle \mathbf{X}(\omega)\mathbf{X}(\omega)^{\dagger} \right\rangle = \mathbf{R}\mathbf{S}_{\alpha}\mathbf{R}^T \tag{B.2}
$$

along with the analogous equation for $\mathbf{Y}$ ($X \rightarrow Y$ & $\alpha \rightarrow \beta$ in the above). As shown in B.8.1, the degree of squeezing is obtained through the variances of these cross quadratures by integrating the spectra in equation (B.2) over the measurement bandwidth.

While this outlines the basis of the calculation, the appearance of such two-mode correlations can be intuitively seen as the result of a coherent interference between the response of the individual resonator modes due to thermomechani-

cal noise and the down-converted field arising from the two-mode nonlinearity. This interference results in a reduction of thermomechanical motion along one quadrature at the expense of amplified motion in the orthogonal quadrature.

In general, the degree of two-mode noise squeezing is sensitive to various experimental considerations such as the 'loss asymmetry' arising from mismatched dissipation rates of the individual membrane modes, their frequency difference and the detuning of the parametric drive from the two-mode resonance. Below, we evaluate the effect of these considerations on the degree of squeezing and find the robust formation of two-mode squeezed states for a wide range of experimental parameters.

B.4.1   Matched losses and frequencies

For notational convenience, we introduce the loss asymmetry parameter $\delta_\gamma = (\gamma_i - \gamma_j)/(\gamma_i + \gamma_j)$ and frequency mismatch parameter $\delta_\omega = (\omega_i - \omega_j)/(\omega_i + \omega_j)$. To build an intuition for quadrature squeezing below threshold, we first consider the simplest case of distinct resonator modes with identical frequencies ($\omega_i = \omega_j = \omega$ or $\delta_\omega = 0$) and identical dissipation rates ($\gamma_i = \gamma_j = \gamma$ or $\delta_\gamma = 0$).

For this case, the evolution matrices in equation (B.16) of B.8.1 reduce to,

$$\mathbf{M}_{\alpha/\beta} = \frac{1}{2} \begin{pmatrix} -\gamma & \mp\gamma\mu & 0 \\ \mp\gamma\mu & -\gamma & 0 \\ 0 & 0 & -\gamma_S \end{pmatrix} \tag{B.3}$$

The spectral density of fluctuations of the collective quadratures is evaluated

185

from equation (B.17) and equation (B.2) to yield

$$\mathbf{S_{X/Y}} = \frac{2}{\pi} \begin{pmatrix} \frac{\gamma}{(\gamma^2(1\pm\mu)^2+4\omega^2)} & 0 & 0 \\ 0 & \frac{\gamma}{(\gamma^2(1\mp\mu)^2+4\omega^2)} & 0 \\ 0 & 0 & \frac{\gamma_S}{(\gamma_S^2+4\omega^2)} \end{pmatrix} \tag{B.4}$$

The variances of the normalized collective quadratures of the mechanical modes are then given by,

$$\sigma_{x_\pm,x_\pm} = \frac{1}{1\pm\mu} = \sigma_{y_\mp,y_\mp} \tag{B.5}$$

We see that x_-, y_+ are amplified quadratures with variances that grow as $\mu \to 1$, while x_+, y_- are squeezed quadratures showing reduction in the variance below the thermomechanical limit. For pump actuation close to parametric threshold ($\mu \to 1$), we obtain a peak noise squeezing of $\frac{1}{2}$, similar to the bound observed in optical parametric amplifiers [224]. The degree of two-mode squeezing versus parametric drive is shown in Fig. B.3.

The existence of a bound for the peak noise squeezing can be intuited by looking at the equations of motion for the collective quadratures, through a rotation of the original equations of motion, i.e.

$$\dot{\mathbf{X}} = \mathbf{M}_X\mathbf{X} + \mathbf{v}'_X \tag{B.6}$$

$$\dot{\mathbf{Y}} = \mathbf{M}_Y\mathbf{Y} + \mathbf{v}'_Y \tag{B.7}$$

where,

$$\mathbf{M}_{X/Y} = \mathbf{R}\mathbf{M}_{\alpha/\beta}\mathbf{R}^T = -\frac{1}{2}\begin{pmatrix} \gamma(1\pm\mu) & 0 & 0 \\ 0 & \gamma(1\mp\mu) & 0 \\ 0 & 0 & \gamma_s \end{pmatrix}$$

and $\mathbf{v}' = \mathbf{R}\mathbf{v}$ represents thermomechanical noise forces.

Two-mode squeezing arises from the fact that while the thermomechanical noise forces remain the same in the presence or absence of the parametric drive,

186
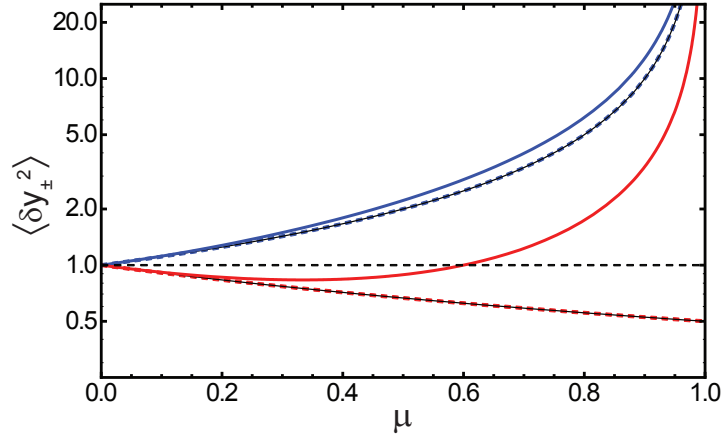
Figure B.3: Normalized variances of amplified and squeezed collective quadratures as a function of the normalized parametric drive. Black lines indicate the variances for matched frequencies ($\delta_\omega = 0$) and loss rates ($\delta_\gamma = 0$). Solid lines indicate the amplified (blue) and squeezed (red) variances for $\delta_\gamma = 0.5$, $\delta_\omega = -0.5$. The dashed lines indicate the amplified and squeezed variances for $\delta_\gamma = \delta_\omega \neq 0$, the case of matched asymmetries where the peak noise squeezing again approaches a factor of $\frac{1}{2}$ as $\mu \to 1$. The dashed horizontal line represents the thermomechanical variance given by $\frac{k_B T}{m\omega^2}$.

the dissipation of the squeezed quadrature goes to twice its bare value near parametric threshold. This results in a reduction in the variance of the squeezed quadrature by a factor of 2. Simultaneously, the decay rate of the amplified quadrature goes to zero, signaling the onset of the parametric instability. The onset of the instability thus explains the 3 dB bound for squeezing through this parametric process.

The variances of the cross-quadratures are calculated by integrating the noise over all frequencies, i.e. they are measured with infinite bandwidth. As the measurement bandwidth decreases, the peak noise squeezing approaches 6 dB, i.e.

$$\frac{S_{x_+,x_+}(\omega = 0, \mu)}{S_{x_+,x_+}(\omega = 0, \mu = 0)} = \frac{1}{(1+\mu)^2} \xrightarrow{\mu \to 1} \frac{1}{4} \tag{B.8}$$

B.4.2 Effect of mismatched frequencies and loss rates

We now consider the case where the frequencies and the damping rate of the two resonators are not the same, i.e. $\delta_\gamma, \delta_\omega \neq 0$. In this situation, the collective quadratures $x_\pm$ and $y_\pm$ are no longer decoupled from each other. This coupling between the collective quadratures has been noted to be detrimental to entanglement [103], and backaction evasion [209] protocols. It also results in a degradation of peak two-mode thermomechanical squeezing. This is a result of the coupled quadratures x_+, x_- and y_-, y_+ being respectively amplified and squeezed in the presence of the parametric drive.

As before, the variances of the collective quadratures are obtained using equation (B.17), subsequent rotation using equation (B.2) and integration over frequency. These are now given by

$$
\begin{aligned}
\sigma_{y_\pm, y_\pm} &= \sigma_{x_\mp, x_\mp} \\
&= \frac{1}{1 - \mu^2}\left\{ 1 + \mu^2 \frac{\delta_\omega(\delta_\omega - \delta_\gamma)}{1 - \delta_\omega^2} \pm \mu \sqrt{\frac{1 - \delta_\gamma^2}{1 - \delta_\omega^2}} \right\}
\end{aligned}
$$

with the cross correlation between (x_+, x_-), (y_+, y_-) given by,

$$
\sigma_{y_+, y_-} = \sigma_{x_+, x_-} = \frac{\mu^2 \left(\delta_\omega - \delta_\gamma\right)}{2\left(1 - \mu^2\right)\left(1 - \delta_\omega^2\right)}
$$

The variances of the amplified and squeezed collective quadratures for the case where $(\delta_\gamma \neq 0, \delta_\omega \neq 0, \delta_\gamma \neq \delta_\omega)$, are shown in Fig. B.3. As can be seen, the presence of loss asymmetry or a frequency mismatch results in a degradation of noise squeezing. In this case, optimal squeezing is obtained for a parametric drive that is significantly below the instability threshold. We also find that the coupling between the amplified and squeezed quadratures leads to a divergence of the squeezed quadrature at the instability threshold.

The dependence of the peak squeezing on the loss asymmetry and frequency

mismatch parameters are summarized in Fig. B.4. Fig. B.4(a) shows a plot of the peak squeezing as a function of the loss asymmetry for the case of distinct mechanical modes with the same frequency ($\delta_\omega = 0$), showing a linear degradation of peak squeezing with loss asymmetry. Correspondingly, Fig. B.4(b) shows the peak squeezing as a function of the frequency mismatch parameter (δ_ω) for the case of no loss asymmetry ($\delta_\gamma = 0$).
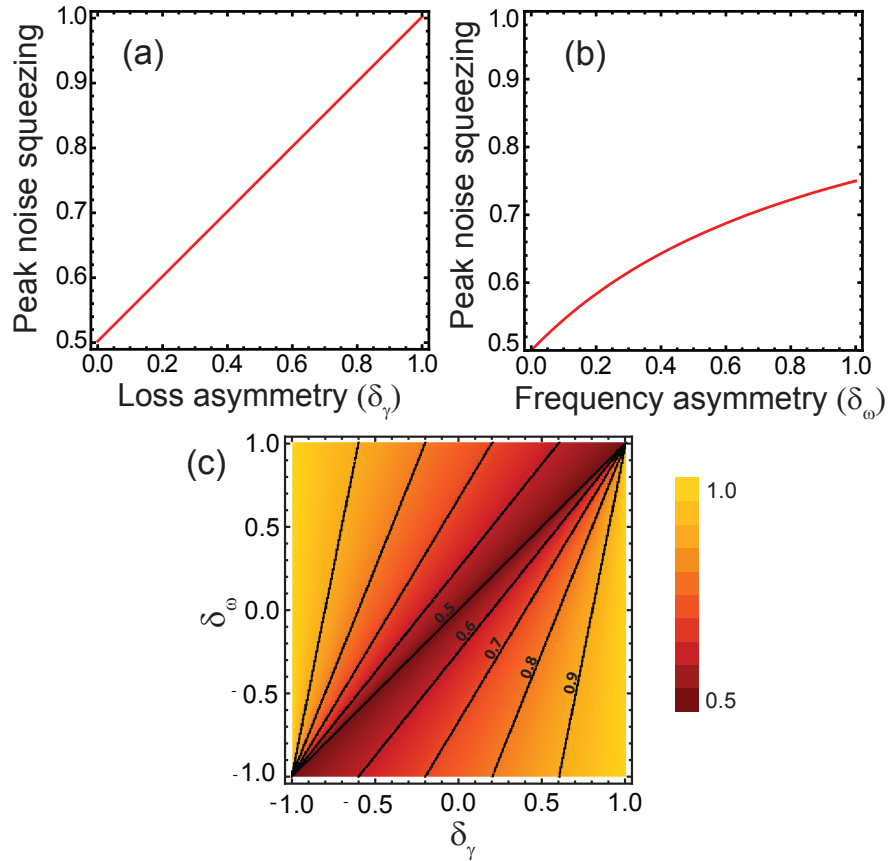
Figure B.4: (a) Peak noise squeezing as a function of loss asymmetry δ_γ for $\delta_\omega = 0$ with the squeezing going linearly from $\frac{1}{2} \to 1$ as $\delta_\gamma = 0 \to 1$. (b) Peak squeezing as a function of the frequency asymmetry δ_ω, for $\delta_\gamma = 0$. (c) Peak squeezing as a function of δ_γ and δ_ω.

Importantly, as can be seen in Fig. B.4(c), we find that the 3 dB squeezing bound can be regained even in the presence of loss asymmetry as long as $\delta_\gamma = \delta_\omega$.

In this case, the normalized cross correlations between amplified and squeezed collective quadratures vanish, and equation (B.9) reduces to equation (B.5). This results in a noise squeezing that is identical to that for the case of symmetric losses and frequencies.

B.4.3 Effect of pump detuning

Finally, we consider the thermomechanical squeezing bound when the pump drive is detuned from parametric resonance. In this case, the drive frequency is given by $\omega_d = \omega_S + \Delta$, where Δ is the drive detuning. This case is of interest since a detuned parametric drive introduces a dynamic coupling between the $\delta\vec{\alpha}$ and $\delta\vec{\beta}$ quadratures. In turn, this leads to correlations between the amplified and squeezed quadratures. Due to these correlations, the amplified quadrature contains information about the squeezed quadrature that can be used for enhanced localization through weak measurements and optimal estimation [101]. Thus, a detuned parametric drive can allow for enhanced noise squeezing in the presence of feedback. An additional point of interest in this case is that special choices of the drive detuning lead to some of the collective quadratures becoming quantum non-demolition observables [103].

The equations satisfied by the slowly varying complex amplitudes ($A_{i,j,S}$) are again given by equations (B.1-B.1), with the only difference now being that the pump actuation $\tilde{F}_S(t)$ is a slowly varying function of time, $\tilde{F}_S(t) = |\tilde{F}_S|e^{-i\Delta t}$. The pump amplitude resulting from this drive force, $\bar{A}_S(t)$ is given by,

$$\bar{A}_S = i\chi_S\tilde{F}_S(t) = i\chi_S|\tilde{F}_S|e^{-i\Delta t} = i|\bar{A}_S|e^{-i\Delta t} \tag{B.9}$$

Here, as we are most interested in pump detunings that are comparable to

the resonator linewidths, we have made the assumption that $\Delta \ll \gamma_S$ and that the pump amplitude is hence related to the instantaneous parametric actuation through the on-resonant susceptibility.

The two-mode correlations are computed in B.8.2, and are given for $\delta_\gamma = \delta_\omega = 0$ by

$$\sigma_{x_\pm, x_\pm} = \left(\frac{k_B T \gamma}{m \omega^2}\right)\left[\frac{\left(\Delta^2 + \gamma^2(1 \mp \mu)^2 - \lambda_-^2\right)}{\lambda_+ \lambda_- (\lambda_+ + \lambda_-)} + \frac{1}{\lambda_+}\right]$$
$$= \sigma_{y_\mp, y_\mp}$$

and

$$\sigma_{x_\pm, y_\pm} = \left(\frac{k_B T \gamma}{m \omega^2}\right)\frac{2\Delta\gamma\mu}{\lambda_+ \lambda_- (\lambda_+ + \lambda_-)} = \sigma_{y_\pm, x_\pm}$$

where $\lambda_\pm^2 = \gamma^2\left(1 + \mu^2\right) - \Delta^2 \pm 2\gamma\sqrt{\gamma^2\mu^2 - \Delta^2}$.

Note that x_+ and y_- are amplified quadratures while x_- and y_+ are squeezed. As mentioned earlier, a nonzero detuning introduces correlations between (x_+, y_+) and (x_-, y_-), i.e. between amplified and squeezed quadratures. This is distinct from the case of loss asymmetry or frequency mismatch considered previously, where correlations were introduced between (x_+, x_-) and (y_+, y_-). As can be seen from the above expressions, these correlations between the $x_\pm$ and $y_\pm$ quadratures are proportional to the drive detuning.

This coupling between amplified and squeezed quadratures also results in a decrease in the peak squeezing at non-zero detunings, as can be seen in Fig. B.5(a). As expected, for the detuned case, the amplified quadrature diverges at $\mu = \sqrt{1 + (\Delta/\gamma)^2}$, the instability threshold for $\Delta \neq 0$.

The peak squeezing as a function of the detuning, normalized with respect to the decay rate (for no loss asymmetry or frequency mismatch) is shown in Fig. B.5(b). We see that squeezing is almost completely lost when the detuning

191
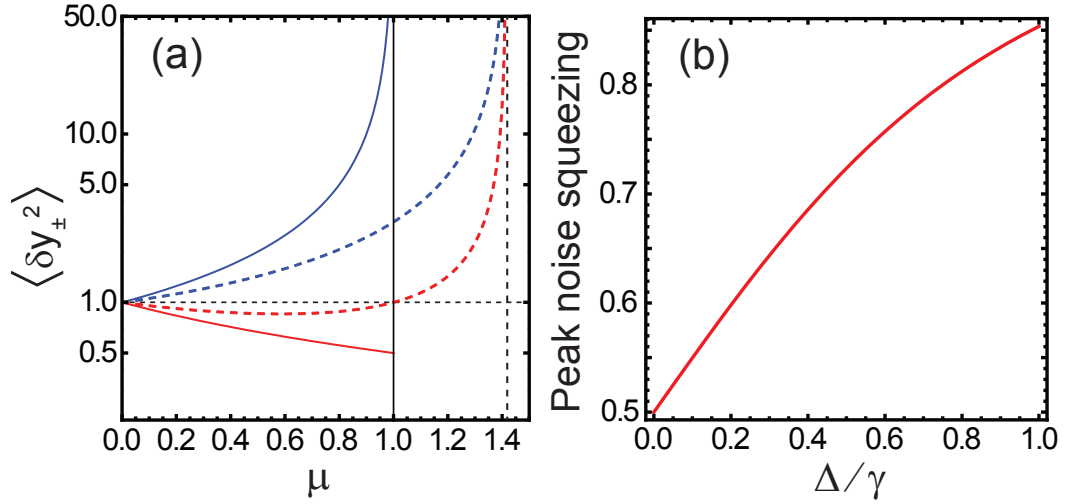
Figure B.5: (a) Normalized variance of the fluctuations in the y_+ (amplified,blue) and y_- (squeezed,red) quadratures for the case of zero detuning (solid lines) and a detuning of $\Delta = \gamma$ (dashed lines). The amplified quadrature diverges at the instability threshold. For $\Delta = 0$, this occurs at $\mu = 1$ (solid black vertical line). For $\Delta = \gamma$, this occurs at $\mu = \sqrt{1 + (\Delta/\gamma)^2} = \sqrt{2}$ (dashed black vertical line). The black horizontal line is at $1/2$. (b) Peak noise squeezing as a function of normalized detuning $\frac{\Delta}{\gamma}$. Both these graphs are shown for the case of no loss or frequency asymmetry, i.e. $\delta_\gamma = \delta_\omega = 0$.

becomes comparable to the linewidth of the signal and idler modes.

B.5 Above threshold dynamics : Amplitude difference squeezing

For pump actuation above the parametric instability threshold, the two-mode nonlinearity results in parametric self-oscillation of the individual membrane modes. In this regime, the correlated production of down-converted phonons in the signal and idler modes results in a reduction of fluctuations in the am-

plitude difference between these two modes. This is the phononic version of intensity difference squeezing observed in optical parametric oscillators [222]. As in the optical case, this form of difference squeezing is of interest in nonlinear interferometric schemes [217] capable of measurement sensitivities surpassing the standard quantum limit.

In this section, we discuss the dynamics of the two-mode nonlinearity above threshold and compute the amplitude fluctuations of the mechanical modes. Additionally, we discuss the fluctuations of their phases. While energy conservation dictates that the sum of the frequencies of the signal and idler modes equal that of the pump drive, it is also the case that the sum of the phases of the signal and idler modes above threshold remain locked to the phase of the pump drive. This follows from equation (B.1), which in steady state can be rewritten in terms of the normalized drive μ and the drive force phase ϕ_S ($F_S = |F_S|e^{i\phi_S}$) as

$$-(\mu - 1)e^{i\phi_S} = \frac{g}{2}\frac{\chi_S}{|A_{S,cr}|}A_i A_j$$

Defining the phases of the resonator modes as $A_{i,j} = i|A_{i,j}|e^{i\phi_{i,j}}$, we see that $\phi_i + \phi_j = \phi_S$. However, the difference in the phases is not constrained and is free to fluctuate.

As before, we quantify these fluctuations in the amplitudes and phases about their steady state values by decomposing the complex amplitude fluctuations $\delta\vec{A}$ into $\delta\alpha_i$ and $\delta\beta_i$ quadratures. The equations of motion of $\delta\vec{\alpha}$ and $\delta\vec{\beta}$ are given by equations (B.14, B.15) in Supplementary Information, Section B.8.1, after substituting $|\bar{A}_S| = \sqrt{\frac{\gamma_i \gamma_j}{\kappa_i \kappa_j}}$ and $\bar{A}_{i,j} = \sqrt{\frac{\gamma_{i,j}\gamma_S}{\kappa_{i,j}\kappa_S}}\sqrt{\mu - 1}$. Here, we have defined the coupling parameter $\kappa_k = \frac{g}{2m_k\omega_k}$.

We choose the drive and resonator mode phases such that $\bar{\phi}_{i,j} = \phi_S = 0$. Given this choice of phases, the complex mean amplitudes $\bar{A}_{i,j}$ and the fluctua-

tions are as shown in the inset of Fig. B.6. With this convention, the amplitude fluctuations are given by $\delta\beta_{i,j}$. The fluctuations in the phase are obtained from $\delta\alpha_{i,j}$ through $\delta\phi_{i,j} = \frac{\delta\alpha_{i,j}}{\bar{A}_{i,j}}$.
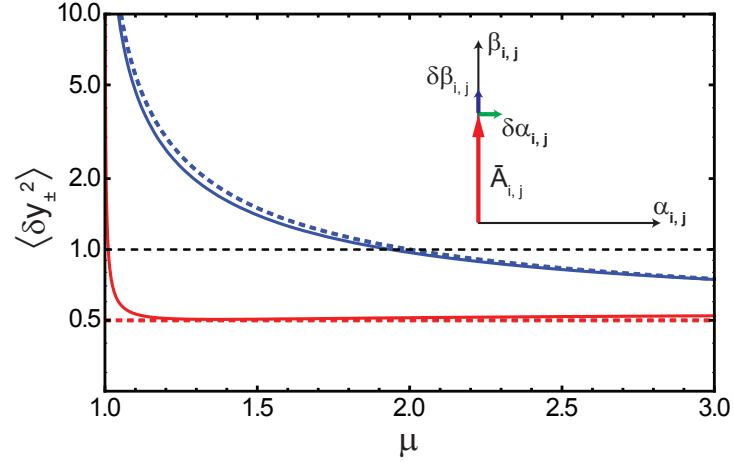
Figure B.6: Variance of the fluctuations in the difference y_- (red) and sum y_+ (blue) quadratures *vs* the parametric drive μ. The dashed lines are computed for $\delta_\gamma = \delta_\omega = 0$. The solid lines are computed for $\delta_\gamma = 0.31, \delta_\omega = 0.09$, corresponding to the experimental parameters in [150]. The amplitude difference quadrature is squeezed for all values above threshold to a value of $\frac{1}{2}$. As can be seen, amplitude difference squeezing is extremely robust to experimental imperfections such as a frequency mismatch or loss asymmetry. Inset: Schematic of the mean value of the membrane mode amplitude $\bar{A}_{i,j}$ and the fluctuations $\delta\alpha_{i,j}$ and $\delta\beta_{i,j}$. $\delta\vec{\beta}$ represent amplitude fluctuations while $\delta\vec{\alpha}$ are related to fluctuations of the phase.

Similar to the below threshold case, the correlations of the fluctuations in the signal and idler modes resulting from the pump drive are manifest in combined quadratures,

$$\delta x_\pm = \frac{1}{\sqrt{2}}(\delta\alpha_i \pm \delta\alpha_j) \propto \delta\phi_\pm$$

$$\delta y_\pm = \frac{1}{\sqrt{2}}(\delta\beta_i \pm \delta\beta_j) = \delta R_\pm$$

where $\delta R_\pm$ are the amplitude sum and difference quadratures and $\delta\phi_\pm$ are the

phase sum and difference quadratures. The spectrum of fluctuations of $\delta\alpha_\pm$ and $\delta\beta_\pm$ are given by equation (B.17).

In contrast to the dynamics below threshold, the fluctuations of the pump mode above threshold have an influence on the correlations generated between the membrane modes. On the one hand, the substrate fluctuations are smaller than those of the membrane modes by a term proportional to the respective mass ratios. Thus, one might assume that these tiny fluctuations should have a negligible influence on the membrane modes. However, the substrate mode fluctuations affect the membrane modes through terms that are proportional to the steady state amplitudes of the latter. These amplitudes are larger than the pump mode amplitude by the mass ratio of the substrate and membrane modes. These ratios cancel each other and lead to pump mode thermal fluctuations influencing the signal and idler modes through terms that are of the same order as the coupling between the signal and idler modes. Thus, the degree of amplitude difference squeezing is independent of the resonator to substrate mass ratio.

Consistent with the experimental system under consideration [150], we assume that the damping rate of the substrate excitation is 3-4 orders of magnitude larger than those of the membrane. In this regime, the pump fluctuations respond instantaneously to those of the membrane modes and can thus be adiabatically eliminated. We use this to simplify the analysis and ignore the time derivative of the pump fluctuations ($\delta\dot{A}_S$) in equation (B.11). Aside from this modification, we extract the fluctuations of the signal and idler modes as before.

195

B.5.1 Matched losses and frequencies

We first consider the case where the damping rates and the frequencies are matched. In this limit, we obtain the following spectral densities for the collective quadratures normalized with respect to the thermal motion amplitude.

$$
\mathbf{S}_Y(\omega) \;=\; \frac{1}{2\pi}
\begin{pmatrix}
\frac{\gamma\mu}{(\gamma^2(-1+\mu)^2+\omega^2)} & 0 \\
0 & \frac{\gamma}{(\gamma^2+\omega^2)}
\end{pmatrix}
$$

$$
\mathbf{S}_X(\omega) \;=\; \frac{1}{2\pi}
\begin{pmatrix}
\frac{\gamma\mu}{(\gamma^2\mu^2+\omega^2)} & 0 \\
0 & \frac{\gamma}{\omega^2}
\end{pmatrix}
$$

We obtain the variances of the fluctuations by integrating the spectra. For the Y quadrature, which relates to amplitude fluctuations, these evaluate to

$$
\sigma_{y_+,y_+} \;=\; \frac{\mu}{2\,(\mu-1)}
$$

$$
\sigma_{y_-,y_-} \;=\; \frac{1}{2}
$$

These variances are plotted as a function of the parametric drive in Fig. B.6.

Above threshold, the amplitude difference between the signal and idler modes is always half the thermal variance. This is the mechanical analogue of intensity difference squeezing seen in optical parametric oscillators. We find that while the individual amplitudes are sensitive to fluctuations of the pump mode, the amplitude difference is insensitive to fluctuations of the pump mode and the degree of squeezing is independent of the pump drive. On the other hand, the variance of the amplitude sum diverges as $\mu \to 1^+$ and decreases with increasing drive, approaching half the thermal variance as $\mu \to \infty$.

The other notable feature of above threshold dynamics is that the phase difference between the signal and idler modes is unspecified and hence free to

fluctuate. The fluctuation in the phase difference is given by

$$
\begin{aligned}
S_{\phi_-,\phi_-}(\omega) &= \left(\frac{x_{th}^2}{A(\mu)^2}\right) S_{x_-,x_-}(\omega) \\
&= \left(\frac{x_{th}^2}{A(\mu)^2}\right)\left(\frac{\gamma}{2\pi\omega^2}\right)
\end{aligned}
$$

where $A(\mu)$ is the amplitude of the membrane modes (identical for the case of matched loss rates), $x_{th}^2 = \frac{k_B T}{m\omega^2}$ is the thermal variance. The integral of the fluctuation spectrum diverges as ω^{-2}, indicating that the difference phase undergoes diffusion. The time scale τ for this diffusion can be estimated by calculating the variance while imposing a low frequency cut off ($\frac{2\pi}{\tau}$) to the integral of the spectral density, i.e.

$$
\begin{aligned}
\langle \delta\phi_-^2 \rangle &= 2 \int_{\frac{2\pi}{\tau}}^{\infty} S_{\phi_-,\phi_-}(\omega)d\omega \\
&= \left(\frac{x_{th}^2}{A(\mu)^2}\right)\frac{\gamma\tau}{2\pi^2}
\end{aligned}
$$

If the parametric nonlinearity were used to actuate the membrane modes to an amplitude of $10^3 \times (x_{th}^2)^{1/2}$, a phase fluctuation of 1 mrad would require a measurement duration of 10 ringdown periods or around 100 seconds for the modes considered in [150]. Thus, while $S_{\phi_-,\phi_-}(\omega)$ diverges, it does not necessarily lead to large fluctuations of the difference phase over experimental time scales.

B.5.2 Effect of mismatched frequencies and loss rates

For the case of non-zero loss asymmetry and frequency mismatch ($\delta_\gamma, \delta_\omega \neq 0$), the fluctuations of the amplitude difference are no longer decoupled from fluctuations of the amplitude sum. These fluctuations are obtained as in the previous section. The calculation, while straightforward, is laborious and we only summarize the results below.

The variances of the amplified and squeezed sum and difference quadratures are shown in Fig. B.6 for $\delta_\gamma = 0.31$ and $\delta_\omega = 0.09$. In this case, the coupling between amplified and squeezed quadratures leads to a divergence in the squeezed quadrature as $\mu \to 1^+$. Unlike in the case below threshold, the fluctuations for the case of matched asymmetries ($\delta_\gamma = \delta_\omega \neq 0$) are not the same as for the case of $\delta_\gamma = \delta_\omega = 0$. Importantly, we note that for pump actuation significantly above threshold, the degree of squeezing is impervious to experimental imperfections such as a loss asymmetry.

B.6 Crossover of correlations at the instability threshold

Finally, we discuss the dynamics of the two-mode nonlinearity in the vicinity of the parametric instability. The crossover regime is most conveniently portrayed by evaluating the variance of $y_\pm$ quadratures in the regimes below and above threshold. In the former regime, these quadratures represent the two-mode correlations arising from phase-sensitive parametric amplification. In the latter regime, these correspond to the sum and difference amplitude fluctuations of the two membrane modes. These are shown in Fig. B.7. In the general case of mismatched dissipation rates ($\delta_\gamma \neq 0$), both these quadratures exhibit diverging variances at the instability.

As for the divergent phase diffusion discussed earlier, finite time effects need to be considered to interpret the divergent steady-state variances depicted in Fig. B.7. For the low frequency, ultrahigh quality factor resonators considered in this work, the divergent response time in the vicinity of the instability threshold can result in inordinately long thermalization times ($\sim 10^4 - 10^5$ seconds).
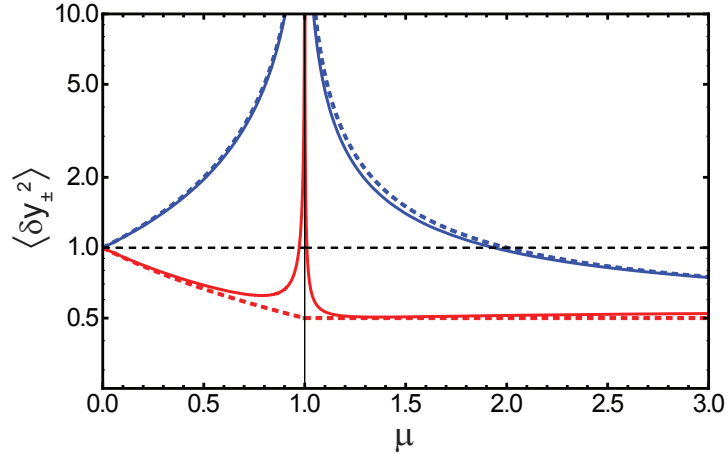
Figure B.7: Two-mode correlations in the vicinity of the threshold for parametric instability. Variance of the fluctuations of the normalized difference (y_-) and sum (y_+) quadratures above and below threshold *vs* the normalized parametric drive μ. The dashed lines represent the variances for $\delta_\gamma = \delta_\omega = 0$. The solid lines represent the variances for $\delta_\gamma = 0.31, \delta_\omega = 0.09$, corresponding to the experimental parameters in [150]. The dashed horizontal line represents the thermomechanical variance given by $\frac{k_B T}{m\omega^2}$.

For typical measurement durations ($\sim$ 100 seconds), the measured squeezing spectra can deviate appreciably from the spectra computed in steady state. Expectedly, these deviations are most significant for parametric actuation around the instability threshold ($\mu \sim 1.0$).

The variances measured over a finite time τ_m are extracted by truncating the integral of the relevant spectral densities by the time of measurement, i.e.

$$\sigma_{\alpha,\beta} = 2 \int_{\frac{2\pi}{\tau_m}}^{\infty} \mathbf{S}_{\alpha,\beta}(\omega) d\omega \tag{B.10}$$

These variances, computed for the parameters in [150], result in the solid black curves shown in Fig. B.8. We see that the singularities in the amplified and squeezed quadratures seen in the steady state variances (solid blue and red lines) are washed out at finite measurement durations.
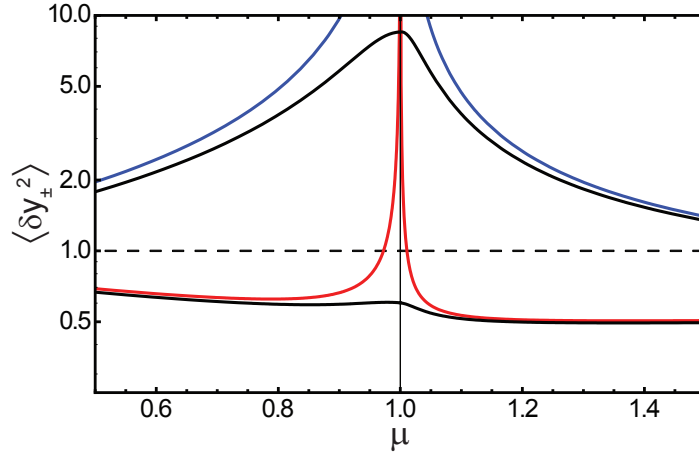
Figure B.8: Corrections to squeezing spectra due to finite measurement duration. Normalized variance of amplified (y_+) and squeezed (y_-) quadratures for a measurement time of 300 seconds (~ 100 ring down periods) (black solid lines). Also shown for comparison are the corresponding amplified (blue) and squeezed (red) quadratures in steady state. These are computed for $\delta_\gamma = 0.31$, $\delta_\omega = 0.09$ ($\gamma \sim 2\pi \times 100$ mHz) and correspond to the experimental parameters in [150]. The divergence at the instability threshold is attenuated for finite measurement times due to the divergent response times.

The regime around $\mu = 1$ is of interest since the system exhibits mechanical bistability and a hysteretic response due to the divergent mechanical susceptibility and diverging response time. This regime offers a clean, mesoscopic and mechanical realization of a second-order phase transition [225, 226, 227, 228] and out-of-equilibrium quantum dynamics on experimentally accessible timescales. Furthermore, quantum tunneling between bistable mechanical states has been discussed in the context of a Duffing nonlinearity as a means of accessing a quantum-to-classical transition [194]. In the system considered here and in [150], the presence of a strong two-mode nonlinearity and compatibility with optomechanical cooling together imply that similar effects can be accessed even in the regime of low phonon number and motion

on the scale of mechanical zero-point fluctuations. The nature of this nonequilibrium phase transition and the response to critical fluctuations as the phonon occupancy is gradually reduced by optomechanical cooling will be described elsewhere.

We also note the close correspondence between the squeezing spectra arising from the two-mode nonlinearity and the properties of the reservoir to which the resonator is coupled. In particular, while we have considered the squeezing spectra in the presence of a Markovian (thermal) reservoir in this work, it is also known that intrinsic defects or two-level systems (TLS) in amorphous resonators such as SiN can couple to mechanical motion [229]. Furthermore, a reservoir of such TLS can acquire non-Markovian properties in certain regimes. In addition to studying the effect of such non-Markovian fluctuations on the second order phase transition and the two-mode correlations near the instability, it is an intriguing prospect to use the exquisite sensitivity of this two-mode nonlinearity as an amplifier of such reservoir interactions to shed light on the intrinsic material properties of the membrane resonator.

B.7 Conclusions

In summary, we describe a phononic nondegenerate parametric amplifier that is realized in a membrane resonator through a substrate-mediated nonlinearity. Motivated by recent work [150, 95], we discuss the creation of multimode phononic correlations arising from this parametric interaction and compute the squeezing spectra in the presence of thermomechanical noise. We address various points of experimental relevance including the presence of frequency mis-

matches and asymmetric dissipation rates between the resonator modes. We find the robust presence of two-mode phononic correlations for a wide range of experimental parameters.

Below the threshold for parametric instability, this system exhibits two-mode noise squeezing of collective quadratures composed from the individual resonator modes. This regime is conducive to back-action evading (BAE) schemes for quantum-enhanced metrology. Above threshold, the system exhibits amplitude difference squeezing due to the correlated production of down-converted phonons in both resonator modes. This regime is promising for non-linear measurement schemes capable of measurement sensitivities surpassing the standard quantum limit.

In the crossover regime between these two limits, the response of the system near the parametric instability threshold is characterized by a divergent mechanical susceptibility and a diverging response time. In this regime, the system exhibits mechanical bistability, a hysteretic response and critical slowing down. This regime is of interest as it offers a mechanical realization of a second order phase transition for the investigation of nonequilibrium critical dynamics, the quantum-to-classical transition and the influence of a non-Markovian reservoir on such critical phenomena. These results will be discussed elsewhere. Due to the combined presence of low intrinsic dissipation and optomechanical compatibility, such nonlinear mechanical systems are promising for extending these studies from the classical realm deep into the quantum regime.

B.8 Supplementary Information

B.8.1 Calculation of fluctuation spectra in the presence of thermal noise

For both the below and the above threshold regimes, we obtain the correlations that develop between the resonator modes in the presence of the pump drive, by analyzing the coupled equations for the resonator modes under the influence of a classical actuation of the pump/substrate mode along with thermomechanical Langevin noise forces acting on the membrane and substrate modes.

We distinguish between the mean displacement and the fluctuations by writing $x_{i,j} = (\bar{A}_{i,j} + \delta A_{i,j})e^{-i\omega_{i,j}t}$ where $\langle \delta A_{i,j} \rangle = 0$. The coupled equations for the fluctuations can be written as,

$$
2\begin{pmatrix} \Psi \delta \dot{A}_i \\ \delta \dot{A}_j \\ \delta \dot{A}_S \end{pmatrix} = \begin{pmatrix} -\gamma_i & 0 & i\kappa_i \bar{A}_j^* \\ \Psi 0 & -\gamma_j & i\kappa_j \bar{A}_i^* \\ i\kappa_S \bar{A}_j & i\kappa_S \bar{A}_i & -\gamma_S \end{pmatrix} \begin{pmatrix} \Psi \delta A_i \\ \delta A_j \\ \delta A_S \end{pmatrix}
$$

$$
+ \begin{pmatrix} 0 & i\kappa_i \bar{A}_S & 0 \\ \Psi i\kappa_j \bar{A}_S & 0 & 0 \\ 0 & 0 & 0 \end{pmatrix} \begin{pmatrix} \Psi \delta A_i^* \\ \delta A_j^* \\ \delta A_S^* \end{pmatrix} + i \begin{pmatrix} \Psi \gamma_i \chi_i F_i \\ \gamma_j \chi_j F_j \\ \gamma_S \chi_S F_S \end{pmatrix}
$$

where we have defined coupling parameters,

$$
\kappa_k = \frac{g\gamma_k \chi_k}{2} = \frac{g}{2m_k \omega_k}; \quad k \in [i, j, S] \tag{B.11}
$$

for notational simplicity. The thermomechanical noise forces are assumed to be white noise correlated and obey,

$$
\langle F_i(t) \rangle = \langle F_i(t) F_j(t') \rangle = 0, \tag{B.12}
$$

$$
\langle F_i(t) F_j^*(t+\tau) \rangle = 8\gamma_i m_i k_B T \delta_{ij} \delta(\tau) \tag{B.13}
$$

203

We decompose the complex displacements into real quadratures according to $\delta \mathbf{A} = \delta \vec{\alpha} + i\delta \vec{\beta}$ and where $\delta \mathbf{A} = (\delta A_i, \delta A_j, \delta A_S)^T$. Correspondingly the noise, $\mathbf{v} = i(\gamma_i \chi_i F_i, \gamma_j \chi_j F_j, \gamma_S \chi_S F_S)^T$ is also decomposed into real and imaginary parts, $\mathbf{v} = \mathbf{v}_\alpha + i\mathbf{v}_\beta$. Expressing equation (B.11) in terms of these quantities gives,

$$\dot{\delta \vec{\alpha}} = \mathbf{M}_\alpha \delta \vec{\alpha} + \mathbf{v}_\alpha \tag{B.14}$$

$$\dot{\delta \vec{\beta}} = \mathbf{M}_\beta \delta \vec{\beta} + \mathbf{v}_\beta \tag{B.15}$$

For the general case, valid both above and below threshold,

$$\mathbf{M}_{\alpha/\beta} = \frac{1}{2} \begin{pmatrix} -\gamma_i & \mp \kappa_i |\bar{A}_S| & \kappa_i |\bar{A}_j| \\ \mp \kappa_j |\bar{A}_S| & -\gamma_j & \kappa_j |\bar{A}_i| \\ -\kappa_S |\bar{A}_j| & -\kappa_S |\bar{A}_i| & -\gamma_S \end{pmatrix} \tag{B.16}$$

and the elements of $\mathbf{v}_{\alpha,\beta}$ satisfy $\langle v_i \rangle = 0$, $\langle v_k(t)v_l(t+\tau) \rangle = \frac{\gamma_l k_B T}{m_l \omega_l^2} \delta_{kl} \delta(\tau)$. In writing equation (B.16), we have made a choice for the pump drive phase ($\phi_S = 0$) and the resonator mode detection phases ($\phi_{i,j} = 0$). In general, these phases can also be chosen such that there is a coupling between the $\delta \vec{\alpha}$ and $\delta \vec{\beta}$ quadratures. When the pump drive phase is not fixed, but evolving in time, for instance with the pump drive being detuned, this coupling is physical and cannot be made to vanish through a suitable choice of detection phases.

The noise spectral density in the steady state is obtained by taking the expectation value after Fourier transforming and inverting equations (B.14, B.15), and are given by the matrix equation,

$$\mathbf{S}_{\alpha/\beta}(\omega) = \frac{1}{2\pi}(\mathbf{M}_{\alpha/\beta} + i\omega \mathbf{I})^{-1} \mathbf{D}(\mathbf{M}_{\alpha/\beta}^T - i\omega \mathbf{I})^{-1} \tag{B.17}$$

where $\mathbf{I}$ is the identity and

$$\mathbf{D} = \langle \mathbf{v}\mathbf{v}^T \rangle = k_B T \begin{pmatrix} \frac{\gamma_i}{m_i \omega_i^2} & 0 & 0 \\ 0 & \frac{\gamma_j}{m_j \omega_j^2} & 0 \\ 0 & 0 & \frac{\gamma_S}{M_S \omega_S^2} \end{pmatrix} \tag{B.18}$$

is a matrix characterizing the diffusion due to thermal forces. The variances in steady state can be obtained from the spectrum using the Wiener-Khintchine theorem, by integrating the fluctuations over frequency, i.e.

$$\sigma_{\alpha/\beta} = \int_{-\infty}^{\infty} \mathbf{S}_{\alpha/\beta}(\omega) d\omega \tag{B.19}$$

B.8.2 Calculation of fluctuation spectra for finite pump detuning

For finite pump detuning below threshold, the actuating force is a slowly varying function of time, i.e. $\tilde{F}_S = |\tilde{F}_S| e^{-i\Delta t}$ where the drive frequency $\omega_d = \omega_S + \Delta$. This results in a pump amplitude given by $\bar{A}_S = i|\bar{A}_S| e^{-i\Delta t}$.

Linearizing about the steady state amplitude, i.e $A_k = \bar{A}_k + \delta A_k(t)$ where $k \in [i, j, S]$, with $\bar{A}_{i,j} = 0$, and defining the vectors $\delta\vec{A} = (\delta A_i, \delta A_j)^T$ and $\delta\vec{v} = (v_i, v_j)^T$, the relevant equations of motion for the fluctuations of the resonator modes reduce to,

$$
\begin{aligned}
2\dot{\delta\vec{A}} &= -\begin{pmatrix} \gamma_i & 0 \\ 0 & \gamma_j \end{pmatrix} \delta\vec{A} \\
&\quad - \begin{pmatrix} 0 & \kappa_i |\bar{A}_S| e^{-i\Delta t} \\ \kappa_j |\bar{A}_S| e^{-i\Delta t} & 0 \end{pmatrix} \delta\vec{A}^* + 2\vec{v}
\end{aligned} \tag{B.20}
$$

By going to a frame rotating at $\frac{\Delta}{2}$, we rewrite $\delta\vec{A} = \delta\vec{B} e^{\frac{i\Delta t}{2}}$ in terms of which equation (B.20) becomes,

$$
\begin{aligned}
2\dot{\delta\vec{B}} &= -\begin{pmatrix} \gamma_i & 0 \\ 0 & \gamma_j \end{pmatrix} \delta\vec{B} - i\Delta\delta\vec{B} \\
&\quad - \begin{pmatrix} 0 & \kappa_i |\bar{A}_S| \\ \kappa_j |\bar{A}_S| & 0 \end{pmatrix} \delta\vec{B}^* + 2\vec{v} e^{-\frac{\Delta t}{2}}
\end{aligned} \tag{B.21}
$$

where $\delta\vec{B}$ are the complex amplitudes of motion, measured at frequencies that are detuned from the individual mechanical modes $\omega_{i,j}$ by $\frac{\Delta}{2}$. We rewrite the complex amplitudes in terms of the real quadratures $\alpha_{i,j}, \beta_{i,j}$ and decompose the noise term into real and imaginary parts, i.e. $\delta\vec{B} = \delta\vec{\alpha} + i\delta\vec{\beta}$ and $\vec{v} = \vec{v}_\alpha + i\vec{v}_\beta$, in terms of which the equations of motion become,

$$\dot{\delta\vec{\alpha}} = \mathbf{M}_\alpha \delta\vec{\alpha} - \frac{\Delta}{2}\delta\vec{\beta} + \vec{v}_\alpha \tag{B.22}$$

$$\dot{\delta\vec{\beta}} = \mathbf{M}_\beta \delta\vec{\beta} + \frac{\Delta}{2}\delta\vec{\alpha} + \vec{v}_\beta \tag{B.23}$$

where

$$\mathbf{M}_{\alpha/\beta} = \frac{1}{2}\begin{pmatrix} -\gamma_i & \mp\kappa_i|\bar{A}_S| \\ \mp\kappa_j|\bar{A}_S| & -\gamma_j \end{pmatrix}$$

and the elements of $\vec{v}_{\alpha,\beta}$ satisfy $\langle v_{k,\eta}\rangle = 0, \eta \in [\alpha, \beta]; k \in [i, j]$ and $\langle v_{k,\eta}(t)v_{l,\eta'}(t+\tau)\rangle = \frac{\gamma_l k_B T}{m_l \omega_l^2}\delta_{kl}\delta_{\eta\eta'}\delta(\tau)$.

The coupling between the $\delta\vec{\alpha}$ and $\delta\vec{\beta}$ quadratures of the individual oscillators resulting from the detuned drive is apparent in the above equations. The steady state correlations between these quadratures can be obtained by forming the following 4 dimensional vectors; $\mathbf{Z} = (\delta\alpha_i, \delta\alpha_j, \delta\beta_i, \delta\beta_j)^T = (\delta\vec{\alpha}, \delta\vec{\beta})^T$ and $\mathbf{v} = (\vec{v}_\alpha, \vec{v}_\beta)^T$, in terms of which the equations of motion become,

$$\dot{\mathbf{Z}} = \mathbf{M}\mathbf{Z} + \mathbf{v}$$

$$\mathbf{M} = \begin{pmatrix} \mathbf{M}_\alpha & -\frac{\Delta}{2}\mathbf{I} \\ \frac{\Delta}{2}\mathbf{I} & \mathbf{M}_\beta \end{pmatrix}$$

and $\mathbf{I}$ is the 2×2 identity matrix.

The noise spectral densities are obtained by solving equation (B.24) in fourier space, as before. The spectrum in the steady state is,

$$\mathbf{S}(\omega) = \left\langle \mathbf{Z}(\omega)\mathbf{Z}(\omega)^\dagger \right\rangle$$

$$= \frac{1}{2\pi}(\mathbf{M} + i\omega\mathbf{I})^{-1}\mathbf{D}(\mathbf{M}^T - i\omega\mathbf{I})^{-1}$$

where **I** is the identity and

$$\mathbf{D} = \langle \mathbf{v}\mathbf{v}^T \rangle = k_B T \begin{pmatrix} \frac{\gamma_i}{m_i \omega_i^2} & 0 & 0 & 0 \\ 0 & \frac{\gamma_j}{m_j \omega_j^2} & 0 & 0 \\ 0 & 0 & \frac{\gamma_i}{m_i \omega_i^2} & 0 \\ 0 & 0 & 0 & \frac{\gamma_j}{m_j \omega_j^2} \end{pmatrix} \tag{B.24}$$

We construct composite quadratures $x_\pm = (\alpha_i \pm \alpha_j)/\sqrt{2}$, $y_\pm = (\beta_i \pm \beta_j)/\sqrt{2}$ as before and represent the fluctuations in these quadratures by the column matrix, $\mathbf{Z}_c = (\delta x_+, \delta x_-, \delta y_+, \delta y_-)^T$, which is related to $\mathbf{Z}$ by

$$\mathbf{Z}_c = \mathbf{R}\mathbf{Z}; \quad \mathbf{R} = \frac{1}{\sqrt{2}} \begin{pmatrix} 1 & 1 & 0 & 0 \\ 1 & -1 & 0 & 0 \\ 0 & 0 & 1 & 1 \\ 0 & 0 & 1 & -1 \end{pmatrix}$$

The correlations of the composite quadratures are therefore given by,

$$\mathbf{S}_c(\omega) = \langle \mathbf{Z}_c(\omega)\mathbf{Z}_c(\omega)^\dagger \rangle = \mathbf{R}\mathbf{S}\mathbf{R}^T$$

We consider the case where the frequencies of the resonator modes are identical and the losses are symmetric ($\delta_\gamma = \delta_\omega = 0$). For this case, the diffusion matrix $\mathbf{D} = \frac{k_B T \gamma}{m\omega^2}\delta_{ij}$.

The correlations between the composite quadratures in this case are given by,

$$\mathbf{S}_c(\omega) = \begin{pmatrix} S_{x_+,x_+} & 0 & S_{x_+,y_+} & 0 \\ 0 & S_{x_-,x_-} & 0 & S_{x_-,y_-} \\ S_{y_+,x_+} & 0 & S_{y_+,y_+} & 0 \\ 0 & S_{y_-,x_-} & 0 & S_{y_-,y_-} \end{pmatrix} \tag{B.25}$$

where the non zero correlations are as indicated above. There are no correlations between (x_+, x_-) and (y_+, y_-), given our choice of detection phases and the fact that we consider the case $\delta_\gamma = \delta_\omega = 0$. The correlations in equation (B.25)

evaluate to,

$$
\begin{aligned}
S_{x_\pm,x_\pm}(\omega) &= S_{y_\mp,y_\mp}(\omega) \\
&= \frac{k_B T \gamma}{m\omega^2} \frac{2\left(\Delta^2 + \gamma^2(1 \mp \mu)^2 + 4\omega^2\right)}{\pi\left(4\omega^2 + \lambda_+^2\right)\left(4\omega^2 + \lambda_-^2\right)} \\
S_{x_+,y_+}(\omega) &= S_{y_+,x_+}(\omega) \\
&= \frac{k_B T \gamma}{m\omega^2} \frac{4\Delta\left(\gamma\mu + 2i\omega\right)}{\pi\left(4\omega^2 + \lambda_+^2\right)\left(4\omega^2 + \lambda_-^2\right)} \\
&= S_{x_-,y_-}(-\omega) = S_{y_-,x_-}(-\omega)
\end{aligned}
$$

where $\lambda_\pm^2 = \gamma^2\left(1 + \mu^2\right) - \Delta^2 \pm 2\gamma\sqrt{\gamma^2\mu^2 - \Delta^2}$. The variances in the steady state obtained using the Weiner-Khintchine theorem are,

$$
\begin{aligned}
\sigma_{x_\pm,x_\pm} &= \left(\frac{k_B T \gamma}{m\omega^2}\right)\left[\frac{\left(\Delta^2 + \gamma^2(1 \mp \mu)^2 - \lambda_-^2\right)}{\lambda_+\lambda_-\left(\lambda_+ + \lambda_-\right)} + \frac{1}{\lambda_+}\right] \\
&= \sigma_{y_\mp,y_\mp}
\end{aligned}
$$

Unlike the case of zero detuning, we obtain non-zero steady state correlations between the x and y quadratures,

$$
\sigma_{x_\pm,y_\pm} = \left(\frac{k_B T \gamma}{m\omega^2}\right)\frac{2\Delta\gamma\mu}{\lambda_+\lambda_-\left(\lambda_+ + \lambda_-\right)} = \sigma_{y_\pm,x_\pm}
$$

The correlations between the $x_\pm$ and $y_\pm$ are now proportional to the drive detuning.

APPENDIX C

EMERGENT PHASES AND NOVEL CRITICAL BEHAVIOR IN A NON-MARKOVIAN OPEN QUANTUM SYSTEM

This chapter will be published in Physical Review A (2018) as *Emergent phases and novel critical behavior in a non-Markovian open quantum system, by H. F. H.Cheung, Y. S. Patil and M. Vengalattore*. In this work, H. F. H. Cheung and Y. S. Patil carried out the modeling and performed the calculations. M. Vengalattore supervised all stages of the work. All authors contributed to the preparation of the manuscript.

C.1   Abstract

Open quantum systems exhibit a range of novel out-of-equilibrium behavior due to the interplay between coherent quantum dynamics and dissipation. Of particular interest in these systems are driven, dissipative transitions, the emergence of dynamical phases with novel broken symmetries, and critical behavior that lies beyond the conventional paradigm of Landau-Ginzburg phenomenology. Here, we consider a parametrically driven two-mode system in the presence of non-Markovian system-reservoir interactions. We show that the non-Markovian dynamics modifies the phase diagram of this system resulting in the emergence of a novel broken symmetry phase in a new universality class that has no counterpart in the corresponding Markovian system. This emergent phase is accompanied by enhanced two-mode entanglement that remains

robust at finite temperatures. Such reservoir-engineered dynamical phases can potentially shed light on universal aspects of dynamical phase transitions in a wide range of non-equilibrium systems, and aid in the development of techniques for the robust generation of entanglement and quantum correlations at finite temperatures with potential applications to quantum control, state preparation and metrology.

C.2 Introduction

Due to the commensurate influence of quantum coherence and dissipation, the dynamical behavior of open quantum systems conforms neither to the framework of unitary quantum evolution nor to thermodynamic descriptions [230, 231]. Motivated by various applications to quantum information science, experimental realizations of such open systems have been developed in platforms spanning trapped ions [232], circuit-QED systems [233], optomechanical systems [78] and hybrid quantum systems [1]. The exploration of novel dynamical phases and the development of techniques for robust quantum state preparation and control in these systems presents significant theoretical and experimental challenges that lie at the interface of atomic physics, quantum optics, and condensed matter physics.

In addition to the traditional approach of Hamiltonian design, open quantum systems are amenable to control by modifying the nature of their environment. As such, the concept of reservoir-engineering [105] has emerged as a promising paradigm for the realization of novel states of open and driven quantum systems. In certain cases, it has been shown that reservoir-engineering

can be used to coax the open quantum system into phases that might not be accessible through more conventional forms of quantum state preparation [167, 106]. Aside from presenting alternate routes to quantum state preparation, such reservoir-engineered quantum phases present intriguing questions in their own right. For instance, it is unclear to what extent driven, dissipative transitions in open quantum systems accommodate the central paradigms of scale invariance, symmetry breaking and universality that underpin our understanding of equilibrium and quantum phase transitions.

Here, we explore the driven, dissipative transitions of a parametrically driven two-mode quantum system in the presence of a non-Markovian environment. This is a minimal physical realization of the parametric oscillator model [170, 234] and is closely connected to the open Dicke model [121, 145, 148], the superradiant phase transition [116] and the Lipkin-Meshkov-Glick model [235]. In the presence of a Markovian reservoir, it has been shown that this system exhibits a non-equilibrium phase transition into an ordered state that develops beyond a critical magnitude of the external drive [228]. Further, recent work has shown that the presence of a sub-ohmic reservoir modifies the critical exponents of this non-equilibrium transition while preserving the steady-state phase diagram [155, 236, 142].

In this work, we go beyond these prior results and identify a class of experimentally accessible non-Markovianity that leads to significant changes in the phase diagram of this system, leading to the emergence of a dynamical phase with novel broken symmetries and critical behavior that is distinct from that observed in the Markovian system. We also demonstrate that this novel emergent phase manifests significantly enhanced correlations and entanglement than can

be realized in the corresponding Markovian system. This two-mode entanglement is shown to persist even at finite temperatures and is a unique feature of the non-Markovian system-reservoir dynamics that allows for the backflow of information from the environment back into the system [237, 238]. This robust entanglement is distinct from Markovian system-reservoir dynamics that usually results in an irreversible loss of information and correlations into the environment. As such, our work points to an experimentally realizable instance where reservoir engineering techniques aid in the creation of robust, finite temperature correlations and entanglement with applications to various forms of metrology and quantum information processing.

C.3   Model

The Hamiltonian of our system is [150, 83]

$$\mathcal{H}/\hbar = \sum_k \omega_k \hat{a}_k^\dagger \hat{a}_k - \chi \hat{x}_P \hat{x}_i \hat{x}_s - (F_P e^{-i\omega_P t} \hat{a}_P^\dagger + \text{h.c.})$$

where the indices $k = \{i, s, P\}$ denote the idler, signal and pump modes at frequencies ω_k, and $\hat{a}_k$ denote their annihilation operators. The second term represents a two-mode interaction of strength χ between the signal and idler modes mediated by the actively driven pump. The third term represents the classical drive of the pump mode with magnitude F_P at its resonant frequency ω_P. The influence of the reservoir is incorporated through a master equation [151] and leads to Heisenberg-Langevin equations of the form

$$\begin{aligned}
\dot{a}_i &= -\frac{1}{2} \int_{-\infty}^t \gamma(t - t') a_i(t') dt' + ig a_s^\dagger a_P + i f_i \\
\dot{a}_s &= -\frac{1}{2} \int_{-\infty}^t \gamma(t - t') a_s(t') dt' + ig a_i^\dagger a_P + i f_s \\
\dot{a}_P &= -\frac{\gamma_P}{2} a_P + ig a_i a_s + i F_P
\end{aligned}$$

where $\gamma(t)$ is the dissipation kernel in the rotating frame, and is related to the Langevin forces $f_{i,s}$ through the fluctuation-dissipation theorem, and the normalized coupling strength is $g = \chi x_{0,i} x_{0,s} x_{0,P}$ with $x_{0,\{i,s,P\}}$ denoting the zero point amplitudes of the respective modes. In the above, we have made the rotating wave approximation, assumed that $\omega_P = \omega_i + \omega_s$ and that the damping rate of the pump mode γ_P is much larger than those of the signal and idler modes, in close accordance with experimental realizations of this model [150]. The equations of motion are invariant under the transformation $(\hat{a}_i, \hat{a}_s) \rightarrow (\hat{a}_i e^{+i\phi}, \hat{a}_s e^{-i\phi})$ for $\phi \in [0, 2\pi)$. In addition, the presence of the classical drive at the pump frequency implies that the equations of motion are also invariant under the transformation $(\hat{a}_i, \hat{a}_s, \hat{a}_P) \rightarrow (\hat{a}_i^\dagger, \hat{a}_s^\dagger, -\hat{a}_P^\dagger)$. Thus, the physical system possesses both a $U(1)$ symmetry and a $\mathbb{Z}_2$ symmetry.

For a Markovian reservoir, i.e. $\gamma(t) = \gamma_0 \delta(t)$, this system exhibits a continuous transition at a critical pump amplitude $F_{cr} = \frac{\gamma_P \gamma_0}{4g}$ from a disordered (parametric amplifier) phase to an ordered phase characterized by parametric self-oscillation of the signal and idler modes. This transition is accompanied by the spontaneous breaking of the $U(1)$ symmetry related to the difference between signal and idler phases [170, 83]. Similar phenomenology also arises in the closely related open Dicke model [121, 149].

Here, we consider the case where the signal and idler modes are in contact with a reservoir through a dissipation kernel $\gamma(t) = \gamma_0 \frac{e^{-t/\tau_r}}{\tau_r}$, where τ_r represents the coherence time or 'memory' of the non-Markovian reservoir. This form of non-Markovian dynamics arises naturally in the context of several cavity optomechanical systems [239, 150, 83, 218] as well as hybrid systems in which an optomechanical system is coupled to coherent ensembles of quantum spins
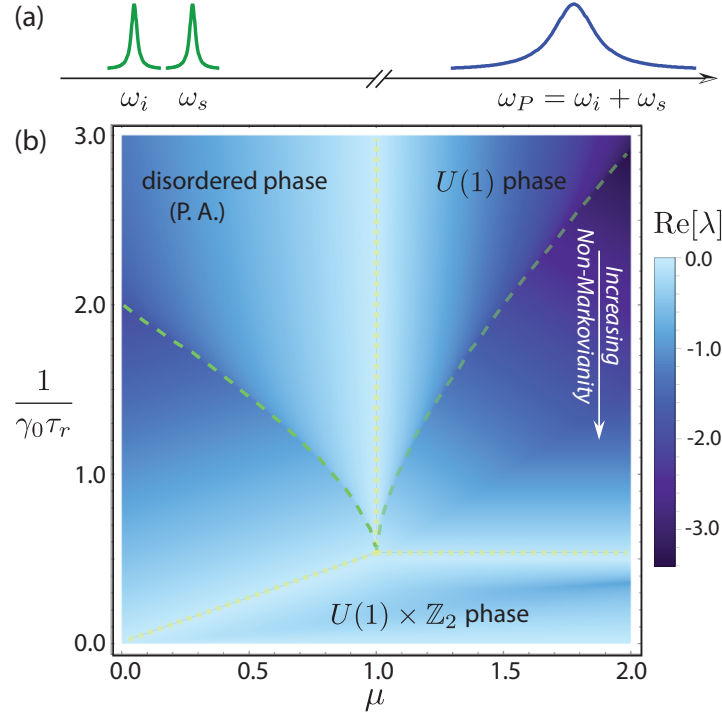
Figure C.1: (a) Schematic of the two-mode system. (b) The phase diagram as a function of the drive strength $\mu \equiv F_P/F_{cr}$ and the normalized reservoir decay rate $(\gamma_0\tau_r)^{-1}$. The color scale indicates the least negative real part of the eigenvalues λ of the dynamical matrix (see text). Critical points and phase boundaries (white dashed lines) correspond to the vanishing of this real part, i.e. a divergent relaxation time. The non-Markovian system-reservoir dynamics leads to the formation of exceptional points both in the disordered phase and the $U(1)$ phase. The trajectory of these exceptional points is indicated by the green dashed lines. (see text).

[240, 241].

C.4 Mean field solutions and the phase diagram

The Heisenberg-Langevin equations yield distinct steady state dynamical phases for this system. Such steady state solutions for the signal and idler

modes can be represented by the form $a_{i,s} = |a_{i,s}|e^{i\theta_{i,s}}e^{-i\Delta_{i,s}t}$. The Heisenberg-Langevin equations can be linearized around these steady state solutions and cast in Fourier space as $-i\omega\mathbf{a} = \Sigma\mathbf{a} + \mathbf{v}$ (see Supplementary Information, Section C.9.3). Here, $\mathbf{a} = (a_i, a_s, a_P)^T$, and the noise forces $\mathbf{v}$ are zero-mean gaussian variables whose correlation function is related to the dissipation kernel via the fluctuation-dissipation theorem. The eigenvalues λ of the inverse susceptibility matrix (or the dynamical matrix) $-\Sigma - i\omega\mathbf{I}$ determine the low energy eigenspectrum and steady-state phase diagram of this system. Phase boundaries between dynamical states of distinct symmetries are associated with a vanishing of the least negative real part of the eigenvalues λ, i.e. a divergent relaxation time [122, 242]. The stability of the mean field dynamical phases to generic perturbations is indicated by non-positive real parts of the eigenvalues. The mean field solutions of this non-Markovian system allow for three stable dynamical phases (Fig. C.1).

Disordered Phase : - In the limit of small pump drive, the intrinsic dissipation dominates the dynamics of the system. The steady state solution has a vanishing amplitude of the signal and idler modes. The nonlinear interaction between the two modes realizes a parametric amplifier with a phase-dependent gain that induces squeezing of composite quadratures formed from linear combinations of the signal and idler quadratures [83]. We denote this regime as the disordered or parametric amplifier (PA) phase.

U(1) Phase : - We first consider the regime of small reservoir coherence time, i.e. $(\gamma_0\tau_r)^{-1} \gg 1$. Note that the Markovian regime is obtained in the limit $(\gamma_0\tau_r)^{-1} \to \infty$. For a normalized pump drive $\mu = F_P/F_{cr} > 1$, the signal and idler modes exhibit parametric self-oscillation at their resonant frequencies $\omega_{i,s}$.

The steady-state solutions are $\bar{a}_{i,s} = i\frac{\sqrt{\gamma_0\gamma_P}}{2g}e^{\pm i\phi/2}\sqrt{\mu - 1}$. The $U(1)$ symmetry corresponding to the unconstrained phase difference ϕ between the signal and idler modes is spontaneously broken at the phase boundary $\mu_{cr} = 1$. As such, we denote this as the $U(1)$ phase. These solutions are consistent with the corresponding phases in a purely Markovian system.

$U(1) \times \mathbb{Z}_2$ *Phase* : - In contrast, as the coherence time τ_r is increased, the system is qualitatively modified due to the competing effects of dissipation and reservoir coherence. As the timescales of these processes become commensurate, the eigenvalues morph into complex conjugate pairs analogous to $\mathcal{PT}$ symmetry breaking. For $(\gamma_0\tau_r)^{-1} < \frac{1}{2}$, a new limit cycle solution emerges given by the solution $\bar{a}_i \propto ie^{i\phi/2}e^{-i\Delta t}\sqrt{\mu - \mu_{cr}}, \bar{a}_s \propto ie^{-i\phi/2}e^{i\Delta t}\sqrt{\mu - \mu_{cr}}$, or by the solution $\bar{a}_i \propto ie^{i\phi/2}e^{i\Delta t}\sqrt{\mu - \mu_{cr}}, \bar{a}_s \propto ie^{-i\phi/2}e^{-i\Delta t}\sqrt{\mu - \mu_{cr}}$. These solutions correspond respectively to a clockwise or counter-clockwise precession of the relative phase between these modes at an emergent limit cycle frequency $\Delta = \tau_r^{-1}\sqrt{\frac{\gamma_0\tau_r}{2} - 1}$ that depends solely on the environmental parameters. The underlying $\mathbb{Z}_2$ symmetry reflecting these two choices is thus spontaneously broken in this limit cycle phase. Further, the critical drive strength monotonically decreases as $\mu_{cr} = \frac{2}{\gamma_0\tau_r}$.

In this emergent limit cycle phase, the signal and idler modes exhibit self-oscillatory behavior not at their nominal resonances but at shifted frequencies $\omega_i \rightarrow \omega_i \pm \Delta, \omega_s \rightarrow \omega_s \mp \Delta$, with the choice of $\pm\Delta$ corresponding to a spontaneous breaking of a $\mathbb{Z}_2$ symmetry. In contrast to the fixed phase difference between the signal and idler modes in the $U(1)$ phase, the phases of these modes now oscillate at a rate Δ in this limit cycle phase. To further establish that this is a distinct phase, we calculate the dynamical states for a fixed drive $\mu > 1$ as the reservoir coherence time is reduced (Fig. C.3). We find that below the phase boundary

(a)

$U(1)$

$\bar{a}_i \propto e^{i\phi/2}$ $\bar{a}_s \propto e^{-i\phi/2}$

ω_i ω_s ω

$U(1) \times \mathbb{Z}_2$

$\bar{a}_i \propto e^{i\phi/2} \times e^{-i\Delta t}$ $\bar{a}_s \propto e^{-i\phi/2} \times e^{i\Delta t}$ $\bar{a}_i \propto e^{i\phi/2} \times e^{+i\Delta t}$ $\bar{a}_s \propto e^{-i\phi/2} \times e^{-i\Delta t}$

$\omega_i - \Delta$ $\omega_s + \Delta$ ω $\omega_i + \Delta$ $\omega_s - \Delta$ ω
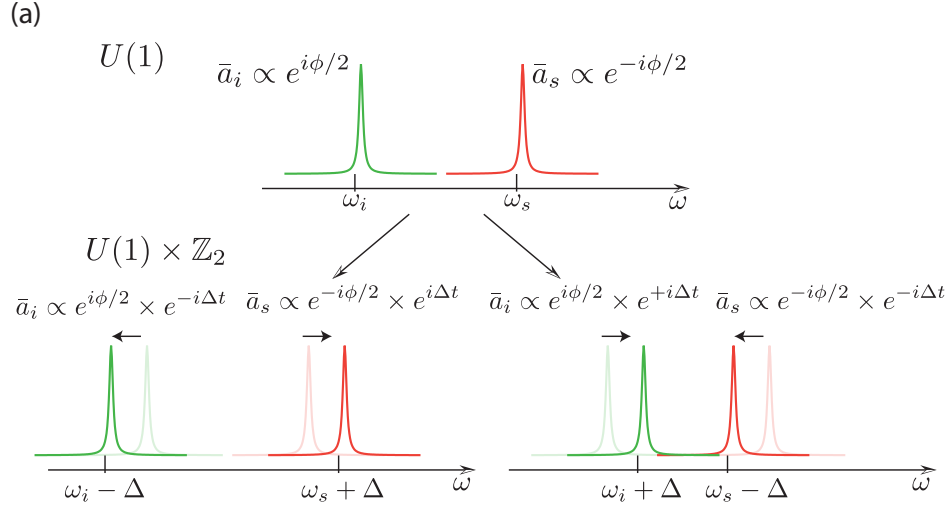
Figure C.2: (a) Schematic distinction between the $U(1)$ and the $U(1) \times \mathbb{Z}_2$ phases. The former phase is characterized by self-oscillation of the signal and idler modes with a spontaneously chosen phase difference ϕ between these modes. In contrast, the latter phase is further characterized by a limit cycle at an oscillation frequency Δ. There are two possible manifestations of such a limit cycle, corresponding to the choice of the sign of the limit cycle frequency. A particular choice of this sign spontaneously breaks the $\mathbb{Z}_2$ symmetry.

$(\gamma_0 \tau_r)^{-1} = \frac{1}{2}$, the limit cycle frequency Δ continuously grows from zero with its magnitude increasing as the square root of the distance from the critical point. We also compute the spectrum of Δ using a linearized equation, and find that its variance diverges at the $U(1) - U(1) \times \mathbb{Z}_2$ phase boundary, $(\gamma_0 \tau_r)^{-1} = \frac{1}{2}$ (see Fig. C.3), Supplementary Information, Section C.9.6). The square root dependence of Δ below the critical point and the divergence of its noise spectrum are characteristic of a continuous phase transition with an order parameter Δ.
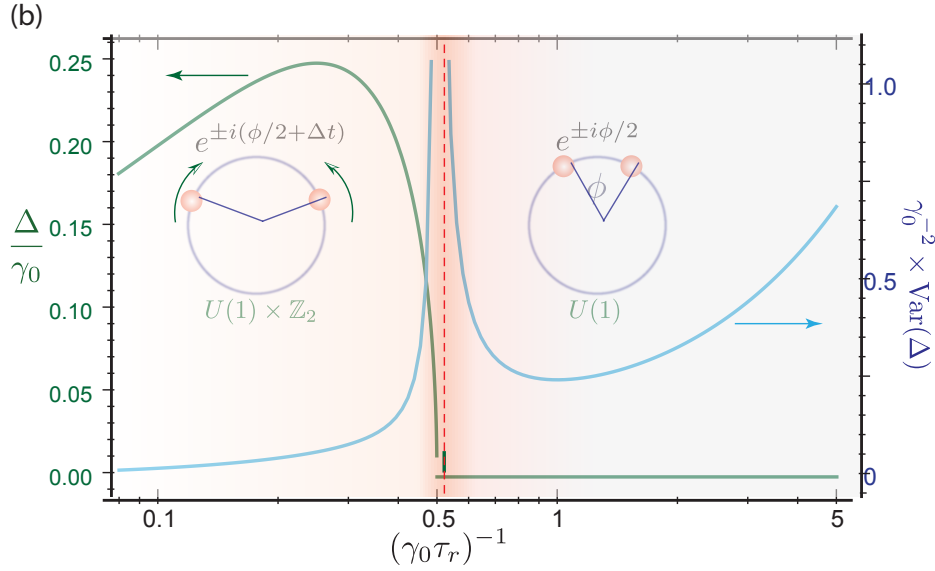
Figure C.3: (b) The transition between the $U(1)$ and the $U(1) \times \mathbb{Z}_2$ phase versus the normalized reservoir decay rate, $(\gamma_0 \tau_r)^{-1}$. The critical point occurs at $(\gamma_0 \tau_r)^{-1} = \frac{1}{2}$, corresponding to a divergent variance, $\mathrm{Var}(\Delta)$, of the limit cycle frequency Δ. Below this critical point, these modes no longer self-oscillate at their nominal resonances but shift to $\omega_i \to \omega_i \pm \Delta, \omega_s \to \omega_s \mp \Delta$, corresponding to a breaking of the $\mathbb{Z}_2$ symmetry (see inset, bottom). In contrast to the spontaneously chosen but constant phase difference between the two modes in the $U(1)$ phase, the phases of these modes now oscillate (see inset, top) at the frequency Δ that continuously grows from zero below the critical point. The calculations in this figure are performed for $\mu = 2$.

C.5 Effect of fluctuations and stability of the mean field phases

Here, we examine the stability of the mean field phases to generic gaussian perturbations. As described in the previous section, the stability of the mean field dynamical phases can be analyzed by evaluating the eigenspectrum of the dynamical matrix that governs the response of the various modes to perturbations. In particular, the stability of each of the dynamical phases is indicated by non-positive real parts of the eigenvalues λ of the dynamical matrix [122]. In other words, the mean field states are stable if the system responds to such perturba-

tions by relaxing back to its steady state with a finite damping rate. Similarly, phase boundaries are indicated in such an analysis by a vanishing real part of the least negative eigenvalue, i.e. a divergent relaxation time. While these calculations are detailed in the Supplementary Information Section C.9.3, we outline the procedure and discuss the main implications of these results below.

The Heisenberg-Langevin equations can be linearized around each distinct steady state solution as $a_{i,s,P} = \bar{a}_{i,s,P} + \delta a_{i,s,P}$, where $\bar{a}_{i,s,P}$ are the respective mean field solutions in the three dynamical phases. Cast in matrix form, the response of the fluctuations $\delta a_{i,s,P}$ to the noise forces is governed by the susceptibility matrix (also referred to as the dynamical matrix [122]). As shown in [83], this analysis is more conveniently performed for the respective cross-quadratures of the signal and idler modes and takes the form $\delta \tilde{\mathbf{x}} = -(\mathbf{\Sigma}(\omega) + i\omega\mathbf{I})^{-1}\tilde{\mathbf{v}}$ (see Supplementary Information, Section C.9.3). The poles of the susceptibility matrix are given by complex frequencies ω satisfying $\mathrm{Det}[\mathbf{\Sigma}(\omega) + i\omega\mathbf{I}] = 0$ and the eigenvalues of the inverse susceptibility matrix are defined as $\lambda = -i\omega$. The real part of these eigenvalues correspond to the damping rate of the system's response to generic perturbations.

This analysis, performed by linearizing the system around the disordered (PA) phase, yields the eigenvalues $\lambda_\pm = \frac{\gamma_0}{4}\left[(\mu - \frac{2}{\gamma_0\tau_r}) \pm \sqrt{(\mu + \frac{2}{\gamma_0\tau_r})^2 - \frac{8}{\gamma_0\tau_r}}\right]$. Deep in the Markovian regime, $(\gamma_0\tau_r)^{-1} \gg 1$, these eigenvalues are purely real and negative for $\mu < 1$ indicating the stability of this phase. As the reservoir coherence time is increased, the eigenvalues remain real and negative in the vicinity of the critical point $\mu = 1$ (orange curves in Fig. C.4). Similar analysis can also be performed by linearizing the system around the mean field solutions for the $U(1)$ and $U(1) \times \mathbb{Z}_2$ phases indicating that these solutions too are stable to

generic perturbations in their respective domains. This stability is illustrated for the three phases for representative choices of the parameter $(\gamma_0\tau_r)^{-1}$ in Fig. C.4.
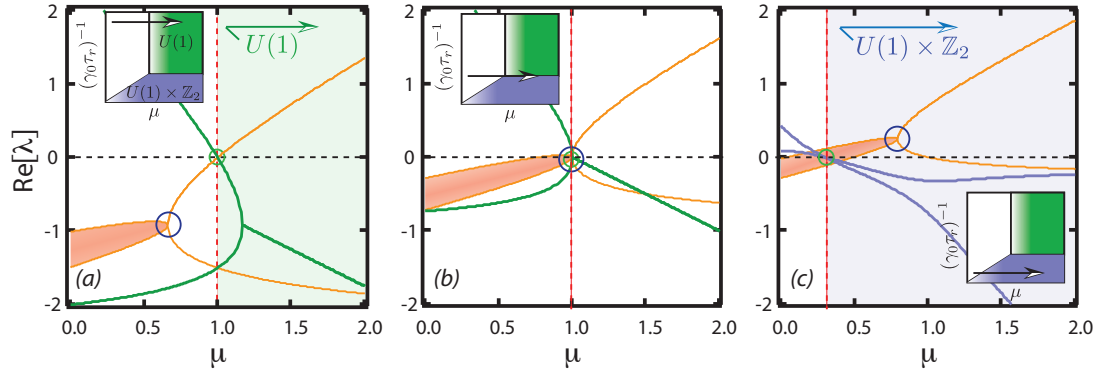
Figure C.4: The behavior of the low lying eigenspectrum corresponding to the disordered phase (orange), $U(1)$ phase (green) and $U(1){\times}\mathbb{Z}_2$ phase (blue). The eigenvalues are obtained by linearizing the equations of motion around the steady state solutions in the three different phases. Shown here are two eigenvalues with the lowest negative real parts for each phase. Figures (a) to (c) demonstrate the trend with increasing reservoir coherence time τ_r showing the relative positions of the exceptional point (blue circle) and the critical point (green circle) *vs* the drive strength μ. For the disordered phase (orange traces), the imaginary part of the eigenvalue is represented as the width of the eigenmode. The exceptional point corresponds to a coalescence of the eigenvalues and eigenmodes and a vanishing imaginary part. The critical point occurs when the disordered phase becomes unstable (Re$[\lambda] > 0$) and gives way to the broken symmetry phases. (a) In the regime $\frac{1}{2} < (\gamma_0\tau_r)^{-1} < 2$, the exceptional point occurs before the critical point governing the transition to the $U(1)$ phase. The eigenvalues are purely real in the vicinity of the critical point. As such, the critical behavior in this regime can be mapped onto a supercritical pitchfork bifurcation. (b) At $(\gamma_0\tau_r)^{-1} = \frac{1}{2}$, the exceptional point and the critical point coincide, i.e. the real and imaginary parts of the eigenvalues vanish simultaneously at the critical point, indicating the emergence of the $U(1) \times \mathbb{Z}_2$ phase. (c) Deep in the non-Markovian regime, i.e. $(\gamma_0\tau_r)^{-1} < \frac{1}{2}$, the critical point occurs before the exceptional point and the transition to the $U(1) \times \mathbb{Z}_2$ phase occurs when the eigenvalues are purely imaginary. Here, the critical behavior corresponds to a supercritical Hopf bifurcation. The displayed eigenspectra correspond to (a) $(\gamma_0\tau_r)^{-1} = 1.25$, (b) $(\gamma_0\tau_r)^{-1} = 0.50$, and (c) $(\gamma_0\tau_r)^{-1} = 0.15$.

In addition to confirming the stability of the mean field phases, the above analysis also sheds light on other features of this system that arise from the non-Markovian system-reservoir interactions. In particular, it reveals the emergence of new phenomenology associated with the presence of exceptional points [243, 244] in the phase diagram. For $(\gamma_0\tau_r)^{-1} > 2$, the eigenvalues corresponding to the disordered phase are purely real and the system can be mapped onto the Markovian system. However, as the coherence time of the reservoir is increased, the eigenvalues morph into complex conjugate pairs for sufficiently small drive μ. This qualitative shift in the nature of the eigenvalues from purely real to complex conjugate values occurs at a distinct point in the system where two eigenvalues (and their corresponding eigenmodes) coalesce. Such distinct points are referred to as exceptional points and are associated with unique topological properties akin to a Berry's phase [244].

In the disordered phase, we find that the locus of exceptional points is described by the contour $(\mu\gamma_0\tau_r + 2)^2 - 8\gamma_0\tau_r = 0$ (see Supplementary Information, Section C.9.5). Similarly, the contour of exceptional points in the $U(1)$ phase is described by the equation $4 + 4\gamma_0\tau_r(4 - 8\mu) + ((2\mu - 3)\gamma_0\tau_r)^2 = 0$. As seen in Fig. C.1, the trajectories of these exceptional points within the disordered and $U(1)$ phase meet at the multicritical point $\mu = 1, (\gamma_0\tau_r)^{-1} = \frac{1}{2}$. At this multicritical point, the exceptional points coincide with a critical point, i.e. both the real and imaginary parts of the eigenvalues λ simultaneously vanish, heralding the emergence of the $U(1) \times \mathbb{Z}_2$ phase.

The relative positions of the exceptional points and the phase boundary is shown in Fig. C.4 for various regimes of reservoir coherence times. For small reservoir coherence time with $(\gamma_0\tau_r)^{-1} > \frac{1}{2}$, the exceptional point occurs for

222

pump drives $\mu < 1$. As such, the eigenvalues of the disordered phase are purely real near the critical point (Fig. C.4(a)). As the reservoir coherence time is increased, the exceptional point approaches the critical point $\mu = 1$ from below. In contrast, for large reservoir coherence times $(\gamma_0 \tau_r)^{-1} < \frac{1}{2}$, the exceptional point occurs for values of pump drive beyond the critical pump strength. As such, the eigenvalues corresponding to the disordered phase are purely imaginary at the critical point separating the disordered phase from the $U(1) \times \mathbb{Z}_2$ phase (Fig. C.4(c)). At the multicritical point $(\gamma_0 \tau_r)^{-1} = \frac{1}{2}$, the critical point $\mu_{cr} = 1$ coincides with the exceptional point and the real and imaginary parts of $\lambda_{\pm}$ simultaneously vanish (Fig. C.4(b)), leading to non-reciprocal behavior and the simultaneous breaking of a discrete ($\mathbb{Z}_2$) symmetry in addition to the U(1) symmetry related to the signal-idler phase difference.

C.6   Novel critical behavior

In addition to the emergence of the novel $U(1) \times \mathbb{Z}_2$ phase, the presence of the non-Markovian system-reservoir interactions also result in novel critical behavior in this system. Note that the phase diagram defines three phase transitions : the $PA - U(1)$ transition, the $PA - U(1) \times \mathbb{Z}_2$ transition, and the $U(1) - U(1) \times \mathbb{Z}_2$ transition. These phase boundaries meet at the multicritical point defined by the parameters $\mu = 1, (\gamma_0 \tau_r)^{-1} = \frac{1}{2}$. Below, we discuss the critical behavior at each of these phase boundaries.

The $PA - U(1)$ phase transition : - In the Markovian limit of this system, i.e. $(\gamma_0 \tau_r)^{-1} \gg 1$, the transition into the $U(1)$ phase occurs at the normalized drive amplitude $\mu = 1$. Accordingly, we can define the reduced distance from critical-

ity as $\epsilon = (\mu - 1)$. The eigenvalues λ corresponding to the disordered phase are purely real in the vicinity of the phase boundary. Moreover, the least negative eigenvalue scales near the critical point as $\lambda(\epsilon) \sim \epsilon$, thereby defining the critical exponent $\nu z = 1$ in this regime. Further, the steady-state amplitudes of the signal and idler modes in the $U(1)$ phase scale as $|a_{i,s}| \sim \sqrt{\epsilon}$, defining the critical exponent $\beta = 1/2$. Lastly, the variance of this steady-state amplitude and the susceptibility of this order parameter diverges near the phase boundary according to the relation $\text{Var}(a_{i,s}) \sim |\epsilon|^{-1}$, defining the critical exponent $\gamma = 1$. These exponents are identical to the $PA - U(1)$ phase transition in the Markovian system. We also note that this phase transition can also be viewed as a supercritical pitchfork bifurcation [245].

The $PA - U(1) \times \mathbb{Z}_2$ phase transition : - In the regime $(\gamma_0 \tau_r)^{-1} < \frac{1}{2}$, the transition between the disordered phase and the $U(1) \times \mathbb{Z}_2$ phase occurs at the critical point $\mu_{cr} = \frac{2}{\gamma_0 \tau_r}$. Defining the reduced distance from criticality as $\epsilon \equiv \frac{\mu - \mu_{cr}}{\mu_{cr}}$, the eigenvalues λ corresponding to the disordered phase are purely imaginary in the vicinity of this critical point, i.e. $\lambda(\epsilon) \sim \epsilon + i(\Delta + O(\epsilon))$. Due to the non-zero limit cycle frequency Δ near the critical point, this transition corresponds to a supercritical Hopf bifurcation [246, 247] with an additional $\mathbb{Z}_2$ symmetry.

From the above discussions, it can be seen that the transition out of the disordered phase morphs from a supercritical pitchfork bifurcation for $(\gamma_0 \tau_r)^{-1} > \frac{1}{2}$ to a supercritical Hopf bifurcation for $(\gamma_0 \tau_r)^{-1} < \frac{1}{2}$. At the multicritical point $\mu = 1, (\gamma_0 \tau_r)^{-1} = 1/2$, the eigenvalues corresponding to the disordered phase coalesce and the critical point coincides with an exceptional point, i.e. both the real and imaginary parts of the eigenvalues simultaneously vanish with $\lambda \sim \epsilon + 2i \sqrt{|\epsilon|}$. As such, in addition to the divergent relaxation time represented

by the vanishing real part of the eigenvalue, the vanishing imaginary part sets an additional divergent timescale near criticality. This latter divergence corresponds to the period of the limit cycle in the $U(1) \times \mathbb{Z}_2$ phase at this multicritical point. Further, this divergent period of the limit cycle at the critical point also implies that the transition cannot be mapped onto to a conventional supercritical Hopf bifurcation. The dual divergence of the relaxation and oscillation timescales, corresponding to the coincidence of a critical point with an exceptional point, is a unique feature of the non-Markovian dynamics. Additionally, the variance of the steady-state amplitudes at the multicritical point diverges as $\mathrm{Var}(a_{i,s}) \sim |\epsilon|^{-2}$, defining the critical exponent $\gamma = 2$.

The $U(1) - U(1) \times \mathbb{Z}_2$ phase transition : - The phase transition between these two phases can be accessed by tuning the normalized system-reservoir coherence time $(\gamma_0 \tau_r)^{-1}$. The phase transition occurs at $(\gamma_0 \tau_r)^{-1} = \frac{1}{2}$, and the appropriate reduced distance from criticality is given by $\epsilon_r = 2(\gamma_0 \tau_r)^{-1} - 1$. As described earlier, the limit cycle frequency Δ grows as $O(\sqrt{|\epsilon_r|})$ and the amplitude of the limit cycle is independent of the distance to the critical point. Again, these scaling relations are distinct from limit cycle behaviors found in other driven dissipative systems or a conventional supercritical Hopf bifurcation where instead, the frequency of the limit cycle scales as $O(1)$ near criticality while the amplitude of the limit cycle scales as $O(\sqrt{\epsilon})$ [245, 123, 248].

C.7 Enhanced squeezing and correlations due to non-Markovian dynamics

Next, we discuss the two-mode squeezing and entanglement in this system and the effect of non-Markovian dynamics on the observed entanglement. As is well known from prior work on this model [170, 83], the two-mode interaction results in correlations, squeezing and entanglement between quadratures of the signal and idler modes. In comparison to the corresponding Markovian system, the presence of the non-Markovian system-reservoir interactions and the appearance of the exceptional point near the $U(1) - U(1) \times \mathbb{Z}_2$ phase boundary result in an enhanced degree of entanglement between the two modes.

As shown in [83], the fluctuation spectra and two-mode correlations are obtained from the power spectral densities of the cross-quadratures via the relation $\mathbf{S}_{X,Y}(\omega) = \frac{1}{2\pi}(\tilde{\boldsymbol{\Sigma}}_{X,Y} + i\omega\mathbf{I})^{-1}\mathbf{D}(\tilde{\boldsymbol{\Sigma}}_{X,Y}^{\dagger} - i\omega\mathbf{I})^{-1}$, where the diffusion matrix is given by

$$\mathbf{D} = \frac{1}{2}\begin{pmatrix} \frac{4g^2}{\gamma_0\gamma_P}\tilde{\gamma}'(\omega)(\bar{n}_{th,i} + \frac{1}{2}) & 0 & 0 \\ 0 & \frac{4g^2}{\gamma_0\gamma_P}\tilde{\gamma}'(\omega)(\bar{n}_{th,s} + \frac{1}{2}) & 0 \\ 0 & 0 & \frac{4g^2}{\gamma_0^2}\gamma_P(\bar{n}_{th,P} + \frac{1}{2}) \end{pmatrix} \qquad \text{(C.1)}$$

where $\tilde{\gamma}'(\omega) = \text{Re}[\tilde{\gamma}(\omega)] = \gamma_0\frac{1}{1+(\omega\tau_r)^2}$ and the thermal phonon numbers are related to the effective temperature of the modes, i.e. $\bar{n}_{th,i,s,P} = (\exp(\frac{\hbar\omega_{i,s,P}}{k_B T}) - 1)^{-1}$. The steady state variances of the cross-quadratures can be obtained from the fluctuation spectrum using the Wiener-Khintchine theorem by integrating the fluctuations,

$$\sigma_{X,Y} = \int_{-\infty}^{\infty} \mathbf{S}_{X,Y}(\omega)d\omega$$

Below threshold, the squeezed and amplified variances (normalized to the

thermal variances) are respectively given by

$$\sigma_{sq} = \frac{2(\gamma_0\tau_r)^{-1}}{(1+\mu)(2(\gamma_0\tau_r)^{-1}+\mu)}$$

$$\sigma_{amp} = \frac{2(\gamma_0\tau_r)^{-1}}{(1-\mu)(2(\gamma_0\tau_r)^{-1}-\mu)}$$

The squeezed variance at steady state is minimized at $\mu = \mu_{cr} = \min(1, 2(\gamma_0\tau_r)^{-1})$. In particular, close to the multicritical point $\mu_{cr} = 1, (\gamma_0\tau_r)^{-1} = \frac{1}{2}$, we obtain a steady state squeezing limit $\sigma_{sq} = \frac{1}{4}$, outperforming the Markovian steady-state squeezing limit of $\sigma_{sq} = \frac{1}{2}$.

Above threshold, in the $U(1)$ phase, the normalized variances of the cross-quadratures are given by

$$\sigma_{x_+} = \frac{\bar{n}_{th,P} + \frac{1}{2}}{\bar{n}_{th} + \frac{1}{2}} \frac{2(\mu-1)(\mu+(\gamma_0\tau_r)^{-1})}{\mu(2(\gamma_0\tau_r)^{-1}+2\mu-1)} +$$

$$\Psi + \frac{(\gamma_0\tau_r)^{-1}}{\mu(2(\gamma_0\tau_r)^{-1}+2\mu-1)}$$

$$\sigma_{x_-} \to \infty$$

$$\sigma_{y_+} = \frac{\bar{n}_{th,P} + \frac{1}{2}}{\bar{n}_{th} + \frac{1}{2}} \frac{2(\mu-1+(\gamma_0\tau_r)^{-1})}{(2(\gamma_0\tau_r)^{-1}+2\mu-3)} +$$

$$\Psi + \frac{(\gamma_0\tau_r)^{-1}}{(\mu-1)(2(\gamma_0\tau_r)^{-1}+2\mu-3)}$$

$$\sigma_{y_-} = \frac{(\gamma_0\tau_r)^{-1}}{1+2(\gamma_0\tau_r)^{-1}}$$

where $x_\pm, y_\pm$ are the cross-quadratures composed of symmetric and anti-symmetric combinations of the signal and idler quadratures (see Supplementary Information, Section C.9.4). Here, we have assumed that $\bar{n}_{th} \equiv \bar{n}_{th,i} \approx \bar{n}_{th,s}$.

In the $U(1) \times \mathbb{Z}_2$ phase, the non-zero limit cycle frequency Δ introduces a coupling between the nominally orthogonal cross-quadratures. Aside from this modification, the computation of the various variances proceeds as before.

By dynamically varying the pump drive strength μ on timescales short compared to γ_0^{-1} and τ_r, we can achieve a degree of transient squeezing much
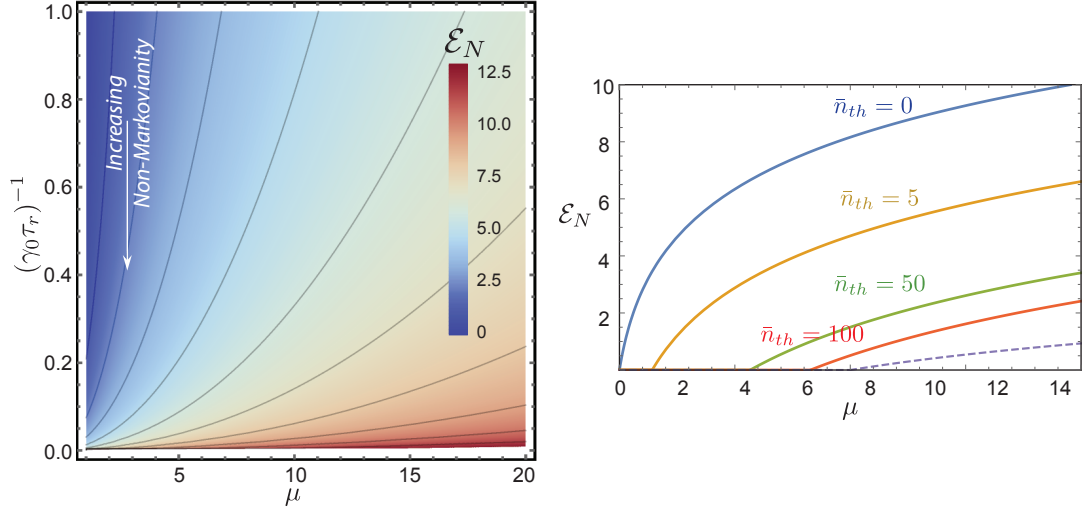
Figure C.5: (Left) The logarithmic negativity $\mathcal{E}_N$ as a measure of the bipartite entanglement [249, 250] between the signal and idler modes *vs* the drive strength μ and the normalized reservoir decay rate $(\gamma_0 \tau_r)^{-1}$. (Right) In the $U(1) \times \mathbb{Z}_2$ phase, the entanglement between the two modes extends well beyond the quantum regime and can be observed even for large thermal occupancy of the two modes. The logarithmic negativity is shown for increasing thermal occupancy $\bar{n}_{th}$ *vs* drive strength for $(\gamma_0 \tau_r)^{-1} = \frac{1}{5}$. For comparison, the logarithmic negativity for a Markovian system with $\bar{n}_{th} = 5$ is shown by the dashed line.

larger than that achievable in steady state [251] (see also Appendix D). In fact, the variance of the transiently squeezed cross-quadratures scales as $(\bar{n}_{th} + \frac{1}{2})\frac{2(\gamma_0 \tau_r)^{-1}}{(1+\mu)(2(\gamma_0 \tau_r)^{-1}+\mu)} \propto \frac{1}{\mu^2}$ for large drive strength, in contrast to the Markovian scaling $(\bar{n}_{th} + \frac{1}{2})\frac{1}{1+\mu} \propto \frac{1}{\mu}$, where $\bar{n}_{th}$ is the average thermal population of the signal and idler modes (see Supplementary Information, Section C.9.4, [83], [251], Appendix D). This enhancement over a Markovian system is also reflected in the logarithmic negativity $\mathcal{E}_N = -\frac{1}{2} \log_2 \left[\min(\frac{\sigma_{sq}}{\sigma_{zpm}}, 1)\right]$, where σ_{zpm} is the zero point variance of the cross-quadratures. As can be seen in Fig. C.5, this enhanced degree of entanglement persists even at large thermal occupancy of the signal and idler modes. We speculate that this enhancement is due to the topological prop-

erties of the exceptional point and the non-reciprocal behavior of the system in its vicinity.

C.8   Conclusions

In summary, we consider a parametrically driven two-mode quantum system and identify a class of non-Markovian system-reservoir interactions that results in the emergence of a novel broken symmetry phase in this quantum system. We analyze the phase diagram of this system and show that the emergent phase is accompanied by the appearance of exceptional points in the system. This emergent phase manifests a larger degree of two-mode entanglement than would be observed in the corresponding Markovian system. We note that the two-mode system and the form of non-Markovianity considered here are readily accessible in cavity optomechanical systems as well as various hybrid quantum systems, paving the way for experimental demonstrations of these predictions well into the quantum regime. Future work will extend this analysis to the regime of spatially multimode optomechanical systems and discuss the interplay between non-Markovian correlations, optomechanical synchronization, spatial fluctuations and driven, dissipative dynamics. In addition to realizing metrologically relevant optomechanical states, we suggest that this interplay also offers a new arena for disorder-free optomechanical realizations of dynamical phases with novel broken symmetries such as have been recently observed in spin systems [163, 162].

C.9 Supplementary Information

C.9.1 Equations of motion

The Hamiltonian for the two-mode driven dissipative system is given by [170, 150, 83]

$$\mathcal{H}/\hbar = \sum_{k=\{i,s,P\}} \omega_k \hat{a}_k^\dagger \hat{a}_k - \chi \hat{x}_P \hat{x}_i \hat{x}_s - (F_P e^{-i\omega_P t} \hat{a}_P^\dagger + \text{h.c.}) \qquad \text{(C.2)}$$

In the interaction picture with $\mathcal{H}_0/\hbar = \sum_k \omega_k \hat{a}_k^\dagger \hat{a}_k$, and making the rotating wave approximation, the interaction Hamiltonian transforms to $\mathcal{H}/\hbar = -g(\hat{a}_s^\dagger \hat{a}_i^\dagger \hat{a}_P + \hat{a}_P^\dagger \hat{a}_s \hat{a}_i) - (F_P \hat{a}_P^\dagger + \text{h.c.})$ where $g = \chi x_{0,i} x_{0,s} x_{0,P}$ and $x_{0,k}$ denotes the zero-point amplitude of the respective modes. Here, we have assumed that the pump mode is actuated by a resonant, classical force and that $\omega_P = \omega_i + \omega_s$.

Further, the influence of the reservoir on these modes is incorporated through noise operators $\hat{f}$ and takes the form $\mathcal{H}_r/\hbar = -\sum_k (\hat{a}_k^\dagger \hat{f}_k + \text{h.c.})$. For the signal and idler modes, these noise forces are zero-mean, gaussian random variables whose two-point correlation is related to the dissipation kernel $\gamma(t)$ in accordance with the fluctuation dissipation theorem. Here, we assume that the signal and idler modes are in contact with a colored reservoir with a dissipation kernel given by $\gamma(t-t') = \gamma_0 \tau_r^{-1} \exp(-(t-t')/\tau_r)\Theta(t-t')$ where $\Theta(t)$ is the Heaviside step function. Accordingly, these noise forces satisfy the following relations, $\langle f_k \rangle = 0$, and $\langle f_k(t) f_l^\dagger(t') \rangle = \delta_{kl} \times (\bar{n}_{th} + 1)\frac{\gamma_0}{2\tau_r} e^{-|t-t'|/\tau_r}$ where $\bar{n}_{th} = (\exp(\frac{\hbar\omega_{i,s}}{k_B T}) - 1)^{-1}$.

In accordance with typical experimental situations in optomechanical systems [150], we assume that the pump mode is in contact with a Markovian reservoir and that its damping rate is much larger than those of the signal and idler modes, i.e. $\gamma_P \gg \gamma_0$. This leads to the Heisenberg-Langevin equations of

the form

$$\dot{a}_i = -\frac{1}{2}\int_{-\infty}^{t} \gamma(t-t')a_i(t')dt' + iga_s^\dagger a_P + if_i \tag{C.3}$$

$$\dot{a}_s = -\frac{1}{2}\int_{-\infty}^{t} \gamma(t-t')a_s(t')dt' + iga_i^\dagger a_P + if_s \tag{C.4}$$

$$\dot{a}_P = -\frac{\gamma_P}{2}a_P + iga_i a_s + iF_P \tag{C.5}$$

Here, we are ignoring the Langevin forces on the pump. As explained in [83], the pump noise can be ignored in evaluating the dynamical steady-state phases or the degree of two-mode correlations below threshold. Above threshold, this pump noise has an appreciable effect on the two-mode squeezing. In our calculations of the squeezing spectra above threshold, this pump noise is included by assuming that the pump mode is in contact with a Markovian reservoir as explained in [83].

These equations can be recast by defining the dimensionless amplitudes $A_{i,s} = a_{i,s}\frac{2g}{\sqrt{\gamma_0\gamma_P}}$ and $A_P = a_P\frac{2g}{\gamma_0}$ to obtain

$$\dot{A}_i = \frac{1}{2}\left[-\int_{-\infty}^{t} \gamma(t-t')A_i(t')dt' + i\gamma_0 A_s^* A_P + i\gamma_0 \tilde{f}_i\right] \tag{C.6}$$

$$\dot{A}_s = \frac{1}{2}\left[-\int_{-\infty}^{t} \gamma(t-t')A_s(t')dt' + i\gamma_0 A_i^* A_P + i\gamma_0 \tilde{f}_s\right] \tag{C.7}$$

$$\dot{A}_P = \frac{1}{2}[-\gamma_P A_P + i\gamma_P A_i A_s + i\gamma_P \mu] \tag{C.8}$$

where $\tilde{f}_{i,s} = \gamma_0^{-1}\frac{4g}{\sqrt{\gamma_0\gamma_P}}f_{i,s}$ and we have defined the normalized drive strength $\mu = F_P/F_{cr}$ where $F_{cr} = \frac{\gamma_P\gamma_0}{4g}$.

C.9.2 Steady state dynamical phases and mean field phase diagram

We consider the situation where the signal and idler modes are not driven, i.e. they are only subject to the Langevin forces originating from their coupling to the colored reservoir. In contrast, the pump mode is actively driven by a classical force represented by the normalized drive μ. In various regimes of the drive strength μ and the reservoir coherence time τ_r, we consider dynamical steady-state phases represented by the ansatz

$$A_{i,s} = \bar{A}_{i,s} e^{-i\Delta_{i,s}t} \tag{C.9}$$

$$A_P = \bar{A}_P \tag{C.10}$$

Substituting this ansatz into Eqns. (C.6 − C.8), we obtain

$$-i\Delta_i \bar{A}_i e^{-i\Delta_i t} = -\frac{1}{2} e^{-i\Delta_i t} \bar{A}_i \tilde{\gamma}(\Delta_i) + i\frac{\gamma_0}{2} \bar{A}_s^* \bar{A}_P e^{i\Delta_s t} \tag{C.11}$$

$$-i\Delta_s \bar{A}_s e^{-i\Delta_s t} = -\frac{1}{2} e^{-i\Delta_s t} \bar{A}_s \tilde{\gamma}(\Delta_s) + i\frac{\gamma_0}{2} \bar{A}_i^* \bar{A}_P e^{i\Delta_i t} \tag{C.12}$$

$$0 = -\frac{1}{2}\gamma_P \bar{A}_P + i\frac{\gamma_P}{2} \bar{A}_i \bar{A}_s e^{-i(\Delta_i + \Delta_s)t} + i\frac{\gamma_P}{2}\mu$$

$$\tag{C.13}$$

Here, we have used the fourier transform of the dissipation kernel, $\tilde{\gamma}(\omega) = \int dt\gamma(t)e^{i\omega t} = \gamma_0(1 - i\omega\tau_r)^{-1}$.

These equations always admit the trivial solution $\bar{A}_i = \bar{A}_s = 0, \bar{A}_P = i\mu$. For dynamical steady-states with finite signal and idler amplitudes, the above equations require $\Delta_i + \Delta_s = 0$. Hence, below we define $\Delta \equiv \Delta_i = -\Delta_s$. Eqns. (C.11,C.12) together yield the following condition

$$\left(\frac{\tilde{\gamma}(\Delta)}{2} - i\Delta\right)\left(\frac{\tilde{\gamma}(-\Delta)}{2} + i\Delta\right)^* \bar{A}_i = \frac{\gamma_0^2}{4}|\bar{A}_P|^2 \bar{A}_i \tag{C.14}$$

Since $\tilde{\gamma}(-\omega) = \tilde{\gamma}^*(\omega)$, this requires steady-state phases with non-zero signal and

idler mode amplitudes to satisfy the condition

$$\left(\frac{\tilde{\gamma}(\Delta)}{2} - i\Delta\right)^2 = \frac{\gamma_0^2}{4}|\bar{A}_P|^2 \tag{C.15}$$

indicating that $\frac{\tilde{\gamma}_0}{2} \equiv \frac{\tilde{\gamma}(\Delta)}{2} - i\Delta$ is real and positive. Further, Eqns. (C.11,C.12) in combination with Eqn. (C.13) yields the following expression for the signal and idler amplitudes,

$$\left(\frac{\tilde{\gamma}_0}{\gamma_0}\right)^2 \left[1 + 2\left|\frac{\gamma_0}{\tilde{\gamma}_0}\right||\bar{A}_{i,s}|^2 + \left|\frac{\gamma_0}{\tilde{\gamma}_0}\right|^2 |\bar{A}_{i,s}|^4\right] = \mu^2 \tag{C.16}$$

$$\Rightarrow |\bar{A}_{i,s}| = \sqrt{\mu - \frac{\tilde{\gamma}_0}{\gamma_0}} \tag{C.17}$$

Accordingly, we define the critical pump amplitude $\mu_{cr} = \tilde{\gamma}_0/\gamma_0$ as the drive strength beyond which the signal and idler modes develop a non-zero amplitude, i.e. the onset of parametric self-oscillation.

Lastly, given the constraint from Eqn. (C.15) that $\tilde{\gamma}_0/2$ be real-valued and positive, we obtain

$$\frac{1}{2}\tilde{\gamma}(\Delta) - i\Delta = \frac{1}{2}\frac{\gamma_0}{1 + \tau_r^2\Delta^2} + i\Delta\left(\frac{1}{2}\frac{\gamma_0\tau_r}{1 + \tau_r^2\Delta^2} - 1\right) \in \mathbb{R} \tag{C.18}$$

yielding $\Delta = 0$, or $\Delta = \tau_r^{-1}\sqrt{\frac{\gamma_0\tau_r}{2} - 1}$. Note that the latter solution is only meaningful for $\gamma_0 \geq 2\tau_r^{-1}$.

Based on these relations, we can identify three distinct dynamical phases in this system.

- In the regime $\gamma_0 \leq 2\tau_r^{-1}$, the coherence time of the reservoir is small compared to the intrinsic damping time of the signal/idler modes. Here, we obtain the condition $\Delta = 0$ and $\tilde{\gamma}_0 = \tilde{\gamma}(0) = \gamma_0$. Hence, the critical drive strength is given by $\mu_{cr} = 1$. In this regime, for drive strengths $\mu < 1$, the only stable phase is the trivial solution $\bar{A}_i = \bar{A}_s = 0, \bar{A}_P = i\mu$. This is the disordered or parametric amplifier phase. As the drive strength is in-

233

creased beyond $\mu_{cr} = 1$, the parametric amplifier phase becomes unstable (Fig. C.4(a)) and gives way to the parametric oscillator phase character-ized by $\bar{A}_{i,s} = ie^{\pm i\phi/2}\sqrt{\mu - 1}, \bar{A}_P = i$. The signal-idler phase difference ϕ is unconstrained and the emergence of this parametric oscillator phase is ac-companied by the spontaneous breaking of the $U(1)$ symmetry associated with the choice of this phase. As such, we denote this to be the $U(1)$ phase.

- In the regime $\gamma_0 > 2\tau_r^{-1}$, the coherence time of the reservoir is long com-pared to the damping time of the signal/idler modes. As seen from Eqns. (C.17, C.18), in this regime the critical point shifts to $\mu_{cr} = 2(\gamma_0\tau_r)^{-1} < 1$. For $\mu < \mu_{cr}$, the only stable phase is the disordered or trivial solution with $\bar{A}_{i,s} = 0$. For drive strengths $\mu_{cr} < \mu$, the disordered phase is unsta-ble and gives way to a self-oscillating phase with non-zero Δ, given by $\bar{A}_{i,s} = ie^{\pm i(\phi/2+\Delta t)}\sqrt{\mu - \mu_{cr}}, \bar{A}_P = i\mu_{cr}$ with $\Delta = \tau_r^{-1}\sqrt{\frac{\gamma_0\tau_r}{2} - 1}$. In this dynamical phase, the signal and idler modes undergo self-oscillation at frequencies that are shifted away from their nominal frequencies by an amount Δ. In addition to the breaking of the $U(1)$ symmetry associated with the choice of the signal-idler phase difference ϕ, this phase also breaks the discrete $\mathbb{Z}_2$ symmetry associated with the sign of the frequency shift Δ. As such, we denote this dynamical phase as the $U(1) \times \mathbb{Z}_2$ phase. For $\mu > 1$, all three solutions exist but the trivial solution and the $U(1)$ solution are unstable, with the $U(1) \times \mathbb{Z}_2$ solution remaining as the only stable dynamical phase.

These three dynamical phases along with the phase boundaries demarcating these phases are shown in Fig. C.1 of the main text.

C.9.3 Exceptional points and stability of mean field dynamical phases

The stability of the mean-field dynamical phases to generic perturbations is demonstrated by evaluating the eigenvalues of the susceptibility matrix $\mathbf{\Sigma} + i\omega\mathbf{I}$ as discussed in the main text. In particular, a stable dynamical phase is indicated by a susceptibility matrix whose eigenvalues have non-positive real parts. We outline the calculation of these eigenvalues for each dynamical phase below. We first distinguish between the mean amplitudes and the fluctuations by writing $A_{i,s} = (\bar{A}_{i,s} + \delta A_{i,s})e^{-i\Delta_{i,s}t}$ with the mean amplitudes in each dynamical phase given by the expressions in the previous section. The equations of motion Eqns. (C.6 – C.8) yield

$$
\partial_t \begin{pmatrix} \delta A_i \\ \delta A_s \\ \delta A_P \end{pmatrix} = \int_{-\infty}^{t} dt' \begin{pmatrix} -\frac{1}{2}\gamma(t-t') & 0 & i\frac{\gamma_0}{2}\bar{A}_s^*\delta(t-t') \\ 0 & -\frac{1}{2}\gamma(t-t') & i\frac{\gamma_0}{2}\bar{A}_i^*\delta(t-t') \\ i\frac{\gamma_P}{2}\bar{A}_s\delta(t-t') & i\frac{\gamma_P}{2}\bar{A}_i\delta(t-t') & -\frac{\gamma_P}{2}\delta(t-t') \end{pmatrix} \begin{pmatrix} \delta A_i(t') \\ \delta A_s(t') \\ \delta A_P(t') \end{pmatrix}
$$

$$
+ \begin{pmatrix} 0 & i\frac{\gamma_0}{2}\bar{A}_P & 0 \\ i\frac{\gamma_0}{2}\bar{A}_P & 0 & 0 \\ 0 & 0 & 0 \end{pmatrix} \begin{pmatrix} \delta A_i^* \\ \delta A_s^* \\ \delta A_P^* \end{pmatrix} + \frac{i}{2} \begin{pmatrix} \gamma_0\tilde{f}_i(t) \\ \gamma_0\tilde{f}_s(t) \\ \gamma_P\mu \end{pmatrix} \tag{C.19}
$$

As shown in [83], the complex fluctuations can be decomposed into real quadratures in the form $\delta \mathbf{A} = \delta\vec{\alpha} + i\delta\vec{\beta}$ such that the above equation can be recast as

$$
\dot{\delta\vec{\alpha}} = \int_{-\infty}^{t} dt' \mathbf{M}_\alpha(t-t')\delta\vec{\alpha}(t') + \mathbf{v}_\alpha(t) \tag{C.20}
$$

$$
\dot{\delta\vec{\beta}} = \int_{-\infty}^{t} dt' \mathbf{M}_\beta(t-t')\delta\vec{\beta}(t') + \mathbf{v}_\beta(t) \tag{C.21}
$$

where $\mathbf{v}_{\alpha\beta}$ are the Langevin noise terms and

$$\mathbf{M}_{\alpha\beta}(t) = \frac{1}{2} \begin{pmatrix} -\gamma(t) & \mp\gamma_0|\bar{A}_P|\delta(t) & \gamma_0|\bar{A}_s|\delta(t) \\ \mp\gamma_0|\bar{A}_P|\delta(t) & -\gamma(t) & \gamma_0|\bar{A}_i|\delta(t) \\ -\gamma_P|\bar{A}_s|\delta(t) & -\gamma_P|\bar{A}_i|\delta(t) & -\gamma_P\delta(t) \end{pmatrix} \qquad (C.22)$$

Further, we define cross-quadratures of the signal and idler modes according to the relations $x_\pm = (\alpha_i \pm \alpha_s)/\sqrt{2}, y_\pm = (\beta_i \pm \beta_s)/\sqrt{2}$ such that the two-mode correlations due to parametric down-conversion are manifest as amplification and squeezing of the above quadratures. The fluctuations of these cross-quadratures are related to the original quadrature fluctuations $\delta\vec{\alpha}, \delta\vec{\beta}$ via the relations

$$\delta\mathbf{X} = \mathbf{R}\delta\vec{\alpha}; \quad \delta\mathbf{Y} = \mathbf{R}\delta\vec{\beta}; \quad \mathbf{R} = \frac{1}{\sqrt{2}} \begin{pmatrix} 1 & 1 & 0 \\ 1 & -1 & 0 \\ 0 & 0 & \sqrt{2} \end{pmatrix} \qquad (C.23)$$

where $\delta\mathbf{X} = (\delta x_+, \delta x_-, \delta x_P)^T, \delta\mathbf{Y} = (\delta y_+, \delta y_-, \delta y_P)^T$. The fluctuations of the cross-quadratures are governed by the equation

$$\partial_t \delta\mathbf{X} = \int_{-\infty}^t dt' \mathbf{\Sigma}_X(t - t')\delta\mathbf{X}(t') + \mathbf{v}_X(t) \qquad (C.24)$$

$$\partial_t \delta\mathbf{Y} = \int_{-\infty}^t dt' \mathbf{\Sigma}_Y(t - t')\delta\mathbf{Y}(t') + \mathbf{v}_Y(t) \qquad (C.25)$$

where $\mathbf{\Sigma}_{X,Y} = \mathbf{R}\mathbf{M}_{\alpha\beta}\mathbf{R}^T$ and $\mathbf{v}_{X,Y} = \mathbf{R}\mathbf{v}_{\alpha\beta}$. By moving to the frequency domain, the above equations can be recast as

$$\begin{pmatrix} \delta\tilde{x}_+ \\ \delta\tilde{x}_- \\ \delta\tilde{x}_P \\ \delta\tilde{y}_+ \\ \delta\tilde{y}_- \\ \delta\tilde{y}_P \end{pmatrix} = -(\mathbf{\Sigma} + i\omega\mathbf{I})^{-1}\tilde{\mathbf{v}} \qquad (C.26)$$

where $\delta\tilde{x}_+$ denotes the fourier transform of δx_+ etc. and

$$\Sigma(\omega) = \begin{pmatrix} \tilde{\Sigma}_X & 0 \\ 0 & \tilde{\Sigma}_Y \end{pmatrix} \tag{C.27}$$

We note that in the $U(1) \times \mathbb{Z}_2$ phase where $\Delta \neq 0$, the susceptibility matrix does not remain block diagonal due to correlations between the various cross-quadratures. However, the procedure for evaluating the eigenvalues and stability remains the same.

The poles of the susceptibility matrix are defined by complex ω satisfying $\text{Det}[-\Sigma - i\omega\mathbf{I}] = 0$ and the eigenvalues of the inverse susceptibility matrix are defined as $\lambda = -i\omega$. The real part of these eigenvalues corresponds to the damping rate of the system's response to generic perturbations. As such, the stability of the mean field dynamical phases is indicated by a non-positive real part of the eigenvalues. Critical points governing continuous transitions between distinct dynamical phases is indicated by a vanishing of this real part or equivalently, a divergent relaxation time. The linearization around the trivial (parametric amplifier) solution yields the eigenvalues

$$\lambda_{\pm} = \frac{\gamma_0}{4} \left[(\mu - \frac{2}{\gamma_0\tau_r}) \pm \sqrt{(\mu + \frac{2}{\gamma_0\tau_r})^2 - \frac{8}{\gamma_0\tau_r}} \right] \tag{C.28}$$

As such, for $(\gamma_0\tau_r)^{-1} > 2$, the eigenvalues are purely real and the system can be mapped onto the Markovian system. As the coherence time of the reservoir is increased, the eigenvalues morph into complex conjugate pairs for sufficiently small drive strength μ. This change from real eigenvalues to complex conjugate eigenvalues occurs at a point where the two eigenvalues (and corresponding eigenmodes) coalesce. Such points are called exceptional points. In this system, the exceptional point approaches the critical point from below as the coherence time τ_r is increased. For $(\gamma_0\tau_r)^{-1} = \frac{1}{2}$, the exceptional point and the critical point coincide at $\mu = 1$. This heralds the emergence of the $U(1) \times \mathbb{Z}_2$ phase. For even

larger reservoir coherence times, $(\gamma_0 \tau_r)^{-1} < \frac{1}{2}$, the exceptional point occurs beyond the critical point governing the transition from the disordered phase to the $U(1) \times \mathbb{Z}_2$ phase. This behavior of the exceptional point relative to the critical point is depicted in Fig. C.4 of the main text.

Similar linearization can also be performed around the $U(1)$ and the $U(1) \times \mathbb{Z}_2$ phases using the formalism described above. The calculations, while straightforward, are laborious and are not reproduced here. The real parts of the respective eigenvalues as a function of drive strength μ and normalized reservoir coherence time $(\gamma_0 \tau_r)^{-1}$ are shown in Fig. C.4. As can be seen, the real parts of the eigenvalues of the susceptibility matrix for these phases are negative for large μ indicating that these dynamical phases are indeed stable to generic perturbations.

The Markovian case is retrieved from Eqn.(C.28) in the limit $\tau_r \to 0$, i.e. $\lambda_+ = \frac{\gamma_0}{2}(\mu - 1)$. Note that $\lambda_- \to 1/\tau_r$ corresponds to the rate at which the reservoir follows the system, and can be adiabatically eliminated in the limit of small τ_r. The exponent with which λ vanishes, $\lambda \sim |\epsilon|$, where $\epsilon = (\mu - \mu_{cr})/\mu_{cr}$ is the reduced distance from criticality, defines the conventional critical exponent vz for the phase transition: $vz = 1$ in the Markovian case. In contrast, for $(\gamma_0 \tau_r)^{-1} = 1/2$, the eigenvalues are

$$\lambda_{\pm} = \frac{\gamma_0}{4}\left[(\mu - 1) \pm \sqrt{(\mu - 1)(\mu + 3)}\right] \tag{C.29}$$

and thus scale near criticality as

$$\lambda_{\pm} = \frac{\gamma_0}{4}\left[\epsilon \pm \sqrt{\epsilon(4 + \epsilon)}\right] \approx \frac{\gamma_0}{4}\left[\epsilon \pm 2i\sqrt{-\epsilon}\right] \sim \epsilon \pm 2i\sqrt{|\epsilon|} \tag{C.30}$$

Both the real and imaginary part of the eigenvalue vanish at criticality, with the real part being proportional to $|\epsilon|$ and the imaginary part being proportional to $\sqrt{|\epsilon|}$. While the divergent dissipation timescale is set by the vanishing real

part, and also occurs in the Markovian case, the vanishing imaginary part of λ sets an additional divergent *oscillation* timescale for the system near criticality. This novel critical behavior is solely attributable to the non-Markovianity of the system-bath interactions.

For $(\gamma_0 \tau_r)^{-1} < 1/2$, i.e. across the $PA - U(1) \times Z_2$ phase transition, the eigenvalues are

$$\lambda_\pm = \frac{\gamma_0}{4} \left[(\mu - \mu_{cr}) \pm i(\Delta + O(\mu - \mu_{cr})) \right] \tag{C.31}$$

where $\mu_{cr} = \frac{2}{\gamma_0 \tau_r} < 1$ and $\Delta = 2 \sqrt{\mu_{cr}(1 - \mu_{cr})} = \tau_r^{-1} \sqrt{\frac{\gamma_0 \tau_r}{2} - 1}$. In particular, while the real part does vanish at criticality ($\mu \to \mu_{cr}$), its imaginary part remains finite at $\Delta > 0$. As such, $\lambda(\epsilon) \sim \epsilon + i\Delta \sim \epsilon + iO(1)$ as $\epsilon \to 0$. Due to the finite limit cycle frequency at the critical point, this phase boundary can be associated with a supercritical Hopf bifurcation [245].

C.9.4 Two-mode correlations and entanglement in the steady state and transient regime

As shown in [83], the fluctuation spectra and two-mode correlations are obtained from the power spectral densities of the cross-quadratures via the relation

$$\mathbf{S}_{X,Y}(\omega) = \frac{1}{2\pi} (\tilde{\mathbf{\Sigma}}_{X,Y} + i\omega\mathbf{I})^{-1} \mathbf{D} (\tilde{\mathbf{\Sigma}}_{X,Y}^\dagger - i\omega\mathbf{I})^{-1} \tag{C.32}$$

where the diffusion matrix is given by

$$\mathbf{D} = \frac{1}{2} \begin{pmatrix} \frac{4g^2}{\gamma_0 \gamma_P} \tilde{\gamma}'(\omega)(\bar{n}_{th,i} + \frac{1}{2}) & 0 & 0 \\ 0 & \frac{4g^2}{\gamma_0 \gamma_P} \tilde{\gamma}'(\omega)(\bar{n}_{th,s} + \frac{1}{2}) & 0 \\ 0 & 0 & \frac{4g^2}{\gamma_0^2} \gamma_P(\bar{n}_{th,P} + \frac{1}{2}) \end{pmatrix} \tag{C.33}$$

where $\tilde{\gamma}'(\omega) = \text{Re}[\tilde{\gamma}(\omega)] = \gamma_0 \frac{1}{1+(\omega\tau_r)^2}$ and the thermal phonon numbers are related to the effective temperature of the modes, i.e. $\bar{n}_{th,i,s,P} = (\exp(\frac{\hbar\omega_{i,s,P}}{k_B T}) - 1)^{-1}$. The steady state variances of the cross-quadratures can be obtained from the fluctuation spectrum using the Wiener-Khintchine theorem by integrating the fluctuations,

$$\sigma_{X,Y} = \int_{-\infty}^{\infty} \mathbf{S}_{X,Y}(\omega)d\omega \tag{C.34}$$

Below threshold, the squeezed and amplified variances (normalized to the thermal variances) are respectively given by

$$\sigma_{sq} = \frac{2(\gamma_0\tau_r)^{-1}}{(1+\mu)(2(\gamma_0\tau_r)^{-1}+\mu)} \tag{C.35}$$

$$\sigma_{amp} = \frac{2(\gamma_0\tau_r)^{-1}}{(1-\mu)(2(\gamma_0\tau_r)^{-1}-\mu)} \tag{C.36}$$

For a given $(\gamma_0\tau_r)^{-1}$, the squeezed variance below threshold is minimized at $\mu = \mu_{cr} = \min(1, 2(\gamma_0\tau_r)^{-1})$. In particular, close to the multicritical point $\mu_{cr} = 1, (\gamma_0\tau_r)^{-1} = \frac{1}{2}$, we obtain a steady state squeezing limit $\sigma_{sq} = \frac{1}{4}$, outperforming the Markovian steady-state squeezing limit of $\sigma_{sq} = \frac{1}{2}$.

To achieve a squeezing better than this steady-state minimum, we can implement a transient protocol, where the pump drive strength μ is set to a value larger than μ_{cr} for a period of time that is short compared to γ_0^{-1}. Within this short duration, pump depletion and saturation effects can be neglected. The amplified quadrature grows with an exponential envelope, and the squeezed quadrature decays with an exponential envelope to the asymptote given by the expression above, yielding a dependence of $\sigma_{sq} \propto \frac{1}{\mu^2}$ for large drive amplitudes. This protocol works when the absolute amplitude of motion is small enough that the linearization around the disordered solution remains valid.

Note that by setting $\tau_r \to 0$, we recover the Markovian case expressions.

240

In particular, the degree of squeezing is $\sigma_{sq} = \frac{1}{1+\mu}$, and the divergence of the amplified quadrature is $\sigma_{amp} = \frac{1}{1-\mu} = \frac{1}{|\mu-\mu_{cr}|} \sim \frac{1}{|\epsilon|}$. In other words, the divergence of the amplified fluctuations has an exponent -1 in $|\epsilon|$ in the Markovian limit. In contrast, for $(\gamma_0\tau_r)^{-1} = 1/2$, the divergence of σ_{amp} has an exponent -2, i.e. $\sigma_{amp} = \frac{1}{(1-\mu)^2} \sim \frac{1}{|\epsilon|^2}$. A change in this exponent compared to the Markovian case is another signature of novel critical behavior induced by the non-Markovian system-bath interactions.

Above threshold, in the $U(1)$ phase, the normalized variances of the various cross-quadratures are given by

$$\sigma_{x_+} = \frac{\bar{n}_{th,P} + \frac{1}{2}}{\bar{n}_{th} + \frac{1}{2}} \frac{2(\mu-1)(\mu+(\gamma_0\tau_r)^{-1})}{\mu(2(\gamma_0\tau_r)^{-1}+2\mu-1)} + \frac{(\gamma_0\tau_r)^{-1}}{\mu(2(\gamma_0\tau_r)^{-1}+2\mu-1)} \tag{C.37}$$

$$\sigma_{x_-} \rightarrow \infty \tag{C.38}$$

$$\sigma_{y_+} = \frac{\bar{n}_{th,P} + \frac{1}{2}}{\bar{n}_{th} + \frac{1}{2}} \frac{2(\mu-1+(\gamma_0\tau_r)^{-1})}{(2(\gamma_0\tau_r)^{-1}+2\mu-3)} + \frac{(\gamma_0\tau_r)^{-1}}{(\mu-1)(2(\gamma_0\tau_r)^{-1}+2\mu-3)} \tag{C.39}$$

$$\sigma_{y_-} = \frac{(\gamma_0\tau_r)^{-1}}{1+2(\gamma_0\tau_r)^{-1}} \tag{C.40}$$

where we have assumed that $\bar{n}_{th} \equiv \bar{n}_{th,i} \approx \bar{n}_{th,s}$.

In the $U(1) \times \mathbb{Z}_2$ phase, the non-zero frequency shifts Δ introduce correlations between the nominally uncorrelated Langevin forces in orthogonal cross-quadratures. In addition, as mentioned previously, this frequency shift also introduces time-dependent correlations between the various cross-quadratures. Aside from these modifications, the computation of the various variances proceeds as before. The final expressions are cumbersome and not reproduced here.

Lastly, the logarithmic negativity is obtained from the squeezed variances as $\mathcal{E}_N = -\frac{1}{2}\log_2\left[\min(\frac{\sigma_{sq}}{\sigma_{zpm}}, 1)\right]$, where σ_{zpm} is the zero point variance of the cross-quadratures. These results are shown in Fig. C.5 of the main text.

C.9.5 Trajectory of exceptional points in the phase diagram

In general, the non-Markovian equations of motion are more challenging to solve analytically than the Markovian equations. The exponential non-Markovian kernel $\gamma(t - t')$ considered in this work, however, allows for the definition of auxiliary variables which greatly simplifies calculations. Defining $h_{i,s} = \int_{-\infty}^{t} \frac{1}{\tau_r} e^{-(t-t')/\tau_r} a_{i,s}(t') dt'$ and its dimensionless version $H_{i,s} = h_{i,s} \frac{2g}{\sqrt{\gamma_0 \gamma_P}}$, the semi-classical equations of motion in Eqns. (C.6 – C.8) are simplified to a set of first order differential equations –

$$\dot{A}_i = \frac{1}{2}\left[-\gamma_0 H_i + i\gamma_0 A_s^* A_P + i\gamma_0 \tilde{f}_i\right] \tag{C.41}$$

$$\dot{H}_i = -H_i/\tau_r + A_i/\tau_r \tag{C.42}$$

$$\dot{A}_s = \frac{1}{2}\left[-\gamma_0 H_s + i\gamma_0 A_i^* A_P + i\gamma_0 \tilde{f}_s\right] \tag{C.43}$$

$$\dot{H}_s = -H_s/\tau_r + A_s/\tau_r \tag{C.44}$$

$$\dot{A}_P = \frac{1}{2}\left[-\gamma_P A_P + i\gamma_P A_i A_s + i\gamma_P \mu\right] \tag{C.45}$$

These equations can be further simplified in the mean-field, i.e. in the limit of zero noise, $\tilde{f}_{i,s} \to 0$.

In the disordered PA phase below threshold ($\mu \leq \max[1, 2/\gamma_0\tau_r]$), A_P can be adiabatically eliminated as $A_P \approx i\mu$, as derived earlier. The complex Eqns. (C.41-C.44) can then be block diagonalized into decoupled blocks formed by the pair of cross-quadratures ($B := A_i - A_s^*, H_B := H_i - H_s^*$) and ($C := A_i + A_s^*, H_C := H_i + H_s^*$). Within the parameter space of B, H_B, the equations of motion are simply

$$\begin{pmatrix} \dot{B} \\ \dot{H}_B \end{pmatrix} = \begin{pmatrix} \gamma_0\mu/2 & -\gamma_0/2 \\ 1/\tau_r & -1/\tau_r \end{pmatrix} \begin{pmatrix} B \\ H_B \end{pmatrix} \tag{C.46}$$

The exceptional points of this dynamical matrix can easily be evaluated by explicitly solving for the eigenvalues and eigenvectors. We find that they coalesce along the contour defined by $(\tau_r\gamma_0\mu + 2)^2 - 8\tau_r\gamma_0 = 0$. Only one of the roots of

this quadratic equation $((\gamma_0\tau_r)^{-1} = 1 - \mu/2 + \sqrt{1-\mu})$ is inside disordered phase. It corresponds to the eigenmode of the system and reservoir with the least negative real part of the eigenvalue, and is shown by the dotted contour for $\mu < 1$ in Fig. C.1 of the main text. The eigenvalues along this contour of exceptional points is $\sqrt{\gamma_0/(2\tau_r)} - 1/\tau_r$ with the eigenvector $(\sqrt{\gamma_0\tau_r/2}, 1)^T$.

We can similarly compute the exceptional points in the $U(1)$ phase ($\mu \geq 1, (\gamma_0\tau_r)^{-1} \geq 1/2$). We linearize the equations of motion about the steady state solution evaluated earlier, i.e. $\bar{A}_{i,s} = ie^{\pm i\phi/2}\sqrt{\mu-1}, \bar{A}_P = i$. Writing $H_{i,s}$ in terms of real quadratures, i.e. $H_{i,s} = H_{x,i,s} + iH_{y,i,s}$, and denoting the deviations from steady state values with prefix δ, the real quadratures $\delta y_+ = (\delta y_i + \delta y_s)/\sqrt{2}$ (see also Eqn. (C.23)) and $\delta H_{y_+} = (\delta H_{y,i} + \delta H_{y,s})/\sqrt{2}$ evolve according to

$$\begin{pmatrix} \dot{\delta y}_+ \\ \dot{H}_{y_+} \end{pmatrix} = \begin{pmatrix} -\gamma_0(2\mu-3)/2 & -\gamma_0/2 \\ 1/\tau_r & -1/\tau_r \end{pmatrix} \begin{pmatrix} \delta y_+ \\ H_{y_+} \end{pmatrix} \qquad (C.47)$$

The contour of exceptional points in the $U(1)$ phase is thus defined by $4 + \tau_r\gamma_0(4 - 8\mu) + ((2\mu-3)\gamma_0\tau_r)^2 = 0$. Both roots of this quadratic equation yield valid solutions in the $U(1)$ phase. One of them $((\gamma_0\tau_r)^{-1} = \mu - 1/2 + \sqrt{2(\mu-1)})$, which corresponds to the system and reservoir's eigenmode with the least negative real part of the eigenvalue, is shown by the dotted contour for $\mu > 1$ in Fig. C.1 of the main text. The eigenvalues and eigenvectors are, again, $\sqrt{\gamma_0/(2\tau_r)} - 1/\tau_r$ and $(\sqrt{\gamma_0\tau_r/2}, 1)^T$, respectively.

C.9.6   Critical behavior of the limit cycle frequency Δ

As described earlier, the limit cycle phase emerges in the regime $(\gamma_0\tau_r)^{-1} < 1/2$. Below this phase boundary, the limit cycle frequency is given by $\Delta = \tau_r^{-1}\sqrt{\frac{\gamma_0\tau_r}{2} - 1}$. Parametrizing the distance from the phase boundary as $\epsilon_r \equiv$

$2(\gamma_0 \tau_r)^{-1} - 1$, we see that the order parameter Δ scales as $\Delta \sim |\epsilon_r|^{1/2}$ with the critical exponent $\beta = 1/2$.

For noise small compared to the steady state amplitude R, we can approximate the phase fluctuations as $\delta\phi_{i,s} = \delta\alpha_{i,s}/R$ (see Eqn. (C.23), [83]). We can thus express the the phase difference as $\phi = \phi_i - \phi_s = \delta\phi_i - \delta\phi_s = \sqrt{2}\delta x_-/R$, where $x_- := (\alpha_s - \alpha_i)/\sqrt{2}$. Its spectrum is $S_{\phi,\phi} = \frac{2}{R^2}S_{x_-,x_-}(\omega)$, with $S_{x_-,x_-}(\omega) = \frac{1}{2\pi}(\tilde{\Sigma}_{x-,x-} + i\omega\mathbf{I})^{-1}\mathbf{D}(\tilde{\Sigma}^\dagger_{x-,x-} - i\omega\mathbf{I})^{-1}$. The limit cycle frequency $\Delta = \frac{1}{2}(\dot\phi_i - \dot\phi_s)$ thus has a spectrum $S_{\Delta,\Delta} = \frac{\omega^2}{4}S_{\phi,\phi}(\omega) = \frac{\omega^2}{2R^2}S_{x_-,x_-}(\omega)$.

In the $U(1)$ phase, the power spectral density of the cross quadrature δx_- with unit thermal noise is given by

$$S_{x_-,x_-}(\omega) = \frac{1}{2\pi}\frac{4\gamma_0}{\omega^2(4 - 4\tau_r\gamma_0 + \tau_r^2(\gamma_0^2 + 4\omega^2))} \tag{C.48}$$

A factor of $1/\omega^2$ here signifies that the phase difference $\phi \propto x_-$ undergoes diffusion. Note also that this quadrature does not have a μ dependence. Thus, the variance of the order parameter and hence, the susceptibility of the order parameter in the vicinity of the phase boundary is given by

$$\mathrm{Var}(\Delta) = \frac{1}{2R^2}\int_{-\infty}^{\infty}d\omega\frac{1}{2\pi}\frac{4\gamma_0}{(4 - 4\tau_r\gamma_0 + \tau_r^2(\gamma_0^2 + 4\omega^2))}$$

$$= \frac{1}{2R^2}\frac{1}{2\tau_r^2(1/(\gamma_0\tau_r) - 1/2)} \tag{C.49}$$

$$\Rightarrow \mathrm{Var}(\Delta) \sim [(\gamma_0\tau_r)^{-1} - 1/2]^{-1} \sim |\epsilon_r|^{-1} \tag{C.50}$$

This yields the critical exponent $\gamma = 1$.

This divergent variance of the limit cycle frequency is depicted in Fig. C.3 of the main text.

C.9.7 RG flow under time rescaling

It is instinctive to think that the finite system-bath interaction timescale τ_r would rescale to zero under a RG flow, thereby taking the system to the Markovian limit of $\tau_r \to 0$. In this section, we show that the system has a RG fixed point (source) in the phase space of $(\mu, (\gamma_0\tau_r)^{-1})$ at the multicritical point $(1, 1/2)$ (see Fig. C.1 of the main text). This fixed point is clearly distinct from the Markovian fixed point at $(\gamma_0\tau_r)^{-1} \to \infty$, and as shown below, the flow around this point can push the system further away from the Markovian limit.

The first order differential equations of motion in the disordered PA phase in the zero noise limit, derived earlier as Eqn.(C.46), can be recast as a second order differential equation in B as

$$\ddot{B}(t) = (\frac{\gamma_0\mu}{2} - \frac{1}{\tau_r})\dot{B}(t) + \frac{\gamma_0}{2\tau_r}(\mu - 1)B(t) \tag{C.51}$$

Rescaling time by b, as $t' = t/b$, we get

$$\frac{1}{b^2}\ddot{B}(t') = \frac{1}{b}(\frac{\gamma_0\mu}{2} - \frac{1}{\tau_r})\dot{B}(t') + \frac{\gamma_0}{2\tau_r}(\mu - 1)B(t') \tag{C.52}$$

Note that being a linear equation, B is itself not rescaled. In order to maintain the functional form of Eqn.(C.51), the renormalized parameters $(\gamma_0', \tau_r', \mu')$ should satisfy

$$\frac{\gamma_0'\mu'}{2} - \frac{1}{\tau_r'} = b(\frac{\gamma_0\mu}{2} - \frac{1}{\tau_r}) \tag{C.53}$$

$$\frac{\gamma_0'}{2\tau_r'}(\mu' - 1) = b^2\frac{\gamma_0}{2\tau_r}(\mu - 1) \tag{C.54}$$

Note that these two equations are under-determined in $(\gamma_0', \tau_r', \mu')$. However, in order to focus on how the system-bath interaction timescale τ_r rescales under this time-rescaling, and how the system flows in the $(\mu, (\gamma_0\tau_r)^{-1})$ parameter space, we fix the parameter γ_0, i.e. constrain $\gamma_0' = \gamma_0$. Note that γ_0 signifies the total strength of dissipation, i.e. $\int_0^\infty dt\gamma(t) = \gamma_0$.
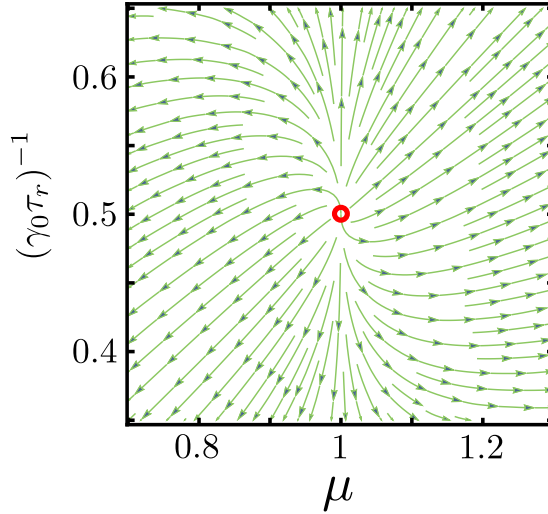
Figure C.6: RG flow of the system following a rescaling of time, shown in the $(\mu, (\gamma_0\tau_r)^{-1})$ parameter space. The open red circle marks an unstable fixed point at the multicritical point ($\mu = 1$, $(\gamma_0\tau_r)^{-1} = 1/2$), distinct from the Markovian fixed point that occurs at $(\gamma_0\tau_r)^{-1} \to \infty$. Contrary to intuition, the flow shows that under time rescaling, the finite system-bath interaction timescale need not rescale to zero (the Markovian limit).

We solve Eqns.(C.53 – C.54) for (μ', τ_r') and evaluate the flow as the vector field $(\frac{d}{db}\mu', \frac{d}{db}(\gamma_0\tau_r')^{-1})$. This flow is shown in Fig. C.6. The open red circle marks the unstable fixed point at ($\mu = 1$, $(\gamma_0\tau_r)^{-1} = 1/2$), the multicritical point of Fig. C.1 of the main text. The flow around this fixed point indicates that the ratio $(\gamma_0\tau_r)^{-1}$ can flow to either larger or smaller values, i.e. the system can rescale either toward or farther from the Markovian limit of $(\gamma_0\tau_r)^{-1} \to \infty$.

Note that the above analyses is done by linearizing the system around the disordered PA solution. While this analysis correctly predicts the presence of the multicritical point at $\mu = 1, (\gamma_0\tau_r)^{-1} = 1/2$ and the emergence of the limit cycle phase for $(\gamma_0\tau_r)^{-1} < 1/2$, the interpretation of the RG flow deep within the $U(1)$ phase or the $U(1) \times \mathbb{Z}_2$ phase would require the linearization of the RG equations about the respective steady solutions in those phases, and is not

considered here.

DEMONSTRATION OF ENHANCED FORCE SENSITIVITY USING A TRANSIENT SQUEEZING PROTOCOL

This chapter will be submitted for peer-review with requisite modifications as *Demonstration of enhanced force sensitivity using a transient squeezing protocol, by H. F. H.Cheung, Y. S. Patil, L. Chang, S. Chakram and M. Vengalattore.* In this work, H. F. H. Cheung, Y. S. Patil, L. Chang and S. Chakram performed the experimental work and data acquisition. H. F. H. Cheung and Y. S. Patil carried out the data analysis and modeling. M. Vengalattore supervised all stages of the work. All authors contributed to the preparation of the manuscript.

D.1 Abstract

Thermal and quantum fluctuations set a fundamental limit on measurement sensitivities. This has spurred the development of various measurement schemes and protocols that use entanglement [252, 180], quantum-noise cancellation [253, 254] and multi-particle interactions [255] to improve the sensitivities beyond this limit. A prominent instance of such a scheme uses a parametric amplifier to generate a high degree of squeezing, achieving a sensitivity scaling of $\delta\phi \sim 1/|A|^2$, where $|A|$ is the amplitude of the measurement resource. Such a scaling is possible because of the suppression of fluctuations of the measured observable. In the paradigmatic optical $SU(1, 1)$ interferometer [256], for example, intensity noise is suppressed to levels lower than the vacuum shot noise at

the dark port [257, 216]. Here, we realize a similar scheme in a fundamentally new platform, using distinct flexural modes of a millimeter-scale mechanical resonator. Using a parametric amplifier coupling between a pair of its mechanical modes, we realize up to 15.4(3) dB of transient, two-mode noise squeezing, and consequently demonstrate up to 13.2(5) dB improvement in the displacement sensitivity. Our work extends the realm of such schemes, hitherto only demonstrated with photons and ultracold atoms, to macroscopic optomechanical systems, and presents new avenues for optomechanical metrology, the manipulation of nonclassical mechanical states, and studies of the nonequilibrium dynamics of multimode optomechanical systems.

D.2 Introduction

Optomechanics has emerged as a promising arena for the study of quantum metrology and the innovation of novel precision measurement technologies [78], due in part to the wide range of size and mass, long coherence times that compare favorably with those realized in atomic or solid state spin systems [79, 258, 259, 260], and the ability to cool, control and measure mechanical motion with radiation pressure. While optomechanical interactions have thus far been mainly in the weak coupling regime, recent work has demonstrated the possibility of realizing strong nonlinear or multimode mechanical interactions via radiation pressure [261], geometric design [95] or reservoir engineering [150]. In this work, we utilize reservoir-engineered mechanical nonlinearities to demonstrate correlation-enhanced displacement, force and phase sensitivities.

D.3 The parametric amplifier coupling

The system in which we implement an enhanced sensing protocol consists of two distinct mechanical modes of a silicon nitride (SiN) membrane resonator, hereafter referred to as the 'signal' and 'idler' modes. A parametric coupling between these modes can be realized by controllably actuating the silicon substrate that the membrane is deposited on. Experimentally, the motion of either mode can be spectroscopically resolved and independently measured in both quadratures via an optical Michelson interferometer, as described in our previous works [79, 150]. See also Supplementary Information, Section D.9.1. For the experiments described below, the resonance frequencies and damping rates of the signal and idler modes are $\omega_s/2\pi$ = 1.233 MHz, $\omega_i/2\pi$ = 1.466 MHz and $\gamma_s/2\pi$ = 0.083(2) Hz, $\gamma_i/2\pi$ = 0.108(3) Hz. Such ultra-high quality factors ensure a large dynamic range of amplitudes for our experiments, and also set the experimental timescales to be on the order of seconds, making the study of the parametric amplifier dynamics easily accessible.

Before describing the enhanced sensing scheme in the following sections, we detail the two-mode nonlinear coupling between the two modes. The model, applicable to a generic pair of parametrically coupled oscillators, is realized by the interaction Hamiltonian (see also Supplementary Information, Section D.9.2)

$$H_{\text{int}}(t) \quad = \quad -gX_P(t)x_{s,l}x_{i,l} \qquad\qquad (\text{D.1})$$

where $x_{s,l} = x_s \cos \omega_s t + y_s \sin \omega_s t$ and $x_{i,l} = x_i \cos \omega_i t + y_i \sin \omega_i t$ are the lab-frame displacements of the signal and idler modes, and (x_s, y_s) & (x_i, y_i) their x and y quadratures. Here, g parametrizes the coupling strength between the modes, and $X_P(t)$ is the amplitude of motion of the 'pump' mode, which is controlled by

driving the silicon substrate with a piezoelectric actuator. A parametric amplifier coupling between the modes is realized by driving the pump mode at the sum frequency $\omega_P = \omega_s + \omega_i$. We first experimentally ascertain this parametric amplifier coupling, which allows for the creation of strong correlations between the modes.

As is well known in quantum optics, the parametric amplifier shows an instability when driven past a critical pump amplitude, $X_{P,\text{cr}}$, at which the system is characterized by a divergent susceptibility and critical dynamics. This instability can be described in terms of a nonequilibrium continuous phase transition [225, 228]. When the pump is driven beyond this critical strength, the signal and idler modes reach a self-oscillatory steady state. The strength of the parametric drive can thus be parametrized by $\mu \equiv X_P/X_{P,\text{cr}}$, with $\mu = 1$ corresponding to the critical drive strength, or threshold, for the onset of self-oscillation.

Below threshold ($\mu < 1$), the mean amplitudes of the signal and idler modes are zero, while their fluctuations are correlated – the cross-quadratures $x_+ \equiv \frac{x_s+x_i}{\sqrt{2}}$ and $y_- \equiv \frac{y_s-y_i}{\sqrt{2}}$ are squeezed, whereas the cross-quadratures $x_- \equiv \frac{x_s-x_i}{\sqrt{2}}$ and $y_+ \equiv \frac{y_s+y_i}{\sqrt{2}}$ are amplified, or anti-squeezed. Above threshold, the mean amplitudes of the signal and idler modes are non-zero. And the relevant fluctuations, those about the signal and idler modes' steady states, are still correlated – the amplitude difference quadrature $\left(r_- \equiv \frac{\delta r_s-\delta r_i}{\sqrt{2}}\right)$ is squeezed, where $r_{s,i} = \sqrt{x_{s,i}^2 + y_{s,i}^2}$, $\delta r_{s,i} = r_{s,i} - \langle r_{s,i}\rangle$, and so is the phase sum [83]. On the other hand, the amplitude sum $\left(r_+ \equiv \frac{\delta r_s+\delta r_i}{\sqrt{2}}\right)$ and phase difference quadrature have a divergent variance near the critical pump drive, with the latter undergoing a diffusive dynamics [83].

The measured variances of these quadratures are plotted in Fig. D.1(a),
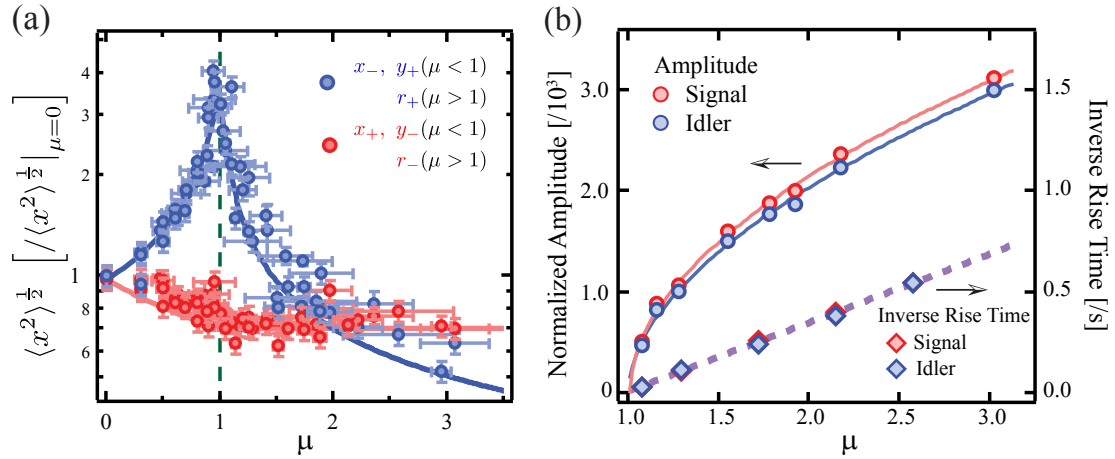
Figure D.1: **The parametric amplifier phase diagram.** (a) Two-mode squeezing below and above the instability threshold ($\mu = 1$): normalized standard deviations of squeezed (red) and amplified (blue) cross-quadratures. The solid lines are no-free-parameter predictions of our model with independently measured damping rates and eigenfrequencies, taking into account finite measurement time and differential substrate temperature effects (see Supplementary Information, Sections D.9.3, D.9.4 & D.9.5). (b) Steady state amplitudes of the signal and idler modes show a power-law growth of 0.53(3) consistent with the prediction of 1/2. The exponential growth rate (in time) of the signal and idler motions increases linearly with parametric actuation μ. (All signal and idler motions are normalized to their respective thermal motions.)

showing excellent agreement with no-free-parameter calculations of the above model based on independently measured damping and frequency parameters. These measurements are performed by allowing the system to relax into a steady state at constant values of the pump drive μ, and acquiring the data at each μ for times $> 200 \, \gamma_{s,i}^{-1}$. The growth of the steady state amplitude of the modes above threshold, shown in Fig. D.1(b), is measured to have a power-law growth with exponent 0.53(3), in close agreement with the theoretical prediction of an exponent of 1/2. The exponential growth rate of the modes' amplitudes

increases linearly in the drive strength μ, also in agreement with the prediction of the model. Having confirmed the parametric amplifier coupling between the signal and idler, we now describe the implemented enhanced sensing protocol.

D.4 Scheme

As seen in Fig. D.1(a), the cross-quadrature steady-state squeezing achieved through a continuous pump drive reaches a 3 dB limit near the threshold, i.e. $\langle x_+^2(\mu) \rangle^{\frac{1}{2}} \xrightarrow{\mu \to 1} \frac{1}{\sqrt{2}} \langle x_+^2 \rangle^{\frac{1}{2}} \big|_{\mu=0}$. To circumvent this limitation, we implement a transient protocol, schematically shown in Fig. D.2(a). The signal and idler modes are initialized in a thermal product state for times $t < 0$. At time $t = 0$, the parametric amplifier is turned on with an amplitude much larger than the critical drive strength ($\mu \gg 1$), but for a time t_{PA} much shorter than the signal or idler ringdown times ($t_{\mathrm{PA}} \ll \gamma_{s,i}^{-1}$) (Fig. D.2(a), row 1). This short burst of parametric coupling creates a highly two-mode-squeezed state which breaks the aforementioned 3 dB limit and has high signal-idler correlations. Following this, before any significant decay of the correlations, the signal mode is actuated by an impulse force (Fig. D.2(a), row 2) that displaces x_s (Fig. D.2(a), row 3). By detecting the quadratures of the idler mode (Fig. D.2(a), row 4), which remain unaffected by the impulse force, and using the persistent signal-idler correlations to cancel out the thermal component of the measured signal mode quadratures, we can achieve enhanced detection sensitivities.
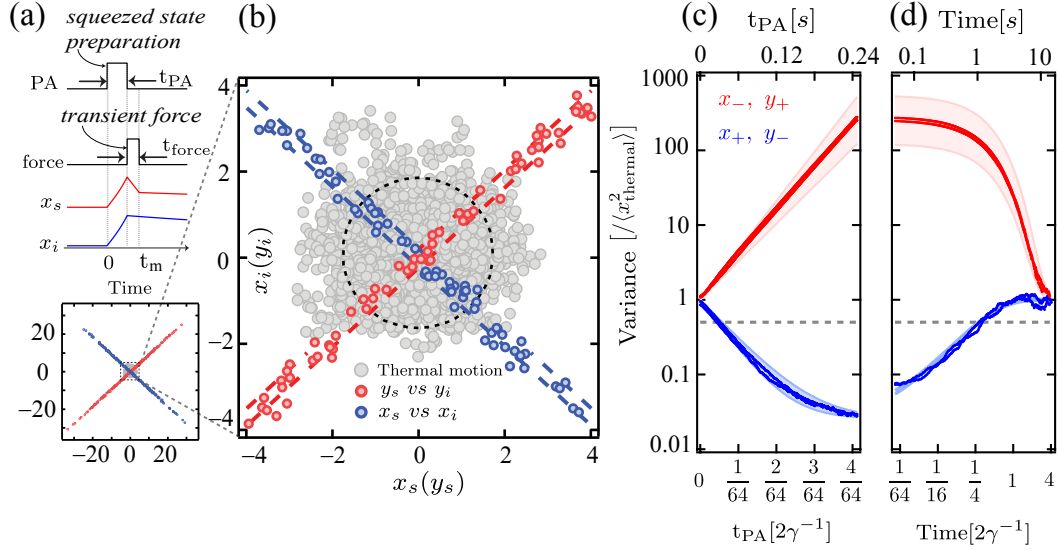
Figure D.2: **Enhanced transient squeezing – scheme, phase space distribution and squeezing dynamics.** By transiently applying a strong parametric amplifier pump drive, we realize two-mode squeezing beyond the steady-state 3 dB bound. (a) The timing sequence : The signal and idler modes are both initialized in a thermal state. At time $t = 0$, a strong pulse realizing a parametric amplifier coupling between the modes is applied for a short time t_{PA}, generating strong correlations between them at the end of the pulse. The signal mode is thereafter subjected to a force for time t_{force}. The modes' amplitudes are continuously measured at all times. (b) Phase space distribution of the 15.4(3)dB squeezed states – (x_s, x_i) (blue) and (y_s, y_i) (red). The thermal state (grey) is shown for reference. (c,d) Dynamics of growth (c) and decay (d) of the two-mode squeezed state. The parametric amplifier pump is driven transiently with strength $\mu = 38(5)$, and the quadrature variances of 236 iterations is plotted *vs* time. For comparison, the steady state bound of 3 dB is indicated in grey. The shaded regions represent no-free-parameter bounds due to variations in the parametric drive μ across the iterations. (All displacements are normalized to their respective thermal amplitudes measured at $t = 0$.)

254

D.5 Transient squeezing

The dynamics of the transient squeezing achieved through the parametric amplifier pulse is governed by the equations of motion for the signal and idler modes: $\dot{A}_{s,i} = \frac{\mu}{2}\sqrt{\gamma_s\gamma_i}A_{i,s}^* - \frac{\gamma_{s,i}}{2}A_{s,i} + \sqrt{\gamma_{s,i}}F_{s,i}^{in}$, where $F_{s,i}^{in}$ are the input noises with correlations $\langle F_{s,i}^*(t)F_{s,i}(t')\rangle = 2\langle x_{th,s,i}^2\rangle\delta(t-t')$, and $\langle x_{th,s,i}^2\rangle$ is the thermal variance of the signal and idler mode displacements, which satisfy equipartition $\frac{1}{2}m_{s,i}\omega_{s,i}^2\langle x_{th,s,i}^2\rangle = \frac{1}{2}k_BT$ at temperature T. (See also Supplementary Information, Section D.9.2 for detailed derivations.) While the simultaneous solution to these equations is straightforward for the experimentally relevant case of mismatched damping rates ($\gamma_s \neq \gamma_i$) [83], we state here the results for identical damping rates ($\gamma_s = \gamma_i = \gamma$) and note that the essential conclusions remain unaltered (see also Supplementary Information, Section D.9.7).

In units of the initial ($t = 0$) thermal variance of the modes, the resultant variances at the end of the parametric amplifier pulse are given by $\langle x_+^2(t_{PA})\rangle = \frac{1}{1+\mu} + \frac{\mu}{1+\mu}e^{-\gamma(1+\mu)t_{PA}}$ and $\langle y_+^2(t_{PA})\rangle = \frac{1}{1-\mu} + \frac{\mu}{\mu-1}e^{\gamma(\mu-1)t_{PA}}$ where $x_+ \equiv \frac{x_s+x_i}{\sqrt{2}}$ and $y_+ \equiv \frac{y_s+y_i}{\sqrt{2}}$ are respectively the squeezed and anti-squeezed cross-quadratures. Note that the squeezed cross-quadrature variance exponentially saturates to $\frac{1}{(1+\mu)}$ with a time constant $[\gamma(1+\mu)]^{-1} \ll \gamma^{-1}$. A large parametric amplifier actuation $\mu \gg 1$ thus allows for significant noise squeezing beyond the steady-state 3 dB bound. Note that the degree of squeezing (and anti-squeezing) can be parametrized by the power gain of the strong parametric amplifier pulse, $G^2 \equiv \langle y_+^2(t = t_{PA})\rangle/\langle y_+^2(t = 0)\rangle \approx e^{\gamma\mu t_{PA}}$. The amplified quadrature increases in variance as G^2, while the squeezed variance reduces approximately as $1/G^2$, the approximation being valid at short times, before the squeezing saturates.

We demonstrate such dynamics, and the resultant noise reduction by 15.4(3) dB, in Fig. D.2(b,c). The slow decay of the highly squeezed state back to the thermal state, shown in Fig. D.2(c), enables a multi fold improvement of the signal to noise ratio (SNR) for the detection of impulsive forces, and an enhanced bandwidth of force detection, as demonstrated below.

D.6 Enhanced displacement sensitivity

The two-mode squeezed state generated at time t_{PA} by the strong parametric amplifier pulse has a high degree of correlation $\zeta_x \equiv \frac{\sum(x_s - \langle x_s \rangle)(x_i - \langle x_i \rangle)}{\sqrt{\sigma_{x_s}} \sqrt{\sigma_{x_i}}}$ between x_s and x_i (see Fig. D.2(b)), where σ denotes the respective quadrature variances. Before these correlations decay and the modes return to their thermal states, which occurs on the timescale of γ^{-1}, we apply a short resonant impulse force on the signal mode for time $t_{force} \ll \gamma^{-1}$. After the impulse force is applied, at time $t = t_m > t_{PA} + t_{force}$, we measure the signal and idler quadratures, and construct a least-variance estimator of the force-induced signal displacement, i.e. $x_{s,IF} = x_s - \zeta_x \sqrt{\frac{\sigma_{x_s}}{\sigma_{x_i}}} x_i$, with all quantities being evaluated at time t_m. Transient squeezing and the resulting signal-idler correlations persist at time t_m (see Fig. D.2(c)), so that this estimator has a variance much smaller than the thermal variance of the signal mode. E.g. consider large power gains $G^2 \gg 1$, for which $|\zeta_x|$ is near unity ($-1 < \zeta_x < -0.9995$ for the squeezed state shown in Fig. D.2(b)). Assuming $\sigma_{x_s} \approx \sigma_{x_i}$, the estimator is $x_{s,IF} \approx x_s + x_i = \sqrt{2}x_+$, so that $\langle \Delta x_{s,IF}^2 \rangle \approx 2\langle \Delta x_+^2 \rangle$. With the variance $\langle \Delta x_+^2 \rangle$ being about $1/G^2$ smaller than the thermal variance, we can realize equally improved displacement sensitivities.

In the experiments, we achieve displacement sensitivities enhanced by up to

more than a factor of 20 [13.2(5) dB] in variance, well below the thermal noise limit (see red data in Fig. D.3). Because the other cross-quadrature $y_- \equiv \frac{y_s - y_i}{\sqrt{2}}$ is also equivalently squeezed, generating correlations ζ_y between y_s and y_i, by using the corresponding estimator $y_{s,\mathrm{IF}} = y_s - \zeta_y \sqrt{\frac{\sigma_{y_s}}{\sigma_{y_i}}} y_i$, the detection sensitivity of y_s is also enhanced (blue data in Fig. D.3).

In our experiments, for concreteness, and to demonstrate the reliable measurement of a sub-thermal displacement using this protocol, the applied force was chosen to produce a signal mode displacement approximately half its thermal motion amplitude. The average over approximately two hundred iterations are shown as red data in the inset of Fig. D.3. The error bars here indicate the uncertainty of a single measurement, which equals the square root of the corresponding variance plotted on the main graph. The decreasing single-shot uncertainty clearly indicates how the SNR of a measured displacement dramatically improves with increasing squeezing (increasing power gain G^2). The measurements match very well with the gray points shown in the inset, which denote the expected displacement, calculated using the applied force strength and the calibrated signal mode susceptibility. The transient squeezing protocol thus reliably realizes accurate measurements with sub-thermal standard errors.

D.7   Improved scaling of sensitivity

While the above description of the enhancement explicitly refers only to the signal mode *displacement*, the protocol in effect achieves a higher *force* detection sensitivity as well, because the two are linked linearly by a susceptibility. As seen in Fig. D.3, the displacement sensitivity, and therefore that of the
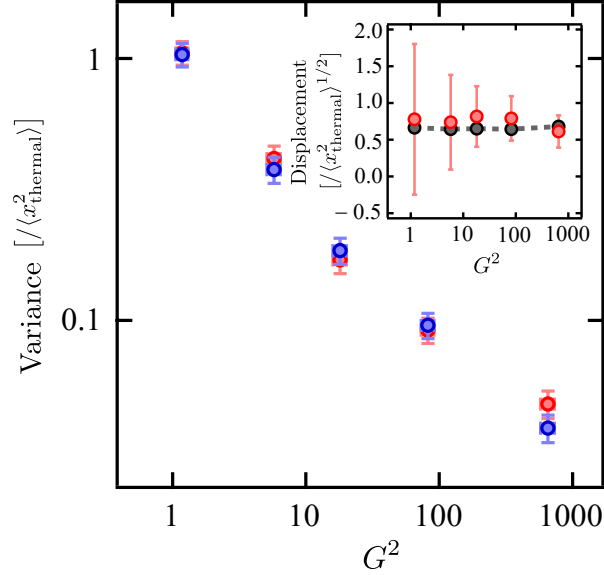
Figure D.3: **Enhanced displacement sensing.** Displacement sensitivities achieved using the transient squeezing protocol beat the thermal noise limit. The measured variances of the signal mode $x(y)$ quadrature are shown in red (blue) as a function of the experimentally measured parametric amplifier power gain G^2 (see text). The degree of squeezing increases with gain, and at the largest gain shown here, the displacement sensitivity is improved by 13.2(5) dB. (Inset) Detected motion and single-measurement uncertainty, as a function of power gain. The signal mode displacement measured here was produced by an impulse force applied along the x (red) quadrature, calibrated to displace it by approximately half the thermal motion amplitude. Grey dots represent the expected displacement based on calibration. The error bars indicate the uncertainty of a single measurement, which equals the square root of the corresponding variance shown on the main graph. The decreasing single-shot uncertainty indicates an improved signal to noise ratio at greater degrees of squeezing (G^2). At the largest gain shown here, the single-shot uncertainty is $\approx 0.22 \times$ thermal motion.

force inducing it, both scale as $1/G$, or equivalently, inversely with the signal mode amplitude after parametric amplification ($1/|A_s|$). This is in contrast to the amplitude-independent sensitivity that is achieved without the use of the transient squeezing protocol. Such an improved scaling with amplitude is achievable for any parameter M that, like a force, couples linearly to the signal mode, $H_{\text{int}} \propto MA_s + M^*A_s^*$ – an impulse of any such M causes a displacement in A_s given by $\int \dot{A}_s dt = \int \frac{\partial H_{\text{int}}}{\partial A_s^*} dt \propto \int M^* dt$. The improvement in the detection sensitivity scaling of A_s thus also results in an improved scaling for the detection of the parameter M.

Parameters other than a force can demonstrate even better sensitivity scaling with the amplitude $|A_s|$. We consider below a quadratic coupling $H_{\text{int}} \propto g_2|A_s|^2$. Such a coupling effects a change in the frequency of the signal oscillator. Over a finite duration t_{int}, the resultant frequency change induces an amplitude-independent phase shift $\phi = g_2 t_{\text{int}}$ of the signal mode. Such interactions are realized in mass sensing protocols, where an itinerant mass causes a frequency change in a calibrated sensor oscillator [262, 263, 264]. A higher sensitivity for the effected phase shift can thus translate to higher mass sensitivities. Moreover, improvements in scaling with amplitude are of particular importance in such applications, where larger amplitudes, though preferred, are plagued by concomitant deleterious effects like Duffing nonlinearities, which adulterate the measured phase shifts.

The transient squeezing protocol can be adapted to this end, to realize a sensitivity that scales as $1/|A_s|^2$. At time $t = 0$, we coherently drive the signal mode to a complex amplitude $iA_{s,0}$, where $A_{s,0} \in \mathbb{R}$, while leaving the idler mode in its thermal state. In this scenario, at the end of the strong parametric ampli-
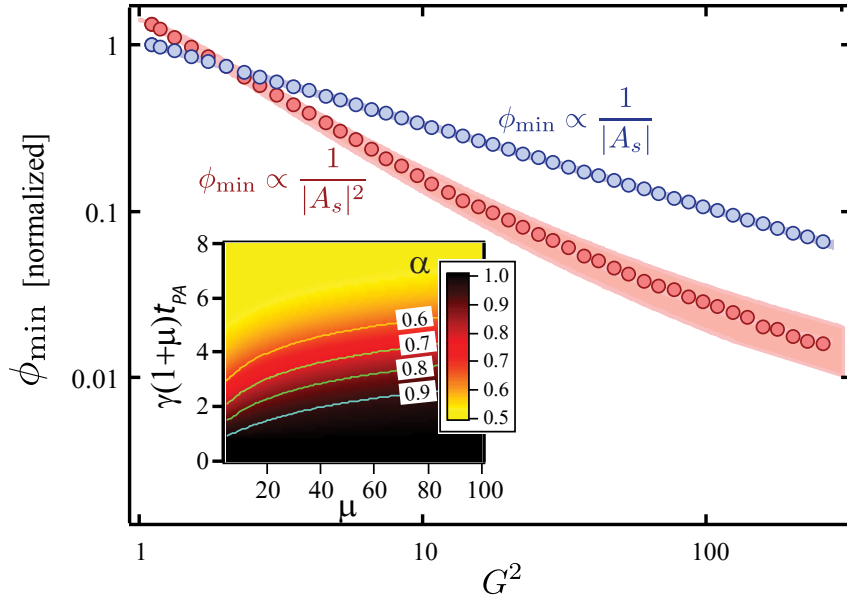
Figure D.4: **Improved scaling of phase sensitivity:** Minimum detectable phase $\phi_{\min}$ using (red) and without using (blue) the transient squeezing protocol as a function of the power gain G^2 experimentally measured in Fig. D.2. Normalized to the thermal noise limited $\phi_{\min}$ (blue) at $G = 1$. The shaded regions represent no-free-parameter bounds due to variations in the parametric drive μ across the iterations. (Inset) Scaling (α) of the achievable phase sensitivity with signal mode amplitude, where $\phi_{\min} \sim 1/|A_s|^{2\alpha}$. The scaling α shown here is calculated by increasing the parametric amplifier pulse duration t_{PA} at a fixed drive strength μ to effect increasing $|A_s|$, as realized in the experiment (main graph). The enhanced scaling of $\alpha = 1$ (scaling as $1/|A_s|^2$) using the transient squeezing protocol reverts to the $\alpha = 1/2$ (scaling as $1/|A_s|$) at long pulse durations (large G^2) as the squeezed variance saturates to $\frac{1}{1+\mu}$. The scaling is recovered by operating at larger drive strengths μ and shorter durations t_{PA} (see Supplementary Information, Section D.9.9).

fier pulse, the system realizes displaced squeezed states – the cross-quadratures x_+, x_- are still respectively highly squeezed and anti-squeezed, with zero means $\langle x_\pm \rangle = 0$, while due to the finite seed $iA_{s,0}$, the y-quadratures $\langle y_s(t_{\mathrm{PA}}) \rangle$ and $\langle y_i(t_{\mathrm{PA}}) \rangle$ take on finite values $\approx G \frac{A_{s,0}}{2\sqrt{2}}$. (See Supplementary Information, Section D.9.8 for exact and detailed derivations.)

260

Having prepared this transient squeezed state, and before it relaxes back to a thermal state, we couple the signal mode to an impulse for a duration $t_{\text{int}} \ll \gamma^{-1}$ such that the signal picks a phase shift ϕ. This signal phase shift causes the finite displacement $\langle y_s(t_{\text{PA}}) \rangle$ to get projected on to the x_s quadrature, i.e. $\langle x_s(t_{\text{PA}} + t_{\text{int}}) \rangle \approx G \frac{A_{s,0}}{2\sqrt{2}} \sin\phi$, while it leaves the idler mode unaffected. We construct the estimator of the phase-induced signal displacement $x_{s,\phi} = x_s - \zeta_x \sqrt{\frac{\sigma_{x_s}}{\sigma_{x_i}}} x_i$, where all the quantities are evaluated at time $t_{\text{PA}} + t_{\text{int}}$, including the correlation ζ_x between x_s and x_i. Like before, this estimator has a variance much smaller than the initial thermal variance of the signal mode, given the persistent correlations. For $t_{\text{PA}} \ll \gamma^{-1}$, the standard error $\langle \Delta x_{s,\phi}^2 \rangle^{1/2} = \sqrt{2} \langle \Delta x_+^2 \rangle^{1/2} \propto e^{-\gamma(\mu+1)t_{\text{PA}}/2} \approx 1/G$. The minimum detectable phase (SNR = 1) is thus given by

$$\phi_{\min} = \frac{\langle \Delta x_{s,\phi}^2 \rangle^{1/2}}{d\langle x_s \rangle / d\phi |_{\phi=0}} \propto \frac{1}{G^2 A_{s,0}} \propto \frac{1}{|A_s|^2} \tag{D.2}$$

showing the enhanced sensitivity and its improved scaling as $1/G^2$, or equivalently $1/|A_s|^2$ (Fig. D.4). At longer parametric pulse durations t_{PA}, the degree of two-mode squeezing saturates to $1/(1 + \mu)$ as described earlier, while the amplitude $|A_s|$ keeps growing exponentially, causing the sensitivity to revert back to the former scaling of $\phi_{\min} \propto 1/|A_s|$, as seen in the inset of Fig. D.4 (vertical cross-section at a fixed μ). The enhanced scaling is recovered by operating at larger drive strengths μ and shorter durations t_{PA} (see Supplementary Information, Section D.9.9).

The improvement in sensitivities and scaling with amplitude in our system can be generalized to higher order interactions, i.e. $H_{\text{int}} \propto g_k |A_s|^k$ [265, 266, 255]. For example, for the case of the Duffing nonlinearity, which has $k = 4$. While straightforward, such a generalization is beyond the scope of the current work and will be considered elsewhere.

D.8 Conclusions

In summary, we implement a transient two-mode squeezing protocol in a system of parametrically coupled mechanical modes in a monolithic SiN membrane resonator. We demonstrate a substantial degree of transient two-mode squeezing, achieving a noise reduction of 15.4(3) dB, well beyond the conventional 3 dB bound, as also a concomitant displacement sensing enhancement of 13.2(5) dB. We further adapt the transient squeezing protocol to effect a phase sensitivity scaling of $\phi_{\min} \propto 1/|A_s|^2$. Owing to the large $f \times Q$ product of the optomechanical modes, this transient state is long lived, surviving on the order of 10^6 mechanical periods. Our work extends the optomechanical toolbox for the quantum manipulation of macroscopic mechanical motion, and enables new techniques for optomechanical metrology and the manipulation of mechanical fluctuations. Extending these techniques to the quantum regime should allow for studies of macroscopic decoherence in highly correlated phononic states. Even in the classical regime, we note that the emergence and decay of two-mode correlations and the ensuing thermalization dynamics are intimately tied to the nature of the reservoir that couples to the optomechanical modes. As such, ultra-precise measurement schemes, such as those demonstrated in this work, enable the study of non-equilibrium optomechanical dynamics, the detection of non-Markovian dynamics [218] arising from non-Ohmic reservoirs, and the harnessing of such reservoirs for the creation and stabilization of macroscopic nonclassical states [229].

D.9 Supplementary Information

D.9.1 Optical detection and stabilization of mechanical modes

The mechanical resonators studied in this work are the eigenmodes of a square silicon nitride membrane resonator fabricated by NORCADA Inc. The membranes have lateral dimensions of 5 mm and a thickness of 100 nm, with typical mechanical quality factors in the range of 10^7 [79]. The displacement of the membrane modes are detected using a Michelson optical interferometer with a position sensitivity of 14 fm/Hz$^{1/2}$ for typical powers of 200 μW incident on the membrane. An external cavity diode laser operating at a wavelength of 780 nm provides the light for this interferometer.

Due to the different thermal expansion coefficients of the membrane and the supporting substrate, temperature fluctuations change the membrane strain and stress, which in turn change the mechanical modes' frequencies. Thermal fluctuations thus lead to frequency fluctuations. The precise measurement of thermomechanical motion and two-mode correlations requires active sub-linewidth stabilization of the mechanical eigenfrequencies. This is accomplished by photothermal control of the silicon substrate. As described in previous work [150], we implement active stabilization by continuously monitoring the mechanical eigenfrequency of a high-Q membrane mode at 2.736 MHz - far from the modes of interest in this work. Phase sensitive detection of this mode generates an error signal with an on-resonant phase slope of 5.91 radians/Hz. Active photothermal stabilization of the substrate is accomplished with typical powers of 600 μW, generated by a diode laser at 830 nm. Under this active stabilization, the rms frequency fluctuations of this 'thermometer mode' are mea-

sured to be below 0.4 mHz, equivalent to temperature fluctuations of less than 2 μK. For the modes of the interferometer, this translates to frequency fluctuations less than $0.002 \times \gamma$.

At low frequencies (< 3 Hz), the optical interferometer used for the detection of mechanical displacement is susceptible to residual amplitude modulation (RAM) which we suspect is caused by the gradual temperature fluctuations and temperature-dependent birefringence of the various optical elements. In our experiments, this low frequency amplitude noise convolves with the mechanical displacement signal leading to a 0.75% contamination of the detected membrane displacement and the two-mode correlations. Due to this low-frequency RAM, the signal-to-noise ratio for the mechanical thermal motion degrades to 1 as the mechanical amplitude approaches 150 times the room-temperature thermal amplitude. This restricts the dynamic range of membrane amplitudes over which we can study the mechanical PA-PO. In this work, we overcome this limitation by artificially increasing the mechanical thermal noise (and effective temperature of the mechanical modes), by driving each mode with gaussian noise centered at each mechanical eigenfrequency over a bandwidth of 100 Hz, much larger than the respective mechanical linewidths. Techniques of active RAM control [267] can be used to extend our measurements to the quantum regime of mechanical motion.

D.9.2 Nonlinear interaction and the equations of motion

We consider the equations of motion of the signal, idler and pump modes. Within the rotating wave approximation, the Hamiltonian (D.1) gives

$$\ddot{z}_{s,i} \quad + \quad \gamma_{s,i}\dot{z}_{s,i} + \omega_{s,i}^2 z_{s,i} = \frac{1}{m_{s,i}}(F_{s,i}(t) + \frac{g}{2}z_P z_{i,s}^*)$$

$$\ddot{z}_P \quad + \quad \gamma_P \dot{z}_P + \omega_P^2 z_P = \frac{1}{m_P}(F_P(t) + \frac{g}{2}z_s z_i)$$

where $z_{s,i,P}$ denote the complex displacement of each mode and $m_{s,i,P}$, $\omega_{s,i,P}$, $\gamma_{s,i,P}$ and $F_{s,i,P}$ denote respectively the masses, frequencies, damping rates and forces on each of the modes. These coupled equations of motion can be solved using two timescale perturbation theory [115] and simplify to the first order coupled equations,

$$2\dot{\tilde{A}}_s \quad = \quad \gamma_s\left[-\tilde{A}_s + i\frac{g}{2}\chi_s\tilde{A}_i^*\tilde{A}_P + i\chi_s\tilde{F}_s(t)\right]$$

$$2\dot{\tilde{A}}_i \quad = \quad \gamma_i\left[-\tilde{A}_i + i\frac{g}{2}\chi_i\tilde{A}_s^*\tilde{A}_P + i\chi_i\tilde{F}_i(t)\right]$$

$$2\dot{\tilde{A}}_P \quad = \quad \gamma_P\left[-\tilde{A}_P + i\frac{g}{2}\chi_P\tilde{A}_s\tilde{A}_i + i\chi_P\tilde{F}_P(t)\right]$$

where $z_k = \tilde{A}_k e^{-i\omega_k t}$, $k \in \{i, s, P\}$; $\tilde{F}_k$ are the slowly varying (complex) amplitudes of the external forces on the individual modes, and $\chi_k = (m_k\omega_k\gamma_k)^{-1}$ are their on-resonant susceptibilities. We ignore terms such as $\ddot{\tilde{A}}_k, \gamma_i\dot{\tilde{A}}_k$ in the slow time approximation. The equations get further simplified to

$$2\dot{A}_s \quad = \gamma_s[-A_s + iA_i^*A_P + i\mathcal{F}_s(t)]$$

$$2\dot{A}_i \quad = \gamma_i[-A_i + iA_s^*A_P + i\mathcal{F}_i(t)]$$

$$2\dot{A}_P \quad = \gamma_S[-A_P + iA_sA_i + i\mathcal{F}_P(t)]$$

where the motion of the pump A_P is normalized with respect to $\tilde{A}_{P,\text{cr}}$ – the critical value which defines the instability threshold $\mu = 1$, $\tilde{A}_{s,i}$ are normalized with respect to their characteristic steady-state motion above threshold $\frac{2}{g\sqrt{\chi_S\chi_{i,s}}}$, and $\mathcal{F}_k$ are normalized forces on the respective modes, with $\mathcal{F}_S(t) = \mu(t)$. Lastly, we

assume that the pump mode, which is a Silicon substrate mode, has a much larger damping rate than the signal and idler resonator modes [150], i.e. $\gamma_P \sim (10^3 - 10^4)\gamma_s, \gamma_i$, thereby ensuring that the pump motion adiabatically follows the signal and idler motions, i.e. $A_P = iA_sA_i + i\mathcal{F}_P(t)$.

D.9.3   Effect of finite substrate temperature

To reduce the contribution of residual amplitude modulation in the optical interferometer to the signal and idler motion readout, all data are acquired by artificially driving the signal and idler modes to an elevated temperature, corresponding to an effective thermal motion around 40-50 times the room temperature amplitude, by driving the two modes with a gaussian noise source with a bandwidth about 100 times larger than the respective mechanical linewidths. The substrate mode, however, is not artificially driven to a larger temperature.

For below threshold steady state ($\mu < 1$), the substrate fluctuations do not couple to signal and idler mode to first order [83]. Above threshold at steady state ($\mu > 1$), however, substrate mode fluctuations couple to the signal and idler mode. In the matched damping case, because they couple equally, the amplitude-difference squeezing $\left(r_- \equiv \frac{\delta r_s - \delta r_i}{\sqrt{2}} \right)$ is independent of and robust to substrate fluctuations. However, substrate fluctuations couple to the amplitude-sum quadrature $\left(r_+ \equiv \frac{\delta r_s + \delta r_i}{\sqrt{2}} \right)$. For equal substrate, signal, and idler temperatures, the amplitude-sum variance is bounded at 1/2 in the limit of large parametric drive strengths, $\mu \gg 1$. However, if the substrate temperature is much *lower* than the signal and idler temperatures, the substrate fluctuations are negligible in comparison, and the amplitude-sum squeezing beats the conventional

3dB limit – in fact, the amplitude-sum variance equals $\frac{1}{2(\mu-1)}$. This difference in the signal and idler and substrate temperatures has been accounted for in Fig. D.1(a) of the main text.

D.9.4   Effect of finite measurement time

To accurately model the measurements described in this work, the effects of finite measurement duration need to be considered. This is particularly relevant for the high-Q resonators used in this work. In the vicinity of the critical point $\mu = 1$, the mechanical parametric amplifier exhibits a divergent response time that results in extremely long relaxation times ($\sim 10^4 - 10^5$ seconds). Thus, for typical measurement duration in this work (~ 100 seconds), the measured squeezing variance can deviate appreciably from those computed in steady state.

In our model, we take the finite measurement duration into account by computing the variances measured over a measurement time τ_m using the truncated integral of the relevant spectral density as indicated below [83],

$$\sigma_{\alpha,\beta} = 2 \int_{2\pi/\tau_m}^{\infty} \mathbf{S}_{\alpha,\beta}(\omega) d\omega \tag{D.3}$$

D.9.5   Parametric amplifier dynamics and transient squeezing

The lossy system here can be formally modelled as a linear coupling of the mechanical modes to an environmental bath of harmonic oscillators. For a Markovian bath, the dynamics for the case of matched frequencies and loss rates is governed by $\dot{A}_{s,i} = -\frac{\gamma}{2}\mu A_{i,s}^* - \frac{\gamma}{2}A_{s,i} + \sqrt{\gamma}F_{s,i}^{in}$, where we have approximated $A_P = i\mu$,

$\mu = X_P/X_{P,\mathrm{cr}}$ parametrizing the parametric pump drive strength at the sum frequency. This approximation is valid when $|A_sA_i| \ll \mu$ (see Section D.9.6 below). Defining the cross-quadrature modes $A_\pm \equiv (A_s \pm A_i)/\sqrt{2}$, the equations of motion are rewritten as

$$\dot{x}_+ = -\frac{\gamma}{2}(\mu + 1)x_+ + \sqrt{\gamma}F^{in}_{x+}; \quad \dot{y}_+ = \frac{\gamma}{2}(\mu - 1)y_+ + \sqrt{\gamma}F^{in}_{y+}$$

$$\dot{y}_- = -\frac{\gamma}{2}(\mu + 1)y_- + \sqrt{\gamma}F^{in}_{y-}; \quad \dot{x}_- = \frac{\gamma}{2}(\mu - 1)x_- + \sqrt{\gamma}F^{in}_{x-}$$

(D.4)

where the real quadratures x, y are defined in terms of the complex amplitudes A, A^* as $x \equiv (A + A^*)/2$, $y \equiv (A - A^*)/2i$, for each, the signal and idler modes, and $x_\pm \equiv (x_s \pm x_i)/\sqrt{2}$, $y_\pm \equiv (y_s \pm y_i)/\sqrt{2}$, and the noise terms $F^{in}_{x\pm}$, $F^{in}_{y\pm}$ are correspondingly defined.

Assuming an initial thermal state for both the signal and idler modes, the dynamics of the cross quadrature variances is evaluated to be $\langle \Delta x^2_+(t) \rangle = \langle \Delta y^2_-(t) \rangle = \frac{1}{1+\mu} + \frac{\mu}{1+\mu}e^{-\gamma(\mu+1)t}$, which are squeezed, and $\langle \Delta x^2_-(t) \rangle = \langle \Delta y^2_+(t) \rangle = \frac{1}{1-\mu} + \frac{\mu}{\mu-1}e^{\gamma(\mu-1)t}$, which are amplified, or anti-squeezed; the variances in these expressions have been normalized to the thermal variances. While these dynamics are correct below threshold ($\mu < 1$), their validity well above threshold, as in this work, is restricted to small times, before the onset of pump depletion, which is detailed in the Section D.9.6 below. Nonetheless, the squeezed quadrature variances reduce exponentially to $1/(1+\mu)$, surpassing the steady state 3 dB bound [83, 150].

D.9.6 Pump depletion

The assumption that $A_P(t) = i\mu$ is a constant over the course of evolution of the parametric amplifier pulse is invalid for $\mu_0 \equiv \mu(t = 0) > 1$. As the signal and idler amplitudes grow, the pump amplitude motion becomes $A_S(t) = i\mu(t) + iA_iA_s \approx$

$i\mu(t) - i|A_iA_s|$. This effect, which arises from the interaction of the signal, idler and pump modes, is referred to as pump depletion.

When the parametric amplifier pulse is switched on, A_s and A_i initially increase as $\exp(\gamma(\mu_0 - 1)t/2)$, thereby causing $A_P(t)$ to decrease and settle to a steady state of $|A_P(t)| \xrightarrow{t \to \infty} 1$ at long times [83]. As such, for $\mu_0 > 1$, the transient squeezing expressions derived assuming a constant $A_P(t) = i\mu_0$ are valid only for small times (see also [268, 269]).

Considering a case where the signal and idler motions are seeded with complex amplitudes $A_{s,0}$ and $A_{i,0}$, a pump depletion by a factor η occurs when $|A_s(t)A_i(t)| = \eta|F_S| = \eta\mu_0$, i.e. when $|A_{s,0}A_{i,0}|e^{\gamma(\mu_0-1)t_{\mathrm{PA}}} = \eta\mu_0$. For time $t_{\mathrm{PA}} \sim \frac{\ln(10\mu_0)}{\gamma(1+\mu_0)}$, the squeezed variances reduce to within 10% of $\frac{1}{1+\mu_0}$, and for this time t_{PA},

$$\eta \sim (10\mu_0)^{\frac{\mu_0-1}{\mu_0+1}} \frac{|A_{s,0}A_{i,0}|}{\mu_0} \xrightarrow{\mu_0 \gg 1} 10|A_{s0}A_{i0}|$$

For the amplitudes in the present study (data in Fig. D.2, Fig. D.3 and Fig. D.4 of the main text), $|A_{s,0}| \approx |A_{i,0}| \approx 0.03$, and $\eta \approx 0.01$, i.e. there is a mere 1% pump depletion even at almost saturated squeezing.

Clearly, the degradation of squeezing for fixed μ due to pump depletion sets in sooner for (i) larger seeds $|A_{s,0}|, |A_{i,0}|$, (ii) larger damping of the signal, idler and pump modes, and (iii) larger nonlinear signal-idler couplings g (see also [269]). We note that the deleterious effects of pump depletion can be avoided by compensating the pump depletion with feedback and other control systems.

D.9.7 Transient squeezing in the presence of mismatched damping rates

In the case of mismatched frequencies and damping rates for the signal and idler modes, the main differences are (i) the minimum variance of the squeezed quadrature becomes mismatch dependent, but agrees with the expression in the main text to within 10% for asymmetry parameters $|\delta_\omega - \delta_\gamma| < 0.20$ where $\delta_\omega = \frac{\omega_s - \omega_i}{\omega_s + \omega_i}$, $\delta_\gamma = \frac{\gamma_s - \gamma_i}{\gamma_s + \gamma_i}$ [83], and (ii) the time constants of transient evolution of the squeezed and amplified quadratures are respectively altered to $|\frac{\gamma_s + \gamma_i}{2}(1 \pm \mu \sqrt{1 - \delta_\gamma^2})|^{-1}$ for $\mu \gg \frac{\delta_\gamma}{\sqrt{1 - \delta_\gamma^2}}$.

D.9.8 Phase sensitivity

If the signal mode is initialized at time $t = 0$ to have a mean complex amplitude $\langle A_s(0) \rangle = iA_{s,0}$ through a coherent drive, and the idler mode is initialized in its thermal state with mean amplitude $\langle A_i(0) \rangle = 0$, the decoupled cross-quadratures take on the values $\langle x_\pm(0) \rangle = 0, \langle y_\pm(0) \rangle = A_{s,0}/\sqrt{2}$. Propagating Eqn.s (D.4) for a parametric amplifier pulse duration t_{PA}, we have

$$\langle x_+(t_{\text{PA}}) \rangle = 0; \qquad \langle y_+(t_{\text{PA}}) \rangle = \frac{A_{s,0}}{\sqrt{2}} e^{\gamma(\mu - 1)t_{\text{PA}}/2}$$

$$\langle x_-(t_{\text{PA}}) \rangle = 0; \qquad \langle y_-(t_{\text{PA}}) \rangle = \frac{A_{s,0}}{\sqrt{2}} e^{-\gamma(\mu + 1)t_{\text{PA}}/2}$$

$$\Rightarrow \quad \langle x_s(t_{\text{PA}}) \rangle = 0; \qquad \langle y_s(t_{\text{PA}}) \rangle = \frac{A_{s,0}}{2\sqrt{2}} \left(e^{\gamma(\mu - 1)t_{\text{PA}}/2} + e^{-\gamma(\mu + 1)t_{\text{PA}}/2} \right) \approx G \frac{A_{s,0}}{2\sqrt{2}} \quad \text{(D.5)}$$

$$\langle x_i(t_{\text{PA}}) \rangle = 0; \qquad \langle y_i(t_{\text{PA}}) \rangle = \frac{A_{s,0}}{2\sqrt{2}} \left(e^{\gamma(\mu - 1)t_{\text{PA}}/2} - e^{-\gamma(\mu + 1)t_{\text{PA}}/2} \right) \approx G \frac{A_{s,0}}{2\sqrt{2}}$$

where the approximation is valid for $G \gg 1$. The subsequent interaction over time t_{int} that results in a phase shift of the signal mode by ϕ causes the signal

quadratures to mix as

$$\langle x_s(t_{\text{PA}} + t_{\text{int}}) \rangle = \quad \cos\phi \, \langle x_s(t_{\text{PA}}) \rangle + \sin\phi \, \langle y_s(t_{\text{PA}}) \rangle \approx G \frac{A_{s,0}}{2\sqrt{2}} \sin\phi$$

$$\langle y_s(t_{\text{PA}} + t_{\text{int}}) \rangle = \quad -\sin\phi \, \langle x_s(t_{\text{PA}}) \rangle + \cos\phi \, \langle y_s(t_{\text{PA}}) \rangle$$

where we have used Eqn. D.5, and the approximation is valid for $G \gg 1$.

Note that the correlations realized by the transient squeezing at time t_{PA} are between the un-rotated signal quadratures, and the idler quadratures. Thus, when constructing the reduced-variance estimator based on the quadratures measured at time $t_{\text{PA}} + t_{\text{int}}$, i.e. after the signal phase has rotated by ϕ, the rotation by ϕ needs to be accounted for. For $\phi \ll 1$, this effect is negligible and may be ignored. For larger phase shifts, the rotation-compensation and phase estimation may be implemented iteratively for yielding higher precision. (Consider, for example, the exaggerated case of $\phi = \pi/2$. Correlations between (x_s, x_i) & (y_s, y_i) at time t_{PA} are transformed to correlations between (y_s, x_i) & $(-x_s, y_i)$ at time $t_{\text{PA}} + t_{\text{int}}$, after the signal's rotation by $\phi = \pi/2$.)

D.9.9 Enhanced scaling with amplitude

In the absence of pump depletion (Section D.9.6), the squeezed variance of x_+ and y_- saturates to $1/(1 + \mu)$ exponentially, with a time constant $[\gamma(1 + \mu)]^{-1}$, as derived earlier. However, the exponential amplification of the signal and idler modes $|A_s|, |A_i|$ continues for times even beyond the saturation timescale. In such a parameter regime of the parametric amplifier pulse durations t_{PA}, while the absolute phase sensitivity keeps improving with increasing amplitude (i.e. increasing gain G^2), the scaling reverts from a $1/|A_s|^2$ dependence to $1/|A_s|$. In

other words,

$$\langle \Delta x_{s,\phi}^2 \rangle^{1/2} \propto e^{-\gamma(1+\mu)t_{\text{PA}}/2} \approx 1/G \xrightarrow{t_{\text{PA}} \gg [\gamma(1+\mu)]^{-1}} \langle \Delta x_{s,\phi}^2 \rangle^{1/2} = \sqrt{2/(1+\mu)}$$

so that

$$\phi_{\text{min}} = \frac{\langle \Delta x_{s,\phi}^2 \rangle^{1/2}}{d\langle x_s \rangle/d\phi|_{\phi=0}} \propto \frac{1/G}{GA_{s,0}} \propto \frac{1}{|A_s|^2} \xrightarrow{t_{\text{PA}} \gg [\gamma(1+\mu)]^{-1}} \phi_{\text{min}} \propto \frac{\sqrt{2/(1+\mu)}}{GA_{s,0}} \propto \frac{1}{|A_s|^1}$$

We can instead choose to increase the amplitude $|A_s|$ and the squeezing not by only increasing t_{PA} but also μ. We can improve the ultimate squeezing bound $\frac{1}{1+\mu}$ by increasing μ, while also ensuring that the squeezing does not saturate in time, by changing t_{PA} appropriately. For example, if we choose a parametric amplifier pulse duration of $t_{\text{PA}}(\mu) = \frac{\log[k\mu]}{\gamma(1+\mu)}$, for a chosen k that is held fixed with increasing μ ($k\mu > 1$ for squeezing), then

$$\langle \Delta x_{s,\phi}^2 \rangle^{1/2} = \sqrt{2(k+1)\mu/(1+\mu)} \; e^{-\gamma(\mu+1)t_{\text{PA}}/2} \propto 1/G$$

for $\mu, G \gg 1$, thereby recovering the $1/|A_s|^2$ scaling of phase sensitivity with amplitude.

BIBLIOGRAPHY

[1] G. Kurizki, P. Bertet, Y. Kubo, K. Mølmer, D. Petrosyan, P. Rabl, and J. Schmiedmayer. Quantum technologies with hybrid systems. *Proceedings of the National Academy of Sciences*, 112:3866, 2015.

[2] www.sites.google.com/view/harassmentatcornellphysics.

[3] W. Ketterle, D. S. Durfee, and D. M. Stamper-Kurn. Making, probing and understanding bose-einstein condensates. In *Proceedings of the International School of Physics "Enrico Fermi", Edited by M. Inguscio, S. Stringari, C.E. Wieman*, page 67. IOS Press, 1999.

[4] I. Bloch. Ultracold quantum gases in optical lattices. *Nature Physics*, 1:23–30, 2005.

[5] I. Bloch, J. Dalibard, and W. Zwerger. Many-body physics with ultracold gases. *Reviews of Modern Physics*, 80:885, 2008.

[6] V. Vuletić, C. Chin, A. J. Kerman, and S. Chu. Degenerate raman sideband cooling of trapped cesium atoms at very high atomic densities. *Physical Review Letters*, 81:5768, 1998.

[7] M. Olshanii and D. Weiss. Producing bose-einstein condensates using optical lattices. *Physical Review Letters*, 89:090404, 2002.

[8] H. M. Wiseman and G. J. Milburn. *Quantum Measurement and Control*. Cambridge University Press, 2009.

[9] A. J. Daley. Quantum trajectories and open many-body quantum systems. *Advances in Physics*, 63(2):77–149, 2014.

[10] H. Ott. Single atom detection in ultracold quantum gases: a review of current progress. *Reports on Progress in Physics*, 79(5):054401, 2016.

[11] A. Omran, M. Boll, T. A. Hilker, K. Kleinlein, G. Salomon, I. Bloch, and C. Gross. Microscopic observation of pauli blocking in degenerate fermionic lattice gases. *Physical Review Letters*, 115:263001, 2015.

[12] M. F. Parsons, F. Huber, A. Mazurenko, C. S. Chiu, W. Setiawan, K. Wooley-Brown, S. Blatt, and M. Greiner. Site-resolved imaging of fermionic ^{6}Li in an optical lattice. *Physical Review Letters*, 114:213002, 2015.

[13] L. W. Cheuk, M. A. Nichols, M. Okan, T. Gersdorf, V. V. Ramasesh, W. S. Bakr, T. Lompe, and M. W. Zwierlein. Quantum-gas microscope for fermionic atoms. *Physical Review Letters*, 114:193001, 2015.

[14] G. J. A. Edge, R. Anderson, D. Jervis, D. C. McKay, R. Day, S. Trotzky, and J. H. Thywissen. Imaging and addressing of individual fermionic atoms in an optical lattice. *Physical Review A*, 92:063406, 2015.

[15] E. Haller, J. Hudson, A. Kelly, D. A. Cotta, B. Peaudecerf, G. D. Bruce, and S. Kuhr. Single-atom imaging of fermions in a quantum-gas microscope. *Nature Physics*, 11:738–742, 2015.

[16] M. Lewenstein, A. Sanpera, V. Ahufinger, B. Damski, A. Sen, and U. Sen. Ultracold atomic gases in optical lattices : mimicking condensed matter physics and beyond. *Advances in Physics*, 56:243, 2007.

[17] A. Polkovnikov, K. Sengupta, A. Silva, and M. Vengalattore. Colloquium: Nonequilibrium dynamics of closed interacting quantum systems. *Reviews of Modern Physics*, 83:863, 2011.

[18] B. J. Bloom, T. L. Nicholson, J. R. Williams, S. L. Campbell, M. Bishof, X. Zhang, W. Zhang, S. L. Bromley, and J. Ye. An optical lattice clock with accuracy and stability at the 10^{-18} level. *Nature*, 506:71–75, 2014.

[19] W. S. Bakr, J. I. Gillen, A. Peng, S. Folling, and M. Greiner. A quantum gas microscope for detecting single atoms in a hubbard-regime optical lattice. *Nature*, 462:74, 2009.

[20] N. Gemelke, X. Zhang, C. L. Hung, and C. Chin. In situ observation of incompressible mott-insulating domains in ultracold atomic gases. *Nature*, 460:995, 2009.

[21] P. Würtz, T. Langen, T. Gericke, A. Koglbauer, and H. Ott. Experimental demonstration of single-site addressability in a two-dimensional optical lattice. *Physical Review Letters*, 103:080404, 2009.

[22] J. F. Sherson, C. Weitenberg, M. Endres, M. Cheneau, I. Bloch, and S. Kuhr. Single-atom-resolved fluorescence imaging of an atomic mott insulator. *Nature*, 467:68, 2010.

[23] K. D. Nelson, X. Li, and D. S. Weiss. Imaging single atoms in a three-dimensional array. *Nature Physics*, 3:556, 2007.

[24] S. E. Hamann, D. L. Haycock, G. Klose, P. H. Pax, I. H. Deutsch, and P. S. Jessen. Resolved-sideband raman cooling to the ground state of an optical lattice. *Physical Review Letters*, 80:4149, 1998.

[25] D. J. Han, S. Wolf, S. Oliver, C. McCormick, M. T. DePue, and D. S. Weiss. 3d raman sideband cooling of cesium atoms at high density. *Physical Review Letters*, 85:724, 2000.

[26] A. J. Kerman, V. Vuletić, C. Chin, and S. Chu. Beyond optical molasses: 3d raman sideband cooling of atomic cesium to high phase-space density. *Physical Review Letters*, 84:439, 2000.

[27] C. Monroe, D. M. Meekhof, B. E. King, S. R. Jefferts, W. M. Itano, D. J. Wineland, and P. Gould. Resolved-sideband Raman cooling of a bound atom to the 3D zero-point energy. *Physical Review Letters*, 75:4011–4014, 1995.

[28] C. Cohen-Tannoudji, J. Dupont-Roc, and G. Grynberg. *Atom Photon Interactions*. Wiley-Interscience, New York, 1998.

[29] N. Syassen, D. M. Bauer, M. Lettner, T. Volz, D. Dietze, J. J. Garcia-Ripoll, J. I. Cirac, G. Rempe, and S. Dürr. Strong dissipation inhibits losses and induces correlations in cold molecular gases. *Science*, 320:1329, 2008.

[30] B. Yan, S. A. Moses, B. Gadway, J. P. Covey, K. R. A. Hazzard, A. M. Rey, D. S. Jin, and J. Ye. Observation of dipolar spin-exchange interactions with lattice-confined polar molecules. *Nature*, 501:521, 2013.

[31] D. Jaksch, C. Bruder, J. I. Cirac, C. W. Gardiner, and P. Zoller. Cold bosonic atoms in optical lattices. *Physical Review Letters*, 81:3108, 1998.

[32] W. Zwerger. Mott-hubbard transition of cold atoms in optical lattices. *Journal of Optics B*, 5:S9, 2003.

[33] K. S. Johnson, J. H. Thywissen, N. H. Dekker, K. K. Berggren, A. P. Chu, R. Younkin, and M. Prentiss. Localization of Metastable Atom Beams with Optical Standing Waves: Nanolithography at the Heisenberg Limit. *Science*, 280:1583, 1998.

[34] A. V. Gorshkov, L. Jiang, M. Greiner, P. Zoller, and M. D. Lukin. Coherent Quantum Optical Control with Subwavelength Resolution. *Physical Review Letters*, 100(9):093005, 2008.

[35] P. Windpassinger and K. Sengstock. Engineering novel optical lattices. *Reports on Progress in Physics*, 76(8):086401, 2013.

[36] M. A. Schlosshauer. *Decoherence: and the Quantum-To-Classical Transition*. Springer, 2007.

[37] W. H. Zurek. Decoherence, einselection, and the quantum origins of the classical. *Reviews of Modern Physics*, 75:715–775, 2003.

[38] E. Joos and H. D. Zeh. The emergence of classical properties through interaction with the environment. *Zeitschrift für Physik B Condensed Matter*, 59(2):223–243, 1985.

[39] *Quantum Optics, Experimental Gravity, and Measurement Theory, NATO Science Series B, Volume 94, Edited by P. Meystre and M. O. Scully*. Springer, 2011.

[40] R. Penrose. On gravity's role in quantum state reduction. *General Relativity and Gravitation*, 28(5):581–600, 1996.

[41] L. Diósi. Models for universal reduction of macroscopic quantum fluctuations. *Physical Review A*, 40:1165–1174, 1989.

[42] G. C. Ghirardi, A. Rimini, and T. Weber. Unified dynamics for microscopic and macroscopic systems. *Physical Review D*, 34:470, 1986.

[43] J. Kofler and Č. Brukner. Classical world arising out of quantum physics

under the restriction of coarse-grained measurements. *Physical Review Letters*, 99:180403, 2007.

[44] H. Jeong, Y. Lim, and M. S. Kim. Coarsening measurement references and the quantum-to-classical transition. *Physical Review Letters*, 112:010402, 2014.

[45] R. Kosloff. Quantum Thermodynamics: A Dynamical Viewpoint. *Entropy*, 15:2100–2128, 2013.

[46] A. M. Kaufman, M. E. Tai, A. Lukin, M. Rispoli, R. Schittko, P. M. Preiss, and M. Greiner. Quantum thermalization through entanglement in an isolated many-body system. *Science*, 353:794–800, 2016.

[47] R. V. Jensen and R. Shankar. Statistical behavior in deterministic quantum systems with few degrees of freedom. *Physical Review Letters*, 54:1879–1882, 1985.

[48] J. M. Deutsch. Quantum statistical mechanics in a closed system. *Physical Review A*, 43:2046–2049, 1991.

[49] M. Srednicki. Chaos and quantum thermalization. *Physical Review E*, 50:888–901, 1994.

[50] M. Rigol, V. Dunjko, and M. Olshanii. Thermalization and its mechanism for generic isolated quantum systems. *Nature*, 452:7189, 2008.

[51] J. M. Deutsch, H. Li, and A. Sharma. Microscopic origin of thermodynamic entropy in isolated systems. *Physical Review E*, 87:042135, 2013.

[52] J. Eisert, M. Friesdorf, and C. Gogolin. Quantum many-body systems out of equilibrium. *Nature Physics*, 11:124, 2015.

[53] L. D'Alessio, Y. Kafri, A. Polkovnikov, and M. Rigol. From quantum chaos and eigenstate thermalization to statistical mechanics and thermodynamics. *Advances in Physics*, 65(3):239–362, 2016.

[54] V. B. Braginsky and F. Y. Khalili. *Quantum Measurement*. Cambridge University Press, 1999.

[55] M. C. Fischer, B. Gutierrez-Medina, and M. G. Raizen. Observation of the quantum zeno and anti-zeno effects in an unstable system. *Physical Review Letters*, 87:040402, 2001.

[56] G. Barontini, R. Labouvie, F. Stubenrauch, A. Vogler, V. Guarrera, and H. Ott. Controlling the dynamics of an open many-body quantum system with localized dissipation. *Physical Review Letters*, 110:035302, 2013.

[57] E. W. Streed, J. Mun, M. Boyd, G. K. Campbell, P. Medley, W. Ketterle, and D. E. Pritchard. Continuous and pulsed quantum zeno effect. *Physical Review Letters*, 97:260402, 2006.

[58] J. M. Raimond, P. Facchi, B. Peaudecerf, S. Pascazio, C. Sayrin, I. Dotsenko, S. Gleyzes, M. Brune, and S. Haroche. Quantum zeno dynamics of a field in a cavity. *Physical Review A*, 86:032120, 2012.

[59] P. Facchi and S. Pascazio. Quantum zeno subspaces. *Physical Review Letters*, 89:080401, 2002.

[60] F. Schäfer, I. Herrera, S. Cherukattil, C. Lovecchio, F. S. Cataliotti, F. Caruso, and A. Smerzi. Experimental realization of quantum zeno dynamics. *Nat. Comm.*, 5(3194), 2014.

[61] A. Signoles, A. Facon, D. Grosso, I. Dotsenko, S. Haroche, J. M. Raimond,

M. Brune, and S. Gleyzes. Confined quantum zeno dynamics of a watched atomic arrow. *Nature Physics*, 10.1038/nphys3076, 2014.

[62] B. Misra and E. C. G. Sudarshan. The zeno's paradox in quantum theory. *Journal of Mathematical Physics*, 18:756, 1977.

[63] W. M. Itano, D. J. Heinzen, J. J. Bollinger, and D. J. Wineland. Quantum zeno effect. *Physical Review A*, 41:2295, 1990.

[64] T. Bhattacharya, S. Habib, and K. Jacobs. Continuous quantum measurement and the emergence of classical chaos. *Physical Review Letters*, 85:4852, 2000.

[65] K. Jacobs and D. Steck. Engineering quantum states, nonlinear measurements and anomalous diffusion by imaging. *New Journal of Physics*, 13:013016, 2011.

[66] J. Javanainen and J. Ruostekoski. Emergent classicality in continuous quantum measurements. *New Journal of Physics*, 15:013005, 2013.

[67] N. Erez, G. Gordon, M. Nest, and G. Kurizki. Thermodynamic control by frequent quantum measurements. *Nature*, 452:724, 2008.

[68] Y. S. Patil, S. Chakram, L. M. Aycock, and M. Vengalattore. Nondestructive imaging of an ultracold lattice gas. *Physical Review A*, 90(3):033422, 2014.

[69] J. J. Garcia-Ripoll, S. Dürr, N. Syassen, D. M. Bauer, M. Lettner, G. Rempe, and J. I. Cirac. Dissipation-induced hard-core boson gas in an optical lattice. *New Journal of Physics*, 11:013053, 2009.

[70] M. Holland, S. Marksteiner, P. Marte, and P. Zoller. Measurement induced localization from spontaneous decay. *Physical Review Letters*, 76:3683, 1996.

[71] M. J. Gagen, H. M. Wiseman, and G. J. Milburn. Continuous position measurements and the quantum zeno effect. *Physical Review A*, 48:132, 1993.

[72] J. I. Cirac, A. Schenzle, and P. Zoller. Inhibition of quantum tunneling of an atom due to the continuous observation of light scattering. *Europhysics Letters*, 27:123, 1994.

[73] Y. Yanay and E. J. Mueller. Heating from continuous number density measurements in optical lattices. *Physical Review A*, 90:023611, 2014.

[74] B. Zhu, B. Gadway, M. Foss-Feig, J. Schachenmayer, M. L. Wall, K. R. A. Hazzard, B. Yan, S. A. Moses, J. P. Covey, D. S. Jin, J. Ye, M. Holland, and A. M. Rey. Suppressing the loss of ultracold molecules via the continuous quantum zeno effect. *Physical Review Letters*, 112:070404, 2014.

[75] V. Giovannetti, S. Lloyd, and L. Maccone. Quantum-Enhanced Measurements: Beating the Standard Quantum Limit. *Science*, 306:1330–1336, 2004.

[76] V. Giovannetti, S. Lloyd, and L. Maccone. Advances in quantum metrology. *Nature Photonics*, 5:222–229, 2011.

[77] B. M. Escher, R. L. de Matos Filho, and L. Davidovich. General framework for estimating the ultimate precision limit in noisy quantum-enhanced metrology. *Nature Physics*, 7:406–411, 2011.

[78] M. Aspelmeyer, T. J. Kippenberg, and F. Marquardt. Cavity optomechanics. *Reviews of Modern Physics*, 86:1391, 2014.

[79] S. Chakram, Y. S. Patil, L. Chang, and M. Vengalattore. Dissipation in ultrahigh quality factor sin membrane resonators. *Physical Review Letters*, 112:127201, 2014.

[80] J. Moses, O. D. Mcke, and C. Vozzi. Special issue on optical parametric processes. *Journal of Optics*, 17(9):090201, 2015.

[81] O. Painter. Presentation at the Optomechanical Systems in the Quantum Regime Gordon Conference, 2018.

[82] A. H. Ghadimi, S. A. Fedorov, N. J. Engelsen, M. J. Bereyhi, R. Schilling, D. J. Wilson, and T. J. Kippenberg. Elastic strain engineering for ultralow mechanical dissipation. *Science*, 2018.

[83] S. Chakram, Y. S. Patil, and M. Vengalattore. Multimode phononic correlations in a nondegenerate parametric amplifier. *New Journal of Physics*, 17:063018, 2015.

[84] T. J. Kippenberg and K. J. Vahala. Cavity optomechanics: back-action at the mesoscale. *Science*, 321:1172, 2008.

[85] M. Aspelmeyer, P. Meystre, and K. Schwab. Quantum optomechanics. *Physics Today*, 65:29, 2012.

[86] P. Meystre. A short walk through quantum optomechanics. *Annalen der Physik*, 525:215, 2013.

[87] J. D. Teufel, T. Donner, D. Li, J. W. Harlow, M. S. Allman, K. Cicak, A. J. Sirois, J. D. Whittaker, K. W. Lehnert, and R. W. Simmonds. Sideband

cooling of micromechanical motion to the quantum ground state. *Nature*, 475:359, 2011.

[88] J. Chan, T. P. Mayer Alegre, A. H. Safavi-Naeini, J. T. Hill, A. Krause, S. Gröblacher, M. Aspelmeyer, and O. Painter. Laser cooling of a nanomechanical oscillator to its quantum ground state. *Nature*, 478:89, 2011.

[89] J. D. Teufel, T. Donner, M. A. Castellanos-Beltran, J. W. Harlow, and K. W. Lehnert. Nanomechanical motion measured with an imprecision below that at the standard quantum limit. *Nature Nanotechnology*, 4:820, 2009.

[90] G. Anetsberger, E. Gavartin, O. Arcizet, Q. P. Unterreithmeier, E. M. Weig, M. L. Gorodetsky, J. P. Kotthaus, and T. J. Kippenberg. Measuring nanomechanical motion with an imprecision far below the standard quantum limit. *Physical Review A*, 82:061804(R), 2010.

[91] D. Rugar and P. Grütter. Mechanical parametric amplification and thermomechanical noise squeezing. *Physical Review Letters*, 67:699, 1991.

[92] V. Natarajan, F. DiFilippo, and D. E. Pritchard. Classical squeezing of an oscillator for subthermal noise operation. *Physical Review Letters*, 74:2855, 1995.

[93] R. B. Karabalin, R. Lifshitz, M. C. Cross, M. H. Matheny, S. C. Masmanidis, and M. L. Roukes. Signal amplification by sensitive control of bifurcation topology. *Physical Review Letters*, 106:094102, 2011.

[94] T. Faust, J. Rieger, M. J. Seitner, J. P. Kotthaus, and E. M. Weig. Coherent control of a classical nanomechanical two-level system. *Nature Physics*, 9:485, 2013.

[95] I. Mahboob, H. Okamoto, K. Onomitsu, and H. Yamaguchi. Two-mode squeezing in an electromechanical resonator. *Physical Review Letters*, 113:167203, 2014.

[96] H. Seok, L. F. Buchmann, S. Singh, and P. Meystre. Optically mediated nonlinear quantum optomechanics. *Physical Review A*, 86:063829, 2012.

[97] A. D. O'Connell, M. Hofheinz, M. Ansmann, R. C. Bialczak, M. Lenander, E. Lucero, M. Neeley, D. Sank, H. Wang, M. Weides, J. Wenner, J. M. Martinis, and A. N. Cleland. Quantum ground state and single-phonon control of a mechanical resonator. *Nature*, 464:697, 2010.

[98] J. Suh, M. D. LaHaye, P. M. Echternach, K. C. Schwab, and M. L. Roukes. Parametric amplification and back-action noise squeezing by a qubit-coupled nanoresonator. *Nano Letters*, 10:3990, 2010.

[99] J. B. Hertzberg, T. Rocheleau, T. Ndukum, M. Savva, A. A. Clerk, and K. C. Schwab. Back-action-evading measurements of nanomechanical motion. *Nature Physics*, 6:213, 2010.

[100] J. Suh, A. J. Weinstein, C. U. Lei, E. E. Wollman, S. K. Steinke, P. Meystre, A. A. Clerk, and K. C. Schwab. Mechanically detecting and avoiding the quantum fluctuations of a microwave field. *Science*, 344:1262, 2014.

[101] A. Szorkovszky, G. A. Brawley, A. C. Doherty, and W. P. Bowen. Strong thermomechanical squeezing via weak measurement. *Physical Review Letters*, 110:184301, 2013.

[102] A. Vinante and P. Falferi. Feedback-enhanced parametric squeezing of mechanical motion. *Physical Review Letters*, 111:207203, 2013.

[103] A. Szorkovszky, A. A. Clerk, A. C. Doherty, and W. P. Bowen. Detuned mechanical parametric amplification as a quantum non-demolition measurement. *New Journal of Physics*, 16:043023, 2014.

[104] A. Pontin, M. Bonaldi, A. Borrielli, F. S. Cataliotti, F. Marino, G. A. Prodi, E. Serra, and F. Marin. Detection of weak stochastic forces in a parametrically stabilized micro-optomechanical system. *Physical Review A*, 89:023848, 2014.

[105] S. Diehl, A. Micheli, A. Kantian, B. Kraus, H. P. Büchler, and P. Zoller. Quantum states and phases in driven open quantum systems with cold atoms. *Nature Physics*, 4:878, 2008.

[106] A. Tomadin, S. Diehl, M. D. Lukin, P. Rabl, and P. Zoller. Reservoir engineering and dynamical phase transitions in optomechanical arrays. *Physical Review A*, 86:033821, 2012.

[107] H. Tan, G. Li, and P. Meystre. Dissipation driven two-mode mechanical squeezed states in optomechanical systems. *Physical Review A*, 87:033829, 2013.

[108] Y. Wang and A. A. Clerk. Reservoir-engineered entanglement in optomechanical systems. *Physical Review Letters*, 110:253601, 2013.

[109] T. P. Purdy, P.-L. Yu, N. S. Kampel, R. W. Peterson, K. Cicak, R. W. Simmonds, and C. A. Regal. Optomechanical Raman-ratio thermometry. *Physical Review A*, 92(3):031802, 2015.

[110] M. Underwood, D. Mason, D. Lee, H. Xu, L. Jiang, A. B. Shkarin, K. Børkje, S. M. Girvin, and J. G. E. Harris. Measurement of the motional

sidebands of a nanogram-scale oscillator in the quantum regime. *Physical Review A*, 92(6):061801, 2015.

[111] E. Gavartin, P. Verlot, and T. J. Kippenberg. Stabilization of a linear nanomechanical oscillator to its thermodynamic limit. *Nature Communications*, 4:2860, 2013.

[112] R. Tang, J. Lasri, P. S. Devgan, V. Grigoryan, P. Kumar, and M. Vasilyev. Gain characteristics of a frequency nondegenerate phase-sensitive fiber-optic parametric amplifier with phase self-stabilized input. *Optics Express*, 13:10483, 2005.

[113] M. D. Reid and P. D. Drummond. Quantum correlations of phase in non-degenerate parametric oscillation. *Physical Review Letters*, 60:2731, 1988.

[114] B.D. Hauer, C. Doolin, K.S.D. Beach, and J.P. Davis. A general procedure for thermomechanical calibration of nano/micro-mechanical resonators. *Annals of Physics*, 339:181 – 207, 2013.

[115] R. Lifshitz and M. C. Cross. Nonlinear dynamics of nanomechanical and micromechanical resonators. In H. G. Schuster, editor, *Reviews of nonlinear dynamics and complexity*, page 1, 2008.

[116] R. H. Dicke. Coherence in spontaneous radiation processes. *Physical Review*, 93:99, 1954.

[117] K. Hepp and E. H. Lieb. On the superradiant phase transition for molecules in a quantized radiation field: the dicke maser model. *Annals of Physics*, 76:360–404, 1973.

[118] K. Hepp and E. H. Lieb. Equilibrium statistical mechanics of matter inter-acting with the quantized radiation field. *Physical Review A*, 8:2517–2525, 1973.

[119] Y. K. Wang and F. T. Hioe. Phase transition in the dicke model of superra-diance. *Physical Review A*, 7:831–836, 1973.

[120] P. Alsing and H. J. Carmichael. Spontaneous dressed-state polarization of a coupled atom and cavity mode. *Quantum Optics*, 3:13–32, 1991.

[121] C. Emary and T. Brandes. Chaos and the quantum phase transition in the Dicke model. *Physical Review E*, 67:066203, 2003.

[122] E. M. Kessler, G. Giedke, A. Imamoglu, S. F. Yelin, M. D. Lukin, and J. I. Cirac. Dissipative phase transition in a central spin system. *Physical Re-view A*, 86:012116, 2012.

[123] M. J. Bhaseen, J. Mayoh, B. D. Simons, and J. Keeling. Dynamics of nonequilibrium Dicke models. *Physical Review A*, 85:013817, 2012.

[124] J. M. Fink, A. Dombi, A. Vukics, A. Wallraff, and P. Domokos. Observation of the photon-blockade breakdown phase transition. *Physical Review X*, 7:011012, 2017.

[125] M. Fitzpatrick, N. M. Sundaresan, A. C. Y. Li, J. Koch, and A. A. Houck. Observation of a dissipative phase transition in a one-dimensional circuit qed lattice. *Physical Review X*, 7:011016, 2017.

[126] T. Vojta. Quantum phase transitions in electronic systems. *Annalen der Physik*, 9(6):403–440, 2000.

[127] S. Sachdev. *Quantum Phase Transitions*. Cambridge University Press, 2011.

[128] *Understanding Quantum Phase Transitions (Condensed Matter Physics), Edited by L. D. Carr*. CRC Press, 2010.

[129] A. Del Campo and W. H. Zurek. Universality of phase transition dynamics: Topological defects from symmetry breaking. *International Journal of Modern Physics A*, 29:1430018, 2014.

[130] W. Casteels, F. Storme, A. Le Boité, and C. Ciuti. Power laws in the dynamic hysteresis of quantum nonlinear photonic resonators. *Physical Review A*, 93:033824, 2016.

[131] S. R. K. Rodriguez, W. Casteels, F. Storme, N. Carlon Zambon, I. Sagnes, L. Le Gratiet, E. Galopin, A. Lemaître, A. Amo, C. Ciuti, and J. Bloch. Probing a dissipative phase transition via dynamical optical hysteresis. *Physical Review Letters*, 118:247402, 2017.

[132] M. Campisi, P. Hänggi, and P. Talkner. Colloquium: Quantum fluctuation relations: Foundations and applications. *Reviews of Modern Physics*, 83(3):771–791, 2011.

[133] R. Zwanzig. *Nonequilibrium Statistical Mechanics*. Oxford University Press, 2001.

[134] S. R. De Groot. *Non-Equilibrium Thermodynamics*. Dover Publications, 2013.

[135] I. Rotter and J. P. Bird. A review of progress in the physics of open quantum systems: theory and experiment. *Reports on Progress in Physics*, 78(11):114001, 2015.

[136] L. M. Sieberer, M. Buchhold, and S. Diehl. Keldysh field theory for driven open quantum systems. *Reports on Progress in Physics*, 79:096001, 2016.

[137] L. M. Sieberer, S. D. Huber, E. Altman, and S. Diehl. Dynamical critical phenomena in driven-dissipative systems. *Physical Review Letters*, 110:195301, 2013.

[138] J. Marino and S. Diehl. Driven markovian quantum criticality. *Physical Review Letters*, 116:070407, 2016.

[139] U. C. Täuber. Phase transitions and scaling in systems far from equilibrium. *Annual Review of Condensed Matter Physics*, 8(1):185–210, 2017.

[140] X.-G. Wen. Colloquium: Zoo of quantum-topological phases of matter. *Reviews of Modern Physics*, 89(4):041004, 2017.

[141] D. Nagy and P. Domokos. Nonequilibrium quantum criticality and non-markovian environment: Critical exponent of a quantum phase transition. *Physical Review Letters*, 115:043601, 2015.

[142] D. Nagy and P. Domokos. Critical exponent of quantum phase transitions driven by colored noise. *Physical Review A*, 94:063862, 2016.

[143] H. F. H. Cheung, Y. S. Patil, and M. Vengalattore. Emergent phases and novel critical behavior in a non-Markovian open quantum system. *arXiv:1707.02622*, 2017.

[144] L. Wu, H. J. Kimble, J. L. Hall, and H. Wu. Generation of squeezed states by parametric down conversion. *Physical review letters*, 57(20):2520, 1986.

[145] K. Baumann, C. Guerlin, F. Brennecke, and T. Esslinger. Dicke quantum phase transition with a superfluid gas in an optical cavity. *Nature*, 464:1301, 2010.

[146] A. H. Safavi-Naeini, T.P.M. Alegre, J. Chan, M. Eichenfield, M. Winger, Q. Lin, J.T. Hill, D.E. Chang, and O. Painter. Electromagnetically induced transparency and slow light with optomechanics. *Nature*, 472:69–73, 2011.

[147] E. G. Dalla Torre, S. Diehl, M. D. Lukin, S. Sachdev, and P. Strack. Keldysh approach for non-equilibrium phase transitions in quantum optics : beyond the dicke model in optical cavities. *Physical Review A*, 87:023831, 2013.

[148] J. Klinder, H. Kessler, M. Wolke, L. Mathey, and A. Hemmerich. Dynamical phase transition in the open Dicke model. *Proceedings of the National Academy of Sciences*, 112:3290, 2015.

[149] J. Léonard, A. Morales, P. Zupancic, T. Esslinger, and T. Donner. Supersolid formation in a quantum gas breaking a continuous translational symmetry. *Nature*, 543:87, 2017.

[150] Y. S. Patil, S. Chakram, L. Chang, and M. Vengalattore. Thermomechanical two-mode squeezing in an ultrahigh Q membrane resonator. *Physical Review Letters*, 115:017202, 2015.

[151] U. Weiss. *Quantum dissipative systems*. World Scientific, 2008.

[152] P. C. Hohenberg and B. I. Halperin. Theory of dynamic critical phenomena. *Reviews of Modern Physics*, 49:435–479, 1977.

[153] A. Chandran, A. Erez, S. S. Gubser, and S. L. Sondhi. Kibble-zurek problem: Universality and the scaling limit. *Physical Review B*, 86:064304, 2012.

[154] J. A. Hoyos, C. Kotabage, and T. Vojta. Effects of dissipation on a quantum critical point with disorder. *Physical Review Letters*, 99:230601, 2007.

[155] E. G. Dalla Torre, E. Demler, T. Giamarchi, and E. Altman. Quantum critical states and phase transitions in the presence of non-equilibrium noise. *Nature Physics*, 6:806, 2010.

[156] M. Buchhold, P. Strack, S. Sachdev, and S. Diehl. Dicke-model quantum spin and photon glass in optical cavities: Nonequilibrium theory and experimental signatures. *Physical Review A*, 87:063622, 2013.

[157] H. P. Breuer, E. M. Laine, J. Piilo, and B. Vacchini. Colloquium: Non-markovian dynamics in open quantum systems. *Reviews of Modern Physics*, 88:021002, 2016.

[158] E. A. Calzetta and B. B. Hu. *Nonequilibrium Quantum Field Theory*. Cambridge Monographs on Mathematical Physics. Cambridge University Press, 2008.

[159] J. Bonart, L. F. Cugliandolo, and A. Gambassi. Critical Langevin dynamics of the O(N) Ginzburg-Landau model with correlated noise. *Journal of Statistical Mechanics: Theory and Experiment*, 2012(01):P01014, 2012.

[160] C. Jarzynski. Nonequilibrium equality for free energy differences. *Physical Review Letters*, 78:2690–2693, 1997.

[161] C. Jarzynski. Comparison of far-from-equilibrium work relations. *Comptes Rendus Physique*, 8(5-6):495–506, 2007.

[162] J. Zhang, P. W. Hess, A. Kyprianides, P. Becker, A. Lee, J. Smith, G. Pagano, I.-D. Potirniche, A. C. Potter, A. Vishwanath, N. Y. Yao, and C. Monroe. Observation of a discrete time crystal. *Nature*, 543:217, 2017.

[163] S. Choi, J. Choi, R. Landig, G. Kucsko, H. Zhou, J. Isoya, F. Jelezko, S. Onoda, H. Sumiya, V. Khemani, C. von Keyserlingk, N. Y. Yao, E. Demler,

and M. D. Lukin. Observation of discrete time-crystalline order in a disordered dipolar many-body system. *Nature*, 543:221, 2017.

[164] G. Heinrich, M. Ludwig, J. Qian, B. Kubala, and F. Marquardt. Collective dynamics in optomechanical arrays. *Physical Review Letters*, 107:043603, 2011.

[165] M. Ludwig and F. Marquardt. Quantum many-body dynamics in optomechanical arrays. *Physical Review Letters*, 111:073603, 2013.

[166] F. Verstraete, M. M. Wolf, and J. I. Cirac. Quantum computation and quantum-state engineering driven by dissipation. *Nature Physics*, 5:633, 2009.

[167] M. Müller, S. Diehl, G. Pupillo, and P. Zoller. Engineered open systems and quantum simulations with atoms and ions. *Advances In Atomic, Molecular, and Optical Physics*, 61:1, 2012.

[168] J. T. Barreiro, M. Müller, P. Schindler, D. Nigg, T. Monz, M. Chwalla, M. Hennrich, C. F. Roos, P. Zoller, and R. Blatt. An open-system quantum simulator with trapped ions. *Nature*, 470:486–491, 2011.

[169] H. Krauter, C. A. Muschik, K. Jensen, W. Wasilewski, J. M. Petersen, J. I. Cirac, and E. S. Polzik. Entanglement generated by dissipation and steady state entanglement of two macroscopic objects. *Physical Review Letters*, 107:080503, 2011.

[170] P. D. Drummond and K. Dechoum. Universality of quantum critical dynamics in a planar optical parametric oscillator. *Physical Review Letters*, 95:083601, 2005.

[171] C. Gardiner. *Stochastic Methods: A Handbook for the Natural and Social Sciences (Springer Series in Synergetics)*. Springer, 2010.

[172] A. H. Romero and J. M. Sancho. Generation of short and long range temporal correlated noises. *Journal of Computational Physics*, 156(1):1 – 11, 1999.

[173] C. M. Caves, K. S. Thorne, R. W. P. Drever, V. D. Sandberg, and M. Zimmermann. On the measurement of a weak classical force coupled to a quantum-mechanical oscillator. 1. issues of principle. *Reviews of Modern Physics*, 52:341, 1980.

[174] V. B. Braginsky, Y. I. Vorontsov, and K. S. Thorne. Quantum nondemolition measurements. *Science*, 209:547, 1980.

[175] R. S. Bondurant and J. H. Shapiro. Squeezed states in phase-sensing interferometers. *Physical Review D*, 30:2548–2556, 1984.

[176] K. S. Thorne, R. W. P. Drever, C. M. Caves, M. Zimmermann, and V. D. Sandberg. Quantum nondemolition measurements of harmonic oscillators. *Physical Review Letters*, 40:667, 1978.

[177] T. Caniard, P. Verlot, T. Briant, P.-F. Cohadon, and A. Heidmann. Observation of back-action noise cancellation in interferometric and weak force measurements. *Physical Review Letters*, 99:110801, 2007.

[178] E. S. Polzik and K. Hammerer. Trajectories without quantum uncertainties. *Annalen der Physik*, 527:A15–A20, 2015.

[179] M. Tsang and C. M. Caves. Coherent quantum-noise cancellation for optomechanical sensors. *Physical Review Letters*, 105:123601, 2010.

[180] W. Wasilewski, K. Jensen, H. Krauter, J. J. Renema, M. V. Balabas, and E. S. Polzik. Quantum noise limited and entanglement-assisted magnetometry. *Physical Review Letters*, 104:133601, 2010.

[181] W. G. Unruh. Quantum nondemolition and gravity-wave detection. *Physical Review D*, 19:2888–2896, 1979.

[182] M. Tsang and C. Caves. Evading quantum mechanics: Engineering a classical subsystem within a quantum environment. *Physical Review X*, 2:031016, 2012.

[183] A. A. Clerk, F. Marquardt, and K. Jacobs. Back-action evasion and squeezing of a mechanical resonator using a cavity detector. *New Journal of Physics*, 10(9):095010, 2008.

[184] T. P. Purdy, R. W. Peterson, and C. A. Regal. Observation of radiation pressure shot noise on a macroscopic object. *Science*, 339(6121):801–804, 2013.

[185] A. Metelmann and A. A. Clerk. Quantum-limited amplification via reservoir engineering. *Physical Review Letters*, 112:133904, 2014.

[186] S. Mancini, V. Giovannetti, D. Vitali, and P. Tombesi. Entangling macroscopic oscillators exploiting radiation pressure. *Physical Review Letters*, 88:120401, 2002.

[187] A. D. Armour, M. P. Blencowe, and K. C. Schwab. Entanglement and decoherence of a micromechanical resonator via coupling to a cooper-pair box. *Physical Review Letters*, 88:148301, 2002.

[188] J. R. Johansson, N. Lambert, I. Mahboob, H. Yamaguchi, and F. Nori.

Entangled-state generation and bell inequality violations in nanomechanical resonators. *Physical Review B*, 90:174307, 2014.

[189] M. Paternostro, D. Vitali, S. Gigan, M. S. Kim, Č. Brukner, J. Eisert, and M. Aspelmeyer. Creating and probing multipartite macroscopic entanglement with light. *Physical Review Letters*, 99:250401, 2007.

[190] D. Vitali, S. Gigan, A. Ferreira, H. R. Böhm, P. Tombesi, A. Guerreiro, V. Vedral, A. Zeilinger, and M. Aspelmeyer. Optomechanical entanglement between a movable mirror and a cavity field. *Physical Review Letters*, 98:030405, 2007.

[191] K. Zhang, F. Bariani, and P. Meystre. Theory of an optomechanical quantum heat engine. *Physical Review A*, 90:023819, 2014.

[192] M. Brunelli, A. Xuereb, A. Ferraro, G. De Chiara, N. Kiesel, and M. Paternostro. Out-of-equilibrium thermodynamics of quantum optomechanical systems. *New Journal of Physics*, 17(3):035016, 2015.

[193] S. Habib, K. Jacobs, H. Mabuchi, R. Ryne, K. Shizume, and B. Sundaram. The quantum classical transition in nonlinear dynamical systems. *Physical Review Letters*, 88:040402, 2002.

[194] I. Katz, R. Lifshitz, A. Retzker, and R. Straub. Classical to quantum transition of a driven nonlinear nanomechanical resonator. *New Journal of Physics*, 10:125023, 2008.

[195] M. Ludwig, B. Kubala, and F. Marquardt. The optomechanical instability in the quantum regime. *New Journal of Physics*, 10(9):095013, 2008.

[196] A. Clerk, M. Devoret, S. Girvin, Florian Marquardt, and R. Schoelkopf.

Introduction to quantum noise, measurement, and amplification. *Reviews of Modern Physics*, 82:1155–1208, 2010.

[197] M. Woolley and A. Clerk. Two-mode back-action-evading measurements in cavity optomechanics. *Physical Review A*, 87:063846, 2013.

[198] A. Szorkovszky, A. A. Clerk, A. C. Doherty, and W. P. Bowen. Mechanical entanglement via detuned parametric amplification. *New Journal of Physics*, 16(6):063043, 2014.

[199] C. A. Muschik, K. Hammerer, E. S. Polzik, and I. J. Cirac. Quantum teleportation of dynamics and effective interactions between remote systems. *Physical Review Letters*, 111:020501, 2013.

[200] L Tian, M S Allman, and R W Simmonds. Parametric coupling between macroscopic quantum resonators. *New Journal of Physics*, 10(11):115001, 2008.

[201] W. W. Johnson and M. Bocko. Approaching the quantum limit for force detection. *Physical Review Letters*, 47:1184, 1981.

[202] M. Blencowe. Quantum electromechanical systems. *Physics Reports*, 395:159, 2004.

[203] K. C. Schwab and M. L. Roukes. Putting mechanics into quantum mechanics. *Physics Today*, 58:36, 2005.

[204] M. Poot and H. S. J. van der Zant. Mechanical systems in the quantum regime. *Physics Reports*, 511:273, 2012.

[205] M. R. Vanner, J. Hofer, G. D. Cole, and M. Aspelmeyer. Cooling-by-

measurement and mechanical state tomography via pulsed optomechanics. *Nature communications*, 4:2295, 2013.

[206] S. Mancini, V. I. Man'ko, and P. Tombesi. Ponderomotive control of quantum macroscopic coherence. *Physical Review A*, 55:3042, 1997.

[207] S. Bose, K. Jacobs, and P. L. Knight. Preparation of nonclassical states in cavities with a moving mirror. *Physical Review A*, 56:4175, 1997.

[208] K. Zhang, F. Bariani, and P. Meystre. Quantum optomechanical heat engine. *Physical Review Letters*, 112:150602, 2014.

[209] M. Woolley and A. A. Clerk. Two-mode squeezed states in cavity optomechanics via engineering of a single reservoir. *Physical Review A*, 89:063805, 2014.

[210] H. Okamoto, A. Gourgout, C. Chang, K. Onomitsu, I. Mahboob, E. Y. Chang, and H. Yamaguchi. Coherent phonon manipulation in coupled mechanical resonators. *Nature Physics*, 9(8):480–484, 2013.

[211] M. D. Reid. Demonstration of the einstein-podolsky-rosen paradox using nondegenerate parametric amplification. *Physical Review A*, 40:913, 1989.

[212] Z. Y. Ou, S. F. Pereira, H. J. Kimble, and K. C. Peng. Realization of the einstein-podolsky-rosen paradox for continuous variables. *Physical Review Letters*, 68:3663–3666, 1992.

[213] S. L. Braunstein and P. van Loock. Quantum information with continuous variables. *Reviews of Modern Physics*, 77:513–577, 2005.

[214] S. F. Pereira, Z. Y. Ou, and H. J. Kimble. Quantum communication with correlated nonclassical states. *Physical Review A*, 62(4):042311, 2000.

[215] R. Ursin, F. Tiefenbacher, T. Schmitt-Manderbach, H. Weier, T. Scheidl, M. Lindenthal, B. Blauensteiner, T. Jennewein, J. Perdigues, P. Trojek, B. Ömer, M. Fürst, M. Meyenburg, J. Rarity, Z. Sodnik, C. Barbieri, H. Weinfurter, and A. Zeilinger. Entanglement-based quantum communication over 144km. *Nature Physics*, 3:481–486, July 2007.

[216] F. Hudelist, J. Kong, C. Liu, J. Jing, Z. Y. Ou, and W. Zhang. Quantum metrology with parametric amplifier-based photon correlation interferometers. *Nature Communications*, 5:3049, 2013.

[217] M. J. Woolley, G. J. Milburn, and C. M. Caves. Nonlinear quantum metrology using coupled nanomechanical resonators. *New Journal of Physics*, 10:125018, 2008.

[218] S. Gröblacher, A. Trubarov, N. Prigge, G. D. Cole, M. Aspelmeyer, and J. Eisert. Observation of non-Markovian micro-mechanical Brownian motion. *Nature Communications*, 6:7606, 2015.

[219] A. F. Estrada and L. A. Pachón. Quantum limit for driven linear non-markovian open-quantum-systems. *New Journal of Physics*, 17(3):033038, 2015.

[220] B. M. Zwickl, W. E. Shanks, A. M. Jayich, C. Yang, A. C. Bleszynski Jayich, J. D. Thompson, and J. G. E. Harris. High quality mechanical and optical properties of commercial silicon nitride membranes. *Applied Physics Letters*, 92(10):103125–103125, 2008.

[221] J. D. Thompson, B. M. Zwickl, A. M. Jayich, F. Marquadt, S. M. Girvin, and J. G. E. Harris. Strong dispersive coupling of a high-finesse cavity to a micromechanical membrane. *Nature*, 452:72, 2008.

[222] C. Fabre, E. Giacobino, A. Heidmann, and S. Reynaud. Noise characteristics of a nondegenerate optical parametric oscillator - application to quantum noise reduction. *Journal de Physique*, 50:1209, 1989.

[223] J. Martinez-Linares and P. Garcia-Fernandez. Non-classical properties of non-degenerate parametric amplifiers and oscillators with pump depletion and non-homogeneous losses using the wigner representation. *Journal of Modern Optics*, 41(1):67, 1994.

[224] G. Milburn and D. F. Walls. Production of squeezed states in a degenerate parametric amplifier. *Optics Communications*, 39:401, 1981.

[225] C. C. Gerry. Ground-state phase transitions of the degenerate parametric amplifier. *Physical Review A*, 37:3619, 1988.

[226] C. J. Mertens, T. A. B. Kennedy, and S. Swain. Many-body quantum theory of the optical parametric oscillator. *Physical Review A*, 48:2374, 1993.

[227] P. Kinsler and P. D. Drummond. Critical fluctuations in the quantum parametric oscillator. *Physical Review A*, 52:783, 1995.

[228] K. Dechoum, P. D. Drummond, S. Chaturvedi, and M. D. Reid. Critical fluctuations and entanglement in the nondegenerate parametric amplifier. *Physical Review A*, 70:053807, 2004.

[229] T. Ramos, V. Sudhir, K. Stannigel, P. Zoller, and T. J. Kippenberg. Nonlinear quantum optomechanics via individual intrinsic two-level defects. *Physical Review Letters*, 110:193602, 2013.

[230] Á. Rivas and S. F. Huelga. *Open Quantum Systems*. Springer, 2012.

[231] I. de Vega and D. Alonso. Dynamics of non-Markovian open quantum systems. *Reviews of Modern Physics*, 89:15001, 2017.

[232] P. Schindler, M. Müller, D. Nigg, J. T. Barreiro, E. A. Martinez, M. Hennrich, T. Monz, S. Diehl, P. Zoller, and R. Blatt. Quantum simulation of open-system dynamical maps with trapped ions. *Nature Physics*, 9:361, 2012.

[233] Z. Xiang, S. Ashhab, J. Q. You, and F. Nori. Hybrid quantum circuits : Superconducting circuits interacting with other quantum systems. *Reviews of Modern Physics*, 85:623, 2013.

[234] M. Wouters and I. Carusotto. Goldstone mode of optical parametric oscillators in planar semiconductor microcavities in the strong-coupling regime. *Physical Review A*, 76:043807, 2007.

[235] H. J. Lipkin, N. Meshkov, and A. J. Glick. Validity of many-body approximation methods for a solvable model : (i). exact solutions and perturbation theory. *Nuclear Physics*, 62:188, 1965.

[236] D. Nagy, G. Szirmai, and P. Domokos. Critical exponent of a quantum-noise-driven phase transition : The open-system Dicke model. *Physical Review A*, 84:043637, 2011.

[237] D. M. Reich, N. Katz, and C. P. Koch. Exploiting non-markovianity for quantum control. *Scientific Reports*, 5:12430, 2015.

[238] M. Cianciaruso, S. Maniscalco, and G. Adesso. Role of non-markovianity and backflow of information in the speed of quantum evolution. *Physical Review A*, 96:012105, 2017.

[239] I. Wilson-Rae. Intrinsic dissipation in nanomechanical resonators due to phonon tunnelling. *Physical Review B*, 77:245418, 2008.

[240] F. Bariani, S. Singh, L. F. Buchmann, M. Vengalattore, and P. Meystre. Hybrid optomechanical cooling by atomic lambda systems. *Physical Review A*, 90:033838, 2014.

[241] F. Bariani, H. Soek, S. Singh, M. Vengalattore, and P. Meystre. Atom-based coherent quantum-noise cancellation in optomechanics. *Physical Review A*, 92:043817, 2015.

[242] M. Höning, M. Moos, and M. Fleischhauer. Critical exponents of steady-state phase transitions in fermionic lattice models. *Physical Review A*, 86:013606, 2012.

[243] T. Kato. *Perturbation theory for linear operators*. Springer Berlin, 1966.

[244] W. D. Heiss. The physics of exceptional points. *Journal of Physics A: Mathematical and Theoretical*, 45:444016, 2012.

[245] S. Strogatz. *Nonlinear dynamics and chaos*. Perseus, 1994.

[246] J. E. Marsden and M. McCracken. *The Hopf Bifurcation and its applications*. Springer-Verlag, 1976.

[247] J. Guckenheimer and P. Holmes. *Nonlinear Oscillations, Dynamical Systems, and Bifurcations of Vector Fields*. Springer-Verlag, 1983.

[248] C. Chan, T. E. Lee, and S. Gopalakrishnan. Limit-cycle phase in driven-dissipative spin systems. *Physical Review A*, 91:051601(R), 2015.

[249] A. Peres. Separability criterion for density matrices. *Physical Review Letters*, 77:1413, 1996.

[250] M. B. Plenio. Logarithmic Negativity : A full entanglement monotone that is not convex. *Physical Review Letters*, 95:090503, 2005.

[251] H. F. H. Cheung, Y. S. Patil, L. Chang, S. Chakram, and M. Vengalattore. Nonlinear phonon interferometry at the Heisenberg limit. *arXiv:1601.02324*, 2016.

[252] D. Leibfried, M. D. Barrett, T. Schaetz, J. Britton, J. Chiaverini, W. M. Itano, J. D. Jost, C. Langer, and D. J. Wineland. Toward heisenberg-limited spectroscopy with multiparticle entangled states. *Science*, 304:1476, 2004.

[253] K. Hammerer, M. Aspelmeyer, E. S. Polzik, and P. Zoller. Establishing einstein-poldosky-rosen channels between nanomechanics and atomic ensembles. *Physical Review Letters*, 102:020501, 2009.

[254] M. Tsang and C. M. Caves. Evading quantum mechanics: Engineering a classical subsystem within a quantum environment. *Physical Review X*, 2:031016, 2012.

[255] M. Napolitano, M. Koschorreck, B. Dubost, N. Behbood, R. J. Sewell, and M. W. Mitchell. Interaction-based quantum metrology showing scaling beyond the heisenberg limit. *Nature*, 471:486, 2011.

[256] B. Yurke, S. L. McCall, and J. R. Klauder. Su(2) and su(1,1) interferometers. *Physical Review A*, 33:4033–4054, 1986.

[257] C. Gross, T. Zibold, E. Nicklas, J. Estève, and M. K. Oberthaler. Nonlinear atom interferometer surpasses classical precision limit. *Nature*, 464:1165–1169, 2010.

[258] M. Yuan, M. A. Cohen, and G. A. Steele. Silicon nitride membrane resonators at millikelvin temperatures with quality factors exceeding 10^8. *Applied Physics Letters*, 107(26):263501, 2015.

[259] C. Reinhardt, T. Müller, A. Bourassa, and J. C. Sankey. Ultralow-Noise SiN Trampoline Resonators for Sensing and Optomechanics. *Physical Review X*, 6(2):021001, 2016.

[260] R. A. Norte, J. P. Moura, and S. Gröblacher. Mechanical Resonators for Quantum Optomechanics Experiments at Room Temperature. *Physical Review Letters*, 116(14):147202, 2016.

[261] A. Pontin, M. Bonaldi, A. Borrielli, L. Marconi, F. Marino, G. Pandraud, G. A. Prodi, P. M. Sarro, E. Serra, and F. Marin. Dynamical Two-Mode Squeezing of Thermal Fluctuations in a Cavity Optomechanical System. *Physical Review Letters*, 116(10):103601, 2016.

[262] K. L. Ekinci, X. M. H. Huang, and M. L. Roukes. Ultrasensitive nanoelectromechanical mass detection. *Applied Physics Letters*, 84, 2004.

[263] Y. T. Yang, C. Callegari, X. L. Feng, K. L. Ekinci, and M. L. Roukes. Zeptogram-Scale Nanomechanical Mass Sensing. *Nano Letters*, 6:583–586, 2006.

[264] K. Jensen, K. Kim, and A. Zettl. An atomic-resolution nanomechanical mass sensor. *Nature Nanotechnology*, 3:533–537, 2008.

[265] A. Luis. Nonlinear transformation and the heisenberg limit. *Physics Letters A*, 329:8–13, 2004.

[266] A. Luis. Quantum limits, nonseparable transformations, and nonlinear optics. *Physical Review A*, 76:035801, 2007.

[267] W. Zhang, M. J. Martin, C. Benko, J. L. Hall, J. Ye, C. Hagemann, T. Legero, U. Sterr, F. Riehle, G. D. Cole, and M. Aspelmeyer. Reduction of residual amplitude modulation to 1×10^{-6} for frequency modulation and laser stabilization. *Optics Letters*, 39:1980, 2014.

[268] M. Wolinsky and H. J. Carmichael. Squeezing in the degenerate parametric oscillator. *Optics Communications*, 55(2):138 − 142, 1985.

[269] H. J. Carmichael and M. Wolinsky. Squeezing in the degenerate parametric oscillator using the positive p-representation. In J. D. Harvey and D. F. Walls, editors, *Quantum Optics IV*, pages 208–220, Berlin, Heidelberg, 1986. Springer Berlin Heidelberg.